

Roman Szewczyk
Cezary Zieliński
Małgorzata Kaliczyńska *Editors*

Progress in Automation, Robotics and Measuring Techniques

Volume 3 Measuring Techniques and
Systems

Advances in Intelligent Systems and Computing

Volume 352

Series editor

Janusz Kacprzyk, Polish Academy of Sciences, Warsaw, Poland
e-mail: kacprzyk@ibspan.waw.pl

About this Series

The series “Advances in Intelligent Systems and Computing” contains publications on theory, applications, and design methods of Intelligent Systems and Intelligent Computing. Virtually all disciplines such as engineering, natural sciences, computer and information science, ICT, economics, business, e-commerce, environment, healthcare, life science are covered. The list of topics spans all the areas of modern intelligent systems and computing.

The publications within “Advances in Intelligent Systems and Computing” are primarily textbooks and proceedings of important conferences, symposia and congresses. They cover significant recent developments in the field, both of a foundational and applicable character. An important characteristic feature of the series is the short publication time and world-wide distribution. This permits a rapid and broad dissemination of research results.

Advisory Board

Chairman

Nikhil R. Pal, Indian Statistical Institute, Kolkata, India
e-mail: nikhil@isical.ac.in

Members

Rafael Bello, Universidad Central “Marta Abreu” de Las Villas, Santa Clara, Cuba
e-mail: rbellop@uclv.edu.cu

Emilio S. Corchado, University of Salamanca, Salamanca, Spain
e-mail: escorchado@usal.es

Hani Hagras, University of Essex, Colchester, UK
e-mail: hani@essex.ac.uk

László T. Kóczy, Széchenyi István University, Győr, Hungary
e-mail: koczy@sze.hu

Vladik Kreinovich, University of Texas at El Paso, El Paso, USA
e-mail: vladik@utep.edu

Chin-Teng Lin, National Chiao Tung University, Hsinchu, Taiwan
e-mail: ctlin@mail.nctu.edu.tw

Jie Lu, University of Technology, Sydney, Australia
e-mail: Jie.Lu@uts.edu.au

Patricia Melin, Tijuana Institute of Technology, Tijuana, Mexico
e-mail: epmelin@hafsamx.org

Nadia Nedjah, State University of Rio de Janeiro, Rio de Janeiro, Brazil
e-mail: nadia@eng.uerj.br

Ngoc Thanh Nguyen, Wroclaw University of Technology, Wroclaw, Poland
e-mail: Ngoc-Thanh.Nguyen@pwr.edu.pl

Jun Wang, The Chinese University of Hong Kong, Shatin, Hong Kong
e-mail: jwang@mae.cuhk.edu.hk

More information about this series at <http://www.springer.com/series/11156>

Roman Szewczyk · Cezary Zieliński
Małgorzata Kaliczyńska
Editors

Progress in Automation, Robotics and Measuring Techniques

Volume 3 Measuring
Techniques and Systems

 Springer

Editors

Roman Szewczyk
Industrial Research Institute for Automation
and Measurements PIAP
Warsaw
Poland

Małgorzata Kaliczyńska
Industrial Research Institute for Automation
and Measurements PIAP
Warsaw
Poland

Cezary Zieliński
Industrial Research Institute for Automation
and Measurements PIAP
Warsaw
Poland

ISSN 2194-5357 ISSN 2194-5365 (electronic)
Advances in Intelligent Systems and Computing
ISBN 978-3-319-15834-1 ISBN 978-3-319-15835-8 (eBook)
DOI 10.1007/978-3-319-15835-8

Library of Congress Control Number: 2015931809

Springer Cham Heidelberg New York Dordrecht London

© Springer International Publishing Switzerland 2015

This work is subject to copyright. All rights are reserved by the Publisher, whether the whole or part of the material is concerned, specifically the rights of translation, reprinting, reuse of illustrations, recitation, broadcasting, reproduction on microfilms or in any other physical way, and transmission or information storage and retrieval, electronic adaptation, computer software, or by similar or dissimilar methodology now known or hereafter developed.

The use of general descriptive names, registered names, trademarks, service marks, etc. in this publication does not imply, even in the absence of a specific statement, that such names are exempt from the relevant protective laws and regulations and therefore free for general use.

The publisher, the authors and the editors are safe to assume that the advice and information in this book are believed to be true and accurate at the date of publication. Neither the publisher nor the authors or the editors give a warranty, express or implied, with respect to the material contained herein or for any errors or omissions that may have been made.

Printed on acid-free paper

Springer International Publishing AG Switzerland is part of Springer Science+Business Media
(www.springer.com)

Foreword

Control, automation, robotics and measuring techniques have been paramount to the development of industry in the last few decades. As currently the process of reindustrialization of European Union has gained importance, so have the mentioned disciplines. For this reason, both theoretical and application oriented developments in automation, robotics and measuring techniques are at the focus of interest of the scientific and engineering community.

It should be underscored that automation, robotics and measuring techniques have a significant innovative potential. In the case of automation and control, currently this potential is mainly connected with discrete systems, emergence of new actuators and sensors, new diagnostic methods, as well as modern design approaches exemplified by fuzzy logic, evolutionary computation, neural networks, probabilistic methods etc.

Development of field and service robots is still the most important part of theoretical and application development in widely perceived robotics. Crucial problems and challenges are associated with control of mechatronic systems in general, perception, navigation, manipulation and grasping, locomotion and reasoning.

Elements of measuring systems are recently developed on the base of such modern and advanced materials as graphene. Moreover, increase in computational power of modern computers fosters new approaches to advanced signal processing and experimental verification of sophisticated problems of the theory of metrology.

This book presents the recent progress in control, automation, robotics, and measuring techniques that are jointly trying to meet those challenges and to fulfil technological, economic and social needs of European Union. It presents the contributions of experts in those fields. Their work is concerned both with theory and industrial practice. Individual chapters present the theoretical analysis of specific technical problems, often supplemented by numerical analysis and simulation and real experiments on prototypes. The implementation of the research results in industrial practice is also reported.

We hope that the presented progress in theoretical analysis and practical solutions will be useful to both the researchers working in the area of engineering sciences and to practitioners solving industrial problems.

Warsaw, January 2015

Roman Szewczyk
Cezary Zieliński
Małgorzata Kaliczyńska

Contents

Distributed Temperature and Humidity Measurement System Utilizing IQMESH Wireless Routing Algorithms	1
<i>Piotr Bazydło, Szymon Dąbrowski, Roman Szewczyk</i>	
Integrated SCADA Checkweigher System	11
<i>Piotr Bazydło, Roman Szewczyk</i>	
Miniature Transducer of Linear Displacement Based on Miniature Hall Effect Sensors	21
<i>Maciej Bodnicki, Janusz Grzybowski</i>	
Hybrid Vision System for Diagnostics of Technical Objects and Processes	27
<i>Piotr Czajka, Wojciech Mizak</i>	
Functional Performance Testing of Routing Devices in Networks Based on IQMESH Protocol	39
<i>Szymon Dąbrowski, Piotr Bazydło, Roman Szewczyk</i>	
Influence of the Humidity on Signal of Strength in Laboratory Weighing Scales	49
<i>Szymon Dąbrowski, Piotr Bazydło, Roman Szewczyk</i>	
Heating Process of the Most Important Mechanical Elements in Laboratory Weighing Scales	59
<i>Szymon Dąbrowski, Michał Nowicki, Piotr Bazydło, Roman Szewczyk</i>	
Modified Monte Carlo Method for Calculating the Expanded Measurement Uncertainty	67
<i>Paweł Fotowicz</i>	

Influence of Environmental Conditions on Graphene Resistance	75
<i>Grzegorz Gawlik, Paweł Nowak, Anna Kozłowska, Mateusz Wojtasiak, Roman Szewczyk</i>	
Unconventional Double R/U Converter for Measurement of Two Quantities by a Single Differential Sensor	83
<i>Adam Idźkowski, Paweł Świętochowski, Zygmunt L. Warsza, Wojciech Walendziuk</i>	
Automatic System for Identification of Temperature Parameters of Resistors Based on Self-heating Phenomena	91
<i>Andrzej Juś, Paweł Nowak, Roman Szewczyk</i>	
Influence of Protective Layer on the Functional Properties of Monolayer and Bilayer Graphene Hall-Effect Sensors	101
<i>Maciej Kachniarz, Oleg Petruk, Maciej Oszwałdowski, Jacek Salach, Tymoteusz Ciuk, Włodzimierz Strupiński, Roman Szewczyk, Wojciech Winiarski, Krzysztof Trzcinka</i>	
Temperature Dependence of Functional Properties of Graphene Hall-Effect Sensors Grown on Si Face and C Face of 4H-SiC Substrate	111
<i>Maciej Kachniarz, Oleg Petruk, Maciej Oszwałdowski, Jacek Salach, Tymoteusz Ciuk, Włodzimierz Strupiński, Roman Szewczyk, Wojciech Winiarski, Krzysztof Trzcinka</i>	
Temperature Influence on the Magnetic Characteristics of Mn-Zn Ferrite Materials	121
<i>Maciej Kachniarz, Jacek Salach, Roman Szewczyk, Adam Bieńkowski</i>	
Graphene Joule Heating Measurements in Environmental Chamber	129
<i>Anna Kozłowska, Maciej Kachniarz, Grzegorz Gawlik, Roman Szewczyk, Mateusz Wojtasiak</i>	
Surface Electromyography Amplifier with High Environmental Interference Resistance	137
<i>Tomasz Mańkowski, Jakub Tomczyński, Piotr Kaczmarek</i>	
Electromagnetic Protection in High Precision Tri-axial Thermometric AC Bridge	147
<i>Aleksander A. Mikhal, Zygmunt L. Warsza</i>	
Simple Methods to Measure the Additive Error and Integral Nonlinearity of Precision Thermometric Bridges	157
<i>Aleksander A. Mikhal, Zygmunt L. Warsza</i>	

Study on Graphene Growth Process on Various Bronzes and Copper-Plated Steel Substrates	171
<i>Tadeusz Missala, Roman Szewczyk, Marcin Kamiński, Marek Hamela, Wojciech Winiarski, Jakub Szatatkiewicz, Jan Tomasiak, Jacek Salach, Włodzimierz Strupiński, Iwona Pasternak, Zdzisław Borkowski</i>	
Study on Tribological Properties of Lubricating Grease with Additive of Graphene	181
<i>Tadeusz Missala, Roman Szewczyk, Wojciech Winiarski, Marek Hamela, Marcin Kamiński, Szymon Dąbrowski, Dawid Pogorzelski, Małgorzata Jakubowska, Jan Tomasiak</i>	
Resistance of MAX 6325 Reference Voltage Source on Operating Temperature Variation	189
<i>Paweł Nowak, Andrzej Juś, Roman Szewczyk</i>	
Magnetic Thermogravimetric Analysis of CuCo and CuFe Amorphous Alloys	197
<i>Michał Nowicki, Peter Švec Sr., Dorota Jackiewicz, Roman Szewczyk</i>	
Advancement in Development of Graphene Flow Sensors	205
<i>Marcin Safinowski, Wojciech Winiarski, Oleg Petruk, Roman Szewczyk, Oskar Gińko, Krzysztof Trzcinka, Marek Maciąg, Waldemar Łoboda</i>	
Noise Assessment in Whitney Elements Based Forward Transformation for High Resolution Eddy Current Tomography	219
<i>Roman Szewczyk, Jacek Salach, Juha Ruokolainen, Peter Råback, Kamil Stefko, Michał Nowicki</i>	
A Problem of a Selection of the Stabilization Technique of False Alarm for Radar Target Detector	225
<i>Ewelina Szpakowska-Peas</i>	
Investigation of the Functional and Environmental Characteristics of Elements with Graphene Coating	237
<i>Krzysztof Trzcinka, Tadeusz Missala, Iwona Pasternak, Włodzimierz Strupiński, Wojciech Winiarski, Marcin Kamiński, Roman Szewczyk, Michał Nowicki</i>	
Influence of Electromagnetic Pulse Disturbance on the Functional Properties of Ultra-High Resolution Analog to Digital Converter	245
<i>Krzysztof Trzcinka, Roman Szewczyk</i>	
Influence of Operating Conditions on the Functional Properties of Ultra-High Resolution Analog to Digital Converter	255
<i>Krzysztof Trzcinka, Roman Szewczyk, Tomasz Charubin, Wojciech Winiarski, Marek Maciąg, Michał Nowicki</i>	

Flowmeter Converter Based on Hall Effect Sensor	265
<i>Michał Urbański, Michał Nowicki, Roman Szewczyk, Wojciech Winiarski</i>	
Analysis of Response Time of Carbon Dioxide Sensor in Chemical Sensor System for Mobile Robot	277
<i>Michał Urbański, Roman Szewczyk</i>	
Examples of Robust Estimation with Small Number of Measurements	285
<i>Evgeniy T. Volodarsky, Zygmunt L. Warsza</i>	
Statistical Properties of Skewness and Kurtosis of Small Samples from Normal and Two Other Populations	293
<i>Zygmunt L. Warsza, Marian J. Korczyński</i>	
About a Certain Way of the Membrane Kinetic Energy Transformation into Electric Energy	303
<i>Aleksandra Waszczuk-Młyńska, Stanisław Radkowski</i>	
Affordable 2D Laser Scanning Device for Accurate Acquisition of Environment Maps	313
<i>Marek Wąsik</i>	
Use of Automated Image Analysis in the Study of Mechanisms of the Formation of Nitrided Layers	323
<i>Tomasz Wójcicki</i>	
Measurement of Selected Parameters Describing Biomechanical Phenomena Occurring in the Implant-Bone System	333
<i>Marcin Zaczyk</i>	
Rotational Speed and Transducer Frequency as Factors Affecting Possibility to Detect Defects in Axisymmetric Elements with a Method of Eddy Currents	339
<i>Andrzej Zbrowski, Wojciech Józwick</i>	
Author Index	349

About the Editors

Professor Roman Szewczyk received both his PhD and DSc in the field of mechatronics. He is specializing in the modelling of properties of magnetic materials as well as in sensors and sensor interfacing, in particular magnetic sensors for security applications. He is the leading the development of a sensing unit for a mobile robot developed for the Polish Police Central Forensic Laboratory and of methods of non-destructive testing based on the magnetoelastic effect. Professor Szewczyk was involved in over 10 European Union funded research projects within the FP6 and FP7 as well as projects financed by the European Defence Organization. Moreover, he was leading two regional and national scale technological foresight projects and was active in the organization and implementation of technological transfer between companies and research institutes. Roman Szewczyk is Secretary for Scientific Affairs in the Industrial Research Institute for Automation and Measurements (PIAP). He is also Associate Professor at the Faculty of Mechatronics, Warsaw University of Technology and a Vice-chairman of the Academy of Young Researchers of the Polish Academy of Sciences.

Professor Cezary Zielinski received his M.Sc./Eng. degree in control in 1982, Ph.D. degree in control and robotics in 1988, the D.Sc. (habilitation) degree in control and robotics in 1996, all from the Faculty of Electronics and Information Technology, Warsaw University of Technology, Warsaw, Poland, and Professorship in 2012. Currently he is Professor both in the Industrial Research Institute for Automation and Measurement (PIAP) and the Warsaw University of Technology, where he is Director of the Institute of Control and Computation Engineering. Since 2007 he has been a member of the Committee for Automatic Control and Robotics, the Polish Academy of Sciences. Professor Zieliński is Head of the Robotics Group in the Institute of Control and Computation Engineering working on robot control and programming methods. His research interests focus on robotics in general and in particular include: robot programming methods, formal approach to the specification of architectures of multi-effector and multi-receptor systems, robot kinematics, robot position-force control, visual servo control, and design of digital circuits. He is the author/coauthor of over 180 conference and journal papers as well as books concerned with the above mentioned research subjects.

Dr. Małgorzata Kaliczyńska received her M.Sc. Eng. degree in cybernetics from the Faculty of Electronics, Wrocław University of Technology, and her Ph.D. degree in the field of fluid mechanics from the Faculty of Mechanical and Power Engineering in this same university. Now she is Assistant Professor in the Industrial Research Institute for Automation and Measurement (PIAP) and Editor of the scientific and technological magazine “Measurements, Automation, Robotics”. Her areas of research interest include distributed control systems, Internet of Things, information retrieval and webometrics.

Distributed Temperature and Humidity Measurement System Utilizing IQMESH Wireless Routing Algorithms

Piotr Bazydło, Szymon Dąbrowski, and Roman Szewczyk

Industrial Research Institute for Automation and Measurements PIAP
Al. Jerozolimskie 202, 02-486 Warsaw, Poland
(pbazydlo, sdabrowski, rszewczyk)@piap.pl

Abstract. The paper presents distributed temperature and humidity measurement system. The base of the system are IQRF radio transmission modules. It is assumed that system consists of one coordinator and multiple nodes. Data exchange is performed by IQMESH discovery routing algorithm. It divides modules into zones and assigns them Virtual Routing Number. Presented solution has several main advantages: modular construction, low price and easy implementation. The paper presents system and its components, describes provided solution (with main algorithms) and discusses usefulness of the application. In addition, paper points out possibility of system modelling (on the basis of example).

Keywords: IQRF, IQMESH, radio transmission, distributed measurement system.

1 Introduction

Wireless measurement systems are more and more popular amongst many industrial applications. Their advantages, such as wide range of operation or wireless connection between components are highly required in hazardous or inaccessible environments. One of the most popular solution, is to use ZigBee radio transmission modules based on an IEEE 802.15.4 standard [1]. It utilizes mesh network for data transmission, with range between nodes reaching 100 m. This solution offers a wide range of possibilities and reliability. However, it is likely that it will require substantial amount of work to implement it in small or medium sized application. Another, less popular solution is usage of IQRF transceiver modules. These constantly evolving radio transmission modules are characterized by SIM card format. It is not certain that IQRF modules are as reliable as ZigBee, due to small amount of articles concerning this solution. First articles associated with IQRF were described as an example of application [2, 3]. Mentioned papers describe case studies of different applications based on IQRF modules. The general knowledge (including advantages and limitations) connected with this solution was collected and presented in 2012 [4]. Recently, one attempt to determine mathematical models of modules efficiency has been noticed [5]. Such models can be useful for network planning and implementation into

any model (for example [8]). These models were determined in the industrial environment, on the basis of simple measuring system. In accordance to all of the available data, it is hard to classify optimal application for each solution. However, IQRF modules have some undeniable benefits such as: modular construction, low power consumption or satisfying efficiency in industrial conditions [5]. In order to research its possibilities in more advanced applications, distributed temperature and humidity measurement system has been prototyped. For the data routing, IQMESH Discovery algorithm has been implemented. The main aim of the system is creation of research platform for radio transmission testing.

2 System Components

Presented system consists of three main components: IQRF transceiver RF (radio frequency) modules, temperature and humidity sensors and end device (every device with USB interface).

2.1 RF Transceiver Modules

First (and main) of the components are IQRF TR-52D series transceiver modules.

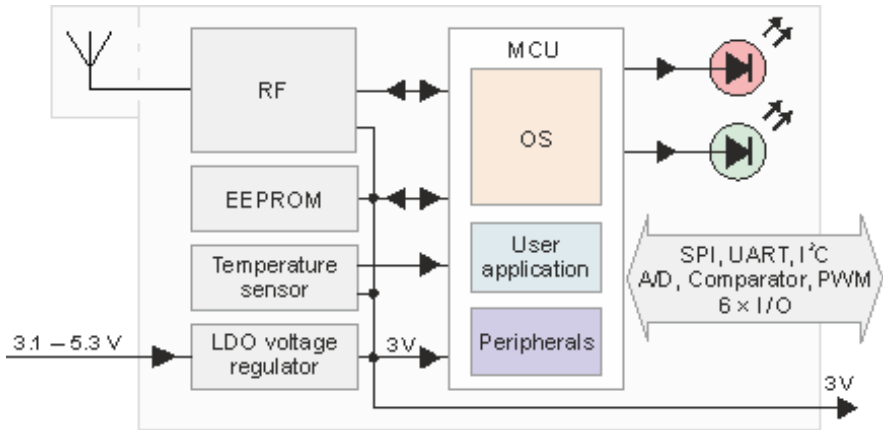


Fig. 1. Schematics of IQRF TR-52D module [6]

Figure 1 presents structure of TR-52D transceiver modules with its primary elements: RF antenna, EEPROM and MCU (with in-built OS). Structure based on SIM card format, provides modularity of the whole system. In case of breakdown, damaged module can be easily replaced. That leads to another important factor – modules variations. There are different antenna mountings available: on-board PCB antenna, soldering pad-hole or coaxial connector for external antenna. In addition, depending on the choice, RF modules can be selected between 868/916 MHz or 433 MHz bands. Switching between node mode (transmitter) and coordinator mode (receiver) can be performed by appropriate command.

2.2 Temperature and Humidity Sensors

Second element of the system is Sensirion SHT 15, digital temperature and humidity sensor (Fig. 2). Its main advantages are: small size, satisfying measurement properties and low power consumption. All of these aforementioned pros are highly desirable for wireless applications. In the presented case, sensor is connected directly to the single node.

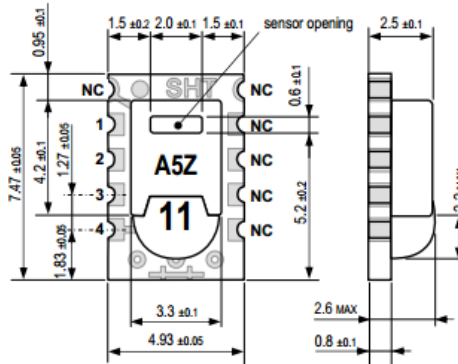


Fig. 2. Sensirion SHT1x sensor [7]

2.3 End Device

In the prototype system, personal computer has been used as an end device. The entire system is operated by C# application, which is responsible for fulfilling the following tasks:

- command sending to the coordinator,
- measurements acquisition.

In general, application reacts to user actions (tasks selection) and forwards appropriate command to the coordinator. When the task is completed, coordinator transmits data back to the end device.

3 System Structure and Operation

This chapter presents system structure and algorithms used for its operation. For the proper work, system requires one coordinator, one end device and at least one pair of node and sensor. Example of the system structure is presented in Fig. 3. In this example, system has 5 pairs of nodes and sensors. However, direct connection between coordinator can be achieved only by nodes 1 and 3. This is caused by the too large distance between receiver and another transmitters. In order to get measurements from transmitter 2, 4 and 5, the routing algorithm should be implemented.

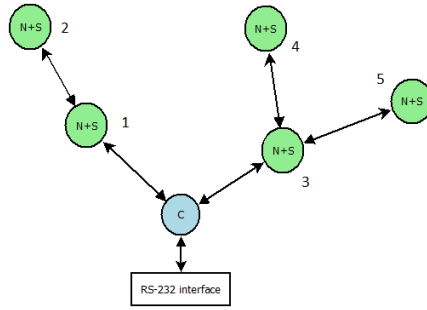


Fig. 3. Example of the system structure, where: C – coordinator, N+S – node + sensor

3.1 IQMESH Discovery Routing Algorithm [6]

Routing algorithm implemented into the system is called IQMESH Discovery. The algorithm will be discussed on the basis of example presented in Fig. 4. In the beginning, coordinator looks for nodes in range. After sending the request, nodes numbered as 2 and 5 replied. After each iteration of network creation, coordinator assigns VRN (Virtual Routing Number) to nodes and creates zones. In the considered case, node 2 has VRN = 1 and node 5 has VRN = 2. At this stage, zone 0 is created. Then, coordinator passes control to node 2 (lowest node number always has priority). This particular node is searching for another nodes in range. It has discovered node 1 and then assigned it VRN = 3. Node 5 has discovered node 3 and then assigned it VRN = 4. In this way, the whole network is created (zones from Z0 to Z4). All of the mentioned operations are repeated, until the last node. To perform discovery algorithm, nodes and coordinator should be bonded [6].

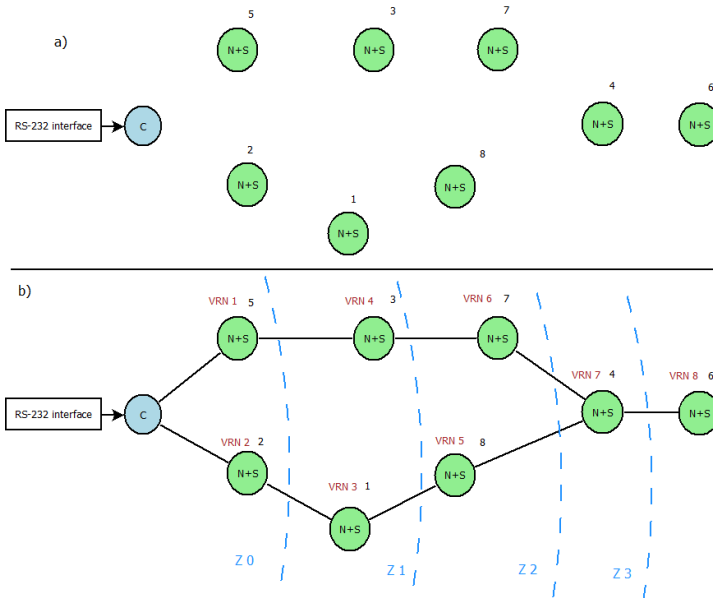


Fig. 4. Example of discovery routing algorithm: a) before discovery b) after discovery

3.2 System Operation – Main Algorithm

This chapter discusses the system operation. Default system task is defined as “measurement task”. However, if during measurement user selects different task, system finishes measurement and enters “user mode” (mode when system waits for user action). Main algorithm is presented in Fig. 5.

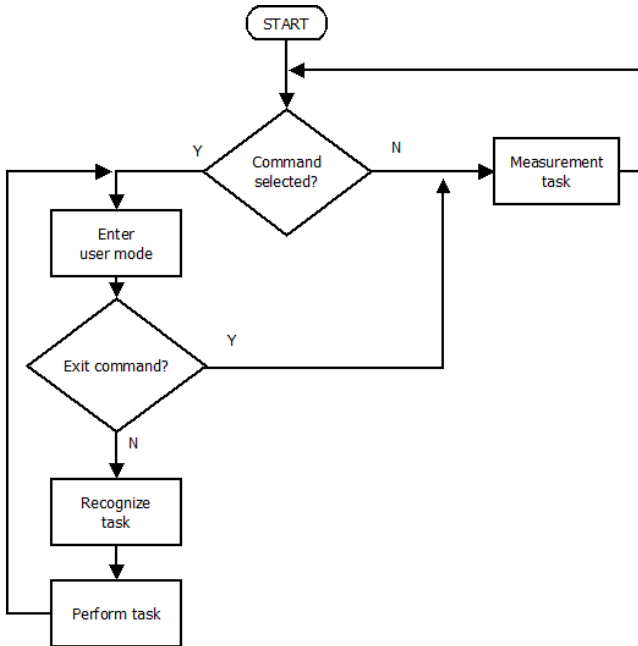


Fig. 5. Main algorithm of the system

Simplified measurement task algorithm is presented in Fig. 6. Firstly, coordinators specifies n_{\max} number (how many nodes are connected). After that, coordinator sends request to every node to perform measurements. All of the nodes perform measurement simultaneously. SHT15 conversion time takes 750 ms (for the 12 bit resolution). Assuming that the system has for example 10 nodes, not simultaneous measurement would extend procedure time by nearly 10 seconds. If every node collected measurement data (temperature and humidity), coordinator request data from single nodes. When the data from the node n is obtained, coordinator forwards data to the end device and requests data from the next node. Whole procedure is repeated, until node number n reaches n_{\max} . In the end, system returns to the beginning of the main algorithm. Important is the fact that every transmitter sends data to receiver one hundred times. This solution partially protects system from disturbances and efficiency decline (caused by large distance between two modules). If coordinator receives measurement from the selected node, additional packets are ignored.

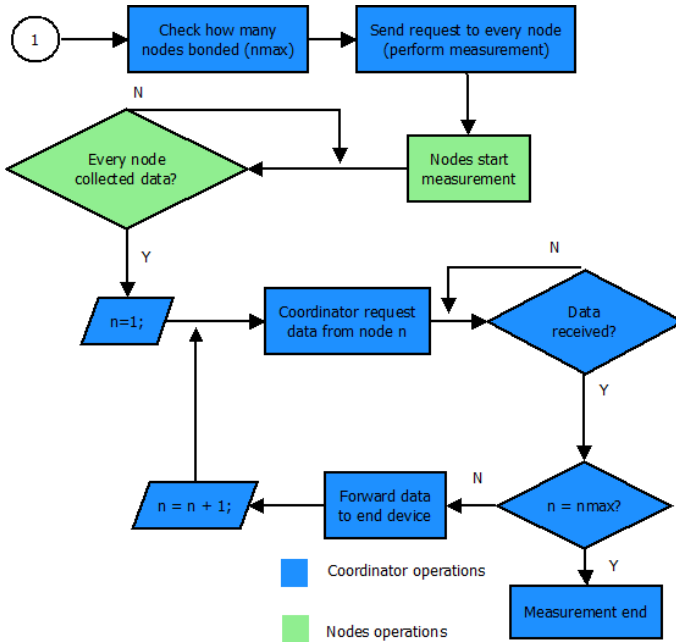


Fig. 6. Simplified measurement task algorithm

It was mentioned that user can interact with the system by the additional commands. All of them are used for tests or system modification purposes. Main tasks selected by the user are:

- Bond new node X.

Coordinator bonds new node and assign it logical address equal X. If X is 0, first free logical address is assigned.

- Remove node X.

Breaks connection between coordinator and node X. If X is 255, breaks connection between coordinator and all nodes.

- Discovery.

Begins IQMESH Discovery algorithm. Used after changes in network topology.

- Identify node X

Tests connection between coordinator and node X. If X is 255, tests connection between all nodes.

- Manual measurement from node X

Manually requests measurement from node X. If X is 255, requests all nodes.

- System info

Prints information about the whole system (number of nodes, zones, VRN etc.).

- Reset X

Resets node X. If X is 255, resets all nodes.

3.3 Coordinator and Node Realization

The last step of system prototyping was physical realization of nodes and coordinator. Fig. 7 presents electrical schemes of these two components.

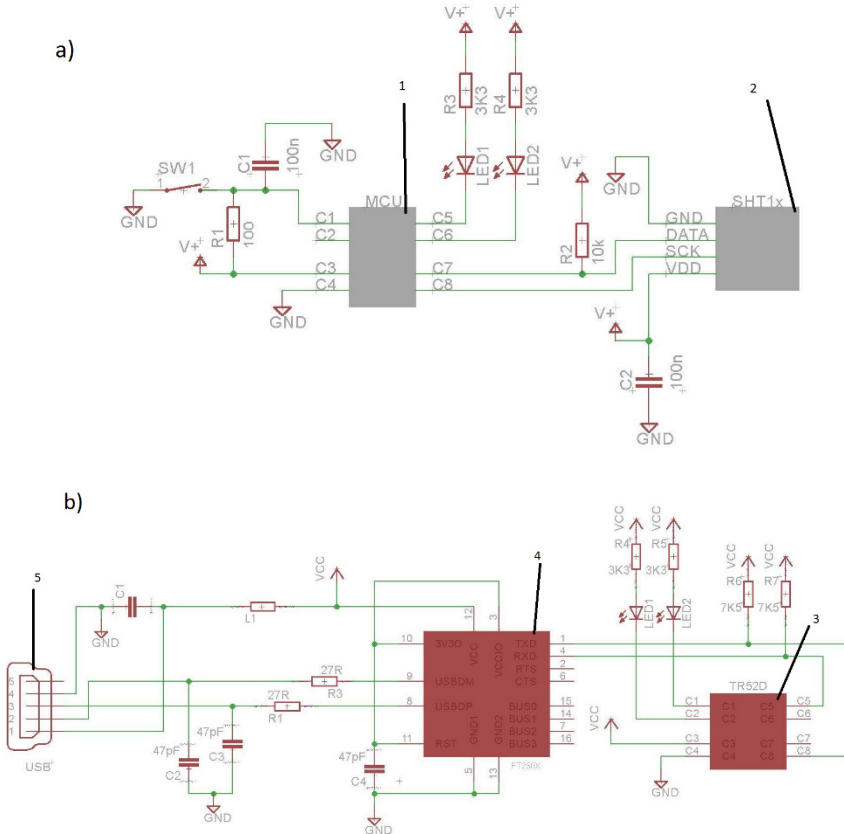


Fig. 7. Wiring diagrams of a) single node, b) coordinator, where: 1 – MCU, 2 – SHT15 sensor, 3 – TR52D module, 4 – RS-232 to USB converter, 5 – USB bus

4 System Modelling

The presented system allows to connect 240 nodes to one coordinator. Such a big number of connections allows to create large networks. However, in such a complex network, system modelling should be taken into consideration. Modelling of the network has a crucial role at the system planning stage, as it allows to initially determine coordinates of nodes. In addition, it simplifies task of maintaining efficiency at the desired level. To create possibility of system modelling, mathematical models should

be determined. Equation 1 presents mathematical model of efficiency in function of distance (for TR52D 868 MHz module with on-board PCB antenna) [6].

$$E = -2.799 * 10^{-5} e^{(0.12x)} + 100e^{(7.187 * 10^{-7}x)}, x \in < 0, 120 > \quad (1)$$

On the basis of equation 1, network model can be created. However, it is important to not forget about two important matters. First of all, this model has been determined for a single coordinator – single node system. There is a possibility that data routing has influence on transmission efficiency. Secondly, model has been determined by averaging multiple measurements. To avoid data loss, safe maximal efficiency level should be established. Figure 8 presents simple example of network verification, where safe efficiency has been determined at level 75%. Red color signalizes too big distance between modules. Different antenna mounting types can be included at the modelling stage. This approach can be also used for much bigger networks.

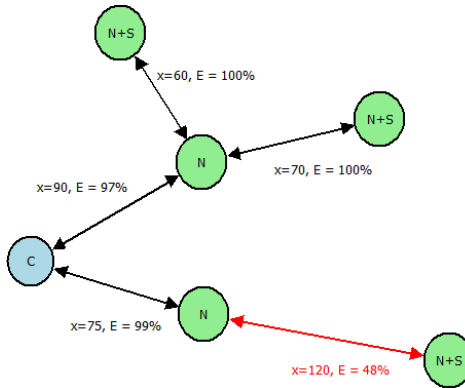


Fig. 8. Simple example of system modelling, where x – distance, E – efficiency

5 Summary

Presented prototype of the wireless temperature and humidity measurement system is fulfilling its role. It allows to connect large amount of sensors to one coordinator and perform measuring operations on wide-range area. System is characterized by its modular structure, low power consumption and low price. Fast and easy modules replacement allows to change RF parameters or replace damaged components.

The system was an attempt to create low budget wireless distributed measurement system with satisfying transmission parameters. It will be basis for the future research concerning transmission parameters with large-scale data routing (using IQRF modules). There is a possibility that accurate mathematical models of efficiency in function of distance will be determined. If so, it will create possibility of rapid distributed wireless systems modelling with many advanced features.

References

1. Pengfei, L., Jiakun, L., Junfeng, J.: Wireless temperature monitoring system Based on the ZigBee technology. In: 2010 2nd International Conference on Computer Engineering and Technology, vol. 1, pp. 160–163 (2010)
2. Kuchta, R., Vrba, R., Sulc, V.: IQRf Smart Wireless Platform for Home Automation: A Case Study. In: Fifth International Conference on Wireless and Mobile Communications, ICWMC 2009, pp. 168–173 (2009)
3. Sulc, V., Kuchta, R., Vrba, R.: IQMESH implementation in IQRf wireless communication platform. In: Second International Conference on Advances in Mesh Networks, MESH 2009, pp. 62–65 (2009)
4. Seflova, P., Sulc, V., Pos, J., Spinar, R.: IQRf Wireless Technology Utilizing IQMESH Protocol. In: 2012 35th International Conference Telecommunications and Signal Processing (TSP), pp. 101–104 (2012)
5. Bazydło, P., Dąbrowski, S., Szewczyk, R.: Wireless temperature measurement system based on the IQRf platform. In: Awrejcewicz, J., Szewczyk, R., Trojnecki, M., Kaliczyńska, M. (eds.) *Mechatronics: Ideas for Industrial Applications*. AISC, vol. 317, pp. 281–288. Springer, Heidelberg (2015)
6. <http://www.iqrf.org>
7. <http://www.sensirion.com>
8. Bogdan, L., Grażyna, P., Studziński, J.: Mathematical modeling and computer aided planning of communal sewage networks. *Journal of Automation, Mobile Robotics & Intelligent Systems* 8(2) (2014), doi:DOI 10.14313/JAMRIS_2-2014/14

Integrated SCADA Checkweigher System

Piotr Bazydło and Roman Szewczyk

Industrial Research Institute for Automation and Measurements PIAP, Warsaw, Poland
{pbazydlo, rszewczyk}@piap.pl

Abstract. The dynamic weighing is a constantly developing field of metrology. The electronic weighing module is vulnerable to many sources of environmental disturbances. Some issues connected with dynamic weighing and the necessity of implementation of signal processing methods are discussed. Implementation of this feature is impossible in majority of SCADA systems. The paper presents integration of three advanced software environments: MATLAB, LabVIEW and iFIX SCADA in prototype dynamic weighing system. They were used for advanced signal processing, data acquisition and visualization/process control. The integration of the three above mentioned environments is an attempt to create the industrial system with capabilities to deal with major dynamic weighing problems. It is innovative because it connects industrial SCADA, laboratory/industrial LabVIEW and MATLAB. Algorithms responsible for process control and data exchange are presented. The paper includes description of capabilities, performance tests, as well as benefits and drawbacks of the system.

Keywords: checkweigher, SCADA, LabVIEW, digital filtering.

1 Introduction

The mass of the final product is one of the most important factors on modern production lines. The dynamic weighing allows automation of the weighing process, which leads to higher efficiency of production. The complete measuring system which comprises all components required for dynamic weighing is called the checkweigher [1, 2]. It selects objects that fulfill the strictly specified requirements connected with mass, at the end of the production line. Commercial devices can, for example, detect the absence of the mandatory leaflet inside a medicines package. The dynamic weighing is associated with several difficulties however, that should be carefully investigated.

Principle of operation of the checkweigher's electronic weighing module is based on the coil displacement. Therefore, it is vulnerable to external disturbances. The sources of these disturbances are as follows: temperature or humidity change, electrostatic charges, constant and variable magnetic fields, air movements and vibrations. Measurement errors are especially connected with vibrations, usually transmitted from the floor [3]. In order to remove the influence of this error source, good quality filters and signal processing algorithms have to be used [4].

In this paper the universal dynamic weighing system is presented, integrating three different environments: industrial iFIX SCADA, laboratory LabVIEW and computing MATLAB. The utilization of three most advanced in their fields environments in a single application is innovative. Engineering literature survey shows examples of LabVIEW and SCADA integration [5, 6]. However, implementation of MATLAB, LabVIEW and SCADA in one, scientific or industrial, application was not done recently.

The main purpose of the presented system is to allow for further works connected with the modeling of device interaction with environmental disturbances, and filter design. The system will be also tested during the design stage of the online digital vibration filter. It's main advantages are flexibility at the prototyping stage and rapid implementation of modifications. Improvement in modifications implementation time is particularly noticeable when compared with FPGA or microcontrollers. Furthermore, selected elements of the system can be easily integrated with existing industrial solutions utilizing iFIX or LabVIEW.

2 Checkweigher Description

Dynamic weighing consists of weight measurements of objects in motion. To perform such an operation, device called the checkweigher can be used (Fig. 1). This particular example is designed to weigh objects of masses up to 750 g with 0.1 g resolution. It is equipped with three conveyor belts, each one driven by a separate BLDC motor to minimize vibrations. The second conveyor belt is directly connected to the electromagnetic weighing module. It is mounted to the main construction frame with vibration damping elements.

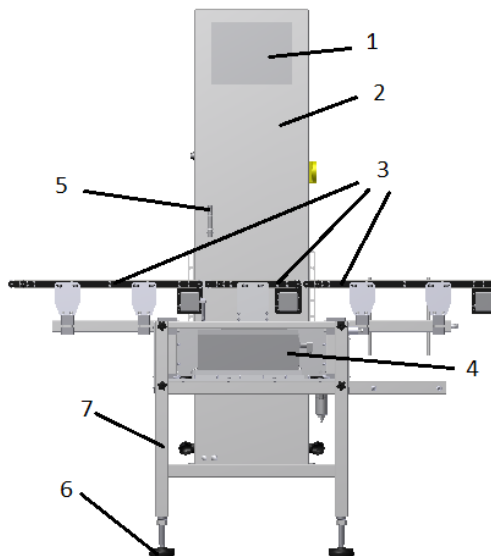


Fig. 1. Checkweigher design: 1 – control panel, 2 – control cabinet, 3 – conveyor belts, 4 – weighing module, 5 – optical sensor, 6 – vibration damping element, 7 – main structure

The measurement procedure is triggered by the optical sensors mounted above the conveyor belts. Just before the object reaches the second conveyor belt, the sensor detects its presence and signals the data acquisition process to begin. The weighing module generates voltage signal as the output. On the Fig. 2 the output voltage signal of checkweigher during weighing is presented. Theoretically, by the selection of the average voltage signal in the stable position (samples from the 5300 to 5400 in this example), and fitting the appropriate mathematical function, it should be possible to determine mass. In reality, the signal is distorted by many factors (such as gap between belts, environmental disturbances, etc.), and the stable position is unobtainable. It should be highlighted that in accordance to a linear approximation model, 1 mV change of the signal equals to 2.87 g. To guarantee high quality measurement and repeatability of the results, advanced signal processing methods and filters have to be implemented.

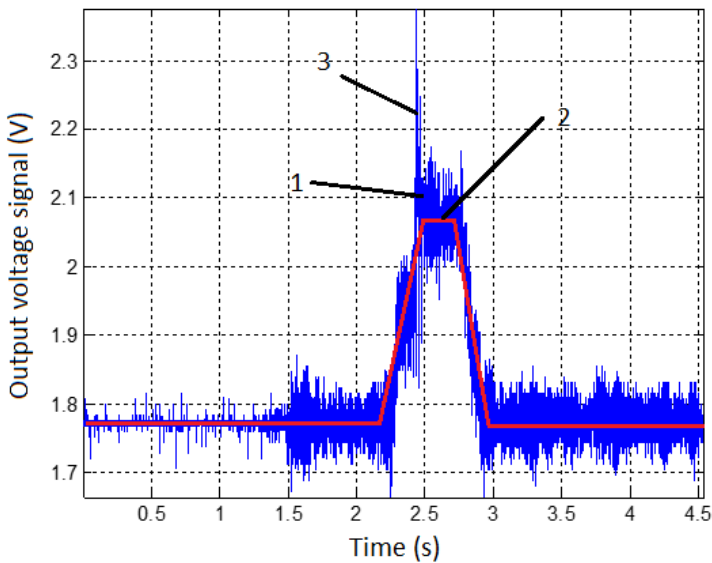


Fig. 2. Measurement signal: 1 – unprocessed signal, 2 – theoretical mass indication, 3 – disturbance

3 System Structure and Requirements

The requirements of the system concern three aspects: data acquisition, control and visualization. The first one is strictly connected with the signal processing, which is the most important part of dynamic weighing. In order to use adaptive processing algorithms, the properly prepared data delivery to the MATLAB is necessary. Primary goals for data acquisition in the investigated dynamic weighing system are:

- fast triggering,
- voltage signal acquisition with sampling frequency above ~ 10 kHz,

- minimum 24 bit Analog-to-Digital Conversion (ADC),
- possibility of saving data into the measurement files and creating reports,
- data exchange with remote access applications (http, ftp, SMTP etc.).

All of these, except for the 24 bit ADC, can be achieved easily with the LabVIEW software.

Control and visualization are connected with the HMI touch screen. Primary requirements are:

- possibility for process parameters control,
- possibility for historical data check,
- alarms and errors management,
- remote access applications connection [7].

The industrial iFIX SCADA with Historian add-on can be used to meet all of the above requirements. The system is complemented by the MATLAB utilization for signal processing.

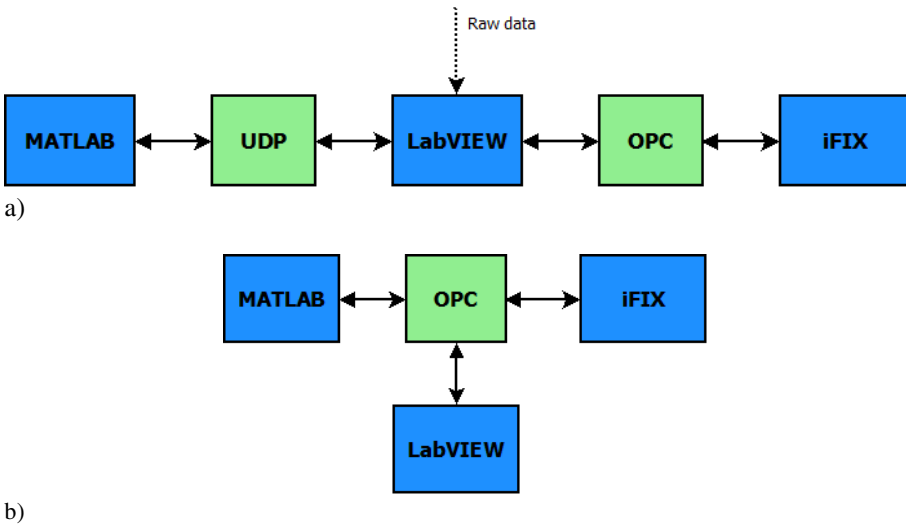


Fig. 3. a) System structure b) System structure based on the OPC

Figure 3a presents the software architecture of the system. LabVIEW transfers data to MATLAB by the UDP (User Data Protocol) after the data acquisition. MATLAB transfers processed data back to the LabVIEW, which then forwards it to the OPC (OLE for process control) server. The iFIX database can be easily connected with the OPC server by the OPC Power Tool. This structure allows to transmit data between all involved software environments. In this case, the LabVIEW is the connecting element between iFIX and MATLAB. However, it is possible to change the system structure to the one which is based on the OPC (Fig. 3b). Both the UDP and OPC are very popular in industrial applications, thus the proposed system architecture is open for further developments.

In the original system, the UDP protocol is included because of the lack of appropriate MATLAB toolbox for OPC connection. During design and testing stages of the project, one can use the free UDP toolbox or transfer data in text files. In case of a real application system, it is recommended to use the OPC Toolbox.

4 Algorithms and System Properties

The main system activity is the singular measurement procedure. It is frequently repeated, with the time between consecutive measurements dependent mainly on the conveyor belts speed.

The measurement procedure can be divided into three consecutive stages: data acquisition, signal processing and data transfer/visualization (Fig. 4). The system switches between different sections on the basis of flags, set by all available environments. Flags are held on the OPC server or/and in the MATLAB variables database.

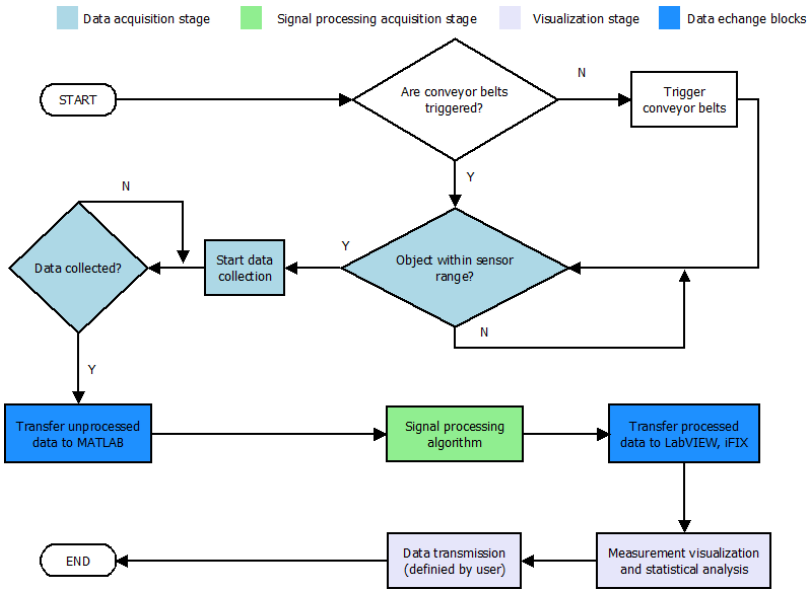


Fig. 4. Simplified algorithm of the single measurement procedure, with three marked stages

4.1 Data Acquisition

Data acquisition operations are described by the simplified algorithm presented in Fig. 5. The procedure starts after object detection. First, the system checks actual parameters of acquisition, as they can be changed in every process iteration. The triggering flag is set and reset. All of the flags in this section (excluding the signal processing flag) are for visualization purpose only. When the voltage signal is acquired, it is forwarded to the MATLAB in the form of a float array. With the array of unprocessed data loaded into the MATLAB database, signal processing stage starts.

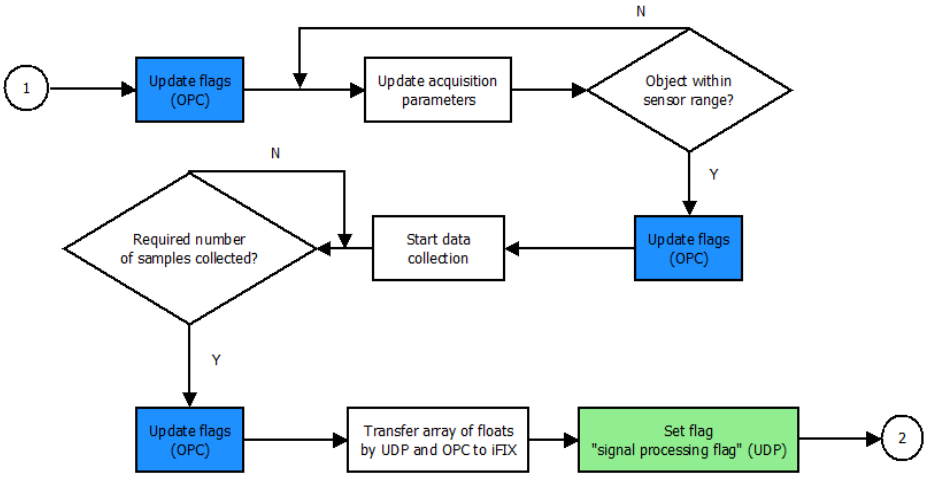


Fig. 5. Simplified algorithm of the data acquisition stage

4.2 Signal Processing

Figure 6 presents the signal processing algorithm implemented in the system [4]. Acquisition of the measurement is realized by parameterized step response function of the first order inertial object fitting:

$$h(t) = -a * e^{-\frac{t}{b}} + c \quad (1)$$

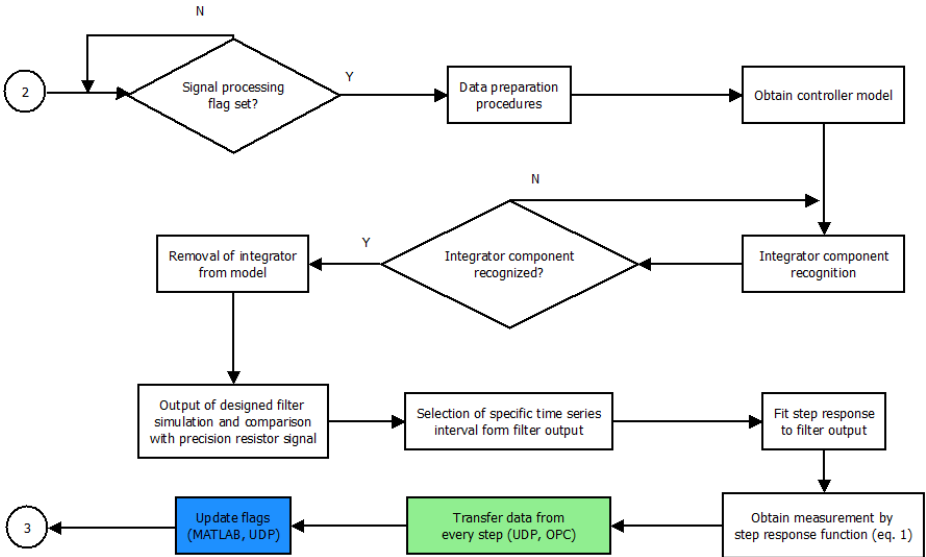


Fig. 6. Simplified algorithm of the data acquisition stage

where c is the value of function as the time goes to infinity (the value of the integral component of PID controller when the signal reaches stability). The outcome of the algorithm is the stable part of the signal, converted from the filtered voltage signal into mass indication (Fig. 7). The mass measurement is calculated as the average of the highlighted samples.

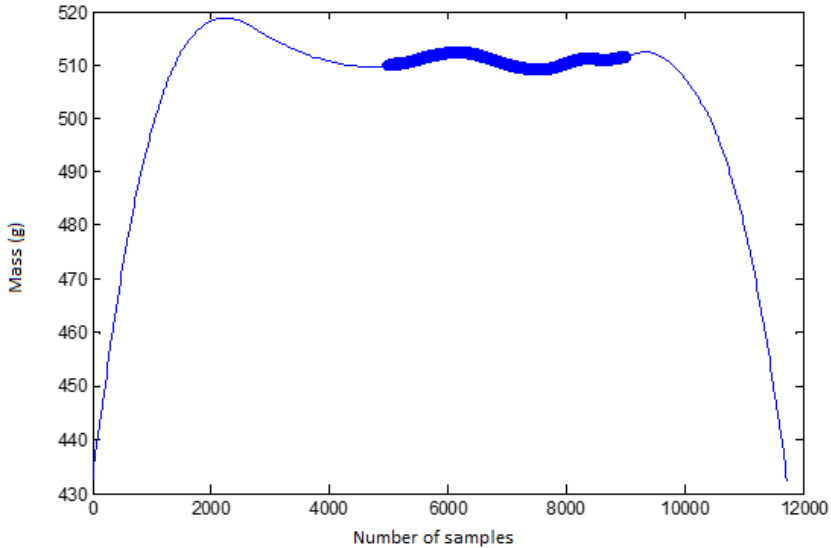


Fig. 7. Final mass indication

Next, selected flags are modified and data arrays from every step of the signal processing procedure are forwarded to the LabVIEW and iFIX.

4.3 Control and Visualization

The first part of the visualization stage is concerned with the final measurement and the signal processing data. After each iteration, when the “final measurement flag” is set, the system logs the data and visualizes it in form of numerical values. It allows the user to track the signal path to its final form. In addition, it updates several statistical parameters: average mass, maximum/minimum mass, etc.

The second part is connected with online visualization of the process. It means, that system informs user about the actual state of the process variables and flags using the appropriate graphical symbol.

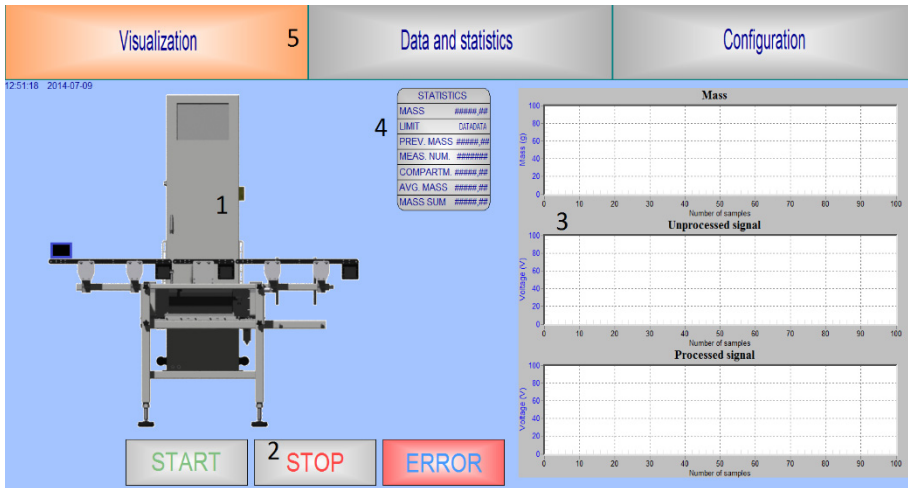


Fig. 8. Main menu of the system in the iFIX: 1 – process stage visualization, 2 – function buttons, 3 – main graphs, 4 – measurement selected statistical data, 5 – main taskbar

The user application main menu is presented in Fig. 8. It consists of buttons, taskbar and visualization objects. The configuration taskbar provides the control panel for both metrological and data transfer parameters. Examples of metrological parameters are: motor speeds, upper and lower acceptable mass limits or filter choice. Motors can be controlled individually with speeds ranging from 0.5 m/s to 1.5 m/s. For the provided signal processing algorithm, 11 filters are currently available.

Data transfer can be specified in many ways. All of the measurement statistics are logged into a text file. For the remote access, it is possible to connect to the OPC server, which holds all of the actual data. The LabVIEW ‘Data communication’ socket allows for use of different kinds of protocols, such as: HTTP, FTP, UDP, TCP and SMTP. For example, the presented system stores the email list in its database, and there is a button in the configuration menu responsible for sending text log file with historical data to the emails from the list.

5 Prototype Evaluation

Evaluation of the system for its compliance with requirements of the dynamic weighing process, described in Section 3, was done on the prototyped example. All of the advantages of the system were discussed in previous chapters. However, there are two drawbacks which can be considered key factors, disqualifying the system from the industrial use.

First of all, the system is composed of expensive environments. The operations presented in the article can be performed by cheaper means like FPGA. Secondly, the system showed to be slow. All of the process operations including (OPC flag setting, signal processing, data acquisition), the whole single measurement procedure lasts about 2 seconds. In accordance to the recent technical notes, where checkweighers are

reported to be capable of weighing about 400–500 objects per minute, this system is about 10 times too slow.

However, the lack of applicability of the complete system in the industry does not exclude its usefulness elsewhere. The two benefits – fast implementation of changes and open architecture – give two possibilities to the system. The first one is that the components created can be used separately to implement the system in the existing industrial application. This case is strictly connected with the use of LabVIEW and iFIX. This will allow to have full control of dynamic weighing system at the production line. The second and the most important one is the rapid implementation of changes very desirable on the stage of prototyping. Designing digital filters and making advanced operations on the signal is much easier with aid of computing environments like MATLAB as compared to programming in VHDL/Verilog or C (FPGA or microcontrollers). Thus, the presented system integrating iFIX, MATLAB and LabVIEW is a very efficient scientific tool.

6 Summary

The innovative system for checkweigher based on integration of the three software environments: MATLAB, LabVIEW and iFIX SCADA was presented. The high degree of flexibility of the system allows to create an application suitable for the specific user. However, its high cost and slow operation prevent complete implementation in an industrial production line, although implementation of the control and visualization modules is possible. On the other hand, the system had been found useful for scientific research works. Its ability for data presentation at different stages of the signal processing, and the visualization of the whole process allows to observe the behavior of the investigated object. Furthermore, MATLAB is a highly advanced computing tool, and can be successfully used for the signal processing. Its main advantage in comparison to the FPGA is the possibility to quickly change the algorithm.

The system turned out to be useful for the planned future checkweigher research, such as mathematical modeling of the checkweigher and environment interaction, and development of digital vibration filter.

Acknowledgements. RADWAG Company is kindly acknowledged for providing checkweighers for experiments, and the necessary technical assistance. The research presented in this work has been supported by the European Union within the European Regional Development Fund program, contract number POIG.01.03.01-14-086/12.

References

1. Dynamic Checkweighers DWT/HL/HPW, RADWAG Information Note (2013)
2. Yamazaki, T., Sakurai, Y., Ohnishi, H., Kobayashi, M.: Continuous mass measurement in checkweighers and conveyor belt scales. In: Proceedings of the 41st SICE Annual Conference 2002, vol. 1, pp. 470–474 (2002)

3. Bazydło, P., Urbanski, M., Kaminski, M., Szewczyk, R.: Influence of the environment on operation of checkweigher in industrial conditions. In: Szewczyk, R., Zieliński, C., Kaliczyńska, M. (eds.) *Recent Advances in Automation, Robotics and Measuring Techniques*. AISC, vol. 267, pp. 567–577. Springer, Heidelberg (2014)
4. Ugodziński, R., Gosiewski, Ł., Szewczyk, R.: FPGA based processing unit for a checkweigher. In: Szewczyk, R., Zieliński, C., Kaliczyńska, M. (eds.) *Recent Advances in Automation, Robotics and Measuring Techniques*. AISC, vol. 267, pp. 713–719. Springer, Heidelberg (2014)
5. Mehmood, M.O., Owais, M., Aftab, M.S., Shamim, F., Nomani, S.: National Instruments LabVIEW based pharmaceutical medication device with supervisory control and data acquisition system (SCADA). In: *Conference Proceedings – IEEE SOUTHEASTCON, 2009*, Article number 5174064, pp. 137–141 (2009)
6. Endi, M., Elhalwagy, Y.Z., Hashad, A.: Three-layer PLC/SCADA system architecture in process automation and data monitoring. In: *2010 The 2nd International Conference on Computer and Automation Engineering, ICCAE 2010*, Article number 5451799, vol. 2, pp. 774–779 (2010)
7. Oprzędkiewicz, K., Barwacz, D.: Systemy SCADA w środowisku Android. *Pomiary Automatyka Robotyka*, 95–99 (December 2014)

Miniature Transducer of Linear Displacement Based on Miniature Hall Effect Sensors

Maciej Bodnicki and Janusz Grzybowski

Institute of Micromechanics and Photonics,
Warsaw University of Technology, Warsaw, Poland
m.bodnicki@mchtr.pw.edu.pl, j.grzybowski1990@gmail.com

Abstract. A measurement setup is proposed for the displacement transducer with a Hall-effect sensors. It is a differential system using “out of phase” signals from two sensors. Nd-Fe-B miniature magnets and Hall-effect sensors mounted in SM technique make possible design of very small size transducers. Simulation studies were carried out upon such differential system, using the curves of the sensor voltage signal obtained experimentally in special test stand. Is possible to propose configuration which allows to obtain a linear signal with a resolution of at least $0.3 \mu\text{m}$ for the range of displacement of 1 mm.

Keywords: linear displacement measurement, Hall-effect sensor, micro sensor.

1 Introduction

A research carried out at the Institute of Micromechanics and Photonics, Warsaw University of Technology, has indicated a necessity of elaborating miniature contact transducers of linear displacements, in which low-cost matrixes for measuring surface topography could be potentially applied.

As far as contact transducers of displacements/dimensions are concerned, usually the following solutions are applied as their structural members [1–3, 9, 10]:

- inductance displacements sensors (including LVDT) with differential system of windings; it is a problem in this case to diminish their range down to ca. 1 mm while keeping the accuracy at the level of ca. few micrometers (at the same time the total length of the sensor is of ca. dozens of millimeters);
- mechanical dial gauges, currently equipped with electric outputs – characterized by considerable overall dimensions;
- capacitive displacement sensors – ensuring e.g. resolution of $1 \mu\text{m}$ and uncertainty of $2 \mu\text{m}$ at the measurement range of 20 mm; they are built both as differential systems or not;
- strain gauges – measuring strain at a surface of a mechanical element of special shape, whose selected fragment is deformed;
- incremental sensors (e.g. optoelectronic encoders);

- optical sensors with an open optoelectronic coupling, in which a change of degree of the coupling results from a displacement of the positioned element with respect to the illuminator and the detector;
- optical sensors with a CCD detector, in which the positioned/measured element masks the surface of the photo-array to various degrees or focuses.

At present, low-cost miniature Hall-effect devices are commercially available, whose dimensions are ca. $2.1 \times 2.1 \times 1$ mm (Fig. 1). They are designed for surface mounting. Making use of such sensors, excited by a magnetic field generated by magnets as miniature as the sensors, would make it possible to build transducers of small displacements having small overall dimensions.

Hard magnetic materials have become more and more important in the modern technology. Despite a great number of applications, the market of the hard magnetic materials consists in essence of four groups of materials (rare earth metal magnets – transition metal – RE-M – i.e. Nd-Fe-B and Sm-Co as well as ferrites and Alnico) [5]. As far as of miniaturization of magnets is concerned, advantages of Nd-Fe-B materials are unquestionable. Various techniques of manufacturing them employing a molding method are used, however so-called bonded magnets are an interesting solution. Bonded Nd-Fe-B magnets, i.e. magnets created by binding particles of a highly coercive Nd-Fe-B powder with a polymer binder have a considerable share of the world market related to magnets. They are applied first of all in devices converting electric energy into mechanical and vice versa (motors and generators). Novel technologies of manufacturing bonded magnets have been elaborated over the last years by the Faculty of Materials Science and Engineering, Warsaw University of Technology [4].

2 Physically Experiments and Preparing of Mathematical Model

At the first stage, a study of a dependency of the signal on the position of a micro-magnet with respect to the sensor was carried out. Optimal values of the air gap were determined as well. The results made it possible to create a mathematic model of the

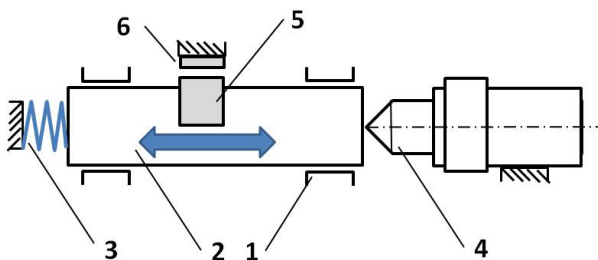


Fig. 1. Scheme of test stand for determination of the Hall-effect sensor characteristics 1, 2 – linear guide system elements, 3 – return spring, 4 – micrometric screw, 5 – micromagnet, mounted in moveable element, 6 – sensor

dependence of the signal generated by a HW 108A miniature Hall-effect sensor in function of displacements of a selected Nd-Fe-B micro-magnet (cylinder, volume about 1 mm^3). Configuration of test stand and results of experiments – signal from sensor during changes of position micromagnet are presented on Fig. 1. and Fig. 2. Central position (symmetry axis) of the sensor surface was located at circa 20.8 mm position of the micrometric screw. The air gap dimension was circa 0.15 mm.

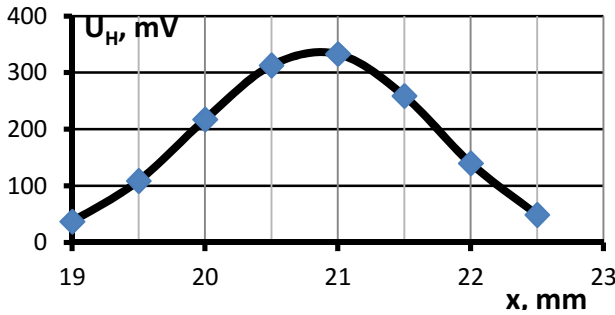


Fig. 2. Physical experiments – signal generated by HW 108A sensor during displacement of micromagnets, U_H – Hall voltage, x – setting of micrometer screw

For the purposes of model parameterization process tabulated results of the preliminary experimental test were estimated by using the polynomial function.

3 Transducer of Linear Displacement – Configuration and Simulation Tests

A measurement configuration, which can be applied in the displacement transducer with a sensor based on a Hall-effect device is a differential system using out of phase signals from two sensors. The signals can be generated by a field of one or two magnets (Fig. 3).

An optimization of the system generating a differential signal was realized using static characteristics of a signal generated by a sensor based on a Hall-effect device, presented in Fig. 2. A mathematical model was created, which makes it possible to select a fragment of the signal edge to be used for processing by the differential system.

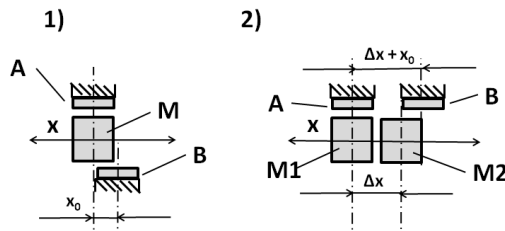


Fig. 3. Two configurations of the differential transducer with Hall-effect sensors: 1) one magnet system, 2) two magnets system M, M1, M2 – micromagnet, A and B – sensors, Δx – distance between centers of magnetic fields, x_0 – phase shift of differential displacements

The mathematical model was applied in a numerical environment of MATLAB/Simulink (see Fig. 4 – scheme, Fig 5 – polynomial curve corresponded signal of sensor), and a simulation study pertaining to operation of the system was carried out introducing variation of its features. First of all were tested conditions of operation of the differential system with various phase shift of signals from the two sensors. The range of measured displacement of 1 mm (± 0.5 mm) was taken into consideration.

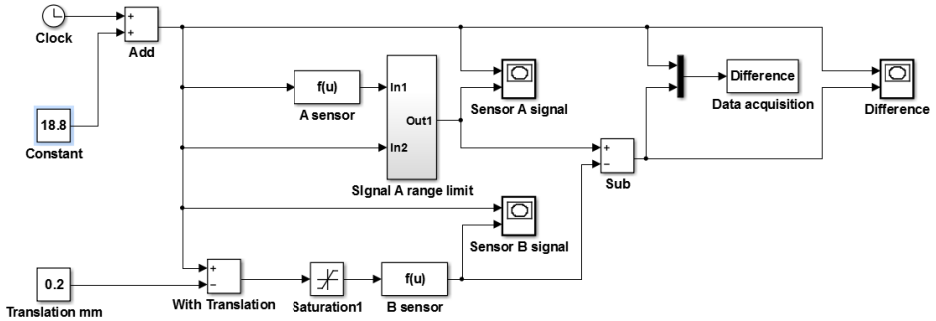


Fig. 4. Scheme of the MATLAB/Simulink procedure

Analysis algorithm was like the following:

- change the value of x_0 ;
- choice of displacement range $\Delta x = \pm 0.5$ mm;
- check the behavior of the condition of linear regression $R^2 \geq 0.9995$ for the widest possible range of ΔU (output signal).

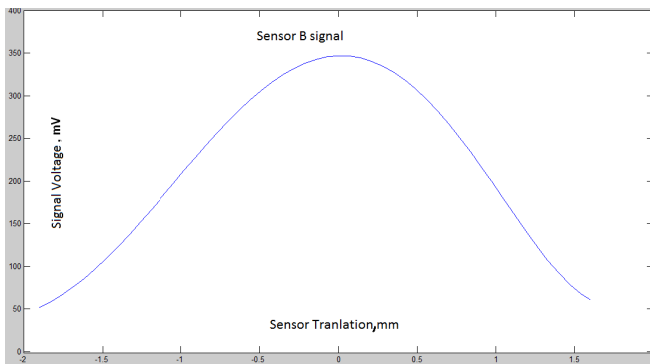


Fig. 5. Sensor signal determined from polynomial function

An example results for configuration sensors and magnets, fulfilling the conditions – minimization of nonlinearity of the differential signal in wide range, is shown in Fig. 6. There was selected solution to provide an output range with value $R^2 = 0.9995$ for range of the output differential signal $\Delta U = 443$ mV.

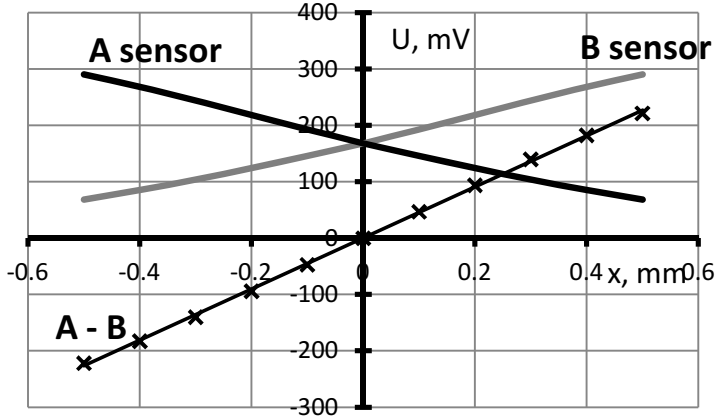


Fig. 6. The signals obtained for selected configuration of sensors and magnets

Using for further signal processing DAQ card with input range of A/D converter ± 250 mV and 12-bit resolution is obtained for a ± 0.5 mm (1 mm) displacement transducer resolution not worse than $0.3 \mu\text{m}$. It is also possible to apply dedicated compartment with $\Delta U = 0.440$ V A/D converter having a greater number of bits resolution.

4 Summary and Conclusions

The works reported in the paper pertain to selection of the operation conditions. One proposed ranges of displacements of the micro-magnet, which are advantageous as far as design of the differential system is concerned. Future works will be focused on stability of indications at various disturbances (temperature first of all) [6, 7].

Results of the study provide a knowledge on detection of the magnetic field of Nd-Fe-B micro-magnets by means of miniature Hall-effect devices as well as use of the signals for measuring purposes, in differential systems first of all. Due to low unit-prices of these elements, it would be possible to manufacture inexpensive and accurate transducers of displacements of the order of tenths of millimeter. Application capabilities of such transducers are considerable – they are related to the following areas: fine and precision devices, miniature consumer products, microrobots, automation and control/inspection system etc.

It should be emphasized that these possibilities do not refer to measurements of linear displacements only. They can be adapted to measurements of angular displacements, and also measurements of such mechanical quantities, in which a measurement of a displacement of the element subjected to some other interaction occurs (e.g. measurement of forces, torques, pressure). Systems of such sensors will enable to build measuring arrays or matrixes of relatively high density of information. That will create e.g. a possibility of building low-cost pressure mats for measuring gait parameters in medicine, motion bioengineering – especially foot sensors for self optimizing orthotic robots, which are designed in IoM&P WUT [8].

References

1. Bishop, R.H.: *Mechatronic Systems, Sensors, and Actuators. Fundamentals and Modeling*. CRC Press, Boca Raton (2008)
2. Bodnicki, M., Paraszka, D., Kalinowski, M.: Optoelectronic measuring unit for tests of accuracy of miniature electromagnetic actuators. In: XVII International Conference on Machine Modeling and Simulation, pp. 363–371 (2012)
3. Bolton, W.: *Mechatronics: a multidisciplinary approach*, Pearson Education Limited, Harlow (2008)
4. Kaszuwara, W., Michalski, B., Leonowicz, M., Bodnicki, M., Ciupiński, Ł., Jaroszewicz, J.: Graded Bonded Nd-Fe-B Magnets. *Composites Theory and Practice* 13(3), 174–178 (2013)
5. Liu, I.E., Marinescu Jasiński, M., Choi, H., Dent, P., Walmer, M.H.: Application Trends of Rare Earth Permanent Magnets. In: 21 International Workshop on Rare-Earth Permanent Magnets and their Applications REPM 2010, Bled, Slovenia, pp. 31–35 (2010)
6. Łuczak, S.: Effects of Misalignments of MEMS Accelerometers in Tilt Measurements. In: Březina, T., Jabłoński, R. (eds.) *Mechatronics 2013. AISC*, vol. 143, pp. 393–400. Springer, Heidelberg (2013)
7. Łuczak, S.: Guidelines for Tilt Measurements Realized by MEMS Accelerometers. *Int. J. Precis. Eng. Manuf.* 15, 489–496 (2014)
8. Wierciak, J., Bagiński, K., Jasińska-Choromańska, D., Strojnowski, T.: Orthotic robot as a self optimizing system. In: Březina, T., Jabłoński, R. (eds.) *Mechatronics 2013. AISC*, vol. 143, pp. 607–614. Springer, Heidelberg (2013)
9. Wilson, J.S. (ed.): *Sensor Technology Handbook*. Elsevier, Oxford (2005)
10. Zakrzewski, J.: *Czujniki i przetworniki pomiarowe. Podręcznik problemowy*. WPS, Gliwice (2004) (in Polish, English title: *Sensors and transducers. Problem textbook*)

Hybrid Vision System for Diagnostics of Technical Objects and Processes

Piotr Czajka and Wojciech Mizak

Institute for Sustainable Technologies – National Research Institute,
6/10 Pulaskiego str., Radom, Poland
{piotr.czajka,wojciech.mizak}@itee.radom.pl

Abstract. The paper presents a hybrid system for vision diagnostics of technical objects and processes simultaneously in the visible and infrared band. The system consists of a hybrid vision head adapted for use in industrial conditions, control and measurement system and the optional cooling system using compressed air. In order to verify the concept of hybrid method the study was performed on selected objects in the laboratory conditions using the developed system. The next stage was to perform the vision diagnostics of technical process in industrial conditions. By combining the analysis of the images in the two spectral bands additional information about the examined object or technical process can be obtained.

Keywords: hybrid vision system, passive and active thermography, diagnostics of technical objects and processes, multi-spectral images.

1 Introduction

Technical diagnostics is a field of knowledge that covers all of theoretical and practical issues relating to the identification and assessment of current, past and future states of the technical object with regard to its surroundings. Technical diagnostics is essential in all phases of an object existence (valuation, construction, manufacturing, operation) and is a tool for improving the quality and reliability of technical objects [1]. This article concerns the vision diagnostics of objects and technical processes at the stage of production and operation. The aim of the diagnosis at the manufacturing stage is to assess the quality of the products. In the production process systematic measurements are performed and the results are compared to the requirements included in the technical documentation. Depending on the outcome of that comparison the following step of the production or corrections are performed [2]. Operational diagnostics uses the results of measurements carried out periodically or continuously in order to determine the current state of the object and to detect damage. To diagnose the state of the device in through the operational diagnostics the state symptoms associated with process variables (e.g. pressure, temperature, power) are used, as well as residual processes that inevitably accompany the operation of each machine: thermal, electrical or vibroacoustical processes. They allow the

diagnostics without stopping the system (non-invasive diagnostics) [3]. In [4] as one of the most commonly used diagnostic methods vision inspection is listed. Among the existing solutions visible band cameras are used for this purpose and infrared cameras are used increasingly. Wherever any issue causes heat generation, thermal imaging measurements become an indispensable tool for diagnostics [5]. Hybrid methods combining the advantages of imaging in multiple spectral bands find their use in an increasing number of applications.

2 The Concept of Hybrid Vision Method

The concept of a hybrid vision method involves the use of two vision tracks to allow simultaneous inspection of the examined objects in the visible – VIS and infrared – IR bands (Fig. 1) [6, 7]. In the presented method, the information from both vision tracks are processed and analysed in order to increase the efficiency of vision inspection.

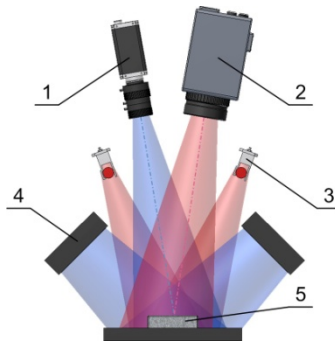


Fig. 1. The concept of the hybrid vision method: 1 – visible band camera, 2 – infrared camera, 3 – infrared radiator, 4 – panel LED lighting, 5 – tested object

Observation in the visible band allows detection and identification of defects in surface structures, detection of the presence and orientation of the individual elements. VIS images are used as auxiliary in order to facilitate and accelerate the localization and identification of controlled objects or to facilitate interpretation of the results of the IR camera. Thermography is an imaging in infrared band that consists in measuring the thermal radiation emitted by the object and on that basis determining the temperature distribution on its surface. This allows the monitoring of the temperature of objects, detection of areas of local temperature differences, e.g. heat accumulation zones. In order to ensure proper illumination of the object in visible band the system of two panels on either side of the target zone was proposed. Infrared inspection can be carried out using the so-called passive infrared thermography or active infrared thermography [5, 6, 8, 9]. In the method of passive infrared thermography, the thermal energy is derived solely from the test object, which remains under the influence of the environment or is in normal operating conditions, without additional thermal stimulation. In the method of active infrared thermography the response of the material subjected to stimulation by an external energy source is

analysed. From the different techniques of active infrared thermography the pulse thermography was selected [5, 6, 8–10]. In this method a stimulation is a heat pulse, and the recording of thermograms usually takes place in the cooling phase. The source of the heat pulse is a system of IR radiators located on both sides of the object.

3 Hybrid Vision System

Hardware structure of a hybrid vision inspection system consists of three main modules:

- vision head with lighting system and thermal stimulation system using IR radiators,
- control and measurement system that allows control of inspection process and acquisition, processing and analysis of measurement data,
- optional pneumatic system for cooling of the vision head with use of compressed air.

Components of the individual modules are shown in the block diagram (Fig. 2).

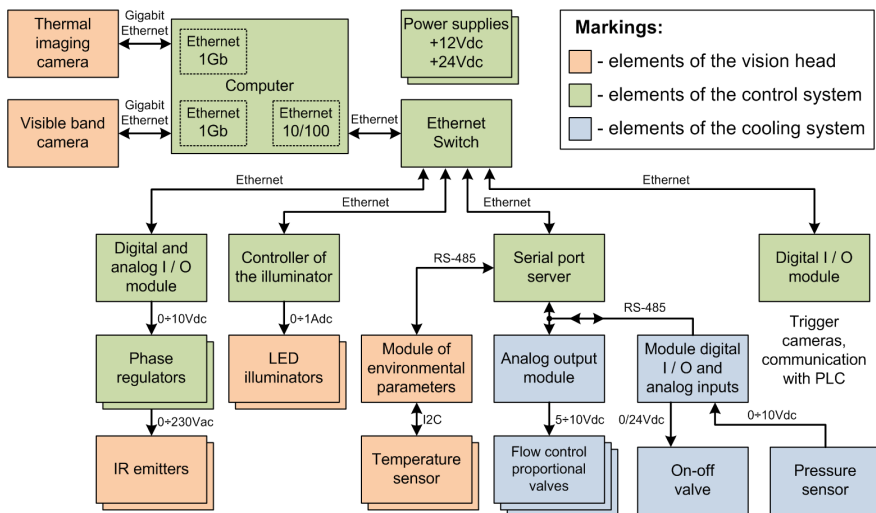


Fig. 2. Block diagram of the hybrid vision inspection system

3.1 Vision Head

The function of the developed vision head (Fig. 3) is to protect the camera module from the adverse effects of raised temperatures of inspected process and possible pollution, dust, moisture or mechanical shocks. In order to eliminate the negative impact of external factors on the vision module, the housing head consist of two bodies. Between the outer body and the inner is a free space, which is designed to isolate the camera module and to protect against high temperatures.

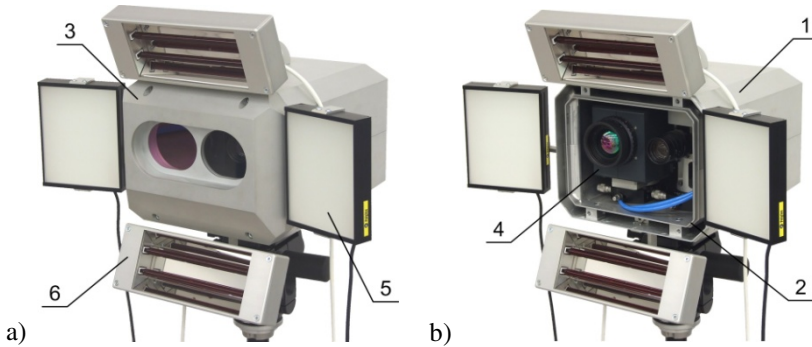


Fig. 3. Hybrid vision head with visible band camera and infrared camera: a) general view, b) view without the front cover: 1 – external body, 2 – internal body, 3 – front cover, 4 – camera module for hybrid inspection, 5 – panel LED lighting module, 6 – infrared radiator module

The design of the vision head allows high flexibility and easy reconfiguration of individual components [6]. The main modules of the developed structure of the head are: camera module for hybrid inspection, LED illuminators, set of two infrared radiators and cooling modules.

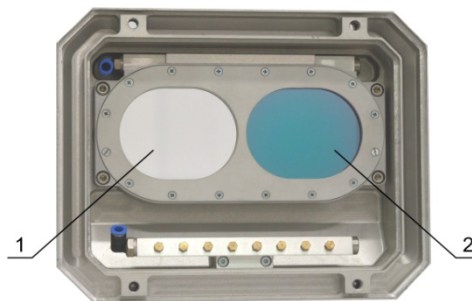


Fig. 4. Front cover with vision windows (view from the interior): 1 – quartz glass window (optical track for visible band camera), 2 – germanium optical window (optical track for infrared camera)

The head chassis is made of aluminium, due to the low specific weight and good thermal conductivity, which in combination with the cooling system provides effective heat dissipation. Reflecting outer surface of the body, however, limits the absorption of energy brought by thermal radiation. The head is equipped with three cooling modules for independent cooling of: the inner zone, where the two cameras for vision tracks are located, the zone between the shells of the housing and the front zone with optical windows. Each module can be independently controlled by adjusting the pressure and air flow. Hybrid vision module allows inspection in two spectral bands. The developed vision system uses a thermal imaging camera from InfraTec with uncooled microbolometric sensor with a resolution of 640×480 pixels. Camera sensor works in the long wave infrared band 7.5–14 μm [11]. To register the images in the visible band Basler camera was used with a monochrome CCD sensor

with a resolution of 1626×1236 pixels [12]. The cameras are placed on the rotary tables that allow precise manual change of the angular position depending on the required viewing distance.

The front cover (Fig. 4), protects the camera module against adverse effects of external factors and mechanical damage. The casing has an independent cooling system, and the face of the optical window is offset to the centre of the housing relative to the end face of the body, which further minimizes the possibility of damage to the optical components. Due to the possibility of changing the angular position of the camera optical windows are of an oval shape so as not to obstruct the viewing area of the lens used.

Since the developed vision head uses two types of cameras that use different spectral ranges of electromagnetic radiation, the optical windows are made of two kinds of materials: quartz glass (for the camera of visible band) and a single crystal germanium (for optical path of the infrared camera). Also important is an application of appropriate anti-reflective coatings, which in the case of germanium approximately doubles the value of transmission of the optical window compared to the material without the coating applied [6, 13].

In order to obtain the correct lighting of the inspected area, on the outer part of the vision head, on both sides, white LED panel illuminators are mounted. Vision head allows optical inspection using both passive thermography without additional thermal stimulation, as well as active thermography pulse stimulation of the tested materials using IR radiators. For this purpose, in the upper and lower parts of the head, modules with infrared radiators are mounted. Each module is equipped with two IR emitters, of a specific power of 500 W. LED illuminator and IR radiator modules can be removed if not used in the selected method of measurement so as not to affect the process of inspection. Vision head is positioned relative to the inspected objects with use of Manfrotto photographic head, which is attached to a tripod-type stand.

3.2 Control and Measurement System

The main components of the control and measurement system are:

- computer system with software,
- console with integrated LCD screen and keyboard,
- components to provide the power and control of hybrid vision system.

All components have been placed in a table top rack cabinet (Fig. 5). In the lower part of the housing there is a console with 19" LCD screen, keyboard and touchpad produced by Austin Hughes. The console includes two drawers equipped with guides to ensure independent ejecting of the LCD screen and keyboard. Over the console there is an industrial PC from Advantech. The computer is equipped with a Core i7 processor, 4 GB of RAM and 1TB HDD. LCD console and computer housing are made in standard 19" rack. The upper part of the housing holds components responsible for the supply and control of hybrid vision system integrated on the mounting plate.

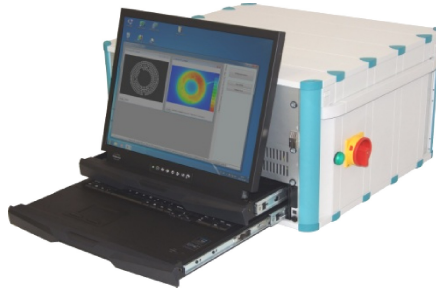


Fig. 5. View of the control and measurement system

The control and measurement system is designed based on input-output modules from ADAM-6000 series. Digital outputs are used for hardware triggering for both cameras. Analogue outputs are used for smooth adjustment, independently in the two channels, of infrared radiators' power by means of a two phase regulators. To control the LED illuminators the specialised driver is used from Latab. It allows independent control of flux in the two channels. Lighting controller, as well as a series of modules ADAM-6000 use the Ethernet interface to communicate with the computer. The system uses three other separate power supplies for independent power lighting controller, ADAM series modules and two cameras. The serial port server is used for communication via RS-485 interface with ADAM-4000 modules, placed in the optional cooling system and temperature sensors in the vision head. With this solution, despite the use of an Ethernet interface and RS-485 communication the computer is only using the Ethernet port.

As part of the project the application IrvisUTP has been developed for controlling optical inspection process and ensuring the acquisition, processing and analysis of images from both vision tracks.

4 Experimental Tests in Laboratory Conditions

In order to verify the concept of the hybrid method of vision inspection, tests were performed on selected objects using the method of passive thermography and active thermography. The possibility of using the hybrid diagnostic for the LED illuminators, electronic components, monolithic and composite materials containing surface and subsurface defects was investigated [6]. The article presents examples of the results from testing the LED illuminator ring and fibreglass with subsurface defects.

4.1 Testing the LED Illuminator

Testing the ring LED illuminator was performed using passive thermography method, without the use of IR radiators. The use of passive thermography method is limited to objects having a temperature different from the environment, which allows analysis of the radiation coming from the object [9]. Tested LED illuminator has several

damaged elements and several elements of reduced light emission with respect to the nominal value. After heating lighting elements, as a result of the nominal current, simultaneous recording of images for both vision tracks was performed (Fig. 6).

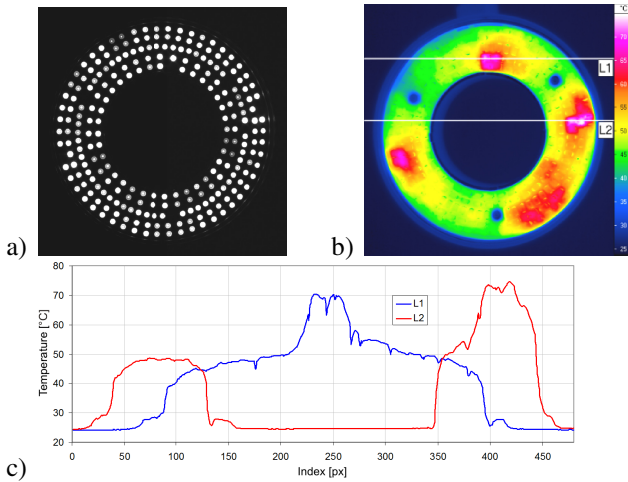


Fig. 6. The results of tests performed on the LED ring illuminator: a) image from the visible band camera, b) image from the infrared camera, c) temperature profiles along L1 and L2 lines

Image obtained by the visible band camera allows the assessment of light emission from individual LEDs. Image from the infrared camera allows analysis of the temperature distribution on the surface of the illuminator and the finding areas of excessive heat accumulation. The figure 6.c presents temperature profiles, taken along the lines L1 and L2 on the thermogram, presenting local increase in temperature. Based on the performed studies the effect of a defective component on the other LEDs in the same line was observed. Defective LED will change the operating point of other elements in the line leading to overheating.

4.2 Testing the Glass Composite with Subsurface Defects

The study on composite materials was performed using active pulse thermography. For the samples made of fibreglass subsurface defects were simulated in the form of blind holes with a diameter of 2, 3, 4 and 5 mm distant from the end surface by 1 mm and 2 mm. Holes are not visible from the side that was observed by the camera. Thermal pulse duration was 7 seconds with radiant power of 1000 W. Images were recorded during the cooling phase after switching off the IR radiators (Fig. 7).

On the observed thermograms of the cooling sample non-uniform temperature distribution on its surface was observed. Areas under which were defects located, had a higher surface temperature than the areas under which the material is homogeneous. Studies have also shown that deeper defects manifest themselves later and with less temperature contrast [8]. The resulting profile graphs (Fig. 7c) show the positions of

the occurrence of defects in both test samples. A combined analysis of images from both vision tracks allow detection of defects for both surface structures and subsurface defects.

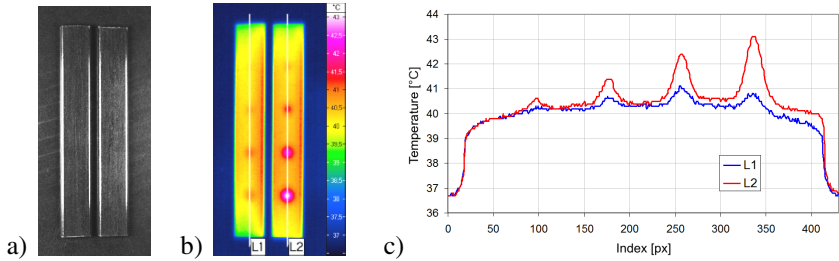


Fig. 7. The results of tests performed on the glass composite: a) image from the visible band camera, b) image from the infrared camera, c) temperature profiles along L1 and L2 lines

5 Testing of the Bottle Cleaning Process in an Industrial Washer

The aim of the study was the vision diagnostics of a bottle cleaning process at industrial washer. Due to the great total length of line, in order to maintain the required resolution of recorded images, the study was performed independently for three positions of the vision head (Fig. 8). For each position of the hybrid vision head the simultaneous recording of images in two spectral bands was performed for about 45 minutes. For diagnostics of bottle cleaning process the passive thermography method was used. To illuminate the field of observation in the visible band a system of two halogen lamps was used.

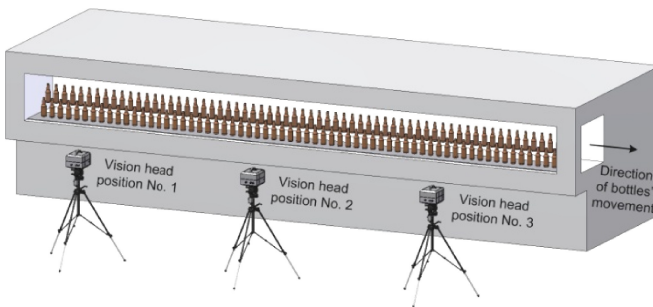


Fig. 8. The model of the stand for vision diagnostics of process of industrial washing of bottles

During the industrial bottle washing process the temperature is gradually raised. Main lye bath is carried out at a temperature of about 80 °C. Then, after rinsing the lye and as a result of successive water sprays, the temperature of bottles is gradually decreased [14]. Monitoring the bottles' temperature after washing is important

because of the danger of microbial growth. Thermal images allow evaluation of the efficiency of the cooling process of the bottles, after washing, by analysing the temperature distribution on their surface. The local temperature rise of bottles leaving the corresponding slot of the washer can be systematic or short-term. The persistent long-term higher temperature of bottles coming from the same slot may indicate obstruction of the local cooling system [7]. Washer design allows the observation of two rows of bottles. Rinsed bottles from the top row fall onto the conveyor (bottom row), and are shifted to the right. The Fig. 9 shows a thermogram for a higher temperature of bottles exiting the slot number 1 (start of line), which is also visible in the bottom row by periodically occurring temperature increase of the bottles.

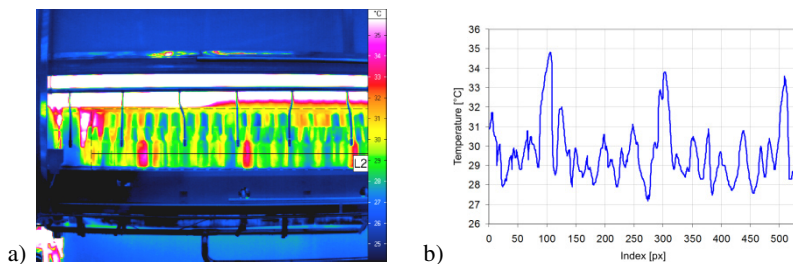


Fig. 9. The result presenting the systematic rise of the temperature on the surface of bottles (position no 1 of vision head): a) infrared image, b) profile diagram along line L2

Impaired cooling process could also show as a short-term temperature rise that is limited to the single bottles (Fig. 10).

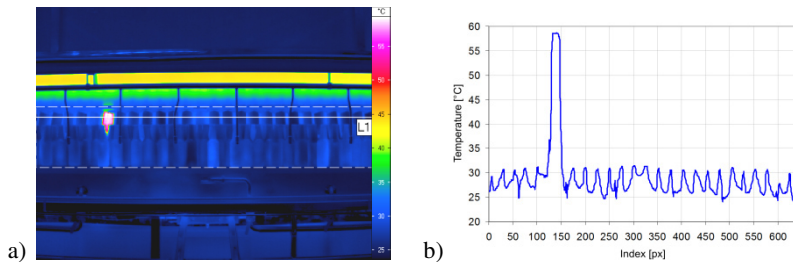


Fig. 10. The result presenting the local rise of the temperature on the surface of single bottle (position no 2 of vision head): a) infrared image, b) profile diagram along line L1

During testing there situations detected where high temperature rises occurred, which likely reasoned from the hot water left in the bottles during washing process [7].

Images from the visible band camera allow detection of the labels not removed from the surface of the bottles. Sample images with marked areas comprising fragments of labels is presented in Fig. 11.

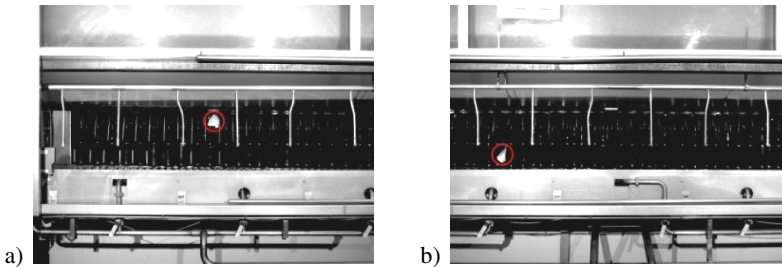


Fig. 11. Sample images obtained from the visible band camera with marked areas with parts of not removed labels on the surface of bottles: a) position no 1 of vision head, b) position no 2 of vision head

6 Summary

Presented hybrid vision system provides highly reconfigurable possibilities for various components depending on the requirements of the target application. Equipment of the vision head with additional external modules in the form of LED lighting modules and infrared radiators allows both lighting inspection area in the visible band as well as thermal stimulation of tested items. This makes it possible to perform vision inspection both by the method of passive thermography and active pulse thermography.

The big advantage of using vision methods for the diagnostics of technical objects and processes is non-contact and non-destructive nature of measurement, the possibility of simultaneous observation of the entire study area, high speed measurement, the wide range of possible applications. Additional benefits are obtained by combining image registration of two spectral bands. Hybrid method of inspection in the visible and infrared band allows increase of the efficiency of the process of vision inspection. By combining the analysis of correlated images of the two spectral bands the additional information about the test object is obtained.

Diagnostics of LED lighting in the visible and infrared bands allows both evaluation of emission of light sources (VIS track) and the detection areas of excessive heat accumulation (IR track). The hybrid vision inspection of composite materials provides detection of defects, both surface structures (VIS track) and subsurface structures (IR track). Vision diagnostics of bottle washing process using a hybrid system allows both assessment of the effectiveness of the bottles' cooling process, by analysis of the temperature distribution on the surface (IR track), as well as detection of not removed label fragments (VIS track).

Acknowledgements. Scientific work executed within the Strategic Programme “Innovative Systems of Technical Support for Sustainable Development of Economy” within Innovative Economy Operational Programme.

References

1. Żółtowski, B., Ćwik, Z.: Academic Publishing House of the Academy of Science and Agriculture, Bydgoszcz (1996) (in Polish)
2. Żółtowski, B., Niziński, S.: Modeling the operation of machinery. MARKAR-BZ Publishing House, Bydgoszcz – Sulejówek (2002) (in Polish)
3. Czech, J.: Selected methods and tools for diagnostics of technical objects. Maintenance (1), 8-12 (2011) (in Polish)
4. Sullivan, G., Pugh, R., Melendez, A., Hunt, W.: Operations & Maintenance Best Practices. A Guide to Achieving Operational Efficiency. Prepared by Pacific Northwest National Laboratory for the Federal Energy Management Program, U.S. Department of Energy (2010)
5. Minkina, W.: Thermographic Measurements – instruments and methods. Czestochowa University of Technology Publishing House, Częstochowa (2004) (in Polish)
6. Czajka, P., Mizak, W.: The modular structure of the hybrid vision head for quality inspection in the visible and infrared band. Assembly and Automation Technology (2), 42-47(2012) (in Polish)
7. Czajka, P., Garbacz, P.: Use of hybrid vision methods for the diagnostics of technical processes. Maintenance Problems (3), 73-85 (2013)
8. Oliferuk, W.: Infrared thermography in non-destructive testing of materials and devices. Gamma Bureau, Warszawa (2008) (in Polish)
9. Szczepanik, M., Stabik, J., Wróbel, G., Wierzbicki, Ł.: The use of thermal imaging systems for testing the polymeric materials. Engineering modeling 36, 279-286(2008) (in Polish)
10. Więcek, B., De Mey, G.: Infrared thermography. Fundamentals and applications. PAK Publishing House, Warszawa (2011) (in Polish)
11. VarioCAM hr head User's Manual, InfraTec GmbH (2012)
<http://www.infratec.eu>
12. Scout GigE User's Manual, Basler AG (2014)
<http://www.baslerweb.com>
13. Tydex information materials: Germanium Windows and Lenses for Thermography,
<http://www.tydexoptics.com>
14. Description of technological process of beer production (in Polish)
<http://biotechnologia.pl/archiwum/piwo-procesy-technologiczne10867>

Functional Performance Testing of Routing Devices in Networks Based on IQMESH Protocol

Szymon Dąbrowski, Piotr Bazydło, and Roman Szewczyk

Industrial Research Institute for Automation and Measurements PIAP,
Al. Jerozolimskie 202, 02-486 Warsaw, Poland
{sdabrowski, pbazydlo, rszewczyk}@piap.pl

Abstract. This paper concerns performance testing of radio communication parameters using routing algorithm implemented in IQMESH protocol. It presents description of research methods and measuring station used during the tests. Three parameters of radio transmission have been checked: efficiency, RSSI and capacity. Measurements were performed in two ways. First, for single router in function of distance between router and coordinator. Second, for variety of routers to determine influence of number of packet jumps on communication parameters. In addition, this paper contains the results of the measurements with the characteristics and mathematical models.

Keywords: IQMESH protocol, radio communication, ISM band, routing parameters.

1 Introduction

Nowadays, communication and data transfer process play a key role in every industry. First of all, link should provide stability of connection, guarantee of sent message delivery and should not distort the transmitted data. There are hundreds of protocols and interfaces designed for the particular applications. For example, some of them allow wireless data exchange [10], other offer very fast bandwidth and another are characterized by high resistance to interference [4]. Sample devices for wireless data transfer could be instruments working in ISM band. It is a free-license bandwidth, used for Industrial, Scientific and Medical purposes, operating in frequencies from 6.75 MHz to 246 GHz [6]. Most commonly, devices based on ZigBee or Wi-Fi standard are used (bandwidth: 868.915 MHz and 2.4 GHz or 5 GHz) [7, 8]. An alternative for this type of systems might be IQRF radio modules which allow development of any wireless radio communication device. In addition, the modules are characterized by small sizes, variety of mechanical solutions and different antenna parameters [3, 2].

The research described in this publication is related to three radio transmission parameters: efficiency as a ratio of received packets to the sent packets, signal strength indicator and link capacity. Tests were performed in two ways. Paper presents the results of measurements and mathematical models developed on the results basis.

2 Research Methodology

Object of the research was a wireless communication link, established via TR52DA radio module used as a router. Description of instruments (including chip) used during the tests is presented in section 3. Measurements were executed in two ways:

- For single router to specify its performance parameters like range of operation and data loss in function of distance between receiver and router.
- For several routing devices to determine influence of number of routers situated in network, on radio data transfer.

The network had to be built from at least three elements, in both cases:

- One transmitter, responsible for sending radio packet.
- Determined number of routers, responsible for passing packets between transmitter and receiver.
- Receiver, responsible for receiving and data analysis.

Network elements were deployed that the packets sent from the transmitter cannot reach receiver directly. Such solution allows to perform tests only for router parameters and routing algorithm. Symbolic network and data flow diagram, for single router tests are presented in Fig. 1.

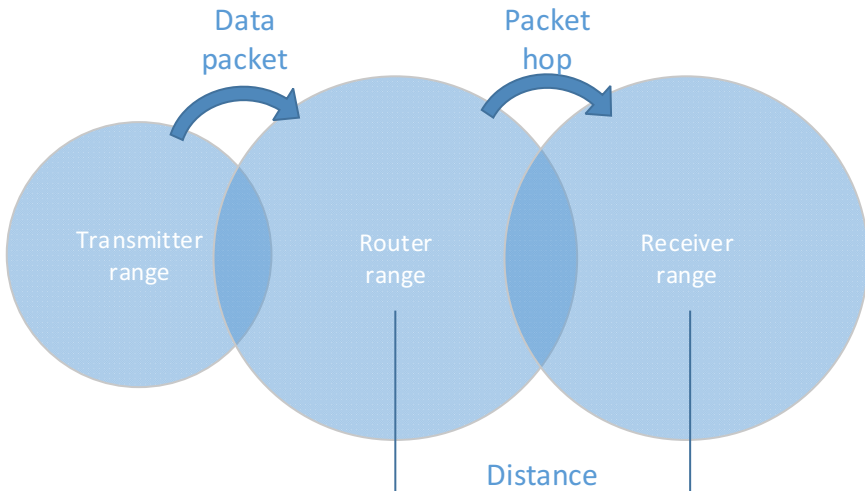


Fig. 1. Network used during tests for single router diagram

Reduction of transmitter power allowed for a larger amount of measuring points. The study consisted of gradual increase of the distance between the transmitter and the router. Router parameters have been checked every 10 meters. Testing was performed under standard conditions for wireless systems (in presence of other radio signals, near electrical installations, with few obstacles in the signal path). Figure 2 presents network schematic used during tests for several routers.

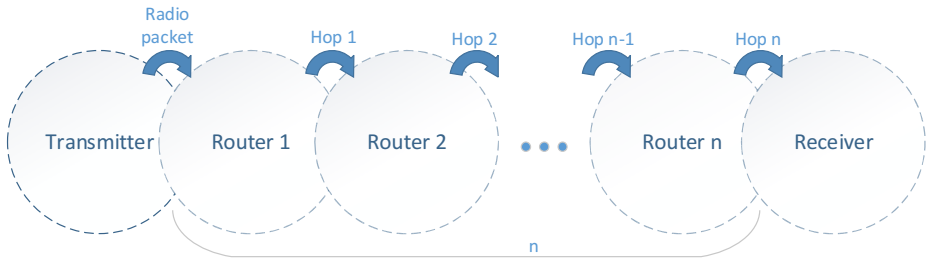


Fig. 2. Network used during tests for variety of routers diagram

Tests were carried out for 5 routing devices. Communication parameters were checked consecutively for one device, then for two devices and so on. In this manner, graph showing the impact of number of data packet hops on transmission parameters was determined.

3 Measuring Setup

The most important element of measuring instruments was TR52DA radio module. Chip allows establishment of radio communication link in band 868/916 MHz modulated by FSK algorithm. Additionally, module allows IQMESH protocol implementation. Interface has software tools used for example in bonding receiver and transmitter, network configuration, filtering and protection of the radio packets, data routing, etc. Figure 4 presents transceiver module with its basic components marked.

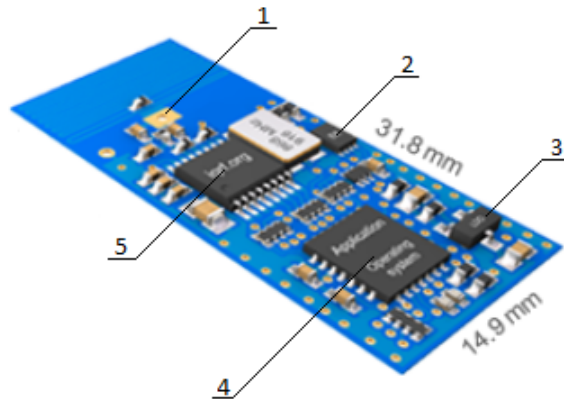


Fig. 3. Structure of TR52DA chip, 1 – PCB antenna, 2 – EEPROM memory, 3 – voltage regulator, 4 – MCU with OS, 5 – MRF49XA ISM Band RF Transceiver [4]

The heart of the chip is PIC16LF1938 microcontroller with IQRF operating system, 28 KB flash memory and 8-bit core with 32 MHz clock. Microchip MRF49XA RF transceiver enables ISM band communication controlled by commands from

MCU. Whole platform has been constructed in the way, that the module can be mounted using SIM card connector. Specified TR52DA and MRF49XA features [4, 5]:

- Supply voltage: 3.1–5.3V
- Maximum transmission speed: 86.2 kB/s
- Standard radio sensitivity: –110 dBm
- Standard radio output power: +7 dBm

Additional instruments used during the tests: CKUSB04 module programmer (for communication with computer), evaluation kits DKEVAL04 (to supply router devices and transmitter) and PC computer (for data acquisition). Each radio transmission parameter has been tested with software, created especially for this purpose. Individual application provides favorable conditions for specific transmission parameter testing.

4 Results

This chapter includes the results of research presented in form of graphs with mathematical models. As mentioned, three transmission parameters have been tested:

- Efficiency – specified graph point was determined as arithmetical mean of 10 measurements. Single measurement consisted of 100 radio packets sent to receiver. Efficiency (E) is calculated as a ratio of received packets (P_r) to the sent packets (P_s). Formula 1 illustrates method of calculation:

$$E = \frac{P_r}{P_s} * 100 [\%] \quad (1)$$

- Capacity [b/s] – amount (n) of received data in time (t), minus time required for data analysis (t_a). Measurement was determined on the basis of time required to receive at least 1 Mb of data. Single packet size was 88b, thus Formula 2 used for a measurement calculation, can be described by a following equation:

$$C = \frac{n * 88[b]}{t[s] - t_a[s]} \quad (2)$$

- RSSI – Received Signal Strength Indicator determining radio power of received signal. Value was specified by arithmetical mean of at least 500 measurements.

5 Single Router Results

Results presented in this chapter, concern tests for single routing device. Described models are introduced as a function of distance d . Chart of transmission effectiveness is demonstrated in Fig. 4.

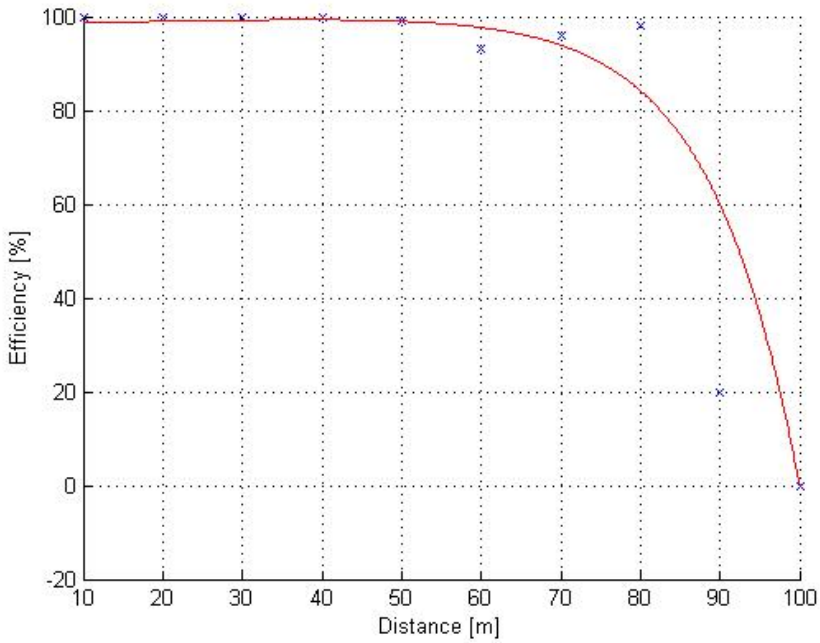


Fig. 4. Transmission efficiency as a function of distance

Mathematical model of efficiency is described by equation 3:

$$E(d) = -0.1315e^{0.0895d} + 98.37e^{e*10^{-4}d} \tag{3}$$

Efficiency is the most important parameter of the radio data transfer. The chart shows, that for 80 meters of transmission, number of received packets fluctuated on level of 100%. That proves connection stability. Thus, it can be assumed that, single routing device usage, can improve network range by 80 meters. In addition, developed model may help with estimation of amount of packets received between 70 and 90 meter of transmission. Compared to results obtained from previous tests, difference between range of single transmitter and router is equal to 30 m [5]. This may be due to the greater number of packets in network. Selected may conflict with each other, what may lead to data loss.

Figure 5 shows chart of link capacity in function of distance. Similar to previous characteristic, complete range loss occurred at 80 meter of transmission. The decrease between graph points is more regular. It proves dependence between distance and connection capacity, despite efficiency level. Mathematical model described by formula 4, enables assessment of capacity value on specified distance. It might be useful in radio systems where bandwidth is a range indicator. For transmission based on ISM band, such systems are quite unique.

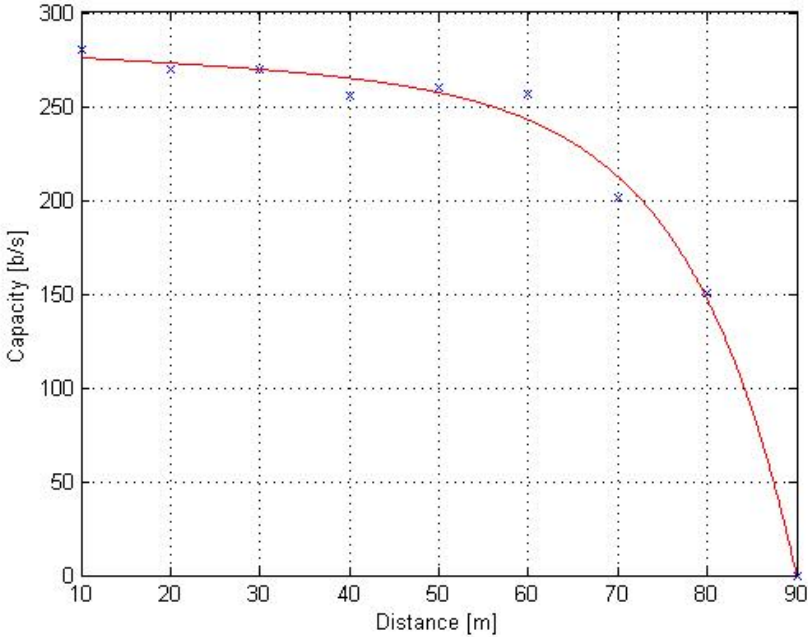


Fig. 5. Change of capacity in function of distance

Model approximating chart shown at Fig. 5:

$$C(d) = -0.1562e^{0.0823d} + 278.6e^{-0.0008d} \quad (5)$$

Next tested parameter was RSSI of received signal. Graph showing indicator value in function of distance is presented in Fig. 6. Changes in the value of the parameter are the most stable and monotonous from all presented results. Decrease is about 10% every 10 meters. Similar to direct communication between transmitter and receiver, the radio signal ceased to be received when the value of the RSSI dropped below 30%. Formula described by equation 6 might be used during the creation of network based on tested modules. Estimation of RSSI value in specific location, allows to determine expected signal power in receiver. In places where the value of the indicator falls below 50%, communication can be easily disturbed or may cause data packet loss. Approximation model of chart presented in Fig. 6:

$$RSSI(d) = -0.0124d^2 + 0.0806d + 82.21; d \in < 10; 90 > \quad (6)$$

It can be assumed that RSSI level is above 95% at first 10 meters of the transmission. All presented results compared with previous studies, are characterized by decrease of 30 meters of transmission range [5]. It is hard to pinpoint the reason for this phenomenon. It may be due to the greater number of devices in network, interference in the signal path or even problems associated with routing algorithm.

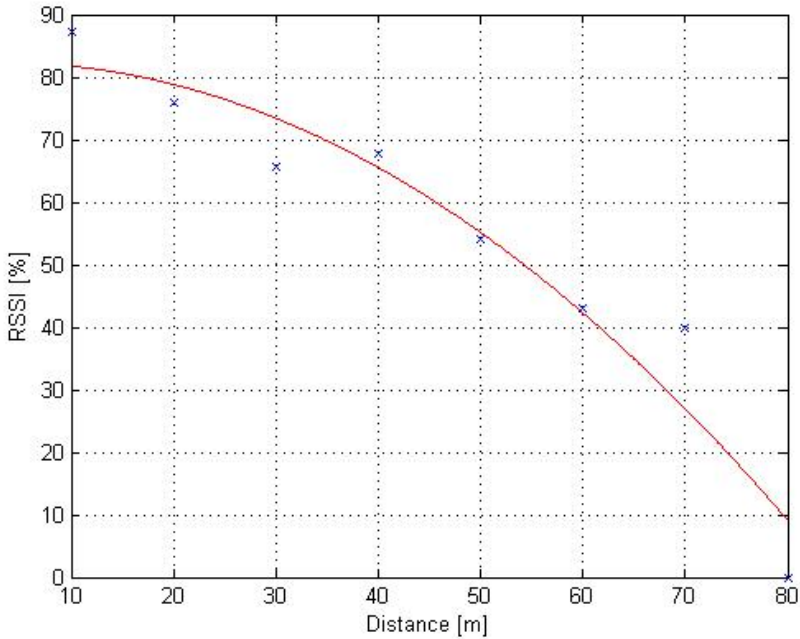


Fig. 6. Received Signal Strength Indicator in function of distance

6 Several Routers Results

Routers were arranged that RSSI value between devices was at the level from range of 70–80%. Such a value of signal strength should prevent data loss and provide the stability of the link. According to the assumption, RSSI tests have shown that, increase of routers amount had no influence on indicator value. This is due to the fact that value is measured between receiver and the nearest router, which did not change its position during the tests. Hence, efficiency value in proper network setup should not change as well. Hypothesis was confirmed by research. Average efficiency value for all measurements was approximately 96%.

Amount of routers affected capacity value only. It is completely understandable. Each device has specified period of time required for background further packet transmission. Therefore, the results could be approximated by linear model. Graph showing capacity changes and its mathematical model, is presented in Fig. 7 and equation 7. It is worth noticing, that characteristics slope level can be configured in software by user. The aim of the studies was to determine stability of networks that use data routing algorithms. Model approximating graph shown in Fig. 7:

$$C(n) = -13.9n + 278.7 \quad (7)$$

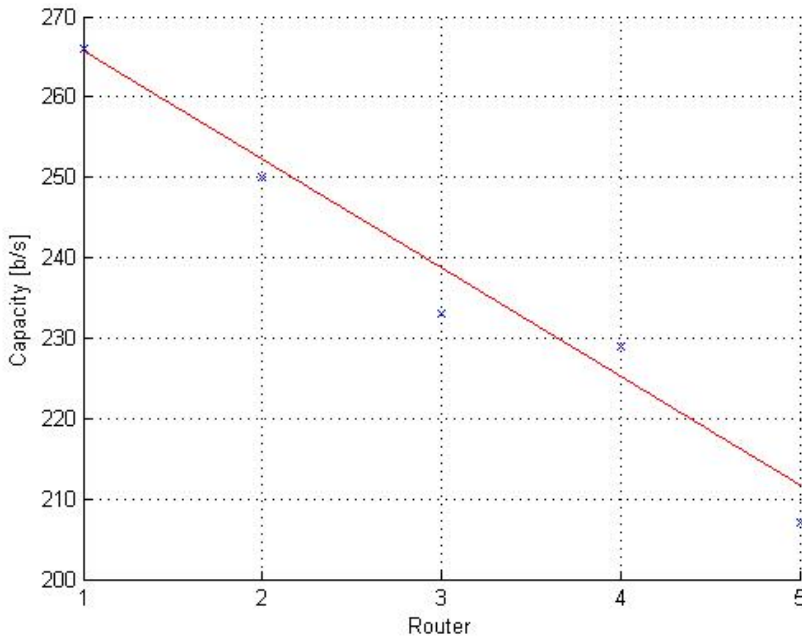


Fig. 7. Link capacity in function of number of routing devices

7 Conclusion

To sum up, described tests focused on the issue of the wireless data exchange using ISM band. The aim of the studies was to determine impact of network data routing on radio transmission parameters. Tests allowed to estimate basic functional parameters of routing devices. The research shows that usage of single router can provide 70 m network range increase. Additionally results proved, that network parameters are not dependent from number of used routers. Proper network setup, ensure stable transmission without data loss, but with decreased bandwidth. Each packet hop causes extension of time required for data reception. Results acquired from single router tests, compared with previous studies, are characterized by decrease of 30 meters of transmission range. Developed mathematical models allow quick estimation of network parameters, on the stage of its design. All tests were performed with specially prepared software and measuring setup.

References

1. Seflova, P., Sulc, V., Pos, J., Spinar, R.: IQRF Wireless Technology Utilizing IQMESH Protocol. In: 2012 35th International Conference on Telecommunications and Signal Processing (TSP), pp. 101–104 (2012)

2. Sulc, V., Kuchta, R., Vrba, R.: IQMESH implementation in IQRF wireless communication platform. In: Second International Conference on Advances in Mesh Networks, MESH 2009, pp. 62–65 (2009)
3. <http://www.iqrf.org>
4. Scherer, R.: Radio zastępuje kable. *Pomiary, Automatyka, Robotyka* 11, 7–8 (2007)
5. Microchip, MRF49XA Data Sheet ISM Band Sub-GHz RF Transceiver
6. Bazydło, P., Dąbrowski, S., Szewczyk, R.: Wireless temperature measurement system based on the IQRF platform. In: Awrejcewicz, J., Szewczyk, R., Trojnacki, M., Kaliczyńska, M. (eds.) *Mechatronics: Ideas for Industrial Applications*. AISC, vol. 317, pp. 281–288. Springer, Heidelberg (2015)
7. Radio Regulations Resolutions and Recommendations, Edition of, ITU-R (2012)
8. Zheng, J., Lee, M.J.: *A Comprehensive Performance Study of IEEE 802.15.4*. IEEE Press Book (2004)
9. Wireless, L.A.N.: *Medium Access Control (MAC) and Physical Layer (PHY) Specifications*. IEEE Computer Society (2012)
10. Goszczynski, T., Pilat, Z.: Considerations on Coverage and Navigation in Wireless Mobile Sensor Network. *Journal of Automation, Mobile Robotics & Intelligent Systems* 1 (2011)

Influence of the Humidity on Signal of Strength in Laboratory Weighing Scales

Szymon Dąbrowski¹, Piotr Bazydło¹, and Roman Szewczyk²

¹Industrial Research Institute for Automation and Measurements PIAP,
Al. Jerozolimskie 202, 02-486 Warsaw, Poland
{sdabrowski, pbazydlo}@piap.pl

²Institute of Metrology and Biomedical Engineering,
Warsaw University of Technology, Warsaw, Poland
r.szewczyk@mchtr.pw.edu.pl

Abstract. This paper concerns impact of the humidity on the weighing result, using ultra-precision laboratory balances. It presents description of research methods and measuring station used during the tests. Measurements were made for two mechanical weight solutions: without additional seals and with additional seals (of selected mechanical elements). In addition, this paper contains the results of the measurements, together with the characteristics and mathematical models illustrating the effect of humidity on the signal of strength.

Keywords: humidity influence, laboratory weighing scales, environmental research.

1 Introduction

The process of mass measurement plays a key role in some industries, for example in the: pharmaceutical, medical, food and chemical industry. It is crucial, because finding the right proportion of mixed ingredients determines the quality of the product or company economics [9]. Usually, mixed substances reach the weight of 10^{-4} gram, what significantly complicates the weighing process. To measure such a small magnitude, the most common laboratory balances are used. They provide accurate measurement with high resolution. In addition, the measurement of such order of magnitude is greatly influenced by environmental conditions, such as: pressure, temperature and humidity [10]. Previous studies have shown that the greatest effect on the measurement has atmospheric pressure, which has strong influence on the air buoyancy inside the weighing chamber [4, 6]. Temperature primarily affects the laboratory balances electronics, what is reflected in the measurement error. The accumulated humidity adversely affects the mechanical components [5]. Due to the fact that different conditions occurs during the measurements in different laboratories, it is necessary to provide adequate compensation of these conditions in the measuring device [8]. Compensation task can be realized by appropriate mechanical modifications or by software, which integrates given electronic solutions. In the case of humidity, the

easiest way is to change the construction of the elements that has the highest absorption, by usage of seals or material shifts.

The research described in this publication is related to the quantitative impact of humidity on the measurement of the laboratory scales. This paper presents the results of measurements and mathematical models developed on the results basis. The study was conducted for two different solutions of RADWAG weighing scales.

2 Research Methodology

Object of the research is laboratory scale XA 82 / 220.3YA, which basic technical parameters are presented below[7]:

- Maximum load: 82/220 g
- Minimum load: 1 mg
- Accuracy: 0,01/0,1 mg
- Operating temperature: 10–40 °C
- Operating humidity: 40% – 80%

The scales allow to measure mass 82 g with precision 0.01 mg, and 220 g with precision equal 0.1 mg. The average stabilization time is 5s, eccentric load deviation 0.2 mg and repeatability for measurement of 82 g is 0.015 mg when for 220 g it is 0.08 mg. Tested weighing scale is presented on Fig. 1.

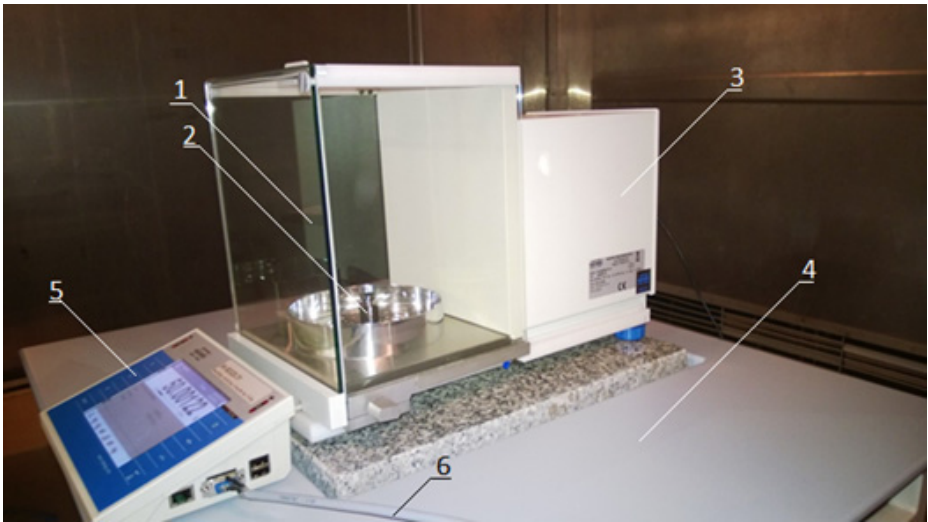


Fig. 1. XA 82 / 220.3YA weighing balance, 1 – weighing chamber, 2 – measured weight, 3 – device control cabin, 4 – weighing table, 5 – human interface, 6 – RS-232 cable

The research was performed for two mechanical structures of scales. Firstly, in the standard version without additional modifications limiting absorption of moisture, by the key scales mechanical elements. Second structure concerns balance with additional seals.

Humidity influence on the weighing result was obtained for a constant temperature of 25°C, which equals half of the temperature range of operation. The moisture had been changed every 10% starting from 40% and ending at 80%. In addition, prior to the test, balance had to be running for 24 hours with the aim of thermal stabilization of the device. Tests were performed using a service self-test feature that allows to carry out a series of measurements of the internal weight of the 179.5496 g mass. Activities executed during a self-test procedure are symbolically depicted at Fig. 2. A single series of measurements consisted of at least 60 measurements recorded with 0.5 minute intervals. In addition, prior to the measurement series, weighing scale was in stable environmental conditions for at least 6 hours. Individual measurements were calculated as the arithmetic mean of a single series.

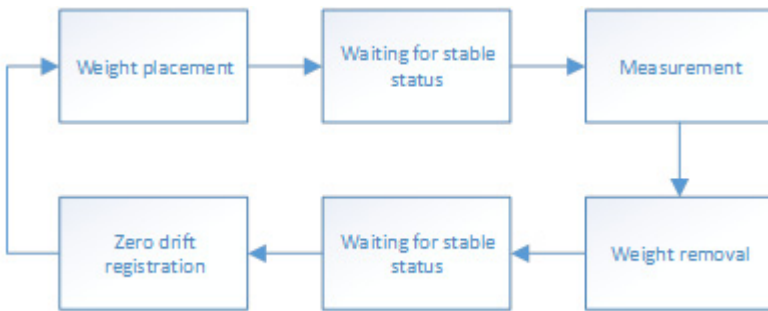


Fig. 2. Activities performed during a scale self-test procedure

3 Measuring Station

Measuring station used during the tests consisted of three main elements:

- Object of study – the weighing balance placed on a special anti-vibration table.
- PC computer for data acquisition.
- Climatic chamber for humidity and temperature control in scale environment.

Station allows to perform tests automatically, in order to elimination of influence of person performing the tests. The connection between the computer and the weighing scale is established via the RS-232 interface. The main problem of the test station was the impact of the vibration caused by the climate chamber. Despite the use of a special weighing table, vibrations heavily influenced the result of the measurement. Because of that, measurement stabilization during operation of the climate chamber was unattainable.



Fig. 3. Measuring station block diagram

For this reason, the climate chamber was switched off until end of measurement test series. After reaching the mechanical stabilization of the device, series of measurements were performed. Figure 4 presents measuring station.

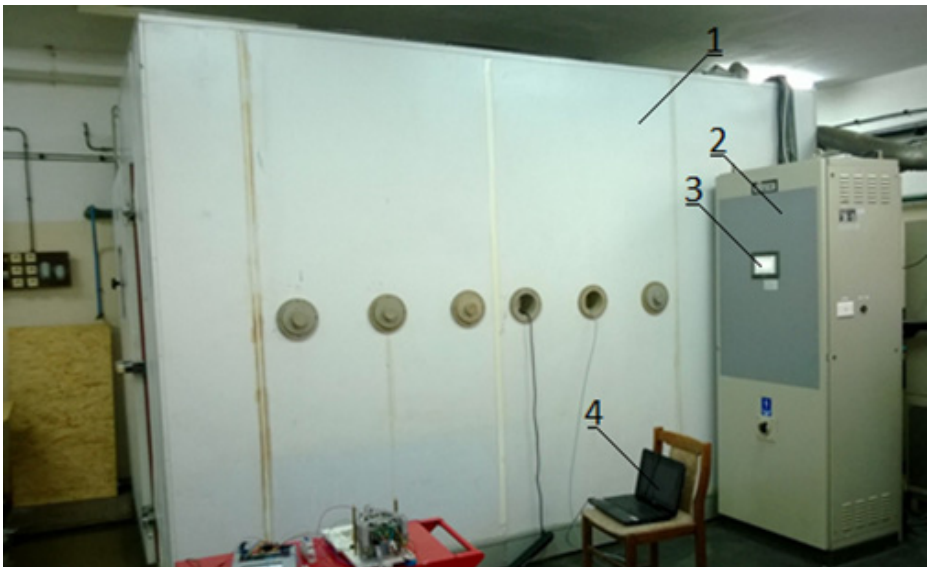


Fig. 4. Real photography of measuring station, 1 – climatic chamber, 2 – control cabin, 3 – HMI panel, 4 – PC computer

4 Results

This chapter presents the results of research presented in form of graphs with mathematical models. Weather conditions prevailing outside the climatic chamber during the tests has contained in the range of values presented in Table 1.

Table 1. Environmental conditions during the tests

Environmental conditions	
Temperature [°C]	5 – 21.8
Humidity [%]	16,7 - 90
Pressure [hPa]	989.9 - 1015

Due to the pressure impact on the result returned by the weight, the results are presented with compensation of conditions prevailing in the device weighing chamber. To properly estimate this impact, the first step is to calculate the density of the air from the formula I [1].

$$\rho_a = \frac{0.348444 * p - h(0.00252 * t - 0.020582)}{273.15 + t} \quad (1)$$

where:

ρ_a – air density [kg/m^3],
 p – atmospheric pressure [hPa],
 h – air humidity [%],
 t – temperature [°C].

Then, after substituting the calculated value to the II equation [2, 3], actual mass of the sample can be calculated from the following formula:

$$m_c = m * \frac{1 - \frac{\rho_a}{\rho}}{1 - \frac{\rho_a}{\rho_c}} \quad (2)$$

where:

m_c – final result,
 ρ – calibration weight density [kg/m^3],
 ρ_c – measured weight density [kg/m^3],
 m – result return by scale.

4.1 Measurements for Standard Construction of Weighing Scale

Standard design of the balance refers to construction without additional seals. Figure 5 presents graph of humidity in function of weight. Mathematical model that approximates the characteristics of Fig. 5 is described by the III equation

$$M[g] = -0.0002683 * h[\%] + 179.6 \quad (3)$$

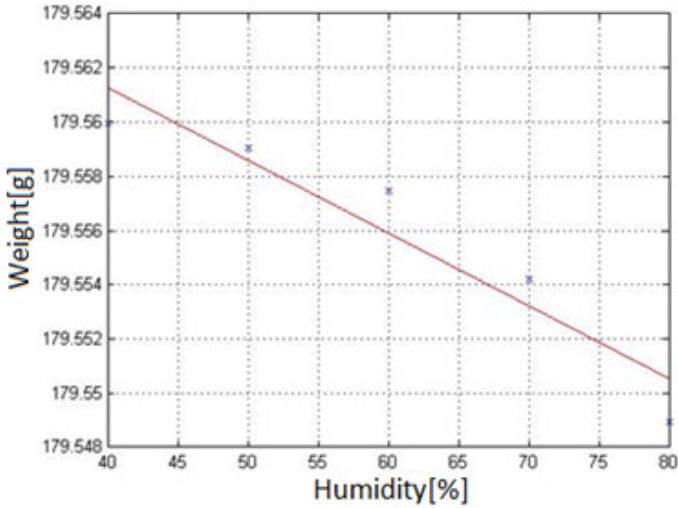


Fig. 5. Impact of humidity on weighing result returned by standard construction weighing scale

According to the assumption, the bigger humidity level in the weight environment, the smaller measurement error. Low humidity causes the formation of electrostatic charges that can disturb the measurement. Equation III describes the measurement model of specific weight. To present the impact of humidity on the measurement of the mass in more universal way, Fig. 6 had been presented. It illustrates the measurement error in function of humidity.

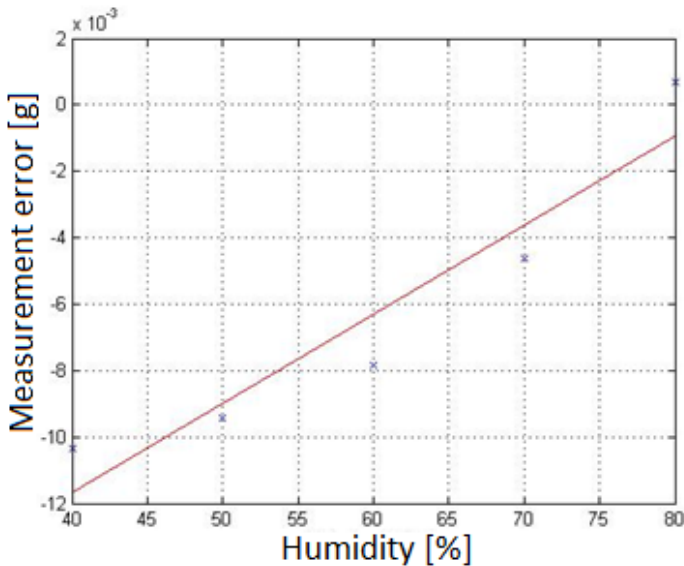


Fig. 6. Measurement error in function of humidity in standard construction scales

Model approximating the characteristics presented in Fig. 6 has been described by the equation IV:

$$e[g] = -0.0002683 * h[\%] - 0.02241 \quad (4)$$

Above mentioned error was calculated as the difference between the actual weight and the arithmetic mean of weight measurement series. Due to the regular distribution of the obtained results, the function is approximated by a linear model. That solution may be advantageous because of the software implementation of moisture compensation procedure.

4.2 Measurements for Modified Construction of Weighing Scale

Modified construction of weighing scale means that the most important mechanical elements had been sealed (for example coils or moving parts). Fig. 7 illustrates the results of measurements of internal weight for the modified design of the device.

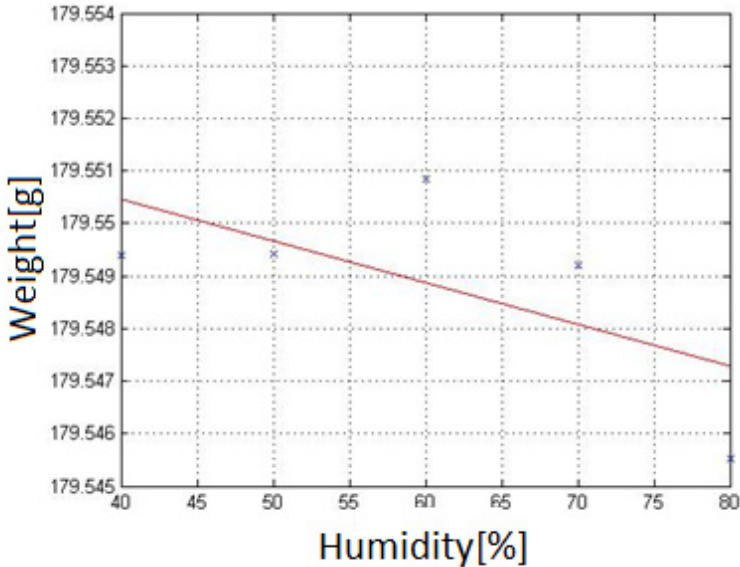


Fig. 7. Impact of humidity on weighing result returned by modified construction weighing scale

Equation V describes approximation model of characteristic presented in Fig. 7:

$$M[g] = -7.935e - 5 * h[\%] + 179.6 \quad (5)$$

In accordance to the theoretical assumption, characteristic direction is the same as in the previous instance. It is worth to notice that the results are more accurate, what proves device performance improvement. Measurement error has strongly decreased, what is easier to observe on the graph shown in Fig. 8.

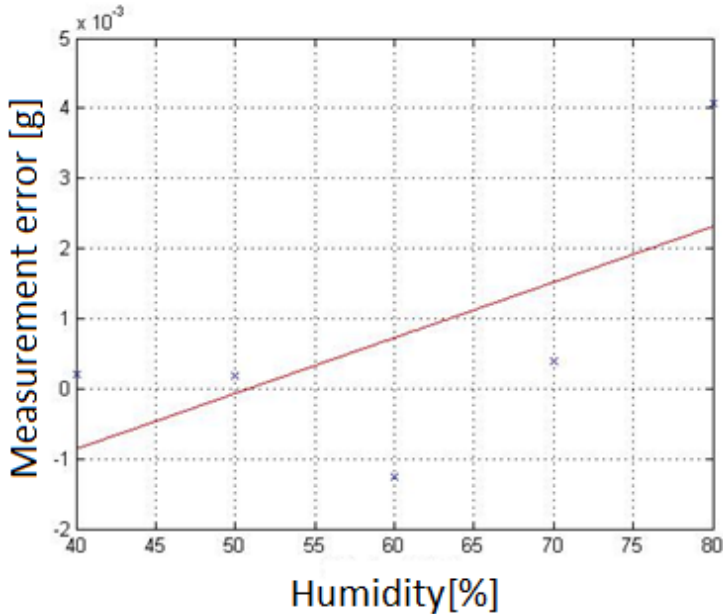


Fig. 8. Measurement error in function of humidity in modified construction scales

Model which approximates the characteristics shown in Fig. 8 is described by the equation VI:

$$e[g] = -7.935e - 5 * h[\%] - 0.004037 \quad (6)$$

In accordance to the Fig. 8, it can be assumed that the higher relative humidity, the higher measurement error. It proves the effectiveness of the seals, which eliminates the influence of electrostatic charges. On the other hand, it shows penetration of moisture through the seals, changing the weighing result thereby. Another parameter which refers to the impact of humidity on the weight mechanism is the scale zero drift. Zero drift comparative characteristic is shown in Fig. 9. Orientation of characteristics in both cases are similar to the characteristics shown in Figures – from 5 to 8. Thus, it can be assumed that the zero drift has strong impact on measurement result. In addition, it can be noticed that the characteristics of the modified mechanism is smoother and the results are five times better than in standard scale construction.

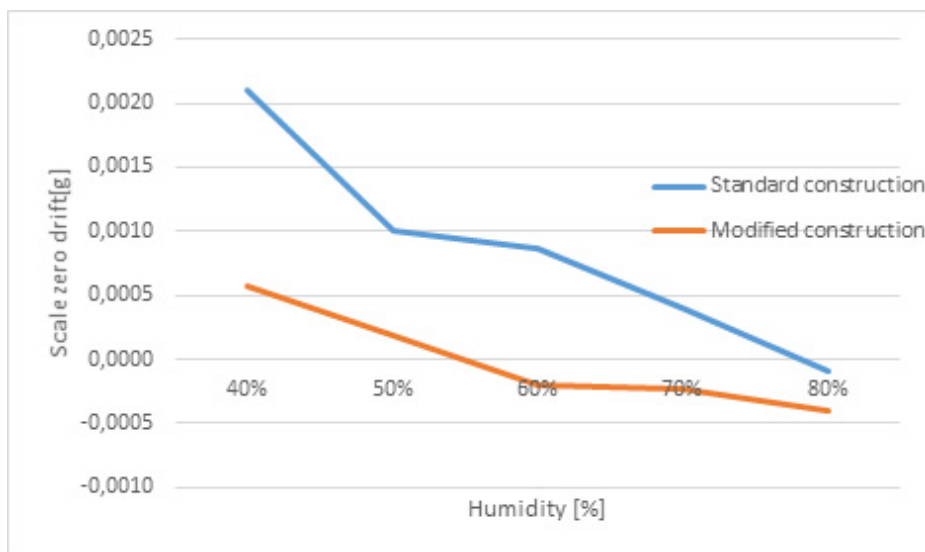


Fig. 9. Comparative characteristic of scale zero drift

5 Conclusion

The aim of the study was to examine the impact of humidity on mass measurement performed by laboratory scales. In addition, research helped to determine the effectiveness of the sealing of balance mechanism. The presented graphs shows that increasing humidity decreases measurement error. This behaviour is justified by the fact that low moisture generates static electricity, which strongly disturbs the measurement. In addition, after the tests it can be concluded that the used balance mechanism modifications leads to almost five times operation improvement. The study was performed using the measurement station, which allows fully automatic measurements. The test results illustrates the applicability of the compensation of humidity in the laboratory scales.

We would like to thank RADWAG Balances and Scales Company for providing us research object XA 82/220.3YA analytical balance, their cooperation and knowledge exchange on the static weighing field.

Acknowledgements. This work has been supported by the National Centre for Research and Development (NCBiR) within the PBS Programme (no. PBS1/B3/8/2012). We would like to thank RADWAG Balances and Scales Company for providing us research object XA 82/220.3YA analytical balance, their cooperation and knowledge exchange on the static weighing field.

References

1. EURAMET/cg-18/v.02, Guidelines on the Calibration of Non-Automatic Weighing Instruments (2009)
2. OIML R 111-1 International Recommendation, Weights of classes E₁, E₂, F₁, F₂, M₁, M₁₋₂, M₂, M₂₋₃ and M₃, Part 1: Metrological and technical requirements, Edition (2004)
3. OIML D 28 International Document, Conventional value of the result of weighing in air, Edition (2004)
4. Reichmuth, A., Wunderli, S., Weber, M., Meyer, V.R.: The Uncertainty of Weighing Data Obtained with Electronic Analytical Balances. *Microchimica Acta* (2004)
5. Pozivil, M., Winiger, W., Wunderli, S., Meyer, V.R.: The Influence of Climate Conditions on Weighing Results. *Microchimica Acta* (2006)
6. Kehl, K.G., Weirauch, K., Wunderli, S., Meyer, V.R.: The influence of variations in atmospheric pressure on the uncertainty budget of weighing results. *Analyst* (2000)
7. RADWAG web page, <http://www.radwag.pl/en>
8. Sławomir Janas, Warunki Środowiskowe Dla poprawnej Pracy Wag Elektronicznych, Centrum Metrologii (2009)
9. Bielawski, P.: Zrównywanie wartości miar cech obiektów technicznych. *Pomiary, Automatyka, Robotyka* 4 (2014)
10. Iwasińska-Kowalska, O.: Metrologiczne podejście do doboru narzędzia pomiarowego. *Pomiary Automatyka Robotyka* 11 (2014)

Heating Process of the Most Important Mechanical Elements in Laboratory Weighing Scales

Szymon Dąbrowski¹, Michał Nowicki², Piotr Bazydło¹, and Roman Szewczyk²

¹Industrial Research Institute for Automation and Measurements PIAP,
Al. Jerozolimskie 202, 02-486 Warsaw, Poland
{sdabrowski, pbazydlo}@piap.pl

²Institute of Metrology and Biomedical Engineering, Warsaw University of Technology,
Warsaw, Poland
{r.szewczyk, m.nowicki}@mchtr.pw.edu.pl

Abstract. This publication refers to the research conducted in the field of the analytical balances mechanical stability. In the publication there is a description of research methodology and the measuring stand used during the test. The aim of the study was to determine the heating time constant of the selected mechanical components of the device. The tests made it possible to estimate the time required to thermally stabilize the balance and to determine the effect of device heating on the measurements. In addition, the publication contains the results reflecting changes in the temperature of selected elements of the device. The characteristics were approximated with the first-order inertial model, which allowed for the determination of the mechanism warm-up time constant value.

Keywords: analytical balances, scale thermal stabilization, heating time constant.

1 Introduction

The process of the mass measurement begins to play an increasingly important role in industry and science [9]. Proper preparation of proportions of mixed ingredients, quality control of the production process, and laboratory testing are just some of the issues in which the question of mass measurement is crucial [8]. Measurement errors or incorrect equipment can lead to significant financial losses for the company (when the high value components are mixed, for example in the chemical industry) or hazardous situations (i.e. pharmaceutical industry) [1, 2]. Sometimes there is a situation that requires a weighing process with a 0.00001 g resolution. Then, the measurement is influenced by numerous factors, such as: the influence of the person performing the measurement, environmental conditions or mechanical and thermal stability of the device [3, 4]. The complexity of the equipment for measuring such small values implies that they must work in a stable laboratory conditions. In addition, the heating of the mechanical components of the device can lead to the zero drift of the unloaded scale. Therefore, before proceeding with the measurements, proper thermal stabilization of the measuring instrumentation must be ensured. To effectively estimate the

time required to thermally stabilize the scales, the time constants of heating up the most important elements must be determined.

The publication refers to studies which aim was to determine the time constants of heating of selected mechanical components of the XA 82/220.3YA analytical balance made by RADWAG company. In addition, the publication presents an overview of the measuring stand used during the measurements.

2 Research Methodology

The investigation object is the XA 82/220.3YA analytical balance made by RADWAG company. Basic technical parameters are as follows [6]:

- Maximum load: 82/220 g,
- Minimum load: 1 mg,
- Accuracy: 0,01/0,1 mg,
- Operating temperature: 10–40 °C,
- Operating humidity: 40% – 80%,
- Sensitivity temperature drift: $1 \times 10^{-6} / ^\circ\text{C} \times \text{Rt}$.

In addition, the weight is characterized by a 5 s mean time of measurement stabilization, 0.2 mg eccentricity, and measurement repeatability of 0.015/0.08 mg. The device is powered by a DC voltage in the range of 13.5–16 V and 600 mA current consumption. The photo of the device is presented in the Fig. 1 [6].

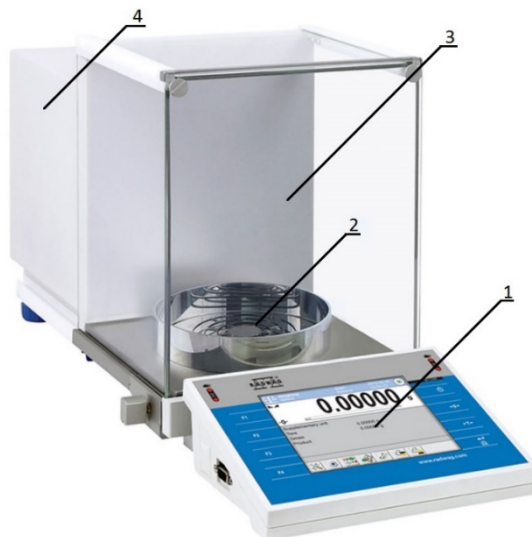


Fig. 1. Object of the research, 1 – human interface, 2 – scale pan, 3 – weighing chamber, 4 – device control cabin

The study consisted of recording the temperature of selected mechanical elements of the scales during the 60 hours operation under 200 g load – 90% of the maximum. Before the measurements, the scale was turned off for 24 hours. The measurement was performed using a the Pt 100 sensors. Sensors have been placed in the body of the device’s mechanism near the elements most likely to warm up, i.e. in the vicinity of moving parts, near the optical sensor and in the actuator coil. In addition, for comparison, one of the sensors was placed near the weighing pan in the weighing chamber.

In addition, during the tests changes in temperature, humidity and pressure in the environment, and the results of weighing given by the device were recorded.

The aim of the research was to determine the warm-up time constants of the scale’s structural components. In addition, investigation allowed for verification of the error associated with measurement performance of the thermally unstable analytical balance.

3 Measuring Station

Measuring station must provide accurate and stable measurements with a resolution of 0.1 °C, because before the measurements temperature changes at the level of 1–2 °C were expected. Therefore, for the construction of the measuring stand Pt 100 sensors were used. As the transducer Keithley 2002 multimeter was used, its main technical parameters for the temperature measurement are as follows [7]:

- Temperature range: from –100 °C to +100 °C,
- Measurement resolution: 0.001 °C,
- Measurement accuracy: +/- 0.021 °C,
- Temperature coefficient: +/- 0.001 °C.

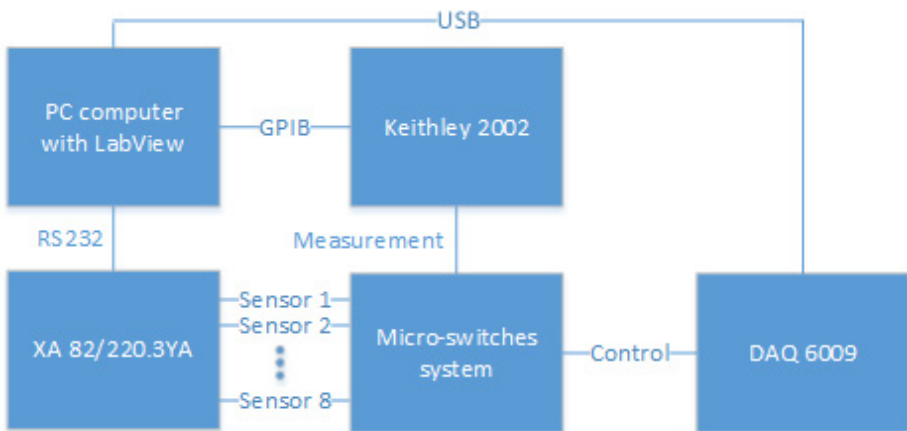


Fig. 2. Schematic block diagram of the measurement stand

There were 8 sensors used in the measurement stand. For this reason, it was necessary to develop and apply system used to switch between the sensors, so that at any given moment multimeter was connected to only one of them. The problem during the construction of the system was the error associated with switching element resistance. For this reason, due to the low resistance it was decided to use a micro-switches. This solution introduces a constant error to measurements, the value of which fluctuates around 30 mOhm. Test stand schematic is shown in the Fig. 2.

The micro-switches system was controlled with the NI DAQ-6009 data acquisition card and software written in LabVIEW environment. In addition, the software has been used for the data acquisition from the multimeter, and to collect the results returned by the scale at the specified frequency. The simplified algorithm of the application controlling the data acquisition and the test station is shown in Fig. 3. It allowed for the fully automated execution of the entire 60-hour measurement.

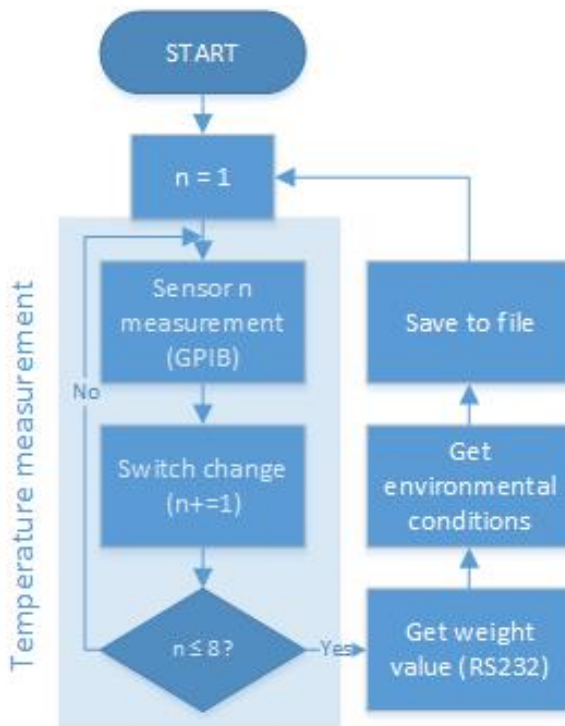


Fig. 3. Schematic algorithm of the test stand control software

The study was conducted under normal operating conditions of the analytical balances. No ambient temperature compensation was used. Additionally, during the measurements, using a thermo-hygro-barometer ambient environmental changes were recorded. Photo of the measuring stand is presented in Fig. 4.



Fig. 4. Photo of the measuring stand: 1 – XA 82/220.3YA, 2 – micro-switches system, 3 – DAQ 6009, 4 – Keithley 2002, 5 – RS-232 cable, 6 – PC with LabVIEW software, 7 – thermo-hygro-barometer

4 Results

The registered changes in environmental conditions during the measurement are shown in Fig. 5. Because the sensors were closed in scale's body and changes in ambient temperature fluctuated at ± 0.5 °C, it can be assumed that environmental conditions have not significantly affected the measurement.

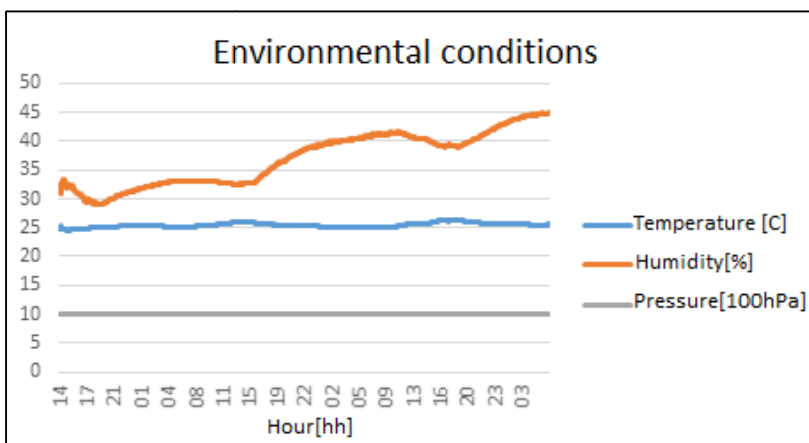


Fig. 5. Environmental conditions during the measurements

The results were approximated with the first-order inertial model. The transmittance of part representing the starting point for modeling is described in equation 1 [5]:

$$G(s) = \frac{k}{T * s + 1} \quad (1)$$

Approximation allows for quick and efficient determination of the value of the time constant T of the heating process. Table 1 shows the values of the time constants estimated on the basis of the obtained results. Due to the length of the measurement, results are shown in hours. In addition, because of the large number of sensors, some of the results are presented as the mean value of the measurements from several sensors.

Table 1. A table containing the list of calculated time constants of selected elements

Sensor placement	Time constant [h]
Actuator coil	3.61
Near weighing pan	3.03
Upper part of the weighing mechanism	2.75
Lower part of the weighing mechanism	3.28

The chart shows that the warm-up time of mechanical components enclosed in scales is similar. The difference between the top and bottom of the body is about 0.5 h. This may be due to the fact that the lower part of the mechanism is constructed from cast parts, of greater mass, which automatically causes the longer heating. Additionally, items that are in the vicinity of the pan and the bottom part of the body are made of steel, which also increases the heating time. The upper part of the balance mechanism heats up fastest, it may be due to the fact that it is close to the electronics unit. The inner part of the actuator is the slowest part to warm up. Comparative characteristic showing the temperature changes of individual components is shown in Fig. 6.

By definition, the time constant is the time needed to reach steady state output. It is estimated that the standard system needs 3–5 time constants to achieve a steady state.

Thus, using the relationships 2, the average time heating up the weighing mechanism (t_{avg}) can be estimated:

$$t_{avg} = 4 * T_{avg} \approx 13 h \quad (2)$$

Thus, in theory, it is required to power on the balance for at least 13 hours prior to the measurements. Taking measurements on thermally unstable weight can cause significant measurement errors. The effect can be easily seen in Fig. 7, illustrating the change in the weighing results during the tests.

The chart shows that the temperature distribution in the housing of the device is regular. The graph clearly shows the scale power up period. After some time, the temperature of all elements stabilized at about 3 degrees higher than the initial value.

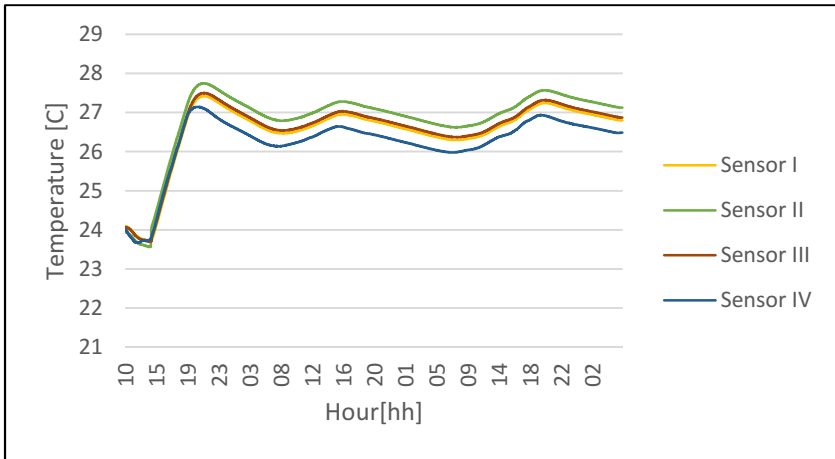


Fig. 6. Comparative temperature characteristics of individual elements, Sensor I – Lower part of the weighing mechanism, Sensor II – Upper part of the weighing mechanism, Sensor III – Near weighing pan, Sensor IV – Actuator coil

The lowest temperature was recorded in the vicinity of the pan. This indicates that the heating of the elements in the body scales does not affect the conditions in the weighing chamber. The highest temperature was recorded in the upper part to the mechanism. As with time constants, such observation may be explained by the influence of electronics unit temperature.

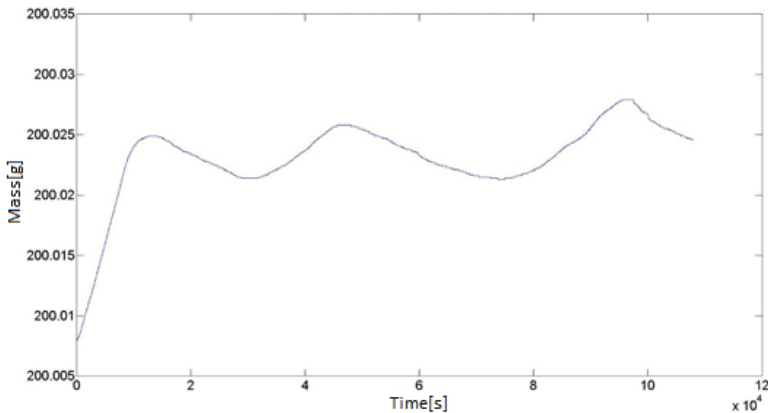


Fig. 7. Changing the force signal as a function of time

Comparing the characteristics of Fig. 6 and Fig. 7 a strong correlation between the force signal returned by the scale and the temperature of its components can be seen. From this follows that the error associated with the measurements performance of thermally unstable scale may even reach a value of 0.015 g, which for some measurements

may prove unacceptable. Differences in the temperatures of the individual elements can be explained by the fact that each element is made of a different material. Different values of the thermal conductivity make every element heats up at different rates.

5 Conclusion

Research described related to the issues connected with time constant of heating of selected mechanical elements of the analytical balances. Research results allowed to determine the time required for thermal stabilization of the scale, and the error associated with the performance measurements on thermally unstable device. In addition, the results presented are the starting point for the process of the mechanical modifications to limit the influence of devices heating. The research shows that the temperature inside scales during its work is about 3 °C higher than the temperature of its environment. In addition, the characteristics presented prove a strong correlation between the signal returned by the scale and the temperature of its components. The tests were performed using fully automatic measurement stand. The error of the measuring stand was calculated during the measuring system calibration tests.

Acknowledgements. This work has been supported by the National Centre for Research and Development (NCBiR) within the PBS Programme (no. PBS1/B3/8/2012). We would like to thank RADWAG Balances and Scales Company for providing us research object XA 82 / 220.3YA analytical balance, their cooperation and knowledge exchange on the static weighing field.

References

1. EURAMET/cg-18/v.02, Guidelines on the Calibration of Non-Automatic Weighing Instruments (2009)
2. OIML R 111-1 International Recommendation, Weights of classes E₁, E₂, F₁, F₂, M₁, M₁₋₂, M₂, M₂₋₃ and M₃, Part 1: Metrological and technical requirements Edition (2004)
3. Reichmuth, A., Wunderli, S., Weber, M., Meyer, V.R.: The Uncertainty of Weighing Data Obtained with Electronic Analytical Balances. *Microchimica Acta* (2004)
4. Pozivil, M., Winiger, W., Wunderli, S., Meyer, V.R.: The Influence of Climate Conditions on Weighing Results. *Microchimica Acta* (2006)
5. Liptak, B.G.: *Instrument Engineers' Handbook*, 4th edn. Process Control and Optimization, vol. 2. CRC Press (2005)
6. <http://www.radwag.pl/en>
7. Model, Multimeter Specifications, Keithley Instruments, Inc. (2002)
8. Iwasińska-Kowalska, O.: Metrologiczne podejście do doboru narzędzia pomiarowego, *Pomiary Automatyka Robotyka*, 11 (2014)
9. Chyla, W.T.: Kierunki zmian we współczesnej metrologii naukowej, *Pomiary Automatyka Robotyka*, 10 (2013)

Modified Monte Carlo Method for Calculating the Expanded Measurement Uncertainty

Paweł Fotowicz

Central Office of Measures, Warsaw, Poland
uncert@gum.gov.pl

Abstract. A modified Monte Carlo method for calculating the measurement uncertainty is presented. The method is based on a random number generator for drawing the possible values associated with the output quantity. The set of the random values are represented by the Flatten-Gaussian distribution, which is a convolution of rectangular and normal distributions. The model of measurand must be defined a linear or linearized mathematical function. The numerical and practical examples of the use of the proposed method are also presented.

Keywords: measurement uncertainty, propagation of distributions, Monte Carlo method.

1 Introduction

An approach of measurement uncertainty calculation is changed in the modern metrology. The traditional conception with the use of the law of uncertainty propagation, presented in [1], is upgraded by the propagation of distributions using a Monte Carlo method, recommended in [2]. The propagation of distributions is done through the mathematical model of measurand. The measurement result is represented by probability distribution associated with the measurand.

2 Measurand

The measurand is treated as a random variable. The measurand is an output quantity in mathematical model of measurement, and may be expressed by the measurement function

$$y = f(x_1, \dots, x_N) \quad (1)$$

where x_i are an input quantities, also treated as a random variables. Any random variable x_i may be characterized by suitable distribution, such as a normal, rectangular, triangular, trapezoidal or Student distributions. When the input quantities are independent and the measurement function is linearized by a Taylor series approximation, the output quantity may be defined

$$y = \sum_{i=1}^N c_i x_i \tag{2}$$

where c_i is a sensitivity coefficient, as the partial derivative of first order. In this case the distribution of measurand is a convolution of all distributions associated with input quantities

$$g(\eta) = g_1(\xi_1) * \dots * g_N(\xi_N) \tag{3}$$

where $g(\eta)$ is a probability density function of measurand, and $g_i(\xi_i)$ is a probability density function of any input quantity. The expanded uncertainty U associated with the measurand, as the output quantity y , satisfies an equation

$$\int_{\bar{y}-U}^{\bar{y}+U} g(\eta) d\eta = p \tag{4}$$

where \bar{y} is an estimate of the measurand and p is a coverage probability (Fig. 1). Usually, the $p = 95 \%$.

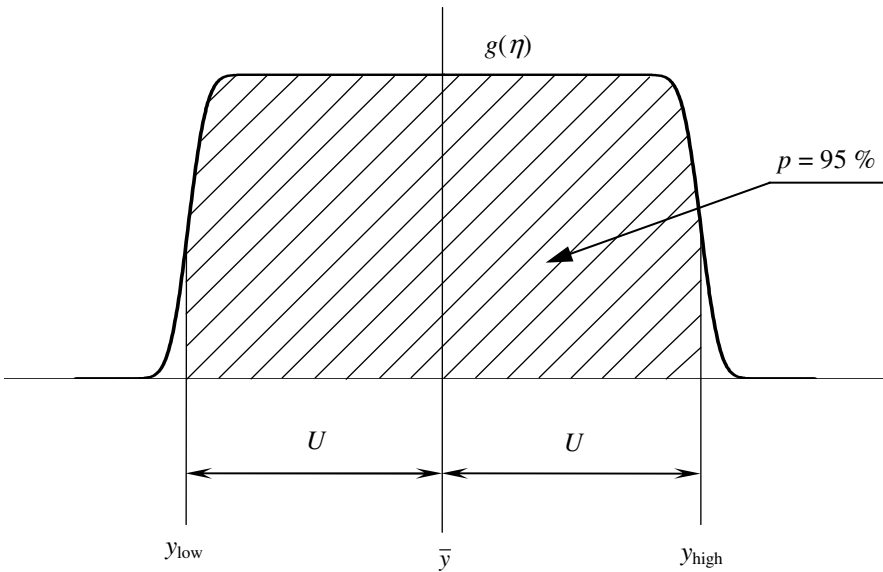


Fig. 1. Distribution for measurand

3 Modified Monte Carlo Method

The Monte Carlo method recommended by document [2] relies on drawing the values associated with the measurand through the measurement model from the distributions of any input quantities. The modified Monte Carlo method relies on drawing that values directly from the distribution anticipated for the output quantity as the approximation of the convoluted distributions. This approximated distribution for output quantity is a Flatten-Gaussian distribution, which is a convolution of one normal and one rectangular distributions. This approximation may be used for linearized measurement functions, and for independent input quantities having distributions, such as the normal, rectangular, triangular, trapezoidal or Student distributions.

The proposed method is based on sampling from the Flatten-Gaussian distribution. This distribution is characterized by the parameter r , which is the ratio of the standard deviation of the rectangular distribution to the standard deviation of the normal distribution [3–4]. Thus, the random number generator of the Flatten-Gaussian distribution can be created from two random number generators [5–6]. One is based on drawing from the rectangular distribution and the second is based on drawing from the normal distribution. The drawing values links the formula

$$y = \frac{r z_R + z_N}{\sqrt{r^2 + 1}} \quad (5)$$

where z_R is a random variable having the rectangular distribution, and z_N is a random variable having the normal distribution. Formula (5) generates the Flatten-Gaussian distribution with the expectation zero and the standard deviation equal one. Bases on this formula we can derived the measurement equation for calculating of the expanded uncertainty, represented by

$$y = u_i z_P + \sqrt{\sum_{j=1, j \neq i}^N \left(\frac{t(\nu)}{k_N} u_j \right)^2} z_N \quad (6)$$

where u_i is a contribution of the largest input quantity having the rectangular distribution, u_j are an other contributions of the input quantities, $t(\nu)$ is the quantile of the Student distribution having ν degrees of freedom, and k_N is the coverage factor associated with the normal distribution. When the input quantities are characterized only by the normal, rectangular, triangular and trapezoidal distributions, then $t(\nu) = k_N$, and the formula (6) takes on the simple form

$$y = u_i z_P + \sqrt{u_c^2 - u_i^2} z_N \quad (7)$$

where u_c is the combined standard uncertainty. Selection of the largest component of triangular and trapezoidal distributions can be done as in [3–4].

The formulas (6) and (7) present the measurement equations for possible values of measurand when the standard uncertainties associated with the input quantities are

known. The standard uncertainties can be calculate as in item 5, and set together with associated them sensitivity coefficients and uncertainty contributions in the uncertainty budget.

The expanded uncertainty may be calculated from equation

$$U = \frac{y_{\text{high}} - y_{\text{low}}}{2} \quad (8)$$

where y_{high} and y_{low} are the maximum and minimum values of measurand fixing an endpoints of the coverage interval for prescribed coverage probability, usually the $p = 95 \%$ (see Fig. 1).

4 Numerical Example

The numerical example represents an additive model with four input quantities having the Student, normal, triangular and rectangular distribution. We assume, that the Student distribution has got four degrees of freedom, $\nu = 4$. The three input quantities have the standard uncertainty equal to one, and the one quantity has the standard uncertainty ten times larger. All the quantities have the expectation zero. Thus, we can calculate the expanded uncertainty U_{MCM} using Monte Carlo method recommended by document [2], and the expanded uncertainty U_{MMCM} using modified Monte Carlo method proposed by the author. The calculation was performed with the numbers of trials $M = 10^6$, and the results are presented in the Table 1. The case A presents the result of calculation when all input quantities have the same standard uncertainty, equal one. The other cases present the result of calculation when one of the input quantities has the standard uncertainty equal ten. The dominant input quantity is characterized respectively by the Student's distribution (case B), normal distribution (case C), triangular distribution (case D) and rectangular distribution (case E).

Table 1. Expanded uncertainty calculated with the use of the recommended Monte Carlo method (MCM) and the modified Monte Carlo method (MMCM) proposed by the author

Case	U_{MCM}	U_{MMCM}
A	4.33	4.36
B	27.96	27.84
C	19.93	19.92
D	19.40	19.58
E	17.14	17.20

5 Practical Use of Method

The modified Monte Carlo method may be applied to evaluation of measurement result in calibration. In calibration of measuring instrument is usually used a linear measurement function as a model of measurand. Let, the measuring instrument is a micrometer calibrated with the use of a gauge block. The measurement equation of the indication error of micrometer, having four input quantities with different distributions, is given as follow

$$e = l + \delta l - l_w - \delta l_t \tag{9}$$

where: l is an indication of micrometer, δl is a resolution of micrometer, l_w is a length of gauge block, and δl_t is a temperature correction.

There are four input quantities in measurement equation:

1) Indication of micrometer – l

The five measurement of the gauge block length are done, which result is presented in the Table 2. The estimate of this quantity is a average of $n = 5$ indications, and the standard uncertainty, as a experimental standard deviation of the mean, is given by

$$u(l) = \frac{s(l)}{\sqrt{5}} = 0.32 \mu\text{m} \tag{10}$$

The probability distribution associated with this quantity is a Student distribution with $\nu = n - 1 = 4$ degree of freedom.

Table 2. Measurement data in calibration of micrometer

Reading l	20.001 mm 20.002 mm 20.001 mm 20.000 mm 20.001 mm
\bar{l}	20.001 mm
$s(l)$	0.71 μm

2) Resolution of micrometer – δl

The resolution of micrometer is 1 μm . It should be take into consideration as well as resolution of zero indication and resolution of indication on the gauge block. So, the probability distribution associated with this input quantity is a triangular distribution. Thus, the standard uncertainty is

$$u(\delta l) = \frac{1}{\sqrt{6}} \mu\text{m} = 0.41 \mu\text{m} \tag{11}$$

3) Length of gauge block – l_w

The length of gauge block is given in the calibration certificate: $l_w = (20.0002 \pm 0.0001)$ mm. The expanded uncertainty ($U = 0.1 \mu\text{m}$) of the length is stated as the standard uncertainty multiplied by the coverage factor $k = 2$, which for a normal distribution corresponds to a coverage probability of approximately 95 %. So, the standard uncertainty is

$$u(l_w) = \frac{0,1}{2} \mu\text{m} = 0.05 \mu\text{m} \quad (12)$$

4) Temperature correction – δl_t

In progress of calibration the laboratory temperature varies between the limits of ± 1 °C, and the coefficient of expansion of gauge block material is $12 \cdot 10^{-6} \text{ }^\circ\text{C}^{-1}$. The standard uncertainty is given as follow

$$u(\delta l_t) = \frac{1 \text{ }^\circ\text{C} \cdot 12 \cdot 10^{-6} \text{ }^\circ\text{C}^{-1}}{\sqrt{3}} 20.0002 \text{ mm} = 0.14 \mu\text{m} \quad (13)$$

All the input quantities are presented in the uncertainty budget (Table 3).

Table 3. Uncertainty budget of calibrated micrometer

Quantity	Estimate	Standard uncertainty	Probability distribution	Sensitivity coefficient	Uncertainty contribution
L	20.001 mm	0.32 μm	Student	1	0.32 μm
δl	0 mm	0.41 μm	triangular	1	0.41 μm
l_w	20.0002 mm	0.05 μm	normal	-1	-0.05 μm
δl_t	0 mm	0.14 μm	rectangular	-1	-0.14 μm
e	0.0008 mm				0.54 μm

The expanded uncertainty calculated with the use of the recommended Monte Carlo method is $U_{\text{MCM}} = 1.198 \mu\text{m}$, but the expanded uncertainty calculated with the use of modified Monte Carlo method proposed by the author is $U_{\text{MMCM}} = 1.217 \mu\text{m}$. The calculation was performed with the numbers of trials $M = 10^6$. If we present the expanded uncertainty with recommended two significant digit the measuring result will be $e = (0,8 \pm 1.2) \mu\text{m}$.

The measuring result may be presented as the numerical distribution association with the measurand. This distribution may be form the distribution function (Fig. 2) as well as the histogram (Fig. 3).

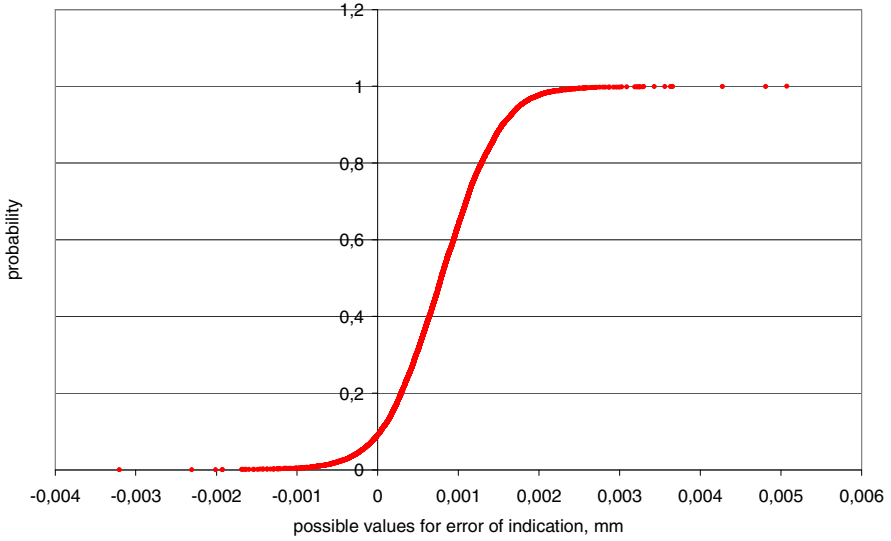


Fig. 2. Numerical distribution function for measurand

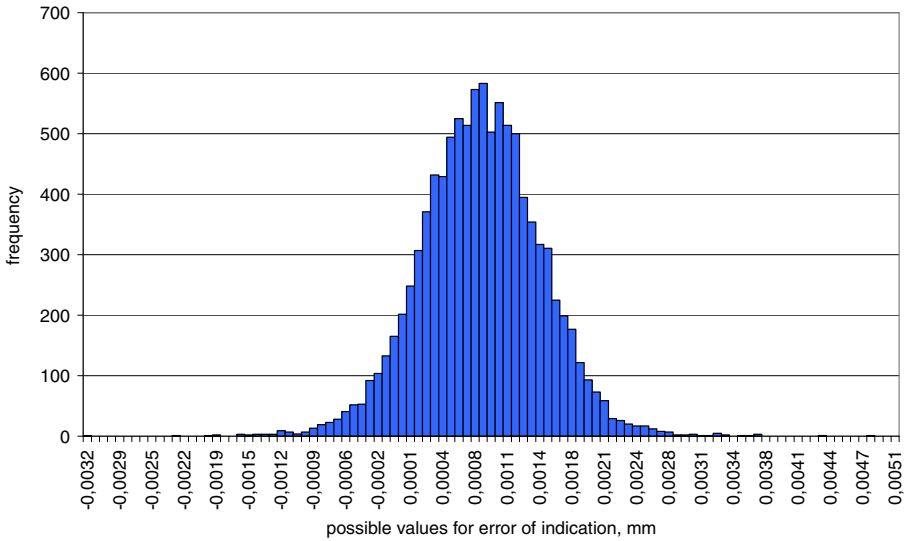


Fig. 3. Histogram for measurand

6 Conclusion

In the case of the linear or linearized mathematical model of measurement, the proposed modified Monte Carlo procedure enables calculation of the expanded uncertainty with

the accuracy close to the accuracy of a Monte Carlo method, which is recommended in [2]. The proposed method is based on the Flatten-Gaussian distribution, that approximates convolution of many random variables having the normal, rectangular, triangular, trapezoidal or Student distributions. The procedure immediately provides the set of possible values of the measurand. The method may be easily implemented with the use of common computational tools, such as the spreadsheet, and the specialized software is not required.

References

1. Guide to the expression of uncertainty in measurement. ISO (1995)
2. Supplement 1 to the “Guide to the expression of uncertainty in measurement” – Propagation of distributions using a Monte Carlo method. JCGM 101:2008 (2008)
3. Fotowicz, P.: Calculating expanded uncertainty by means of analytical method basis of convolution of input quantities distributions. *Pomiary Automatyka Robotyka* 1, 5–9 (2005) (in Polish)
4. Fotowicz, P.: An analytical method for calculating a coverage interval. *Metrologia* 43, 42–45 (2006)
5. Fotowicz, P.: Use of the Flatten-Gaussian distribution for calculating the measurement uncertainty. *PAK* 57, 595–598 (2011) (in Polish)
6. Fotowicz, P.: Methods for calculating the coverage interval based on the Flatten-Gaussian distribution. *Measurement* 55, 272–275 (2014)

Influence of Environmental Conditions on Graphene Resistance

Grzegorz Gawlik¹, Paweł Nowak², Anna Kozłowska¹,
Mateusz Wojtasiak³, and Roman Szewczyk⁴

¹Institute of Electronic Materials Technology,
Wólczyńska 133, 01-919 Warsaw, Poland

{Grzegorz.Gawlik,Anna.Kozłowska}@itme.edu.pl

²Industrial Research Institute for Automation and Measurements PIAP,
Al. Jerozolimskie 202, 02-486 Warsaw, Poland

³Warsaw University of Technology, Institute of Control and Computation Engineering,
Nowowiejska 15/19, 00-665 Warsaw, Poland

⁴Warsaw University of Technology, Faculty of Mechatronics,
sw. A. Boboli 8, 02-525 Warsaw, Poland

Abstract. The influence of the wet and warm atmosphere on CVD graphene was investigated. The CVD graphene grown on Cu foil and then transferred onto the BK7 glass substrate was applied in the experiments. The environmental conditions were established using designed environmental chamber. The wet (RH = 80%) and warm (T = 32 °C) atmospheres were applied for up to eight hours every day for nine days experiment. Rest of time the sample was stored in room conditions. The small changes of the graphene resistance were observed during experiment. SEM and EDS observations demonstrated crystallization of the water impurities like chlorides and organics on the graphene surface under applied conditions. The changes of the graphene wettability caused by condensed contamination may cause the observed resistance changes.

Keywords: graphene, resistance, thermal coefficient.

1 Motivation

Graphene (monolayer carbon sheet) has the potential for various technical applications. Its electrical and thermal parameters, such as high electron mobility, low resistivity at room temperature and high thermal conductivity are extremely interesting. Devices such as Hall effect sensors [1], effective solar cells [2] or graphene based transistors [3] are presenting possibility for common use.

Parameters measured under laboratory conditions may change, when graphene-based device is set to operate in industrial environment. Therefore, basic tests of graphene properties must be conducted before developing commonly used and reliable device.

Described tests were undertaken to observe graphene properties in environment similar to potential applications (significant temperature gradient and variable humidity).

2 Environmental Chamber

2.1 General Idea

Schematic block diagram of designed environmental chamber is presented in Fig. 1.

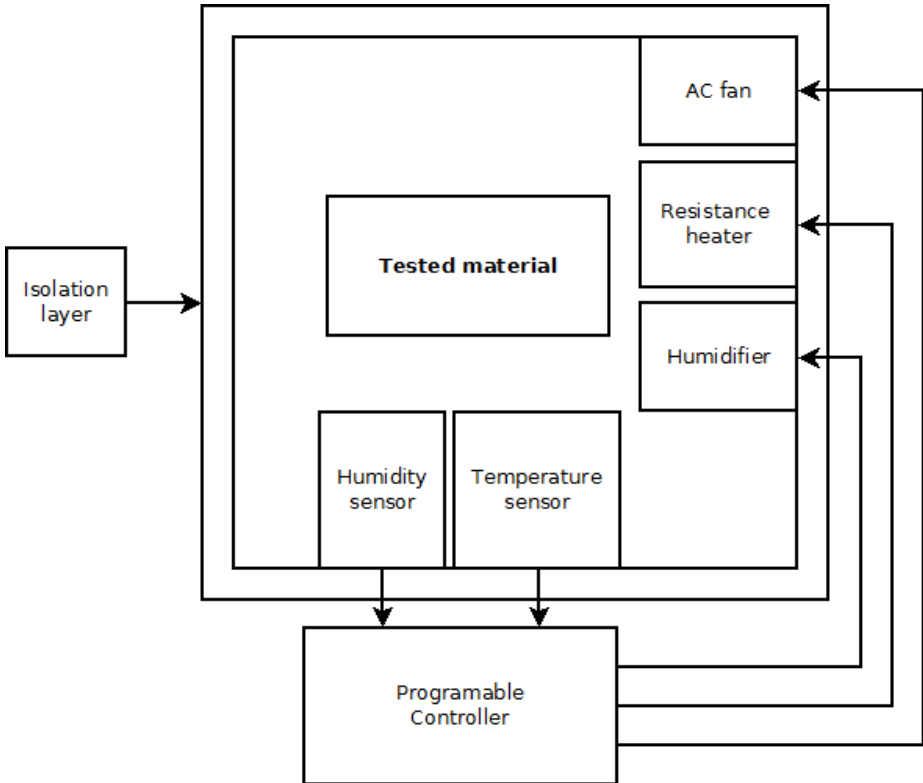


Fig. 1. Schematic block diagram of the environmental chamber

Investigated material is placed inside the chamber. Environmental conditions are measured by temperature and humidity sensors. Based on sensors signals and controller set-points, proper actuators are switched.

Test chamber was designed to recreate typical industrial temperature range (from 15 °C to 45 °C) as well as wide humidity range (from 23% RH to 96% RH), and keep them stable during long-time measurements.

2.2 Implementation

CAD model of the implemented chamber is presented in Fig. 2.



Fig. 2. CAD model of the environmental chamber

Isolation layer was made from 5mm thick temperature-isolating polycarbonate sheets. To achieve required constant temperature and humidity, ultrasound humidifier was utilized. That way humidified air has room temperature (contrary to the air from hot steam humidifiers), which allows easier and more stable regulation of temperature inside the chamber.

To achieve variable temperature resistance heater was implemented. To minimize temperature and humidity gradient inside chamber AC circulating fan was used.

Environmental conditions inside the chamber are measured by integrated sensor SHT11, which contains capacitive sensor for measuring relative humidity and band-gap temperature sensor. Measurement accuracies are in the limit of ± 3 %RH and ± 0.4 °C, which combined with controller hysteresis (± 1 %RH, ± 0.5 °C) results in ± 4 %RH and ± 1 °C reliability.

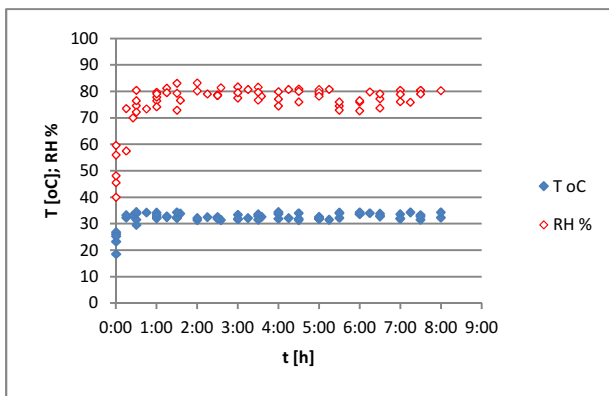


Fig. 3. Aggregated data of the temperature and humidity measurements in the environmental chamber during 9 stabilization tests. Temperature and humidity were set at 32 °C and 80% respectively

Stabilization efficiency was checked during few tests which lasted up to eight hours each. Recorded data of temperature and humidity inside the chamber during nine tests are presented in Fig. 3. The temperature and humidity was set at $T = 32\text{ }^{\circ}\text{C}$ and $\text{RH} = 80\%$ respectively. After approximately half of hour conditions inside the chamber became stable. Then the temperature inside the chamber varied between $31.5\text{ }^{\circ}\text{C}$ and $34\text{ }^{\circ}\text{C}$ and humidity varied in the range from $\text{RH} = 74\%$ up to $\text{RH} = 82\%$. In both cases stabilization accuracy is close to the calculated limit however mean temperature ($32.7\text{ }^{\circ}\text{C}$) was slightly over and mean humidity (78.5%) was slightly under the specified values.

3 Graphene Testing

3.1 Experiment Design

The tested sample was produced by CVD graphene growth on Cu foil and then transfer of the graphene layer from the copper surface onto the BK7 glass substrate. The graphene layer covers all the substrate surface of area $1'' \times 1''$. The Ti/Au electrodes on the edges of the sample were deposited by using the e-beam vacuum evaporation through the mechanical mask. The shape of the substrate and electrodes is presented in the Fig. 4.

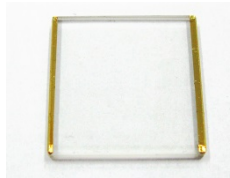


Fig. 4. Sample of CVD graphene layer deposited on the BK7 glass substrate. Sample dimensions: $1'' \times 1''$

The sample was subjected to the controlled environmental conditions in the chamber for few hours day by day for nine days. The temperature and humidity in the chamber was set at $32\text{ }^{\circ}\text{C}$ and 80% , respectively. Rest of the time the sample was left in room conditions at temperature $19\text{--}25\text{ }^{\circ}\text{C}$ and humidity $40\%\text{--}60\%$. The resistance of the sample was monitored during the test in environmental chamber. Finally, the sample was examined by Scanning Electron Microscopy (SEM) and Energy-dispersive X-ray spectroscopy (EDS) methods.

3.2 Test Results

The sample resistance before test was stable in time and was about $R = 1.95\text{ k}\Omega$. Taking into account square geometry of the sample the measured resistance is close to

resistivity per square. During test in environmental chamber the sample resistance changed. Initially, at first day the resistance slightly diminished. Next three days resistance became almost stable both in room and in chamber conditions. Finally, the resistance increase was observed during the test in the chamber. The resistance of the sample recovered after storing in the room conditions for the rest of day before the next cycle in the environmental chamber. Evolution of the sample resistance during tests in environmental chamber is presented in the Fig. 5.

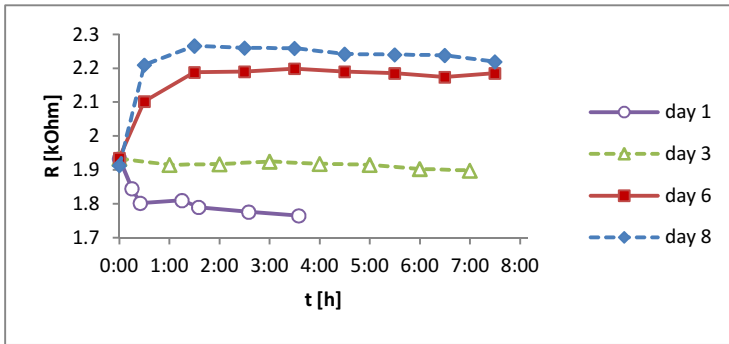


Fig. 5. The graphene sample resistance changes during exposition on environmental conditions $T = 32\text{ }^{\circ}\text{C}$ and $\text{RH} = 80\%$ in the environmental chamber

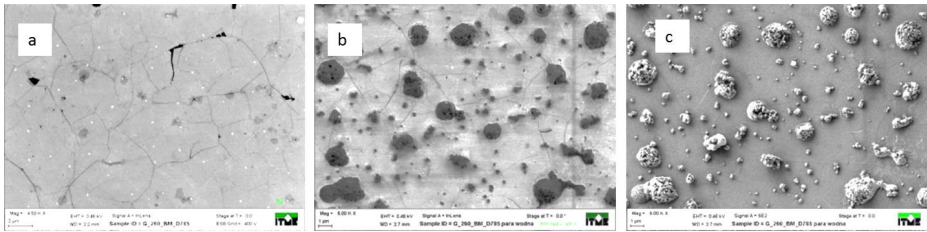


Fig. 6. The SEM micrographs of the graphene sample: a) the graphene surface of the freshly prepared sample, b) and c) The graphene surface after environmental test

The graphene sample was examined using SEM imaging before and after test. SEM micrographs of the sample are presented in the Fig. 6. The big and dense particles are visible on all over the surface of the sample after exposition on wet and warm atmosphere in the environmental chamber. The composition of the new particles was estimated using EDS method and results are presented in Fig. 7. The elements like Cl, Ca and Mg are typical for water contamination by metal chlorides. However, presence of the sulfur (S) and carbon (C) suggests presence of organic matter as well.

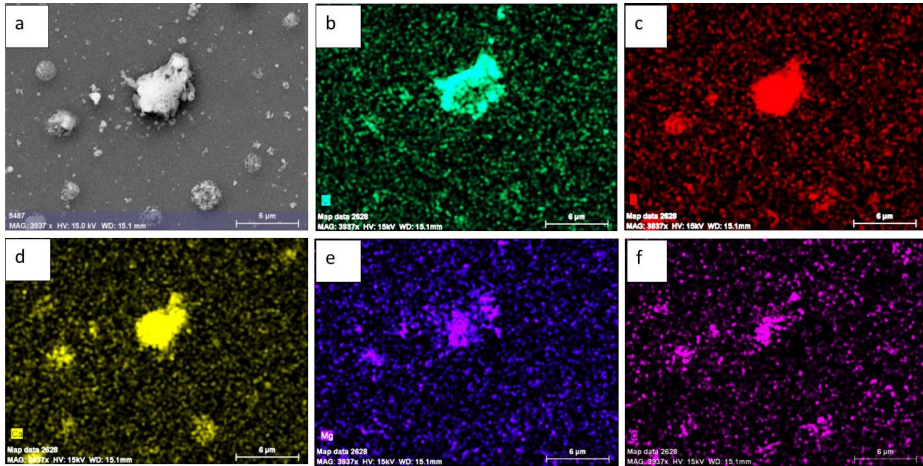


Fig. 7. The EDS images of the graphene sample after environmental test: a) the view of the graphene surface, b–f) EDS images of the same area in energies characteristic for following elements: b) Cl, c) S, d) Ca, e) Mg, f) C

4 Conclusions

The environmental chamber confirmed its usability for simulation of some environmental conditions. Its stability was sufficient for practical use in presented experiments. Graphene in a simulated environment was stable; however, some changes in resistance were observed. The resistance evolution is probably caused by water condensation on the graphene surface. The theoretical predictions of the thermal dependence of graphene resistivity and experimental results presented in [4, 5] suggest that increasing a temperature under room conditions should cause the diminishing of the graphene resistance. On the other hand, the investigation of water-graphene interactions presented in [6] makes possible increasing of the graphene resistance under water condensed on the graphene surface. Crystallization of the water contaminants on the graphene surface may increase the wettability of the hydrophobic graphene surface and increase the water volume on the graphene surface in a wet environment.

The observed effect of crystallization of water contaminants on the graphene surface in a wet atmosphere and its effect on the evolution of the graphene electric parameters suggests a possible mechanism of degradation of the graphene layer when exposed to the natural outdoor atmosphere. The observed crystallization of impurities from the atmosphere on the graphene surface leads to the general conclusion that graphene protection or surface cleaning methods should be developed in case of outdoor applications of graphene.

References

1. Petruk, O., Szewczyk, R., Ciuk, T., Strupiński, W., Salach, J., Nowicki, M., Pasternak, I., Winiarski, W., Trzcinka, K.: Sensitivity and offset voltage testing in the hall-effect sensors made of graphene. In: Szewczyk, R., Zieliński, C., Kaliczyńska, M. (eds.) *Recent Advances in Automation, Robotics and Measuring Techniques*. AISC, vol. 267, pp. 631–640. Springer, Heidelberg (2014)
2. Zhu, S.-E., Yuan, S., Janssen, G.C.A.M.: Optical transmittance of multilayer graphene. *EPL (Europhysics Letters)* 108(1), 17007 (2014)
3. Sordan, R., Traversi, F., Russo, V.: Logic gates with a single graphene transistor. *Appl. Phys. Lett.* 94(7), 73305 (2009)
4. Shao, Q., Liu, G., Teweldebrhan, D., Balandin, A.A.: High-temperature quenching of electrical resistance in graphene Interconnects. *Appl. Phys. Lett.* 92, 202108 (2008)
5. Vasko, F.T., Ryzhii, V.: Voltage and temperature dependencies of conductivity in gated graphene. *Phys. Rev. B* 76, 233404 (2007)
6. Yavari, F., Kritzinger, C., Gaire, C., Song, L., Gullapalli, H., Borca-Tasciuc, T., Ajayan, P.M., Koratkar, N.: Tunable Bandgap in Graphene by the Controlled Adsorption of Water Molecules. *Small* 6(22), 2535–2538 (2010)

Unconventional Double R/U Converter for Measurement of Two Quantities by a Single Differential Sensor

Adam Idźkowski¹, Paweł Świętochowski², Zygmunt L. Warsza³,
and Wojciech Walendziuk¹

¹Białystok University of Technology, Białystok, Poland
{a.idzkowski,w.walendziuk}@pb.edu.pl

²Mektron, Białystok, Poland
biuro@mektron.pl

³Industrial Research Institute for Automation and Measurements PIAP, Warsaw, Poland
zlw@op.pl

Abstract. This paper describes an original four arm single mesh resistance circuit. It has the similar structure as the bridge circuit but is unconventionally supplied by the current source which is switched over between opposite arms. The two output signals of this circuit are sums of two voltages obtained after switching on each bridge diagonal. The processing of this signals allows to find two measured variables which differently influencing arm resistances. The two dimensional (2D) converter of the resistance changes to voltages based on this input circuit is build. It is described in detail and its dynamic properties are examined. The achieved results confirm that this unconventional signal conditioning circuit can be successfully used in continues measurements of two parameters, e.g. two geometrical components of the strain or the strain and temperature by a single differential sensor.

Keywords: sensor systems, two dimensional signal processing converter.

1 Introduction

Many different constructions of the strain, temperature, force or pressure transducers have been in use in industry and laboratory measurements for many years. Usually sensors and primary transducers are designed to measure a single physical quantity. Constructions of transducers are typically based on applications of the properly configured imbalanced Wheatstone bridge powered by a voltage or current source. The influence of temperature changes on the measured quantity sensor is eliminated by use of a separate temperature sensor located very near to this sensor or by temperature sensitive elements if the sensor and its circuit are integrated. The problem is more complicated if there is a need to measure a two-dimensional quantity or two different quantities in the same point and simultaneously register their dynamic changes – as for example in medical measurement devices described in [1, 2]. Some solutions of strain sensors with thermocouple or double-bridged structures for pressure measurements are given in [3, 4].

In this paper the design details and dynamic properties of the model of primary converter to measure two quantities (2D) simultaneously is described. The original idea

of the unconventionally supplied bridge, proposed in previous Warsza works [5], [6], under acronym 2x1J, has been applied. As alternative, the application of cascade bridge for the single and double differential sensor has been also described in [6] and [7]. The commonly known possibility of compensation the temperature influence on a strain measurement by the second similar, but not stressed resistance strain gauge without using additional temperature sensors, are presented in [8]. This is also possible to achieve by an indirect method which relies on simultaneous measurement of voltages on both diagonals of the unconventionally supplied a strain gauge bridge [6, 7, 9]. These voltages depend differently on the gauge resistance changes from temperature and strain. Then these voltages could be processed appropriately in a digital part of the measurement system. Simultaneous measurement of bending force and temperature changes in the measurement point by the single differential strain sensor with 2D bridge supplied by two identical current sources was described in [9, 10].

The main aim of this work was to test the utility of this 2D circuit supplied by one switched current source in dynamic measurements. This was done by analyzing the parameters of voltage waveforms in its major test points.

2 Theory of Operation of the Unconventional Converter

The concept of the variant of unconventional 2D bridge circuit, given in Fig 1, relies on the use of the single current source J and electronic switches Q1 and Q2.

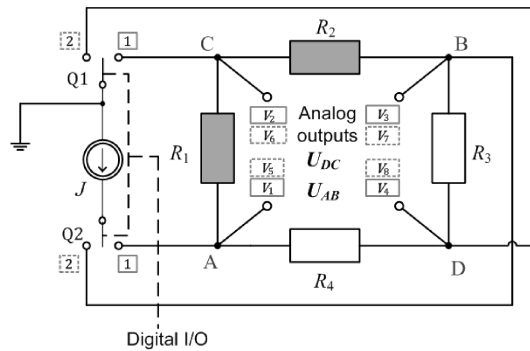


Fig. 1. The idea of unconventionally supplied bridge (2x1J) for 2D measurements, J – switched current source; R_1, R_2 – sensors; R_3, R_4 – resistors; Q1, Q2 – synchronic electronic switches

It works with a pair of separate sensors or the integrated differential sensor of resistances R_1, R_2 . These resistances depend on two physical quantities X_1, X_2 :

$$R_1 = R_{10}(1 + \varepsilon_1(X_1, X_2)) \tag{1}$$

$$R_2 = R_{20}(1 + \varepsilon_2(X_1, X_2)) \tag{2}$$

where R_{10}, R_{20} – initial resistances and $\varepsilon_1, \varepsilon_2$ their relative increments, respectively.

In general the relative increments $\varepsilon_1, \varepsilon_2$ of both above resistances are not equal, i.e.:

$$\varepsilon_1(X_1, X_2) \neq \varepsilon_2(X_1, X_2). \quad (3)$$

This is the two-output pre-conditioning circuit. As shown in Fig. 1, the electronic switches work simultaneously in pairs. Two of them are switched on while the other two - switched off. The measurement of output voltages is conducted subsequently:

$$U_{AB1} = V_1 - V_3, \quad U_{DC1} = V_4 - V_2, \quad (4)$$

$$U_{AB2} = V_5 - V_7, \quad U_{DC2} = V_8 - V_6. \quad (5)$$

Assuming that other resistances of the bridge are not changed, i.e.: $R_3=R_{10}, R_4=R_{20}$ (their relative increments are $\varepsilon_3=\varepsilon_4=0$). If modules of the values $|\varepsilon_1|, |\varepsilon_2|$ are small enough [6] and all initial resistances are equal $R_{10}=R_{20}=R_{30}=R_{40} \equiv R_0$, equations (4) and (5) are simplified to:

$$U_{DC} = 0.5(U_{DC1} + U_{DC2}) = 0.125 JR_0(\varepsilon_1 + \varepsilon_2) \quad (6)$$

$$U_{AB} = 0.5(U_{AB1} + U_{AB2}) = 0.125 JR_0(\varepsilon_1 - \varepsilon_2). \quad (7)$$

If the sum $\varepsilon_1+\varepsilon_2$ of resistance increments depends only on quantity X_1 and difference $\varepsilon_1-\varepsilon_2$ only on quantity X_2 then U_{DC} and U_{AB} depends separately on X_1 and X_2 .

3 Electrical Circuit of Unconventional Converter

With the small varying relative increments $\varepsilon_1, \varepsilon_2$ the changes of voltages (6) and (7) are too small. There is a need to add the proper signal conditioning module to amplify the useful part of output voltages and to eliminate considerably higher DC offset. In Fig. 2, the block diagram of the model of unconventional 2D converter is presented.

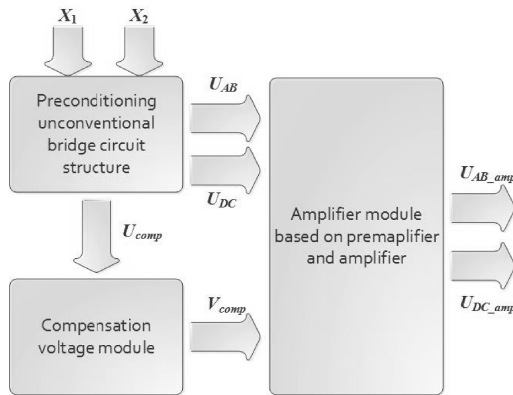


Fig. 2. Block diagram of the unconventional converter for two-parameter X_1, X_2 measurement

It consists the three modules: the input circuit as pre-conditioning converter, a compensation voltage module and an amplifier module.

The way of operation of the input circuit of 2D converter may be presented in two cycles (Fig. 3). In the first cycle the electronic keys Q1 and Q3 are turned on, while Q2 and Q4 are turned off. In the second cycle the states of Q1 – Q4 (low $R_{DS(on)}$ MOSFET transistors) are opposite. After two cycles the arithmetic means (6), (7) of the analog output voltages U_{AB} and U_{DC} are calculated. In this application direct current ($I_s=50$ mA) is provided by the LT3092 [11]. Measured voltages can be positive or negative. Then the amplifiers of the U_{AB} and U_{DC} voltages have to be supplied in the bipolar way.

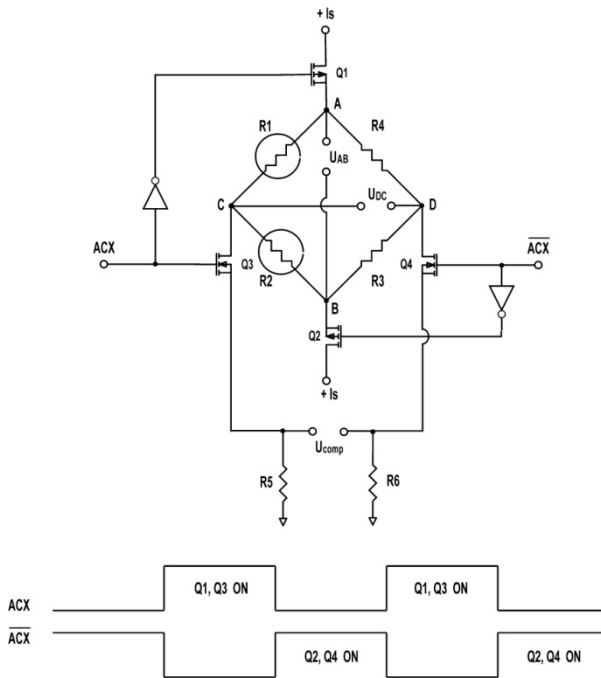


Fig. 3. Practical scheme and cycles of work of the input circuit of 2D converter

Additionally, the compensation voltage output U_{comp} is produced. The compensation module is shown in Fig. 4. It consists of non-inverting preamplifiers (OP727ARU) and an instrumental amplifier (AD8221AR). The main task of this module is to create compensation voltage V_{comp} (single-ended). It is set up only once by potentiometers P1-P3. This is used for making U_{AB-amp} and U_{DC-amp} equal to zero (Fig. 5).

This module makes measurement independent from drifts of a current source (J). The change of current causes the changes of U_{AB} and U_{DC} , which affects the change of U_{comp} . However, the value subtracted in the final stage of the amplifier module (Fig. 5) remains unaltered.

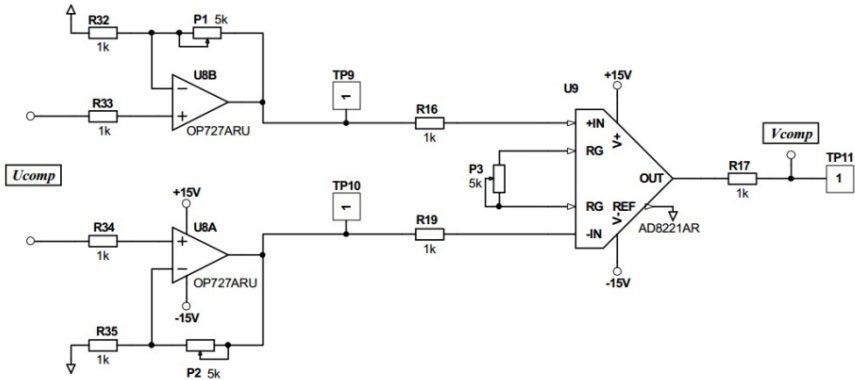


Fig. 4. The compensation voltage module

Improved resolution of measurement is the another advantage of compensation module. This is caused by the amplifying module, connected to the bridge outputs, shown in Fig. 5. Both channels consist of preamplifier and amplifier (AD8221AR). The preamplifiers create single-ended voltages $U_{AB-preamp}$ and $U_{DC-preamp}$. The amplifiers amplify the differences ($V_{comp} - U_{AB-preamp}$) and ($V_{comp} - U_{DC-preamp}$) with a differential gain of 500 (setup by potentiometers P4, P5).

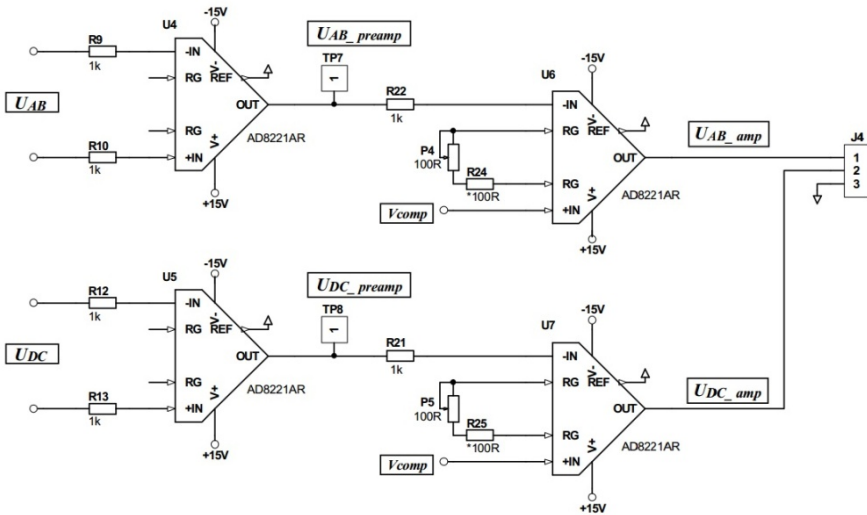


Fig. 5. The amplifier module

4 Voltage-Time Characteristics in Test Points of the Converter

The waveforms in both channels of U_{AB} and U_{DC} are of square type. The frequency of electronic keys was set to 1 Hz, in order to show the rise and fall part of the transient

state characteristics. Synchronized voltages U_{AB} and $U_{AB-preamp}$ are shown in Fig. 6. In this case, the rise time equals $90 \mu\text{s}$. During this time the voltages reach the stable state. Rise/fall times of the voltages V_{comp} , $U_{AB-preamp}$ and their difference (equal zero) are presented in Fig 7.

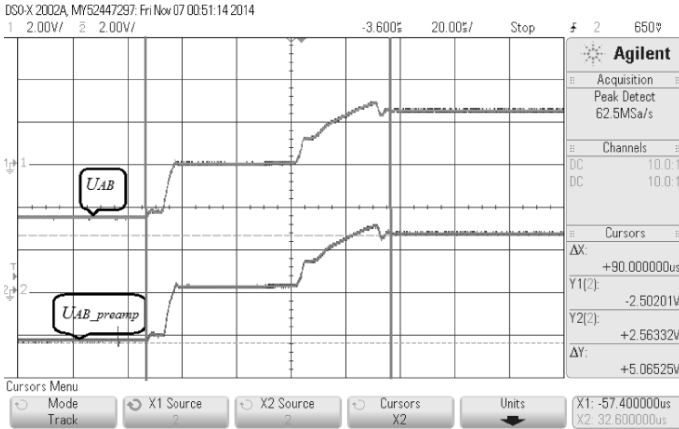


Fig. 6. Rise time of the voltages U_{AB} and $U_{AB-preamp}$

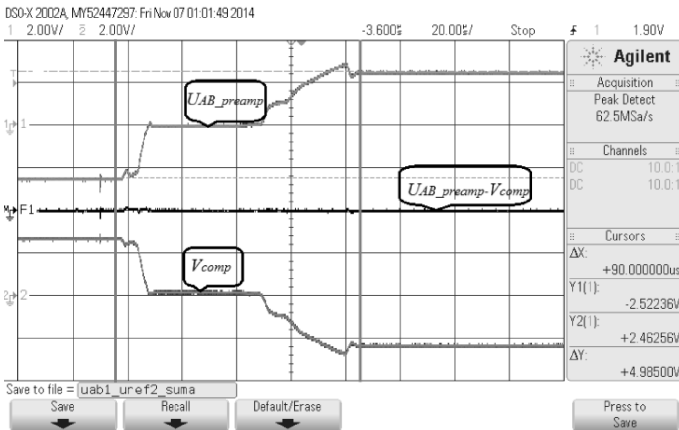


Fig. 7. Rise/fall times of the voltages $U_{AB-preamp}$, V_{comp} and their difference

In test points $U_{AB-preamp}$ and U_{AB-amp} , the achieved rise/fall times were considerably longer. Duration of the unsteady state of U_{AB-amp} was even longer ($\geq 318.4 \mu\text{s}$, Fig. 8) as a result of the incorrect grounding and shielding. It seems that this was caused by the interference due to common-mode voltage [12].

The problems encountered with similar ac-excitation were described in [13]. They occurred by settling time of the analog input signals after switching, especially in applications where there are long leads from the bridge to the data acquisition system. If processing signals are not fully settled, the converter could produce erroneous data.

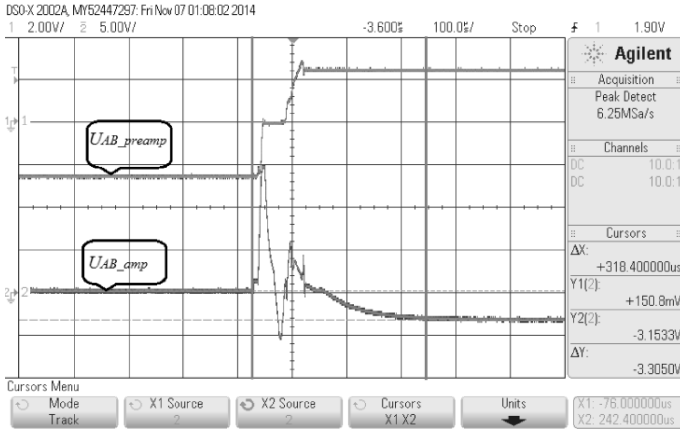


Fig. 8. Settling times of the voltages $U_{AB-preamp}$ and U_{AB-amp}

5 Conclusions

In this paper the new type of two quantities conditioner was presented. The tested unconventional circuit has more complex construction than the imbalanced Wheatstone bridge with the output voltage amplifier. It is so, because this conditioner is dedicated for two dimensional (2D) measurements. Then it needs additional elements, e.g. the stable current source switched by electronic switches for the unconventional connections to opposite bridge arms.

In the tested preliminary circuit version, high amplitudes of voltages make signal conditioning part of the circuit expanded. This is the reason of dedicated compensation voltage module usage. It subtracts V_{comp} from measured voltage and amplifies it. High differential gain of instrumental amplifier, switching of electronic keys, grounding and connecting with oscilloscope cause the unsteady state of output voltage last much longer (more than 318.4 μs). This fact limits the frequency of R/U converter in the case of dynamic measurements. In the presented construction, the maximal frequency of pulsing the electronic switches can not be higher than 100 Hz. Depending on this value, the cut-off frequency of low-pass filter should be selected. It should not disfigure the bipolar square wave.

The single pulsed current source supplying is the advantage of this unconventional 2D converter. Measuring two components of output voltages for both sensors currents directions makes the possibility of using this kind of circuit for various purposes, e.g. compensation of thermoelectric voltages. Moreover, the circuit works properly with the sensors of low relative resistance increments (i.e. strain gauges).

This work is the first stage of research, and the results of its continuation will be presented in further papers.

Acknowledgements. This paper was prepared within a framework of S/WE/1/2013 project of the Bialystok University of Technology, which is sponsored by Polish Ministry of Science and Higher Education.

References

1. Walendziuk, W.: Measurement Uncertainty Analysis of the Strain Gauge Based Stabiligraphic Platform. *Acta Mechanica et Automatica* (8, part. 2), 74–78 (2014)
2. Walendziuk, W., Idźkowski, A.: Portable acquisition system for domiciliary uroflowmetry. *Journal of Vibroengineering*, (11, part. 3), 592–596 (2009)
3. Cappa, P., Marinozzi, F., Sciuto, S.A.: A novel method for the simultaneous measurement of temperature and strain using a three-wire connection. *Measurement Science and Technology* 12(4), 502–506 (2001)
4. Pedersen, C., Jespersen, S.T., Krog, J.P., Christensen, C., Thomsen, E.V.: Combined differential and static pressure sensor based on a double-bridged structure. *IEEE Sensors Journal* 5(3), 446–454 (2005)
5. Warsza, Z.L.: Bridges supplied by two current sources – new tool for impedance measurements and signal conditioning. In: *Proc. of IMEKO-TC 7 Symposium*, pp. 231–236. Cracow University of Technology (June 2002)
6. Warsza, Z.L.: Four-terminal (4T) immittance circuits in multivariable measurements. Monograph. Industrial Research Institute for Automation and Measurements, PIAP Warsaw (2004) (in Polish)
7. Warsza, Z.L.: Backgrounds of two variable (2D) measurements of resistance increments by bridge cascade circuit. *Proc. of SPIE* (6347 part 2), R63472 (2006)
8. Stefanescu, D.M.: *Handbook of Force Transducers: Principles and Components*, p. 612. Springer (2011)
9. Warsza, Z.L.: Two-parameter measurements and signal conditioning in double – current supply four-terminal resistance circuits. *Metrology and Measurement Systems XIII*(1), 49–65 (2006)
10. Idźkowski, A., Makal, J., Warsza, Z.L.: Simultaneous measurement of two parameters by double current supplied bridge. *Journal of Automation, Mobile Robotics and Intelligent Systems (JAMRIS)* 6(2), 26–31 (2012)
11. LT3092 – programmable current source datasheet, Linear Technology
12. Shielding and Guarding, Analog Devices application note AN-347
13. O’Grady, A.: Transducer/Sensor Excitation and Measurement Techniques. *Analog Dialogue* 34(5), 1–6 (2000)

Automatic System for Identification of Temperature Parameters of Resistors Based on Self-heating Phenomena

Andrzej Juś¹, Paweł Nowak¹, and Roman Szewczyk²

¹ Industrial Research Institute for Automation and Measurements,
Al. Jerozolimskie 202, 02-486 Warsaw, Poland

² Warsaw University of Technology, Faculty of Mechatronics,
sw. A. Boboli 8, 02-525 Warsaw, Poland
{Pnowak, Ajus}@Piap.Pl

Abstract. Paper presents new way of identification of temperature parameters of precise resistors. Presented method allows removing heating system and temperature measurement system from the test stand, and is suitable for resistors with extremely low TCR. This approach is based on observation of resistance variation caused by the flow of constant current of known value. Presented method has high measurement accuracy. It is also suitable for process automation, and allows for the simplification of the test stand and shortening of the time required to perform the resistor TCR measurement.

Keywords: Resistance measurement, stable resistors, temperature coefficients, TCR.

1 Introduction

Constant increase of precision of constructed devices requires application of more accurate electronic elements. In some applications even the best elements available on the market do not fulfil requested accuracy. Also cost of those elements can be decisive in production profitability. In those applications selection of elements became crucial. This solution not only provides elements with required parameters but also allows selection from lower quality (cheaper) elements.

For the selection of elements proper test stand of high measurement accuracy is required. For industrial applications test stand with minimalized operator influence is required. This allows for significant single-element cost reduction.

This paper presents modification of the test stand utilized for measurements of temperature coefficient of ultra-precise resistors presented previously in [6]. Those resistors are used as a current-voltage drop converter and are crucial part of analytical scales. Presented method allows simplification of the test stand – no heating or temperature measurement systems are required. It also provides reliable data about resistors temperature coefficient in significantly lower time. Presented method allows for conducting measurements of TCR for resistors of different type, initial accuracy and

nominal value of TCR. Some initial time is required when different kind of resistors are measured, or changed value of measurement current is used. Thus it is highly recommended for usage in industrial production lines, where big numbers of the same type resistors are measured.

2 Resistance Measurement Methods

Resistance is typically measured with DC methods. The most common ways are ohmmeters, Wheatstone and Kelvin-Thompson bridges, and DC compensators [3].

Analogue ohmmeters typically achieve accuracy of few percent. Better measurement accuracy can be achieved by the usage of DC bridges (Wheatstone or Kelvin-Thompson) [2, 9]. Bridge methods require significant number of resistors and potentiometers, which combined with low accuracy and stability of digital potentiometers [7, 8] makes them significantly harder for automation.

Methods utilizing DC compensators have high measurement accuracy and are suitable for process automation. Base principle of DC compensation is presented in fig. 1

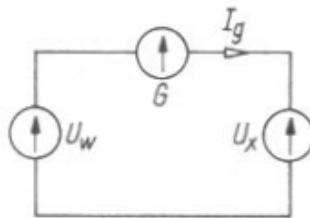


Fig. 1. Principle of DC compensation measurements. U_w – reference voltage source, U_x – measured voltage, G – galvanometer [2]

If voltage sources U_w and U_x would be replaced by resistor of similar values R_x , and R_w conducting the same current I_g , galvanometer measure difference of voltage drop on resistors. This allows to calculate difference of resistances based on (1):

$$R_x - R_w = \frac{U_x - U_w}{I_g} \quad (1)$$

Paper presents measurement method based on this principle. Though some modifications has been applied in order to increase measurement accuracy and for ease of automation.

3 Test Stand

Measurements were conducted on test stand previously presented in [6]. New approach based on self-heating phenomena allowed to remove heating and temperature measurement systems. Block diagram of modified test stand is presented in Fig. 2.

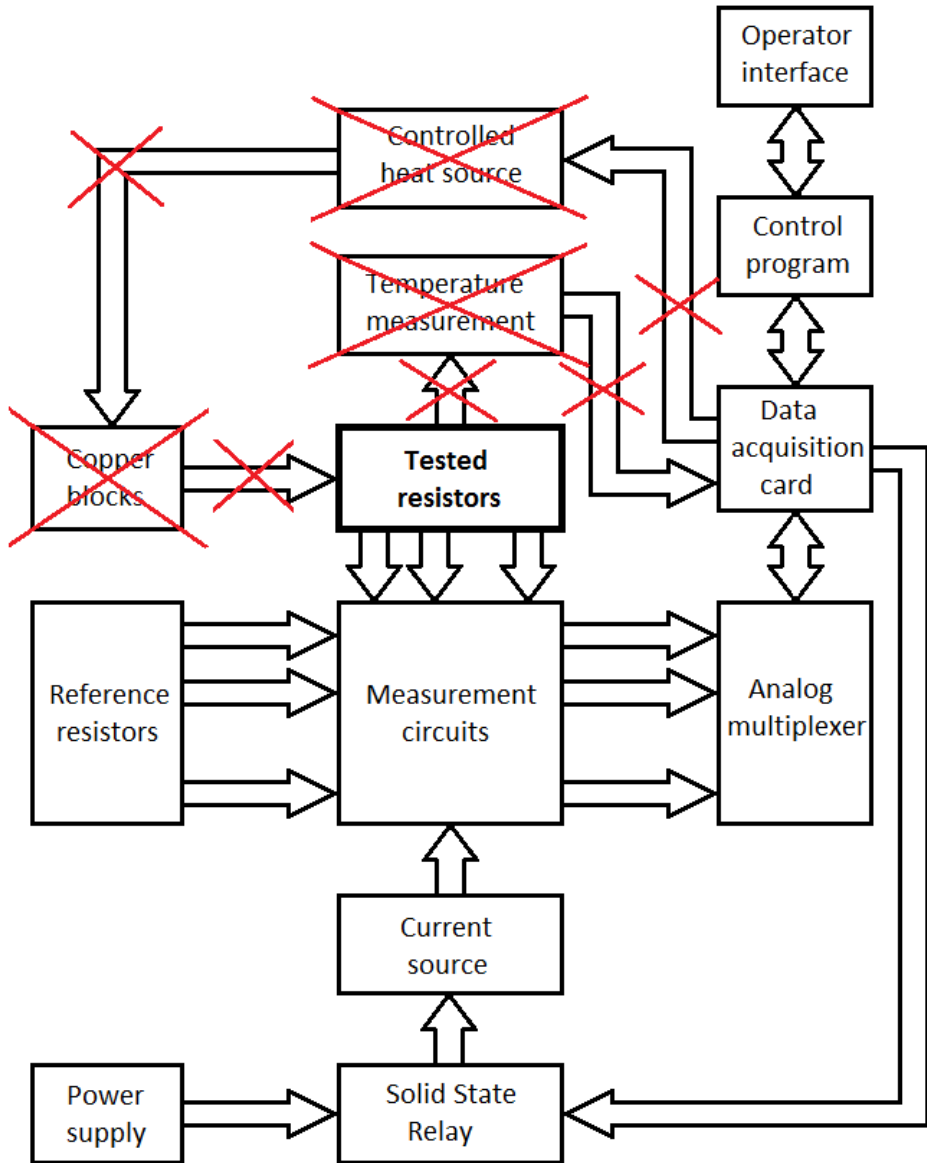


Fig. 2. Schematic block diagram of the test stand. Crossed blocks can be removed (referenced to base method [6])

The most important element of presented test stand is the measurement circuit, presented in Fig.3.

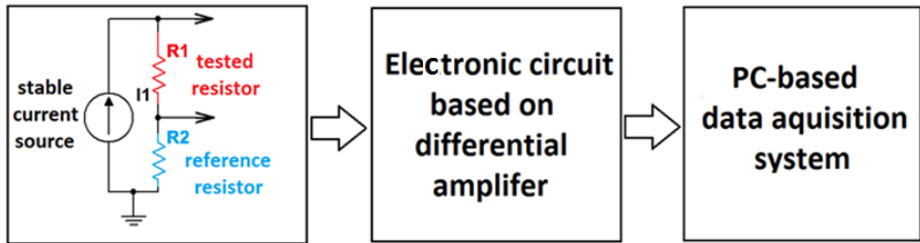


Fig. 3. Simplified electronic scheme of measurement circuit idea [5]

Circuit is based on differential measurement. Resistors are combined in twos and are serially connected with constant current source. Due to current flow I_1 voltage drops on resistors based on Ohm's law appear [4] (2):

$$U = R I \quad (2)$$

Voltage drops based on (2) equal: $U_1 = R_1 \cdot I_1$ and $U_2 = R_2 \cdot I_1$. Those drops are proceeded by electronic circuit based on differential amplifier to output value (V_{out}) described by (3):

$$V_{out} = (U_1 - U_2) \cdot k \quad (3)$$

where k – amplification of differential amplifier, in presented test stand $k=100$.

Thus value of output voltage (based on (2) and (3)) can be calculated as (4):

$$V_{out} = (U_1 - U_2) \cdot k = I_1 \cdot (R_1 - R_2) \cdot 100 \quad (4)$$

Output voltage passes through analog multiplexer (which allows to connect up to 8 measurements circuits to one analog input of data acquisition card) and based on (4) is processed in order to achieve data about resistance difference. Measurement procedure is based on voltage measurement right after powering the circuit by the solid state relay and begins automatically.

Presented method is based on self-heating phenomena, which is caused by current flow. The initial value of the output voltage (V_{out0}) is compared with value of output voltage after the circuit stabilisation (V_{out1}). Based on that, temperature coefficient of the tested resistor (R_1) can be measured. Algorithm of TCR determination is described in next paragraph.

4 Measurement Methodology and Exemplary Test Results

Paragraph presents results achieved for metallized resistors. Measurements were conducted to show possibility of utilizing presented method for selecting resistors with high TCR. This chapter presents step by step algorithm of fast TCR determination.

Results achieved for ultra-stable UPR resistors are also presented. During those tests influences such as shift caused by the test stand were analysed, which resulted in high accuracy measurements. Measurement results are highly analogous to results achieved in typical way [5, 6].

4.1 Metallized Resistors

Tests were conducted on typical low-cost metallized resistors with nominal value of 150 Ω and 0,25 W power dissipation. Those resistors have average temperature parameters – better than cheapest carbon resistors but not as good as ultra-stable resistors with extremely low TCR [10, 11].

Presented algorithm of TCR determination requires:

- determination of TCR of reference resistor with utilizing other method or usage of resistor with already known temperature coefficient,
- comparison of output voltage (4) right after circuit supply (V_{out0}) with the value of output voltage after circuit stabilisation (V_{out1}),
- calculation of temperature increase caused by self-heating. Calculation is based on resistor with known TCR and must be conducted once for every resistor type and measurement current,
- (optional) confirmation of temperature increase with the usage of another resistor of the same type,
- fast measurements of TCR of new resistors

The following summarizes the characteristics and calculations in the algorithm order.

Based on data presented in Fig. 4 $\Delta R/\Delta T$ dependency was acquired. Slope of this characteristic (automatically calculated with the usage of least square method [1]) is the required TCR and equals -230 ppm/°C. Calculated value is adequate to value calculated with two-point method:

$$TCR = \frac{\Delta R}{\Delta T} = \frac{R_{stop} - R_{start}}{T_{stop} - T_{start}} = \frac{-1950 (ppm)}{35,2(^{\circ}C) - 26,7(^{\circ}C)} = -230 \left(\frac{ppm}{^{\circ}C} \right) \quad (5)$$

where: ΔR – resistance deviation during heating, ΔT – temperature increment during heating.

Temperature coefficient of reference resistor equals 230 ppm/°C. In the next step time characteristic of reference deviation caused by self-heating (right after powering measurement circuit) is acquired.

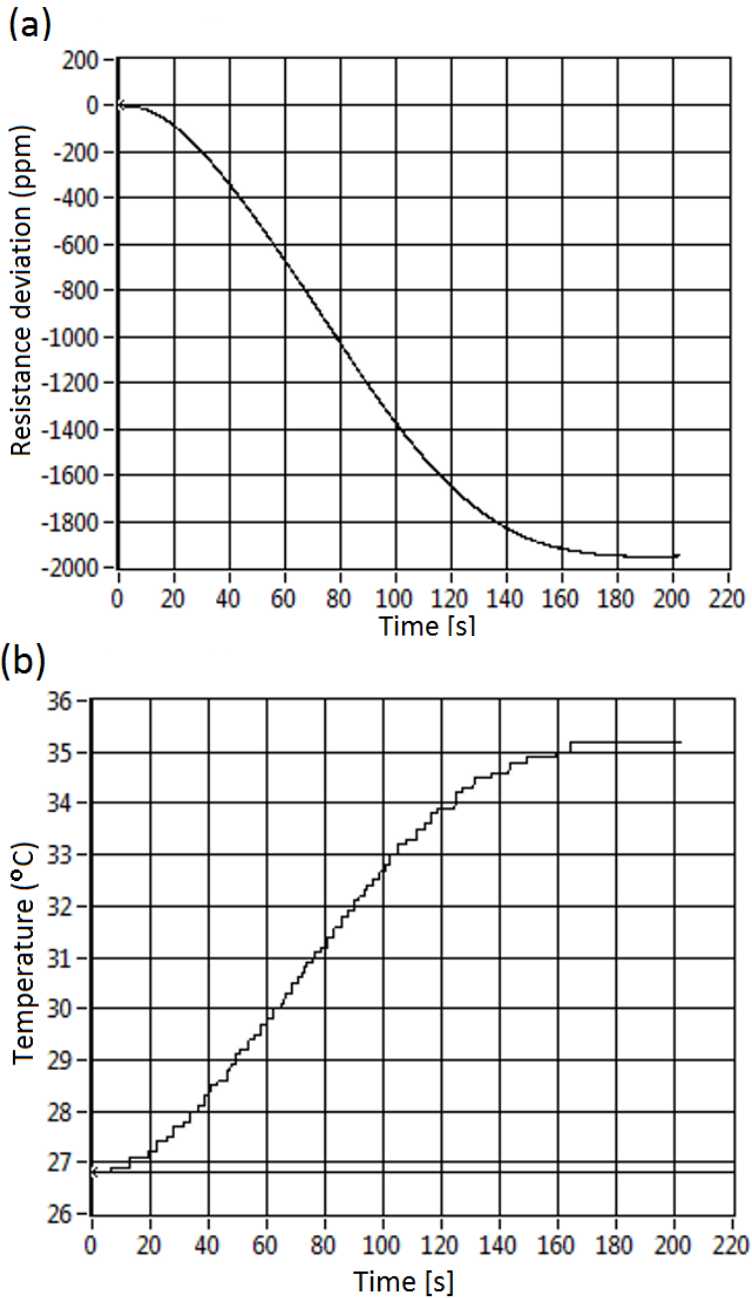


Fig. 4. Resistance deviation in function of time (a) achieved during heating (b) of metalized resistor (150Ω , $0,25 \text{ W}$)

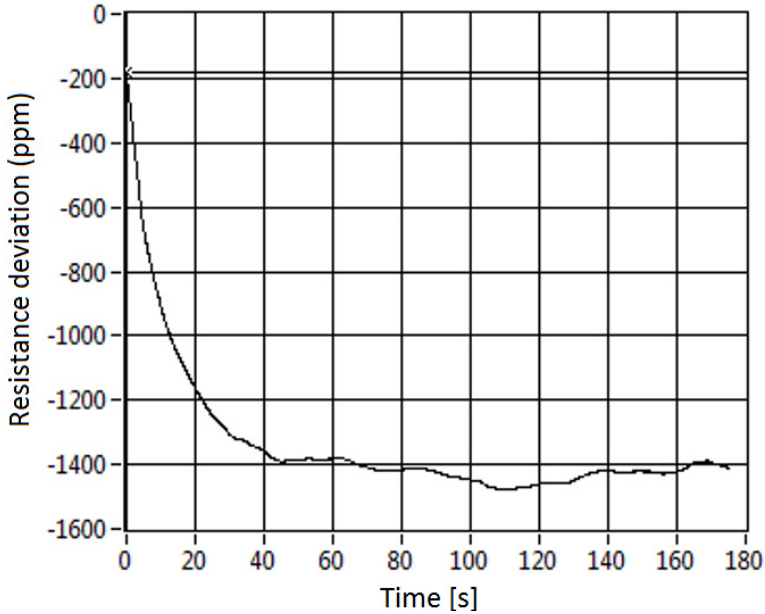


Fig. 5. Self-heating characteristic acquired right after supplying measurement circuit

Based on presented characteristic (Fig. 5) resistance deviation (-1220 ppm) can be calculated. With the data about resistance deviation caused by self-heating and resistor TCR, temperature increment can be calculated:

$$\Delta T = \frac{\Delta R}{TCR} = \frac{R_{stop} - R_{start}}{TCR} = \frac{-1220 \text{ (ppm)}}{230 \frac{\text{ppm}}{^{\circ}\text{C}}} = 5,3(^{\circ}\text{C}) \quad (6)$$

The same steps were conducted on two other resistors in order to confirm value of temperature deviation caused by self-heating phenomena for this particular type of resistors. Results of measurements are presented in the table below.

Table 1. Comparison of results of temperature deviation caused by self-heating phenomena for three samples of metalized 150 Ω resistors

Resistor no.	TCR (ppm/ $^{\circ}\text{C}$)	ΔR (ppm)	ΔT [$^{\circ}\text{C}$]
1	-230	-1220	5,3
2	-226	-1125	5,0
3	-210	-1100	5,1

Results confirm consistent character of self-heating phenomena for all samples of same type resistors – all temperature and resistance deviation have similar values.

After value confirmation of temperature deviation caused by self-heating further measurements for other samples can be conducted with high speed. Comparison of resistance deviation right after circuit supply (ΔR_0) with value after circuit stabilisation (ΔR_{out1}) can be easily automated and provide data about TCR values of resistors in a short time. For presented type of resistors stabilisation is achieved after $40 \square 60$ s but this time may vary, depending mostly on resistors casing.

4.2 Resistors UPR

During previously described tests no variation of reference resistor (R2 on Fig. 3) was assumed. Reference resistor had the same nominal value but it's TCR was lower by many orders of magnitude, thus influence of his self-heating was unnoticed. Due to the same reasons temperature variation of the test stand and wires had no influence on measurements. During measurements of extremely temperature-stable resistors those factors had to be taken into account.

Tests were conducted on ultra-stable resistors UPR0.5 D10 of nominal value 200Ω and values of TCR presented in table 2.

Table 2. Juxtaposition of tested pairs of resistors

Resistor no.	Resistor 1		Resistor 2	
	Number	TCR (ppm/°C)	Number	TCR (ppm/°C)
1	B	-0.21	D	+0.71
2	B	-0.21	C	+0.09
3	A	+0.35	E	-0.36

Tests were conducted on each pair of resistors in two combinations (resistor 1 as a R1 in Fig. 3 and resistor 2 as a R2 and resistor 1 as a R2 and resistor 2 as R1). Each time shift caused by measurement circuit was noticed (results should be symmetrical in opposite combinations but they vary). Results for first pair of resistors in both combinations are presented in Fig. 6. Their mean value (shift caused by test stand) is also presented.

The same measurements were conducted for other pairs of resistors. Based on their previously measured TCR, value of temperature increment caused by self- heating was calculated (based on (6)).

Table 3. Comparison of measurement results achieved for UPR resistors 200Ω

Resistor no.	Resistors	Difference of their TCR (ppm)	Resistance deviation caused by self-heating (ppm)	Temperature deviation caused by self-heating (°C)
1	B,D	0.92	4.8	5.2
2	B,C	0.3	1.6	5.3
3	A,E	0.71	3.65	5.15

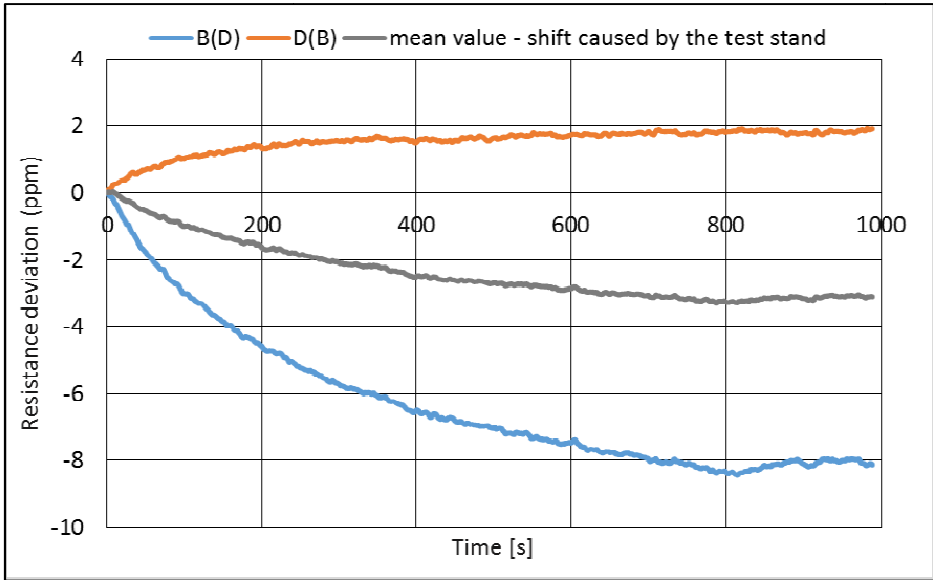


Fig. 6. Deviation generated by the test stand with measurement results for resistors B and D

Analogously knowledge about temperature increment caused by self-heating of that type of resistors combined with data about shift caused by the test stand can be effective way for TCR determination. In measurements of low-TCR resistors TCR of reference resistor (R_2 in Fig. 3) must be known and taken into account during calculations. Similar value of self-heating temperature increment, as well as constant shift caused by test stand confirms high accuracy of new approach. Results acquired by this method are converging with results acquired in classical [5, 6] way.

5 Conclusion

Presented measurements confirmed usefulness of new method of determination of resistors thermal coefficients, based on self-heating phenomena. For resistors with high TCR it can be used for selection of most stable resistors with average accuracy. Higher accuracy is not needed due to instability of their thermal parameters. Determination of TCR of extremely stable resistors has increased accuracy due to taking more factors into account. Similar accuracy to a classical method [5, 6] was reached, and in shorter time. As a result presented method can be effectively used in industrial applications.

Acknowledgments. This work was partially supported by The National Center for Research and Development with PBS Program – Grant no. PBS 1/B3/8/2012.

References

1. Cowan, G.: Statistical data analysis. Oxford University Press (1988)
2. Buckingham, H., Price, E.N.: Principles of Electrical Measurements. English Universities, London (1966)
3. Golding, E.W.: Electrical Measurement and Measuring Instruments, 3rd edn. Sir Issac Pitman and Sons (1960)
4. Horowitz, P., Hill, P.: The art of electronics, 2nd edn. Cambridge University Press, Cambridge (1989)
5. Juś, A., Nowak, P., Szewczyk, R., et al.: Assesment of Temperature Coefficient of Extremely Stable Resistors for Industrial Applications. In: Awrejcewicz, J., Szewczyk, R., Trojnacki, M., Kaliczyńska, M. (eds.) Mechatronics: Ideas for Industrial Applications, pp. 297–306. Springer International Publishing (2015)
6. Nowak, P., Juś, A., Szewczyk, R., et al.: Test Stand for Temperature Characteristics of Ultraprecise Resistors. In: Awrejcewicz, J., Szewczyk, R., Trojnacki, M., Kaliczyńska, M. (eds.) Mechatronics: Ideas for Industrial Applications, pp. 345–352. Springer International Publishing (2015)
7. Korytkowski, J.: Cyfrowo sterowane potencjometry do układów pomiarowych – właściwości i przykładowe schematy sterowania. *Pomiary, Automatyka, Robotyka* 15, 58–63 (2011)
8. Korytkowski, J.: Układ elektroniczny cyfrowej syntezy rezystancji do dokładnej symulacji rezystancyjnych czujników temperatury. *Pomiary Automatyka Robotyka* 5, 86–92 (2013)
9. Warsza, Z.L.: New approach to the accuracy description of unbalanced bridge circuits with the example of Pt sensor resistance bridges. *Journal of Automation Mobile Robotics and Intelligent Systems* 4, 8–15 (2010)
10. Design and selector guide for high precision resistors, Vishay (2011)
11. UPR Series Resistors. Thunder Precision Resistors (datasheet)

Influence of Protective Layer on the Functional Properties of Monolayer and Bilayer Graphene Hall-Effect Sensors

Maciej Kachniarz¹, Oleg Petruk¹, Maciej Oszwałdowski¹, Jacek Salach², Tymoteusz Ciuk³, Włodzimierz Strupiński³, Roman Szewczyk¹, Wojciech Winiarski¹, and Krzysztof Trzcinka¹

¹ Industrial Research Institute for Automation and Measurements PIAP,
Al. Jerozolimskie 202, 02-486 Warsaw, Poland
{mkachniarz, opetruk, rszewczyk}@piap.pl

² Warsaw University of Technology, Institute of Metrology and Biomedical Engineering,
św. A. Boboli 8, 02-525 Warsaw, Poland

³ Institute of Electronic Materials Technology, Wólczyńska 133, 01-919 Warsaw, Poland
wlodek.strupinski@itme.edu.pl

Abstract. Paper presents the results of investigation of the influence of protective layer on the basic functional properties of experimental graphene Hall-effect sensors. Both monolayer and bilayer type of graphene structure was investigated under external magnetic field. Measurement system for obtaining $U_H(B)$ characteristics of Hall-effect sensors was developed using Helmholtz coils as a source of magnetic field. Results of executed tests are presented in the paper as charts, which were analyzed and discussed. Finally, the conclusions were formulated, which are included in the last section of the paper.

Keywords: graphene, Hall-effect sensor, magnetic field measurement.

1 Introduction

The Hall effect is a physical phenomenon of generation of electric potential difference (known as the Hall voltage) across an electric conductor, which is transverse to the direction of electric current flowing through the conductor, when it is subjected to magnetic field perpendicular to direction of the current flow [1]. The Hall effect is applied in Hall-effect sensors of magnetic fields, where value of the Hall voltage is proportional to the external magnetic field. The most important parameter of such a sensor is its sensitivity, which is determined by the electron mobility in the material of conductor [2].

Graphene is a crystalline allotrope of carbon. It is a 2-dimensional structure with thickness of a single atomic layer, where atoms of carbon are organized in sp^2 -bonded hexagonal pattern [3]. Experimental results show, that graphene has a significantly high electron mobility, about $15\,000\text{ cm}^2\cdot\text{V}^{-1}\cdot\text{s}^{-1}$, with the highest reported values over $200\,000\text{ cm}^2\cdot\text{V}^{-1}\cdot\text{s}^{-1}$ at a carrier concentration of $2\times 10^{11}\text{ cm}^{-2}$ (in suspended graphene sheet) [4].

Thus, graphene, with its high electron mobility, is a good material for high-sensitivity Hall-effect sensors, but it is also susceptible to the environmental conditions and pollutants from the air [5]. Therefore, there is a need to protect the graphene Hall-effect structure from this influence. One method to achieve this purpose is to apply the protective layer, separating graphene structure from the environment. In this paper, the possibility of using the protective layer is discussed and its influence on the properties of magnetic Hall-effect sensors is investigated.

2 Investigated Graphene Samples

During the investigation, several graphene samples with different protective layers were tested, both monolayer and quasi-free-standing bilayer (QFS-bilayer) type. Both types were grown using the Chemical Vapor Deposition (CVD) method on the Si face of semi-insulating on-axis 4H-SiC(0001) substrates. The growth process was performed in a standard hot-wall CVD Aixtron VP508 reactor [6]. After the growth process was completed, the substrates were photolithographically patterned to form graphene Hall structures in the shape of symmetrical, equal-arm crosses.

Monolayer graphene structure contains single layer of carbon atoms resting on the buffer layer, also made of carbon atoms, which are covalently bound to the SiC substrate [7]. The buffer layer is necessary to separate the active graphene layer from the substrate. In monolayer graphene, dominant type of charge carriers are electrons.

QFS-bilayer graphene is formed from monolayer structure by decoupling buffer layer from the substrate. It is obtained through in situ intercalation of hydrogen atoms [8]. As the result, QFS-bilayer graphene structure is formed, partly screened from the substrate, with domination of hole transport.

The basic transport properties of both types of investigated graphene structures are presented in Table 1. As it can be seen, monolayer graphene has higher carrier mobility, even at a lower carrier concentration. Thus it is expected, that monolayer structure should have higher sensitivity, than QFS-bilayer.

Table 1. Transport properties of graphene samples

Structure type	Dominant carriers	Carrier mobility ($\text{cm}^2 \cdot \text{V}^{-1} \cdot \text{s}^{-1}$)	Carrier concentration (cm^{-2})
Monolayer	electrons	1000	$4 \cdot 10^{12}$
QFS-bilayer	holes	630	$1.8 \cdot 10^{13}$

3 Protective Layers

For the experiment, four different materials for protective layers were chosen and applied to the graphene samples. All of them were popular adhesive materials commercially available, providing high resistance against the environmental conditions influence.

- Epoxy resin – material with high chemical resistance, high environmental influence resistance, high mechanical strength and good electrical properties.
- Acrylic lacquer – transparent material often used for electronic devices with high resistance for changes of temperature and humidity, providing good protection against chemicals, but with low mechanical resistance.
- Polyurethane resin – material with high chemical resistance, high environmental influence resistance, high wear resistance and good electrical properties.
- Cyanoacrylate adhesive – cheap and easily available adhesive material with high resistance to a wide range of chemicals and high resistance for changing environmental conditions.

All investigated materials were applied to the graphene samples, both monolayer and QFS-bilayer type. In Fig. 1 QFS –bilayer graphene sample with five Hall-effect structures is presented, with (b) and without (a) protective layers.

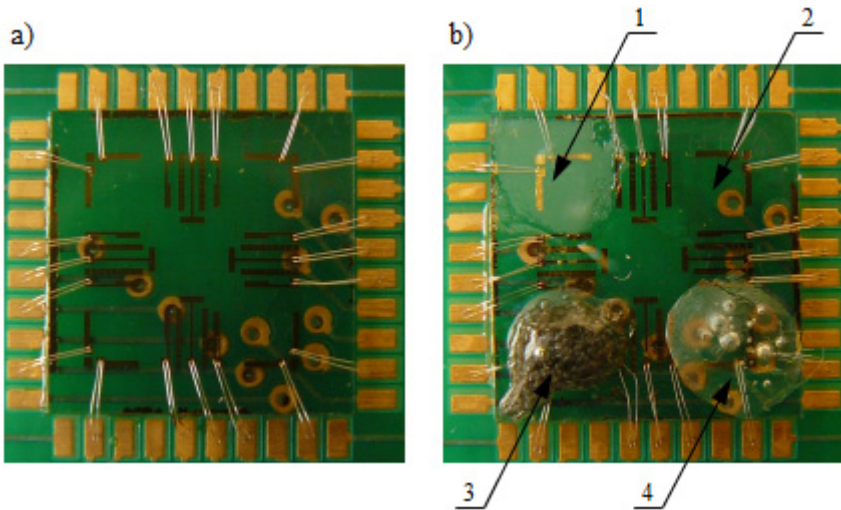


Fig. 1. Graphene sample before (a) and after (b) application of protective layers: 1 – epoxy resin, 2 – acrylic lacquer, 3 – polyurethane resin, 4 – cyanoacrylate adhesive

Before application of protective layers, surface of the graphene sample was cleaned with isopropyl alcohol. After that, protective layers were applied and so prepared sample was resting three days to allow adhesives to harden.

4 Measurement System

Functional properties of the graphene Hall-effect sensors with protective layers applied were tested with the special computer controlled measurement system with the Helmholtz coils used as a source of reference magnetic field. The schematic diagram of the measurement system is presented in Fig. 2.

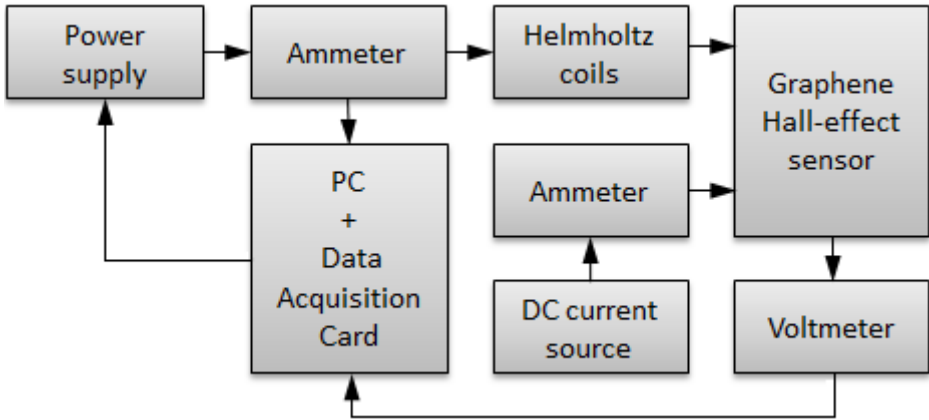


Fig. 2. Schematic block diagram of the measurement system used for investigating functional properties of graphene Hall-effect sensors

The Helmholtz coils were powered by KEPCO BOP 36-6M bipolar power supply with current output, which was controlled by PC with Data Acquisition Card installed. The current in the Helmholtz coils was measured by multimeter APPA 207 working as an ammeter. Ammeter indications were transferred to the PC, where the values of magnetic field acting upon the graphene structure were calculated according to the formula [1]:

$$B = \left(\frac{4}{5}\right)^{\frac{3}{2}} \frac{\mu_0 n I}{R}, \quad (1)$$

where μ_0 is vacuum magnetic permeability, n is number of the coils, I is an electric current in the coils and R is radius of the coil. DC current produced by KEPCO power supply allowed to obtain magnetic field between the coils in range ± 6 mT.

The graphene structure was placed between the Helmholtz coils, perpendicular to the direction of magnetic field. The structure was powered by the current of 1.20 mA generated by INMEL 60 calibrator working as a DC current source. The current powering the graphene structure was measured by METROL DM 22 multimeter. With the powering current and the perpendicular magnetic field, the Hall voltage was generated across the graphene structure, which was measured by precise voltmeter Fluke 8808A. Obtained values of Hall voltage U_H were send to the PC and used to determine the $U_H(B)$ characteristic of the graphene Hall-effect structure. Based on this characteristic, the basic functional properties of the structures were calculated: sensitivity, offset voltage and coefficient of linear determination of the characteristic.

5 Experimental Results

Each investigated structure was measured before and after application of the protective layer. The resulting charts are divided into two groups. First, the results for

monolayer graphene structures testing are presented for all four protective layers types. Next, the same charts for QFS-bilayer structures are included. All structures were tested before applying of protective layers and three days after application, when protective materials hardened. All measurements were performed in normal room temperature of 20 °C.

5.1 Monolayer Graphene Structure

Four monolayer structures were investigated, with different types of protective layers applied. $U_H(B)$ characteristics for each structure is presented in Fig. 3–6 and calculated values of basic functional properties are presented in Table 2.

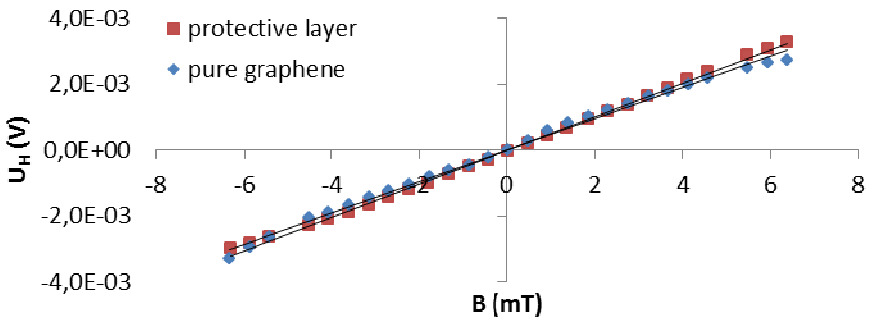


Fig. 3. $U_H(B)$ characteristic of monolayer structure with epoxy resin as protective layer

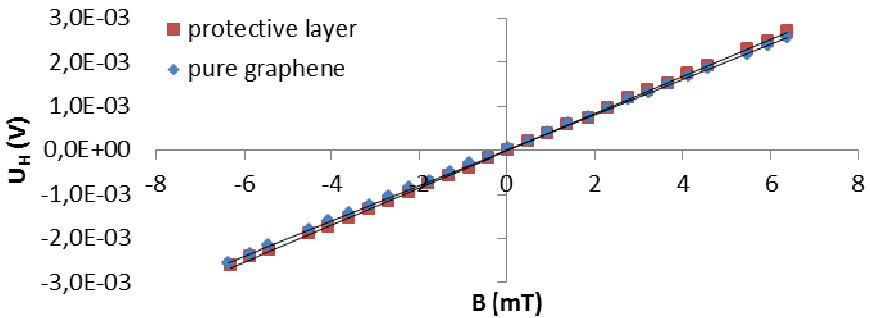


Fig. 4. $U_H(B)$ characteristic of monolayer structure with acrylic lacquer as protective layer

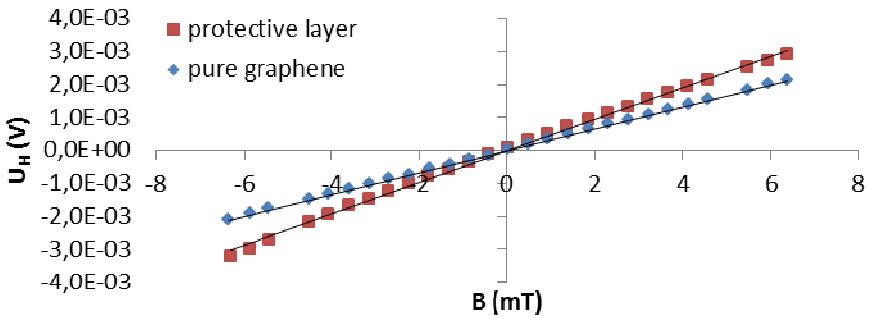


Fig. 5. $U_H(B)$ characteristic of monolayer structure with polyurethane resin as protective layer

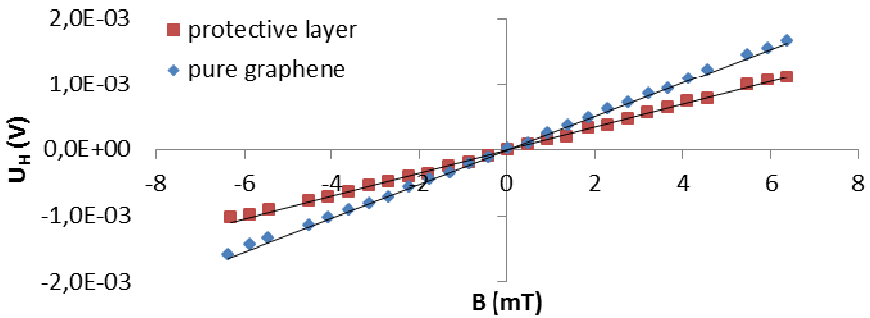


Fig. 6. $U_H(B)$ characteristic of monolayer structure with cyanoacrylate adhesive as protective layer

Table 2. Basic functional properties of monolayer graphene structures with different protective layers applied

Protective material	Sample	Sensitivity [mV/mT]	Offset voltage [mV]	R^2
Epoxy resin	Pure graphene	0.475	191.1	0.9958
	Protective layer	0.507	397.2	0.9984
Acrylic lacquer	Pure graphene	0.401	428.5	0.9998
	Protective layer	0.421	310.8	0.9997
Polyurethane resin	Pure graphene	0.332	176.1	0.9998
	Protective layer	0.479	1.7	0.9980
Cyanoacrylate adhesive	Pure graphene	0.257	180.2	0.9994
	Protective layer	0.173	167.3	0.9982

As it can be noticed in the charts, most of applied protective layers causes a slight increase of monolayer graphene Hall-effect structure sensitivity. The only exception is cyanoacrylate adhesive, which slightly reduces sensitivity. All investigated protective layers have significant influence on the value of offset voltage, especially epoxy resin and polyurethane resin. Influence of the protective layers on the coefficient of linear determination R^2 is insignificant.

5.2 QFS-bilayer Graphene Structure

Four QFS-bilayer structures were investigated, with different types of protective layers applied. $U_H(B)$ characteristics for each structure is presented in Fig. 7–10 and calculated values of basic functional properties are presented in Table 3.

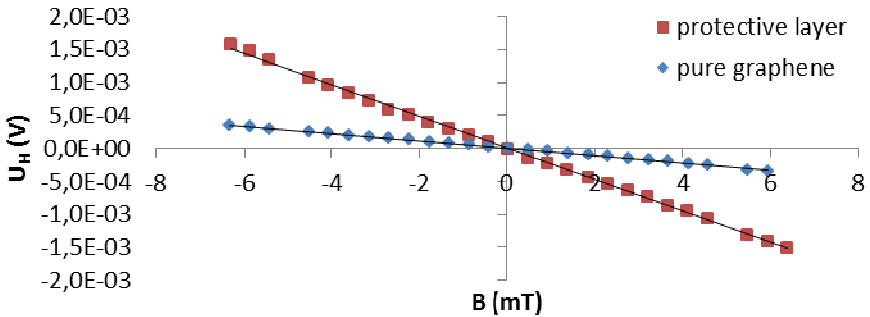


Fig. 7. $U_H(B)$ characteristic of QFS-bilayer structure with epoxy resin as protective layer

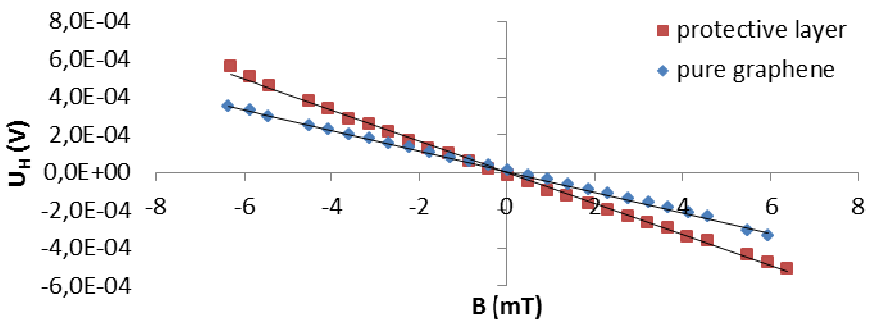


Fig. 8. $U_H(B)$ characteristic of QFS-bilayer structure with acrylic lacquer as protective layer

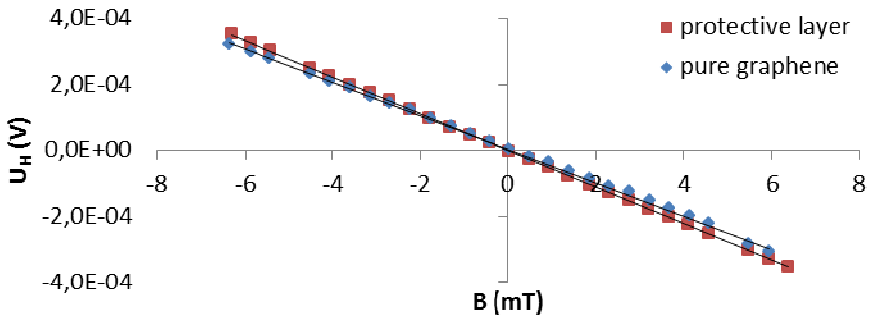


Fig. 9. $U_H(B)$ characteristic of QFS-bilayer structure with polyurethane resin as protective layer

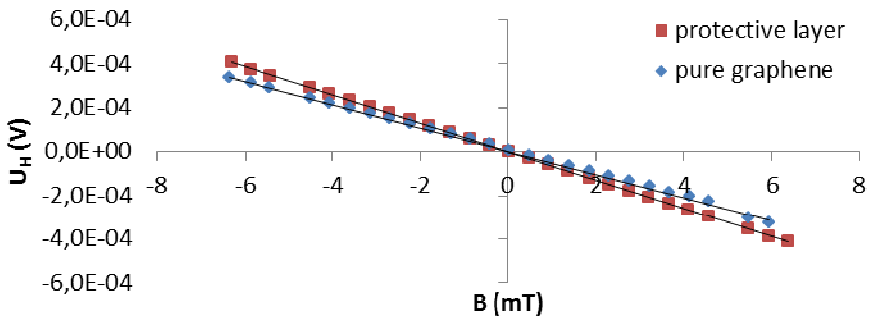


Fig. 10. $U_H(B)$ characteristic of QFS-bilayer structure with cyanoacrylate adhesive as protective layer

Table 3. Basic functional properties of QFS-bilayer graphene structures with different protective layers applied

Protective material	Sample	Sensitivity [mV/mT]	Offset voltage [mV]	R ²
Epoxy resin	Pure graphene	0.056	65.5	0.9987
	Protective layer	0.239	156.1	0.9988
Acrylic lacquer	Pure graphene	0.054	72.2	0.9987
	Protective layer	0.083	57.7	0.9980
Polyurethane resin	Pure graphene	0.051	26.3	0.9992
	Protective layer	0.055	28.7	0.9999
Cyanoacrylate adhesive	Pure graphene	0.053	13.9	0.9990
	Protective layer	0.065	7.0	0.9999

All investigated protective layers causes less or more significant increase of the sensitivity of QFS-bilayer structures. Influence on the value of offset voltage is clearly visible, but some of the investigated protective layers increase the value of this parameter, while the other decrease it. As in the case of monolayer structures, influence of the protective layers on the R^2 coefficient is insignificant.

6 Conclusion

Performed investigation have shown, that all tested materials are good candidates for protective layers of graphene Hall-effect sensors. None of them has worsen the sensitivity and linearity of graphene sensor and some of them affect the reduction of offset voltage, which is a desirable effect. It is also very important matter to find a way to reduce he values of values of the offset voltage in graphene Hall-effect sensors. Very promising method is to compensate offset voltage in the resistance bridge [9].

Obtained results are very promising and will help to improve resistance of Hall-effect sensors made of graphene to changes of environmental conditions. But taking into account high values of the thermal coefficients of investigated protective materials, it is very important to study the influence of protective layers on thermal characteristics of graphene Hall-effect sensor, so further investigations should be carried out.

Acknowledgments. This work was partially supported by The National Center of Research and Development within GRAF-TECH program.

References

1. Nałęcz, M., Jaworski, J.: *Miernictwo magnetyczne*. WNT, Warsaw (1968)
2. Ramsden, E.: *Hall-Effect Sensors: Theory and Application*. Newnes (2006)
3. Krupka, J., Strupiński, W.: Measurements of the sheet resistance and conductivity of thin epitaxial graphene and SiC films. *Applied Phys. Letts.* 96, 82101 (2010)
4. Bolotin, K.I., Sikes, K.J., Jiang, Z., et al.: Ultrahigh electron mobility in suspended graphene. In: *Solid State Communications*, vol. 146(9-10), pp. 351–355. Elsevier (2008)
5. Petruk, O., Szewczyk, R., Ciuk, T., Strupiński, W., Salach, J., Nowicki, M., Pasternak, I., Winiarski, W., Trzcinka, K.: Sensitivity and offset voltage testing in the hall-effect sensors made of graphene. In: Szewczyk, R., Zieliński, C., Kaliczyńska, M. (eds.) *Recent Advances in Automation, Robotics and Measuring Techniques*. AISC, vol. 267, pp. 631–640. Springer, Heidelberg (2014)
6. Strupiński, W., Grodecki, K., Wymolek, A., et al.: Graphene Epitaxy by Chemical Vapor Deposition on SiC. *Nano Lett* 11(4), 1786–1791 (2011)
7. Ray, N., Shallcross, S., Hensel, S., Pankratov, O.: Buffer layers limited conductivity in epitaxial graphene on the Si face of SiC. *Phys. Rev. B* 86125426 (2012)
8. Riedl, C., Coletti, C., Iwasaki, T., et al.: Quasi-Free-Standing Epitaxial Graphene on SiC Obtained by Hydrogen Intercalation. *Phys. Rev. Lett.* 103, 246804 (2009)
9. Warsza, Z.L.: New Approach to the Accuracy Description of Unbalanced Bridge Circuits with the Example of Pt Sensor Resistance Bridges. *Journal of Automation, Mobile Robotics & Intelligent Systems, PIAP, Warsaw* 4(2), 8–15 (2010)

Temperature Dependence of Functional Properties of Graphene Hall-Effect Sensors Grown on Si Face and C Face of 4H-SiC Substrate

Maciej Kachniarz¹, Oleg Petruk¹, Maciej Oszwałdowski¹, Jacek Salach²,
Tymoteusz Ciuk³, Włodzimierz Strupiński³, Roman Szewczyk¹,
Wojciech Winiarski¹, and Krzysztof Trzcinka¹

¹ Industrial Research Institute for Automation and Measurements PIAP,
Al. Jerozolimskie 202, 02-486 Warsaw, Poland
{mkachniarz, opetruk, rszewczyk}@piap.pl

² Warsaw University of Technology, Institute of Metrology and Biomedical Engineering,
św. A. Boboli 8, 02-525 Warsaw, Poland

³ Institute of Electronic Materials Technology, Wólczyńska 133, 01-919 Warsaw, Poland
wlodek.strupinski@itme.edu.pl

Abstract. Paper presents the results of investigation of the temperature influence on the basic functional properties of graphene Hall-effect sensors. The measurement system utilizing Helmholtz coils as a source of external magnetic field and environmental chamber for setting temperature was developed. Two types of monolayer graphene structures grown on both Si and C face of SiC substrate were investigated in the room temperature (about 20 °C) and their functional properties were compared. Next, the temperature influence on functional properties of both types of graphene structures was investigated using environmental chamber. The results of measurements are presented as charts and analyzed in the paper. On the basis of the results, conclusions were formulated, which are included in the last section of the paper.

Keywords: graphene, Hall-effect sensor, magnetic field measurement, temperature influence.

1 Introduction

The Hall-effect sensors of magnetic field are utilizing the phenomenon of voltage generation (known as Hall voltage) across an electric conductor subjected to the flow of electric current under the influence of external magnetic field perpendicular to the direction of the current flow, which is known as Hall effect [1]. They are used in many industrial applications, being dominant type of sensors in the market of industrial measurements of magnetic field with more than 70% of the market share [2]. Main area of their implementation is DC current transformer, but they can also be used in different applications, for example in magnetovision systems [3]. It is the reason, why these sensors are intensively developed. The most attention is paid to

increasing sensitivity of the sensors. It is obtained by searching new materials with higher charge carriers mobility, which is determining the sensitivity of the Hall-effect sensor [1].

With its high electron mobility graphene, 2-dimensional crystalline allotrope of carbon is expected to be a good material for high-sensitivity Hall-effect sensors. Results of the performed experiments show, that electron mobility of the graphene reaches the value of $15\,000\text{ cm}^2\cdot\text{V}^{-1}\cdot\text{s}^{-1}$ at a carrier concentration of $2\times 10^{11}\text{ cm}^{-2}$ [4]. Conducted experiments indicate that Hall-effect sensors utilizing graphene have significantly higher sensitivity than sensors made of other materials [5].

For possible industrial applications, it is very important matter to investigate the influence of environmental conditions on graphene Hall-effect sensors. This paper presents methodology and results of investigating of temperature influence on the functional properties of monolayer graphene Hall-effect sensors grown on both Si and C face of SiC substrate.

2 Measurement System

For performed measurements of temperature influence on the functional properties of graphene Hall-effect sensors special computer controlled measurement system was used, presented in Fig. 1.

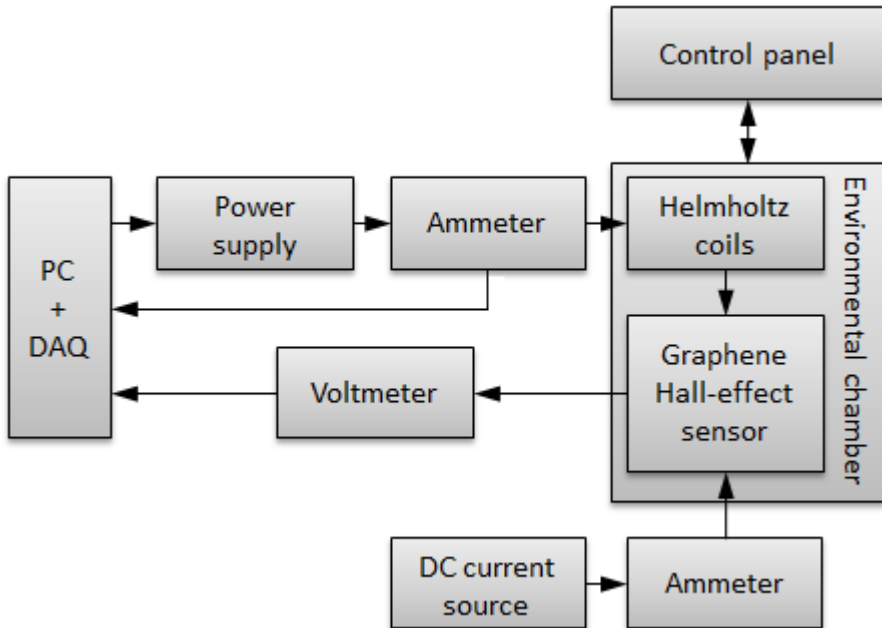


Fig. 1. Schematic block diagram of the measurement system used for investigating temperature dependence of functional properties of graphene Hall-effect sensors

The investigated graphene structures were supplied by INMEL 60 calibrator working as precise DC current source with the current of 1.20 mA. The supply current was measured by METROL DM 22 multimeter.

The graphene Hall-effect structures were placed between the Helmholtz coils, perpendicular to the direction of external magnetic field. The coils were powered by KEPCO BOP 36-6M bipolar power supply with current output. The power supply was controlled by PC with Data Acquisition Card (DAQ) installed. Values of current I in the Helmholtz coils were measured by APPA 207 multimeter and send to the PC, where the values of magnetic field perpendicular to the graphene structure were calculated according to the formula [6]:

$$B = \left(\frac{4}{5}\right)^{\frac{3}{2}} \frac{\mu_0 n I}{R}, \quad (1)$$

where μ_0 is vacuum magnetic permeability, n is number of the coils and R is radius of the coil. The magnetic field acting upon the graphene structure reached values in the range of ± 6 mT. For measurements of the output voltage U_H , precise Fluke 8808A voltmeter was used. Voltmeter's indications were sent to the PC, where $U_H(B)$ characteristic of the graphene Hall-effect structures were determined and basic functional properties like sensitivity, offset voltage and coefficient of linear determination of the characteristic were calculated.

The Helmholtz coils with graphene Hall-effect structures between them were placed inside of the digitally controlled environmental chamber Heraeus HCZ 3004E. The temperature and humidity in the chamber could be determined by user's settings entered via the control panel. The control panel was also used to read the current values of environmental parameters in the chamber.

3 Investigated Graphene Structures

During the investigation, two monolayer graphene Hall-effect structures were tested. One was grown on the Si face of semi-insulating on-axis 4H-SiC(0001) substrate and the other one on the C face of the same substrate. Monolayer graphene structure is a single layer of carbon atoms. This active layer is separated from the SiC substrate by buffer layer, also made of carbon atoms, which are covalently bound to the substrate [7].

Both structures were grown using the Chemical Vapor Deposition (CVD) in a standard hot-wall CVD Aixtron VP508 reactor [8]. After completion of the growth process, the substrates with graphene layer were photolithographically formed into graphene Hall-effect structures in the shape of symmetrical, equal-arm crosses presented in Fig. 2. Each structure has four electrodes. Two opposite horizontal electrodes are used to power the structure and under the influence of external magnetic field perpendicular to the surface of the structure Hall voltage is generated between vertical electrodes.

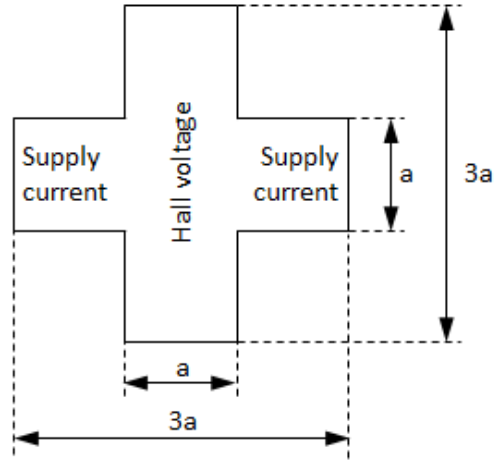


Fig. 2. Outline of the cross-shaped graphene Hall-effect structure, in both investigated structures $a = 800 \mu\text{m}$

All graphene Hall-effect structures are characterized by some basic transport properties, like dominant charge carriers, carrier mobility and carrier concentration. The most important is the carrier mobility, which determines sensitivity of Hall-effect structure. In Table 1, the basic transport properties of investigated graphene Hall-effect structures grown on Si and C face of SiC substrate are presented. Both investigated structures were monolayer type, so dominant type of charge carriers in each of them are electrons. As it can be seen, structure grown on the Si face of SiC substrate has over two times higher carrier mobility even at lower carrier concentration.

Table 1. Basic transport properties of investigated graphene structures

Substrate	Dominant carriers	Carrier mobility ($\text{cm}^2 \cdot \text{V}^{-1} \cdot \text{s}^{-1}$)	Carrier concentration (cm^{-2})
Si face of SiC	electrons	1300	$4 \cdot 10^{12}$
C face of SiC	electrons	620	$1.2 \cdot 10^{13}$

First, both investigated structures were measured in normal room temperature of 20°C , to compare their functional properties. Obtained $U_H(B)$ characteristics are presented in Fig. 3, while calculated values of sensitivity, offset voltage and coefficient of linear determination of the characteristic R^2 for each structure are compared in Table 2.

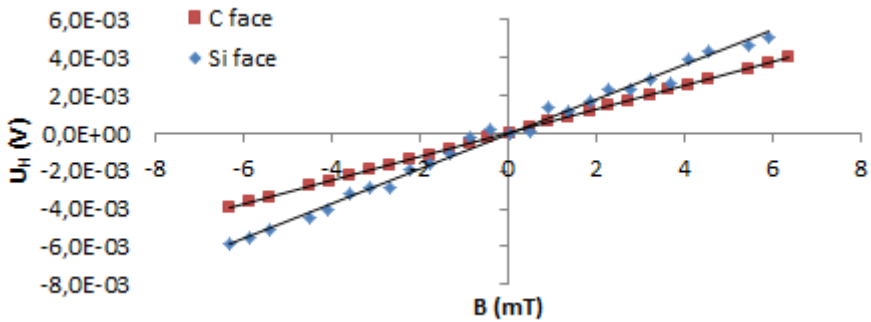


Fig. 3. $U_H(B)$ characteristic of graphene Hall-effect structures grown on Si and C face of SiC substrate

Table 2. Basic transport properties of investigated graphene structures

Substrate	Sensitivity (mV/mT)	Offset voltage (mV)	R ²
Si face of SiC	0,0912	518,3	0,9915
C face of SiC	0,0625	12,2	0,9999

Presented characteristics and functional properties indicates that graphene structure grown on Si face of SiC substrate has slightly higher sensitivity than structure grown on C face. It is connected with higher carrier mobility of Si face structure. This structure has also much higher value of offset voltage, which is probably the result of some imperfections in the investigated structure.

4 Experimental Results

Both investigated structures together with Helmholtz coils were placed inside the environmental chamber. The temperature values were set within the range of $-20\text{ }^{\circ}\text{C}$ to $40\text{ }^{\circ}\text{C}$ with the step of $10\text{ }^{\circ}\text{C}$. Obtained results are presented as charts which are showing changes of $U_H(B)$ characteristics under the influence of temperature and temperature dependence of sensitivity and offset voltage of the investigated structures. Two sets of charts are presented – one for Si face and other for C face structure.

4.1 Graphene Structure Grown on Si Face of SiC Substrate

For graphene structure grown on Si face of SiC substrate $U_H(B)$ characteristics for each investigated temperature were drawn in one common hart in order to show temperature influence on the characteristics. This chart is presented in Fig. 4. Figure 5 presents temperature dependence of sensitivity of investigated structure and Fig. 6 shows temperature influence on the values of offset voltage.

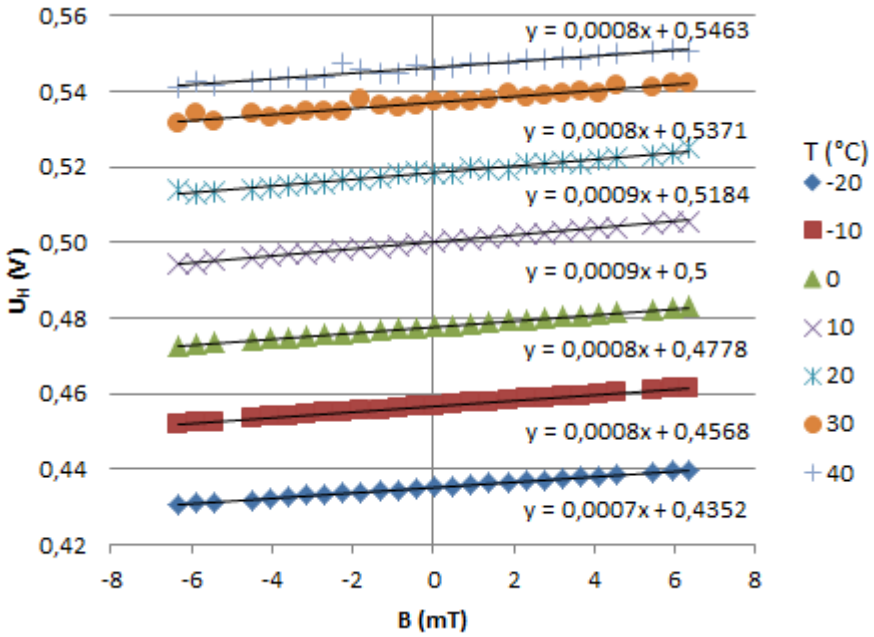


Fig. 4. $U_H(B)$ characteristic of graphene Hall-effect structure grown on Si face of SiC substrate at investigated temperatures

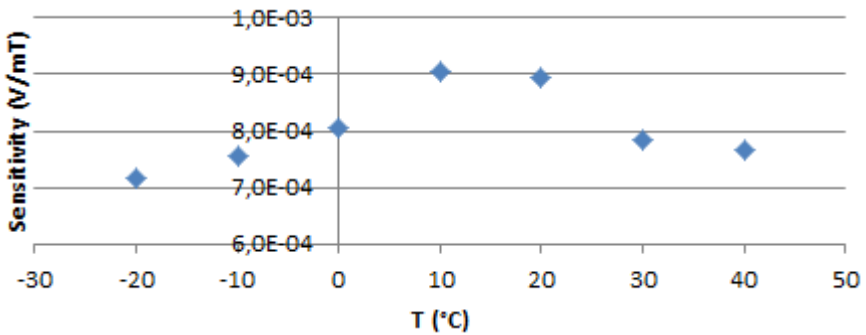


Fig. 5. Temperature dependence of sensitivity of graphene Hall-effect structure grown on Si face of SiC substrate

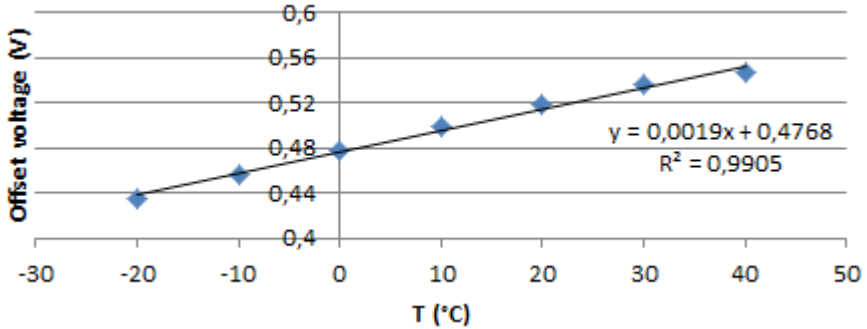


Fig. 6. Temperature dependence of offset voltage of graphene Hall-effect structure grown on Si face of SiC substrate with a linear fit

As it can be noticed in the charts, values of offset voltage are growing with the temperature increase. Fig. 6 indicates that this growth is linear, which is confirmed by high value of R^2 coefficient of linear fit of temperature dependence of offset voltage. Temperature dependence of sensitivity for investigated structure is nonlinear. For low temperatures sensitivity is rising to reach its maximum value somewhere between 10 °C and 20 °C. Then sensitivity starts to decrease with temperature growth. Temperature influence on the sensitivity is rather small but noticeable.

4.2 Graphene Structure Grown on C Face of SiC Substrate

For graphene structure grown on C face of SiC substrate the same set of charts is presented. $U_H(B)$ characteristics for each investigated temperature are presented in Fig. 7. Temperature dependence of sensitivity and offset voltage are shown in Fig. 8 and Fig. 9.

The charts indicates that temperature has less influence on the functional properties of C face graphene structure than on the same parameters of structure grown on Si face. Both sensitivity and offset voltage are linear dependent on the temperature and are decreasing with the temperature growth. Temperature characteristic of sensitivity has slightly lower value of R^2 coefficient, but it is high enough to observe linear dependence. As in the Si face structure case, temperature dependence of sensitivity is small.

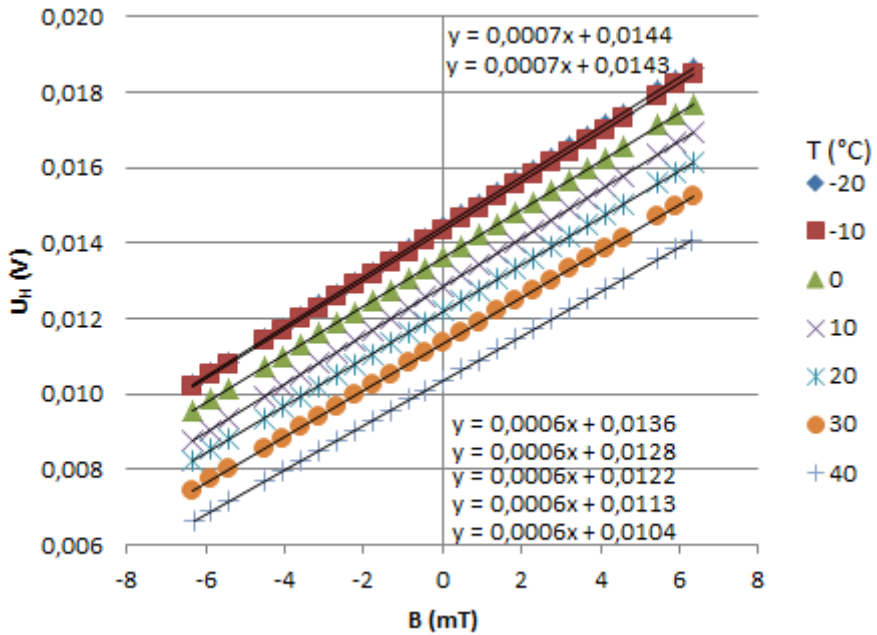


Fig. 7. $U_H(B)$ characteristic of graphene Hall-effect structure grown on C face of SiC substrate at investigated temperatures

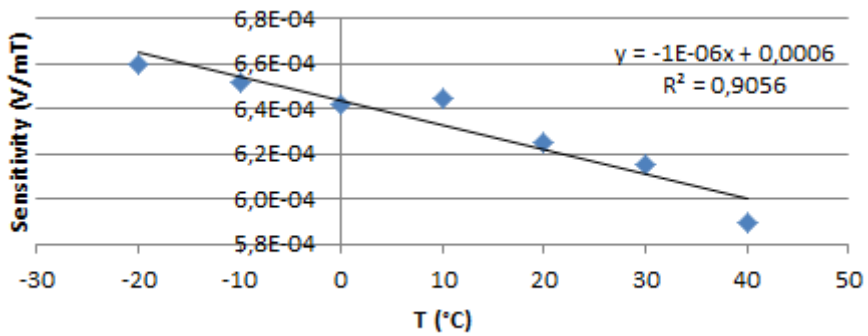


Fig. 8. Temperature dependence of sensitivity of graphene Hall-effect structure grown on C face of SiC substrate with a linear fit

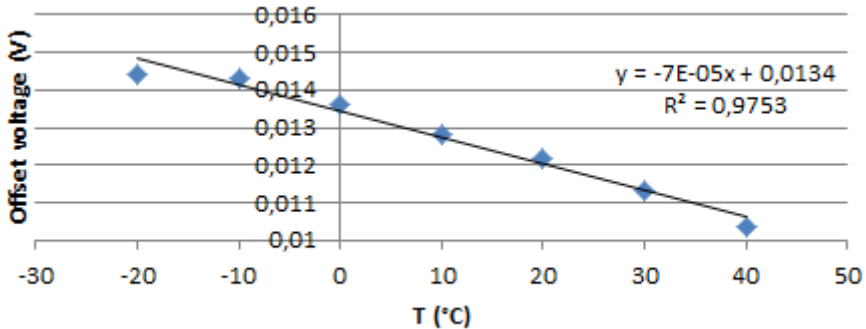


Fig. 9. Temperature dependence of offset voltage of graphene Hall-effect structure grown on C face of SiC substrate with a linear fit

5 Conclusion

Performed measurements have shown that temperature has significant influence on the functional properties of graphene Hall-effect structure irrespective of the type of substrate. Temperature dependence of sensitivity in both structures is rather small but noticeable. Nonlinear temperature characteristic of Si face structure could be the result of some imperfections in the graphene structures which seems to be confirmed by high values of the offset voltage in this structure. Temperature influence on the offset voltage is in both structures noticeable and in both cases is linear.

Obtained results indicate that there is a need to consider the temperature influence on the functional properties of graphene Hall-effect sensors in possible industrial applications. Linear dependence of the offset voltage could be easily compensated. Nonlinear character of temperature dependence of sensitivity in graphene structure grown on Si face of the SiC substrate is little disturbing and could be hard to compensate, but it can just be the result of imperfections in the structure, especially considering linear temperature characteristic of sensitivity in the other structure.

Presented results proofs, that graphene Hall-effect structure are very promising. There is a need to find a way to reduce the influence of temperature on their functional properties, but considering in most cases linear character of this influence it should not be a problem in their possible industrial applications. Nonetheless, further studies in this matter should be carried out.

Acknowledgments. This work was partially supported by The National Center of Research and Development within GRAF-TECH program.

References

1. Ramsden, E.: *Hall-Effect Sensors: Theory and Application*. Newnes (2006)
2. *Magnetic Field Sensors Market by Type (Hall Effect, Magnetoresistive, SQUID, Others), Technology, Applications (Automotive, Consumer Electronics, Industrial & Infrastructure, Medical, Aerospace & Defense) & Geography – Forecasts & Analysis to 2013 – 2020*. Marketsand Markets (2014), <http://www.marketsandmarkets.com>
3. Nowicki, M., Szewczyk, R.: Application of Magnetovision for Detection of Dangerous Objects. *Journal of Automation, Mobile Robotics & Intelligent Systems* 7(2), 70–74 (2013)
4. Bolotin, K.I., Sikes, K.J., Jiang, Z., et al.: Ultrahigh electron mobility in suspended graphene. *Solid State Communications* 146(9-10), 351–355 (2008)
5. Petruk, O., Szewczyk, R., Ciuk, T., Strupiński, W., Salach, J., Nowicki, M., Pasternak, I., Winiarski, W., Trzcinka, K.: Sensitivity and offset voltage testing in the hall-effect sensors made of graphene. In: Szewczyk, R., Zieliński, C., Kaliczyńska, M. (eds.) *Recent Advances in Automation, Robotics and Measuring Techniques*. AISC, vol. 267, pp. 631–640. Springer, Heidelberg (2014)
6. Nałęcz, M., Jaworski, J.: *Miernictwo magnetyczne*. WNT, Warsaw (1968)
7. Ray, N., Shallcross, S., Hensel, S., Pankratov, O.: Buffer layers limited conductivity in epitaxial graphene on the Si face of SiC. *Phys. Rev. B* 86125426 (2012)
8. Strupiński, W., Grodecki, K., Wymołek, A., et al.: Graphene Epitaxy by Chemical Vapor Deposition on SiC. *Nano Lett* 11(4), 1786–1791 (2011)

Temperature Influence on the Magnetic Characteristics of Mn-Zn Ferrite Materials

Maciej Kachniarz¹, Jacek Salach², Roman Szewczyk², and Adam Bieńkowski²

¹ Industrial Research Institute for Automation and Measurements PIAP,
Al. Jerozolimskie 202, 02-486 Warsaw, Poland
mkachniarz@piap.pl

² Warsaw University of Technology,
Institute of Metrology and Biomedical Engineering,
św. A. Boboli 8, 02-525 Warsaw, Poland

{j.salach,r.szewczyk,a.bienkowski}@mchtr.pw.edu.pl

Abstract. The subject of this paper was to investigate the temperature influence on the magnetic characteristics B-H of crystalline soft magnetic materials. Four different Mn-Zn ferrite material were investigated. The investigated ferrites were formed into ring-shaped cores with closed magnetic circuit and magnetizing and sensing windings were coiled on them. All cores were placed in the cryostat which was used to set temperature. Magnetic B-H characteristics was measured by computer controlled hysteresis graph. The results of the investigations were presented in the paper and analyzed. On the basis of presented results, the conclusions were formulated, which are also included in the paper.

Keywords: ferrite, temperature influence, magnetic characteristics, ferromagnetic material.

1 Introduction

Researches on magnetic properties and characteristics of magnetic materials are very important from the point of view of modern electronic, where inductive components play very significant role. One of the most important materials for technical applications are ferrites, which are widely used as magnetic cores for inductive components as chokes, filters and transformers [1].

Ferrites are ceramic materials composed of iron oxide (Fe_2O_3) chemically composed with one or more metallic elements [2]. They are ferrimagnetic materials and due to their magnetic properties they can be classified into two groups: soft ferrites, which are used as magnetic cores of transformers and other inductive elements and hard ferrites, which are the materials for permanent magnets. One of the most popular groups of soft ferrites for technical applications are Mn-Zn ferrites, containing magnesium and zinc as additive metallic elements.

The most complete description of magnetic properties of the magnetic material is its B-H characteristic [3]. It presents all changes in the structure of magnetic material and its magnetic properties due to changes of external magnetizing field.

For the technical applications it is very important to determine the influence of environmental conditions on magnetic characteristics of ferrite. It is commonly known, that environmental conditions, especially temperature, is more or less affecting magnetic properties of magnetic materials [4–7]. This paper presents the methodology and results of investigation of temperature influence on magnetic characteristics of Mn-Zn ferrite materials.

2 Investigated Samples

During the investigation, four Mn-Zn ferrite material samples of different chemical composition were tested. Chemical composition of all materials can be described by the general formula $Mn_{1-x}Zn_xFe_2O_4$. The difference between the materials was the content ratio of magnesium and zinc (value of the x parameter). Two of them (F-3001, F-807) were fabricated by POLFER (Poland) and the other two (T38, N41) by TDK-EPC Epcos (Germany).

All investigated samples were formed into ring-shaped magnetic cores, as presented in Fig. 1. Based on the geometrical dimensions of the core, basic geometrical parameters: the flow path of the magnetic flux in the magnetic circuit l_e and cross-sectional area of the core S_e , were calculated. They were necessary to correctly designate the values of magnetic field strength H and magnetic flux density B .

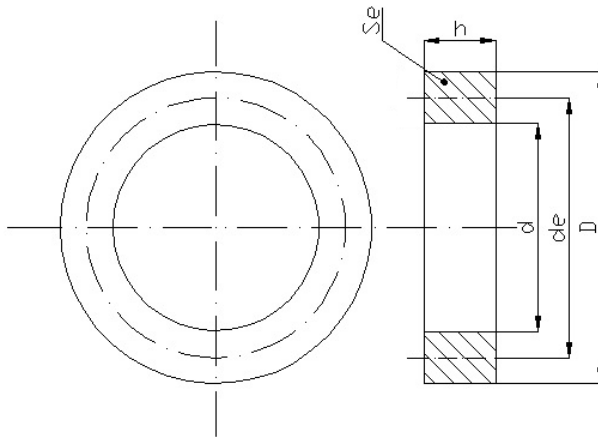


Fig. 1. Shape and geometrical dimensions of investigated Mn-Zn ferrite cores, D – outer diameter, d – inner diameter, d_e – average diameter, h – thickness

On each investigated core magnetizing and sensing windings were made. Sensing winding was located under magnetizing winding in order to decrease influence of demagnetization effects. Geometrical parameters and numbers of coils in each winding for all samples are presented in Table 1.

Table 1. Geometrical parameters and numbers of magnetizing (N_m) and sensing (N_s) coils of investigated Mn-Zn ferrite cores

Sample	F-3001	F-807	N41	T38
l_e (mm)	62.8	82.0	92.3	62.8
S_e (mm ²)	60	60	99	39
N_m	5	5	10	5
N_s	25	25	50	25

3 Measurement System

Temperature influence on the magnetic characteristics of Mn-Zn ferrite materials was tested with the special computer controlled measurement system with cryostat for temperature stabilization. The block diagram of the measurement system is presented in Fig. 2.

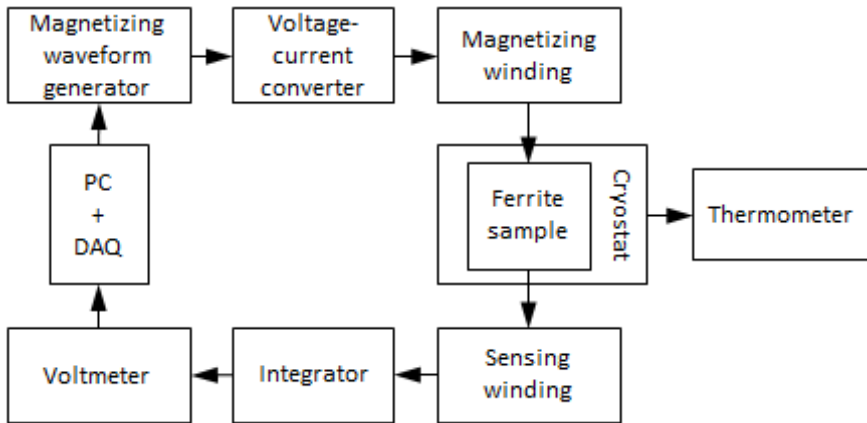


Fig. 2. Schematic block diagram of the measurement system

To control the measurement system, PC with Data Acquisition Card (DAQ) and special control software installed was used. Magnetizing waveform was generated as voltage waveform and then converted into current magnetizing waveform by voltage-current converter. The parameters of the waveform, such as frequency and amplitude, were set in the control program. Magnetizing waveform was sent to magnetizing winding, changing magnetizing field H acting on the investigated sample in time according to the formula:

$$H(t) = \frac{N_m i(t)}{l_e}, \tag{1}$$

where $i(t)$ is function describing changes of magnetizing current in time. Changes of magnetizing field H caused changes of the voltage induced in sensing winding. The induced voltage waveform was integrated over time by integrator to obtain values proportional to the values of magnetic flux density B in the investigated sample. Integrated values of voltage were measured by voltmeter and sent to the PC, where values of the flux density B were calculated in control program. Changes of B in time depending on the induced voltage can be described by the formula:

$$B(t) = \frac{K_c}{N_s S_e} \int u(t) dt, \quad (2)$$

where $u(t)$ is function describing changes of induced voltage in time and K_c is the constant of the integrator. Having the values of both $H(t)$ and $B(t)$, B-H magnetic characteristic could be determined.

The investigated samples were placed in the cryostat chamber filled with thermally conductive fluid. The chamber was built as Dewar flask. The cryostat was able to both cool and warm the objects placed in the chamber. The temperature inside the chamber was measured by digital multimeter with K-type thermocouple connected.

4 Experimental Results

For all four investigated samples B-H magnetic characteristics were measured within the temperature range of $-20\text{ }^\circ\text{C}$ to $60\text{ }^\circ\text{C}$. For each investigated core maximum value of magnetizing field was equal or close to the saturation value. In Fig. 3-6 hysteresis loops of investigated ferrites are presented. For each sample, three hysteresis loops are shown: in minimum temperature of $-20\text{ }^\circ\text{C}$, in normal room temperature of $20\text{ }^\circ\text{C}$ and in the maximum temperature of $60\text{ }^\circ\text{C}$.

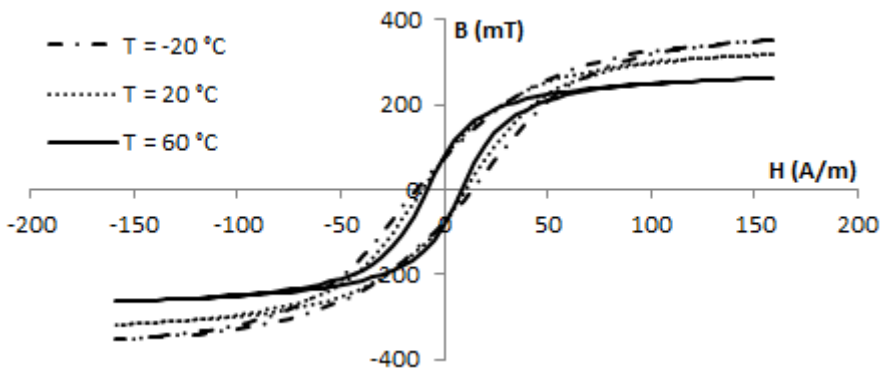


Fig. 3. The temperature dependence of B-H magnetic characteristics of F-3001 Mn-Zn ferrite material, $H_m = 160\text{ A/m}$

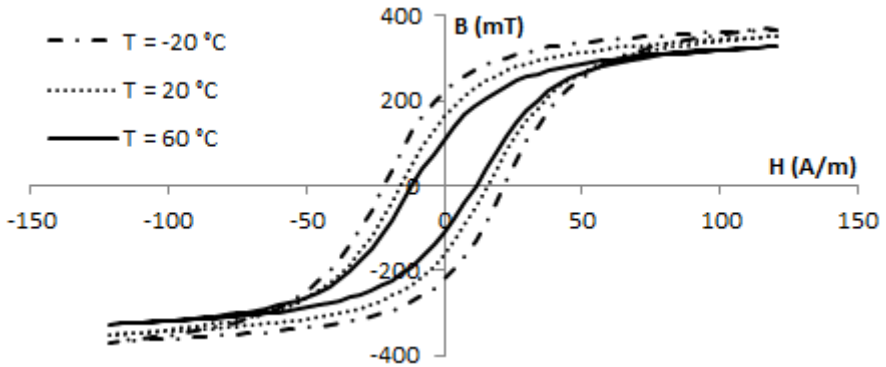


Fig. 4. The temperature dependence of B-H magnetic characteristics of F-807 Mn-Zn ferrite material, $H_m = 120$ A/m

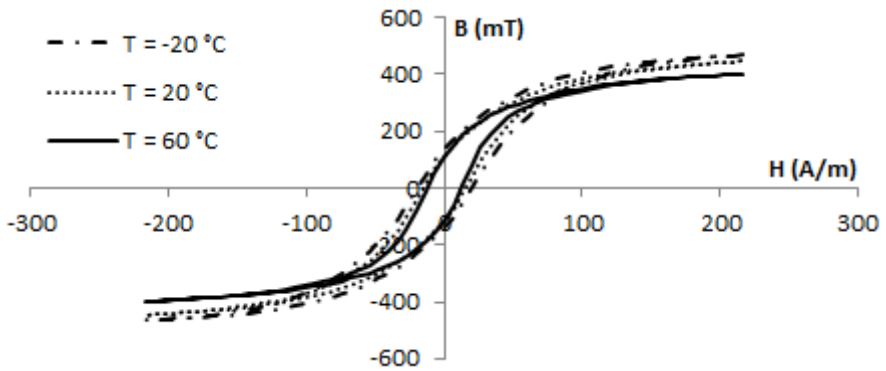


Fig. 5. The temperature dependence of B-H magnetic characteristics of N41 Mn-Zn ferrite material, $H_m = 215$ A/m

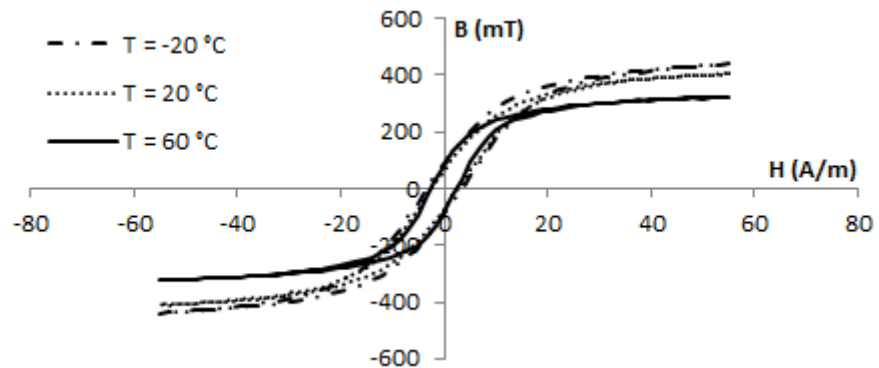


Fig. 6. The temperature dependence of B-H magnetic characteristics of T38 Mn-Zn ferrite material, $H_m = 55$ A/m

As in can be seen in the presented charts, temperature influence on the magnetic B-H characteristics of Mn-Zn ferrite materials is clearly noticeable. With increasing temperature, the area of the hysteresis loop of Mn-Zn ferrite is decreasing. For the maximum temperature the area of hysteresis loop is the smallest. It means, that with increasing temperature, values of all parameters of the hysteresis loop, such as coercive field, remanence and maximum flux density, are decreasing. Changes of remanence are clearly seen especially for F-807 material. Decreasing values of coercive field can be observed in all investigated materials.

The most noticeable effect of temperature influence on the magnetic B-H characteristics of Mn-Zn ferrite materials is a decline in the values of maximum flux density with increasing temperature. It is presented in Fig. 7, which shows temperature characteristics of maximum value of flux density B_m . Presented results were obtained for the amplitude of magnetizing field $H_m = 120$ A/m for all investigated samples.

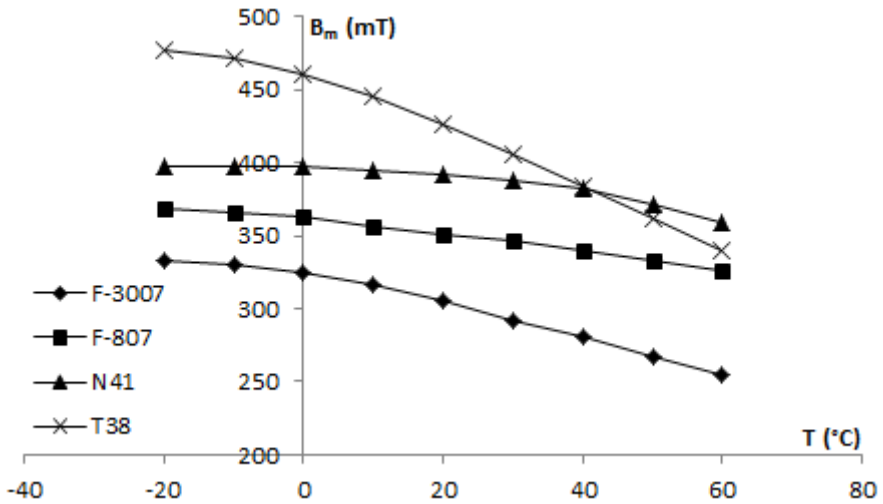


Fig. 7. Temperature dependence of maximum flux density B_m for investigated Mn-Zn ferrite materials, $H_m = 120$ A/m

The temperature dependence of maximum value of flux density B_m in all investigated cores is monotonic. For low temperatures, under 0 °C, maximum flux density reaches the highest values. With increasing temperature, maximum flux density values are decreasing. For the highest investigated temperature (60 °C), B_m takes a minimum value. The most significant difference between the highest and the lowest value of B_m occurs in T38 material. In other samples temperature dependence of maximum flux density is slightly smaller. This may be due to chemical composition of T38 material, which could be significantly different from the other investigated materials.

5 Conclusion

Presented results are consisted with the Weiss theory of molecular field [8] and show that there is a significant temperature dependence of magnetic properties of Mn-Zn ferrite materials. It is caused by processes occurring in the atomic structure of the material. If ferrite material is placed in the magnetizing field, magnetic moments of the ferrite's atoms are setting according to the direction of the field. When temperature is increasing, the thermal energy of atoms in the crystalline structure is also rising. Thermal vibrations of atoms become stronger, so it is easier for magnetic moments to change their directions in the direction of external field. This causes a decrease in the values of coercive field and remanence of the material in higher temperatures. But strongly vibrating atoms also makes it harder to achieve full arrangement of magnetic moments when external magnetizing field is reaching saturation values, so maximum flux density of material is lower for high temperatures. So in high temperatures it is easier to demagnetize the material but magnetic moments of atoms cannot reach full arrangement in saturation area of the hysteresis loop.

Results of the research shows, that there is a strong correlation between the temperature and magnetic properties of Mn-Zn ferrite materials. This connection is so significant, that it cannot be neglected in technical applications. It is very important matter when designing electronics containing inductive components with Mn-Zn ferrite cores to take into account the operating temperature range of the device and to assess whether the inductive components will work properly in such thermal conditions.

References

1. O'Handley, R.: Modern magnetic materials – principles and applications. John Wiley & Sons, New York (2000)
2. Carter, C.B., Norton, M.G.: Ceramic Materials: Science and Engineering. Springer (2007)
3. Jiles, D.: Introduction to magnetism and magnetic materials. Chapman & Hall, London (1998)
4. Szewczyk, R., Švec, P., Švec, P., et al.: Thermal annealing of soft magnetic materials and measurements of its magnetoelastic properties. *Pomiary Automatyka Robotyka* 2(2013), 513–518 (2013)
5. Szewczyk, R.: Modeling the influence of temperature on the magnetic characteristics of $\text{Fe}_{40}\text{Ni}_{38}\text{Mo}_4\text{B}_{18}$ amorphous alloy for magnetoelastic sensors. In: *Recent Advances in Mechatronics*, pp. 586–590. Springer (2007)
6. Kulikowski, J., Bieńkowski, A.: Field, Temperature and Stress Dependence of Magnetostriction in Ni-Zn Ferrites Containing Cobalt. *Phys. Scripta*. 44, 382–383 (1991)
7. Jackiewicz, D., Szewczyk, R., Salach, J.: Modelling the Magnetic Characteristics and Temperature Influence on Constructional Steels. In: *Solid State Phenomena*, vol. 199, pp. 466–471. Trans Tech Publications, Switzerland (2013)
8. Cullity, B.D., Graham, C.D.: Introduction to magnetic materials. John Wiley & Sons, New York (2009)

Graphene Joule Heating Measurements in Environmental Chamber

Anna Kozłowska¹, Maciej Kachniarz², Grzegorz Gawlik¹, Roman Szewczyk³,
and Mateusz Wojtasiak⁴

¹ Institute of Electronic Materials Technology, Wólczyńska 133, 01-919 Warsaw, Poland
{anna.kozłowska, grzegorz.gawlik}@itme.edu.pl

² Industrial Research Institute for Automation and Measurements PIAP,
Al. Jerozolimskie 202, 02-486 Warsaw, Poland
mkachniarz@piap.pl

³ Warsaw University of Technology, Institute of Metrology and Biomedical Engineering,
św. A. Boboli 8, 02-525 Warsaw, Poland
r.szewczyk@mchtr.pw.edu.pl

⁴ Warsaw University of Technology, Faculty of Electronics and Information Technology
Nowowiejska 15/19, 00-665 Warsaw, Poland

Abstract. The paper presents results of Joule heating measurements in graphene samples performed in a specially designed environmental chamber. The experimental stand was designed and described in the paper, paying particular attention to the project of the environmental chamber. The graphene samples preparation process was also discussed. Results of the testing were presented and analyzed and the conclusions are formulated, which are also included in the paper.

Keywords: Graphene, Joule heating, environmental chamber.

1 Introduction

Graphene is a crystalline allotrope of carbon with thickness of a single atomic layer that can be considered as 2-dimensional structure. Carbon atoms in graphene are densely packed in a regular sp^2 -bonded hexagonal pattern. As an electronic material, graphene is a semiconductor with closed energy gap. The most important parameters of graphene are high electron mobility, about $15\,000\text{ cm}^2\cdot\text{V}^{-1}\cdot\text{s}^{-1}$, with potential limit of $200\,000\text{ cm}^2\cdot\text{V}^{-1}\cdot\text{s}^{-1}$, electron concentration in the range of 2×10^{12} to $9\times 10^{12}\text{ cm}^{-2}$ and excellent thermal conductivity in room temperature which reaches the values of $(4.84 \pm 0.44) \times 10^3$ to $(5.30 \pm 0.48) \times 10^3\text{ W}\cdot\text{m}^{-1}\cdot\text{K}^{-1}$. This properties makes graphene the best conductor of heat and electricity ever known.

Joule heating (also known as resistive heating) is the process of releasing heat when electric current passes through the electric conductor. The amount of heat released in the process is described by Joule's Law of Heating and is proportional to the square of the electric current, the electrical resistance of conductor and time of current flow. In microscopic description, this phenomenon is caused by interactions between

charge carriers and ions of conductor material. Each time, when the charge carrier collides with the ion of conductor, its kinetic energy is transformed into thermal energy emitted by the conductor as Joule heat.

Infrared imaging was successfully used for investigations of thermal phenomena in various electronic systems and devices such as integrated circuits and diode lasers [1–3]. In the case of graphene transistors the method allowed to obtain the temperature distributions as well as carrier densities [4, 5]. The deterioration of temperature distribution uniformity due to various mechanical defects of the graphene layers was demonstrated [6]. The results indicated the need of graphene protection, especially in transparent heater applications. One of possible solutions to this problem is proposed in this work.

With high electron mobility and thermal conductivity of graphene, it is very interesting matter to study the phenomenon of Joule heating in graphene sample. In this work specially prepared bonded sample is investigated and infrared imaging is implemented to register temperature distributions during Joule-heating of the device. The use of environmental chamber allowed gathering of thermal maps in controllable conditions. Obtained results give interesting indications for further studies on graphene application in electronic devices.

2 Sample under Test

Graphene was synthesized by chemical vapor deposition (CVD) on Cu foil and transferred on glass substrate. Ohmic contacts to graphene were formed by using silver conductive paste. Graphene coated optical glass (rectangle) bonded with counter-specimen by NOA61 adhesive and then UV cured. The photograph of the specimen is shown in Fig. 1.

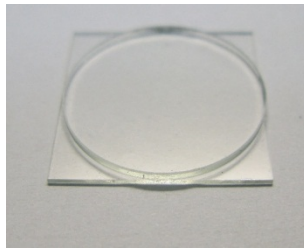


Fig. 1. A photograph of a sample under test

3 Environmental Chamber

For the purposes of performed investigation, special environmental chamber with stabilization system for temperature and humidity was designed. The schematic block diagram of the chamber is presented in Fig. 2. The chamber was made of poly(methyl methacrylate) commonly known as Plexiglas. The door of the chamber was sealed

with rubber seal. In the walls several holes were made for the wires of control system, which were sealed with silicone resin. For the performed experiment, special window made of polished silicon plate was created in the door of the chamber, which transmits the infrared emission from the sample. Investigated graphene samples were placed inside the chamber.

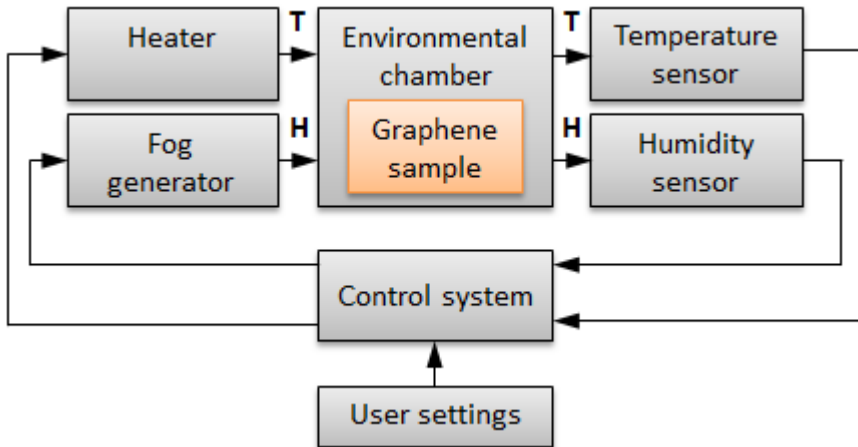


Fig. 2. Schematic block diagram of the environmental chamber, T – temperature, H – humidity

To control the process of stabilization of temperature and humidity, programmable PID controller APAR AR247 was used. The device includes PID controller module and both temperature and humidity sensors placed in one probe. The probe was placed inside the chamber, while controller module was placed outside, fixed to the wall of the chamber. The probe was connected to the module by wire running through the hole in one of the chamber's walls. Controller module allows user to set required values of temperature and humidity and shows actual values of these parameters in LCD display. For the temperature setting, resistive heater with fan was used and fog generator was used for changing humidity in the chamber. Both heater and fog generator were connected to the PID module.

Designed environmental chamber allows to obtain temperatures up to 80 °C with the accuracy of $\pm 0,5$ °C and humidity in the range of 20–80 %RH with the accuracy of ± 3 %RH (outside this range the accuracy of humidity setting is ± 5 %RH).

4 Experimental Technique

Experimental technique used in this work is infrared imaging. It is based on the analysis of the thermal radiation emitted by an object according to the Planck's blackbody radiation law. One of the radiometric quantities derived from this law is a spectral intensity M_c , which gives the power irradiated by a unit area of blackbody into a half space at the wavelength λ :

$$M_e(\lambda, T) = \left(\frac{2\pi^5 k^4}{15 \lambda^5} \right) \left[\exp\left(\frac{hc}{\lambda kT} \right) - 1 \right]^{-1} \quad (1)$$

where k is the Boltzmann's constant, and T is absolute temperature. The radiation of a real object is usually lower than M_e and depends on the object's emissivity, $\varepsilon(\lambda)$. In the case of single graphene layer the emissivity value $\varepsilon = (1.6 \pm 0.8)\%$ can be expected [4]. In our experiment, however, the object under test is more complex than a single layer graphene on a glass substrate and the precise temperature calibration is needed in order to obtain quantitative temperature data.

Thermographic experiments have been performed using InSb 640 M camera (Thermosensorik/DCG Systems). Camera detection range 1.1–4.9 μm was restricted to 3.0–4.9 μm using filters. A wide-field lens with the focal length of 28 mm was used. The sample was placed in the environmental chamber during the experiments and supplied with power using voltage source. The schematic of electrical connections provided to the sample is shown in Fig. 3.

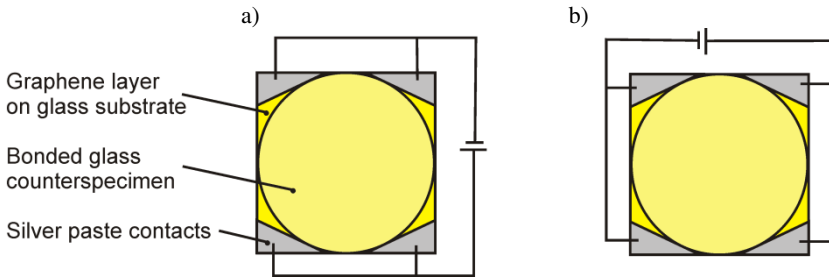


Fig. 3. Schematic view of the electrical connections of the graphene sample during the experiment

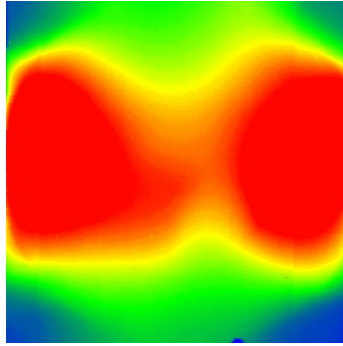
Temperature calibration was performed for a non-biased device at environmental chamber's temperature stabilized in the range 22–50 $^{\circ}\text{C}$. For each temperature setting a thermal image of the device was captured with the camera. The calibration data approximated by third-order polynomial was used to recalculate the camera counts to temperature.

5 Results

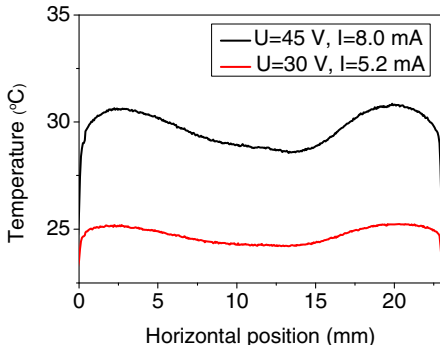
The results of thermographic characterization for a Joule heated bonded sample are shown in Fig. 4. The electrical connections to the sample are in this case configured as in Fig. 3a. The thermal map (Fig. 4a) reveals quite uniform hot areas without significant hot-spots. The horizontal and vertical cross-sections through the middle of the sample recalculated to temperature are presented in Fig. 4b and c. The temperature of the glass cover plate exceeds 30 $^{\circ}\text{C}$ for $I = 8$ mA and $V = 45$ V. The results show that the graphene layer operates well as transparent heater in the bonded sample

configuration. The obtained temperature distribution is a result of a current flow in graphene layer with contacts deposited at the corners of the sample.

a)



b)



c)

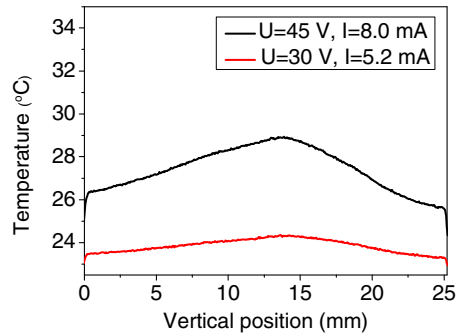


Fig. 4. (a) Thermal image for a bonded graphene sample biased with $I = 8.0$ mA and $U = 45$ V biased according to the schematic shown in Fig. 3a; horizontal (b) and vertical (c) cross-sections for two supply power levels

In order to better elucidate this effect the electrical connections were provided to another electrode pair, as shown in Fig. 3b. Resulting thermal map and temperature cross-sections are shown in Fig. 5. Most possibly, non symmetrical silver paste contacts shape made contribution to stronger Joule-heating at one-side of the sample.

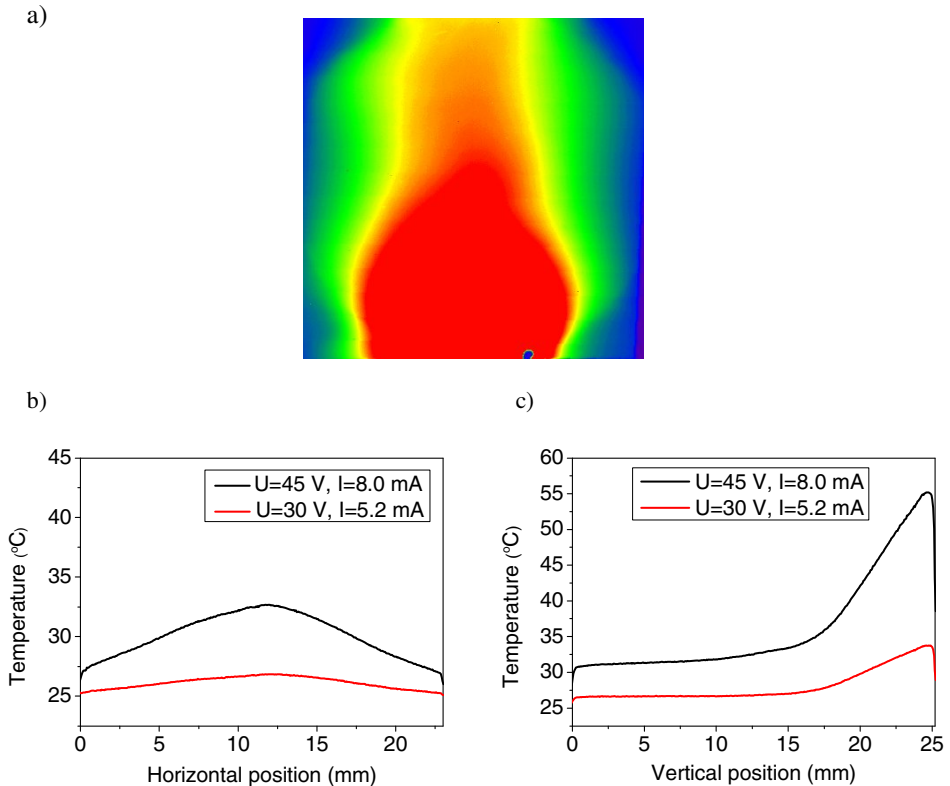


Fig. 5. (a) Thermal image for a bonded graphene sample biased with $I = 8.0$ mA and $U = 45$ V according to the schematic shown in Fig. 3b; horizontal (b) and vertical (c) cross-sections for two supply power levels

6 Conclusions

Analysis of thermal properties of Joule-heated sample with graphene layer was presented. Specially designed environmental chamber allowed to perform the experiments in stabilized conditions. Thanks to the use of the chamber an uniform external heating of the sample was possible allowing the precise temperature calibration for infrared imaging method. The temperature distributions of Joule-heated sample in various bias conditions were obtained. Presented results demonstrate how heat emission from graphene can be influenced by the complex electrode shape.

Acknowledgements. This work was supported by the Polish National Center for Research and Development under the project no GRAF-TECH/NCBiR/06/30/2012.

References

1. Breitenstein, O., Langenkamp, M., Altmann, F., Katzer, D., Lindner, A., Eggers, H.: Microscopic lock-in thermography investigation of leakage sites in integrated circuits. *Rev. Sci. Instrum.* 71, 4155–4159 (2000)
2. Małag, A., Dąbrowska, E., Teodorczyk, M., et al.: Asymmetric Heterostructure With Reduced Distance from Active Region to Heatsink for 810-nm Range High-Power Laser Diodes. *IEEE J. Quant. Electron.* 48(4), 465–471 (2012)
3. Kozłowska, A., Wawrzyniak, P., Małag, A., et al.: Reliability Screening of Di-ode Lasers by Multispectral Infrared Imaging. *J. Appl. Physics* 99(5), 053101-1-053106 (2006)
4. Freitag, M., Chiu, H.Y., Steiner, M., Perebeinos, V., Avouris, P.: Thermal infra-red emission from biased graphene. *Nature Nanotechnology* 5, 497–501 (2010)
5. Luxmoore, I. J., Adlem, C., Poole, T., Lawton, L.M., Mahlmeiter, N.H.: Thermal emission from large area chemical vapor deposited graphene devices. *Appl. Phys. Lett.* 103 131903-1–131906 (2013)
6. Kozłowska, A., Gawlik, G., Szewczyk, R., Piątkowska, A., Krajewska, A.: Infra-red Thermal Emission from Joule-Heated Graphene with Defects. In: *Conference Materials of Asia Communications and Photonics Conference, Optical Materials and Novel Devices (ATh4B)*, Shanghai China, November 11-14 (2014)

Surface Electromyography Amplifier with High Environmental Interference Resistance

Tomasz Mańkowski, Jakub Tomczyński, and Piotr Kaczmarek

Poznan University of Technology,
Institute of Control and Information Engineering, Poznań, Poland
{jakub.l.tomczynski,tomasz.pr.mankowski}@doctorate.put.poznan.pl,
piotr.kaczmarek@put.poznan.pl
<http://www.cie.put.poznan.pl>

Abstract. In this paper design of a miniature, low cost surface electromyography amplifier is proposed. Presented device can be considered to be resistant to common environmental interferences. Proposed design consists of main amplifier board and second board containing DRL circuit and reference voltage source. Major disturbance is provided by mains (50/60 Hz) - most emphasized interference in this paper. Design includes appropriate set of filtration circuits. Moreover comparison with four commercial and hobbyist devices is provided.

Keywords: sEMG, amplifier, electromyography, DRL, interference.

1 Introduction

1.1 Problem Statement

Design of an EMG/ECG amplifier is an interest of many researchers, has very long history and is considered to be well researched and described. However every constructor takes a slightly different approach to protecting measured signals from environmental interferences.

E.M.Spinelli et. al [19] put emphasis on proper AC-coupling of the design, leveling out electrode offset potentials and leading to an increase in common mode rejection ratio. Y.Shimomura et. al. [18] used double differential technique to minimize crosstalk and raise CMRR. All these approaches cause boost in interference resistance, providing that it occurs in both differential channels. Hao Li et. al [10] suggest active filtering using a notch filter targeted at mains frequency. This approach, however, affects acquired signal and can lead to misinterpretation in further signal analysis.

In this paper design of an environmental interference resistant surface electromyography (sEMG) amplifier, further called "CIE-sEMG", is described (section 2). Presented module is a part of a multi-channel, portable sEMG acquisition system intended as human-machine interface device. Properly prepared set of amplifiers provides wide spectrum of possibilities in EMG signal analysis and interpretation. This can lead to development of a flexible controller for computer, games and even tasks of driving prosthetic limbs or mobile robots.

The possibility of using the module to control electromechanical devices outside the laboratory environment requires resistance to environmental interference including mains interference. In the present paper the amplifier's mains interference resistance is investigated and the results are compared with other commercial and hobbyist's devices available at Poznan University of Technology (section 3.2).

1.2 Physiological Background

Electromyography (EMG) is a technique of measuring and assessment of skeletal muscles activity. Nowadays intramuscular and surface electromyography is successfully used in evaluation of human muscle activity and its disorders [2]. The EMG is generated by electrical activity of muscle fibers associated with muscle contraction process [4]. Electrical activation of muscle fiber is an effect of subsequent depolarization and repolarization of its membrane which propagate along muscle fiber. This phenomenon is called action potential (AP) and it is a trigger signal generating a fiber contraction [12]. Action potentials have discrete character and evoke a fiber contraction lasting 30-100 ms. AP is generated by neuronal or electrical stimulation of motor end-plate. Increase of contraction force is caused by recruitment of subsequent motor units (MUs - synchronously activated group of muscle fibers) or increase of activation frequency of particular MUs [16]. This phenomenon, can be measured using differential bipolar pair of surface electrodes located along muscle fibers. In fact recorded EMG is a superposition of many asynchronously activated MUs[8]. sEMG frequency range falls between 6 to 400 Hz, whereas maximum power is recorded in band of 20-150 Hz [15].

1.3 Environmental Interferences in Electromyography

Recorded signal quality can be degraded by several factors. The contamination may come from imperfections of used measurement method or from shortcomings of equipment used to perform recordings. Contaminants caused by measurement method itself can be further classified into several main categories including electrocardiogram (ECG) crosstalk, general muscle crosstalk, and movement artifacts [6].

ECG crosstalk may occur when recording muscle activity from torso, with electrodes placed near heart, due to relatively high electric activity of heart muscles [7], [17].

Due to skin conductivity, voltage measured at skin surface is a superposition of several muscles activity, which introduces muscle crosstalk, further influenced by size of the electrodes. Movement artifact is generated when muscles move underneath skin surface or when force generated by the muscle causes movement at the electrode-skin contact point[3].

Shortcomings of used equipment include varying impedance at electrode-skin barrier, causing a drop in measured signal levels. Amplifiers used in EMG measurement also introduce a number of artifacts, due to their non-flat frequency

response and non-linear phase shift, together with susceptibility to EMF interference generated by appliances operating nearby.

The most significant contaminant is mains frequency (50 or 60 Hz, depending on country) [3], [5], which falls into the middle of EMG frequency range, thus cannot be simply filtered out. Therefore, the minimization of mains interference should be considered as one of the crucial goals in EMG amplifier design process.

Mains interference resistance can be increased in several ways. One of them is using a Driven-Right-Leg (DRL) circuit. Basic EMG amplifiers drive reference electrode with constant voltage, which positions the instrumentation amplifier in proper operating point. Properly implemented DRL circuit feeds the reference electrode with amplified, inverted common mode signal from the differential electrodes. This method has been long used in electromyography, and while efficient in eliminating common mode interference, it can produce unpredictable results during exposure to differential interference [9]. Other important factors include electrical design properties such as proper device and cable shielding and optimal PCB layout.

Higher frequency interference, coming from voltage converters or radio communication, although does not affect the EMG signal directly, may cause other negative effects such as amplifier saturation.

Perfecting the measurement equipment may minimize errors caused by its shortcomings. Eliminating artifacts caused by the measurement method itself, however, can only be done using techniques that would filter out the artifacts, leaving desirable signal possibly unaffected. This can be accomplished by using either hardware filters or further, post-acquisition signal processing.

2 CIE-sEMG Amplifier Design

Proposed design of a bipolar sEMG amplifier consists of a two stage miniature amplifier board intended to be used as a part of multichannel acquisition system and a DRL&Ref board used as reference voltage source and DRL signal driver. In multichannel system the DRL&Ref module is shared among all amplifiers.

The amplifier module has undergone miniaturization process sufficient to place it directly over one of the electrodes, while the second one is connected with a short, shielded cable. Various researchers have shown designs with driven shield, where signal from each of the electrodes is buffered and returned to their respective shielding [14], [13] or where common mode signal is applied to both shields [1]. However, with proposed design, no signal quality improvement was observed in comparison to ground shielding, probably due to exceptionally low length of electrode cables. Because of this, driven shielding has been dropped.

The first amplification stage consists of Texas Instruments INA326 precision instrumentation amplifier (Fig. 1). Using this integrated circuit helps minimize susceptibility to EMF interference, while retaining ability to extract common mode signal, necessary to feed the DRL electrode. Inputs of the amplifier are protected against electrostatic discharge using ESD suppressor diodes. Input signals are passed through a first order low-pass passive filter with cutoff frequency

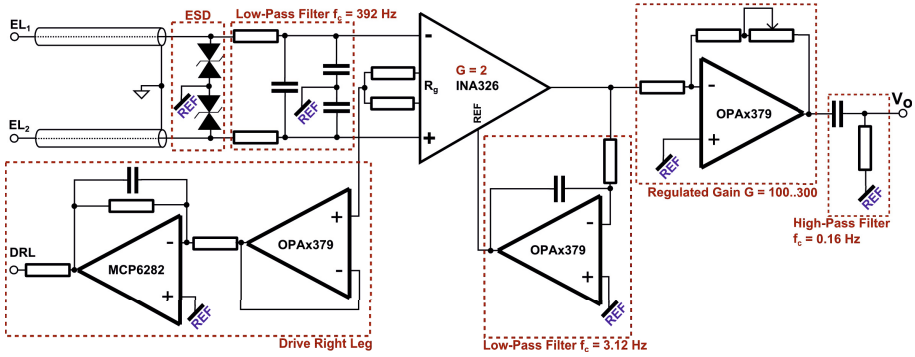


Fig. 1. Surface electromyography amplifier - proposed circuit

392 Hz, to suppress high-frequency interferences above useful EMG bandwidth. Amplifier gain is set to 2. Output reference terminal (REF) is used to create a negative low pass feedback with cutoff frequency 3.12 Hz. Subtracting low frequencies from signal helps prevent saturation of the instrumentation amplifier. This configuration effectively creates a high pass filter, which additionally eliminates majority of movement artifacts.

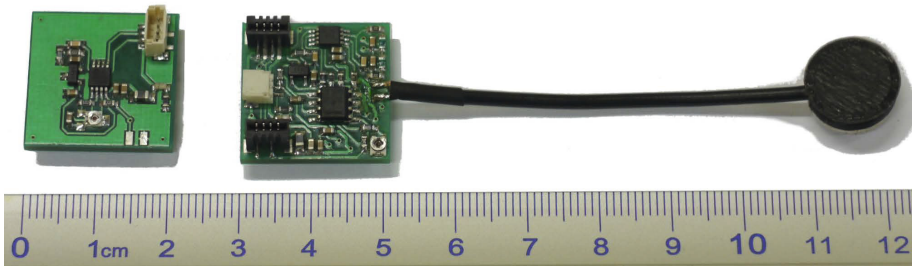


Fig. 2. Surface electromyography amplifier outlook; Left - DRL&Ref module; Right - main amplifier board

The second stage of CIE-sEMG module is based on Texas Instruments OPA2379 operational amplifier, with gain adjustable from 100 to 300, resulting in 200 to 600 total amplifier gain. Output DC offset is set at V_{REF} using a passive high-pass filter with cutoff frequency 0.16 Hz.

A separate DRL&Ref module consists of a reference voltage source, which sets operating point of all amplifiers at a common level $V_{REF} = 1.5$ V, and the second stage of DRL circuit. Common mode signals coming from all connected CIE-sEMG modules are summed and fed into the DRL electrode.

3 Environmental Interference Resistance Performance

3.1 Methods

In order to evaluate CIE-sEMG's resistance to interference, several commercially available EMG acquisition solutions were taken into account in the course of performed tests. As a reference, MEBA amplifier manufactured by OT Bioelettronica was used. MEBA is a 32-channel professional desktop amplifier, allowing for acquisition of various bioelectrical signals. The tests also included single channel μ EMG, a portable EMG acquisition device with integrated memory card storage interface, also manufactured by OT Bioelettronica. For additional comparison, a low-cost hobbyist's solution by Olimex, EKG-EMG-SHIELD (EES) was tested. EES is designed to operate as an Arduino add-on, allowing hobbyists to incorporate EKG or EMG activity measurement into their designs.

Table 1. Comparison of EMG amplifiers' parameters; ^acommercial product; ^badvanced DRL with input and output DRL; ^c12-bit ADC was used; ^dsampling frequency of 5 kHz was used; ^euser-adjustable sampling frequency

	CIE-sEMG	MEBA	μ EMG	EKG-EMG-SHIELD
Channels max	tested up to 7	32	1	stackable up to 6
Type	portable	desktop ^a	portable ^a	portable
DRL	+	+ ^b	-	-
Case type	no	metal	plastic	no
Cable shield	+	+	+	-
Instrumental Amplifier	INA326	-	INA333	INA321
CMRR [dB]	100	-	100	90
Noise at 1kHz[nV/rt(Hz)]	33	-	50	100
Bandwidth(-3dB)[kHz]	1	-	3.5	50
ADC [bits]	- ^c	12	8	- ^c
Mains noise notch filter	-	-	-	-
Sampling frequency [kHz]	- ^d	5 ^e	1	- ^d

All signals were acquired using a set of adhesive disposable Ag/AgCl electrodes. The differential electrodes were placed over extensor carpi radialis longus muscle. The DRL electrode was placed under the wrist, over wrist flexor tendons. During tests performed with MEBA amplifier, two additional wet strap electrodes were used, providing connection for 'Reference' and 'DRL in' signals. The electrodes were placed beside the DRL electrode and on the opposite wrist, respectively. All tested amplifiers were placed as close to the electrodes as possible, except for MEBA amplifier, where only the first active stage of signal path could be placed near the electrodes.

Signals amplified by EES and CIE-sEMG were recorded using auxiliary inputs of MEBA amplifier. All signals were sampled at 5 kHz. Due to lack of analog output in μ EMG, its results were captured to a memory card, sampled at 1 kHz.

To evaluate amplifiers' susceptibility to interference, an AC motor was used as the source of EMF field. Throughout the tests, periods of idle noise were captured during muscle relaxation at various distances from interference source. At each distance, EMF field intensity was measured using a triaxial ELF magnetic field meter TM-192 sensitive to frequencies ranging from 30 to 2000 Hz [20]. The resultant magnitude was used as a measured value of EMF intensity. The tests were performed for EMF values ranged from 0.04 to 120 μT , where reference levels for general public exposure to electric and magnetic fields in frequency range 25-400 Hz recommended by ICNIRP is 200 μT [11].

The EMG amplifiers' performances were compared with respect to signal-to-noise ratio (SNR). First, a desired EMG signal power was evaluated for each amplifier during stress ball squeezing exercise. The tests were performed with interference source turned off. Then, for each amplifier and set of selected EMF intensities background noise was recorded and SNR values were calculated.

3.2 Results

Frequency Response. As mentioned in section 1.3, easiest to reject are those interferences which can be cut out by means of simple analog filtration. Proposed amplifier design incorporates a few filters which band pass only frequencies of highest EMG activity. Adequate test was performed to confirm theoretical values of rejection.

Amplifier's response to a series of sinusoidal inputs was captured in order to obtain Bode magnitude plot - Fig. 3. The input frequency ranged between 0.5 Hz and 2.2 kHz.

Band pass of proposed amplifier is between 3.3 Hz and 330 Hz which covers most of the EMG signal frequency range. Although the design performs properly in rejecting muscle/electrode movement and high frequency interferences, mains, the most significant source of interference remains unfiltered.

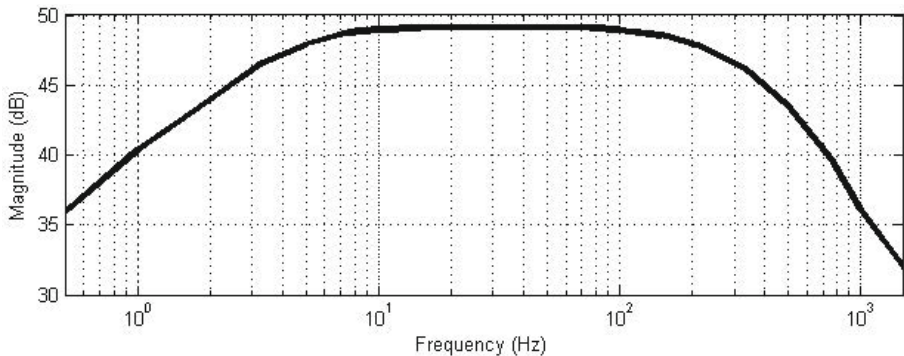


Fig. 3. Proposed design's Bode magnitude plot

Mains Interference Resistance. Achieved results are shown in Fig. 4. It can be seen that when interference source was turned off the best performance was obtained with μ EMG which is 8.7 dB higher than MEBA device, while CIE-sEMG had SNR ratio 12.7 dB lower than the referenced value.

For intermediate noise level of $48 \mu\text{T}$, a rapid SNR value decrease was observed in case of MEBA (a fall of 20.9 dB), μ EMG (31.6 dB) and EES (28.3 dB), while for CIE-sEMG the change was significantly lower - 5.2 dB. The SNR level is slightly higher for CIE-sEMG, and similar to those estimated for MEBA and μ EMG (CIE-sEMG 3.0 dB higher, μ EMG 2.1 dB lower than MEBA). The SNR for EES is the lowest among the tested devices (21.3 dB lower than reference).

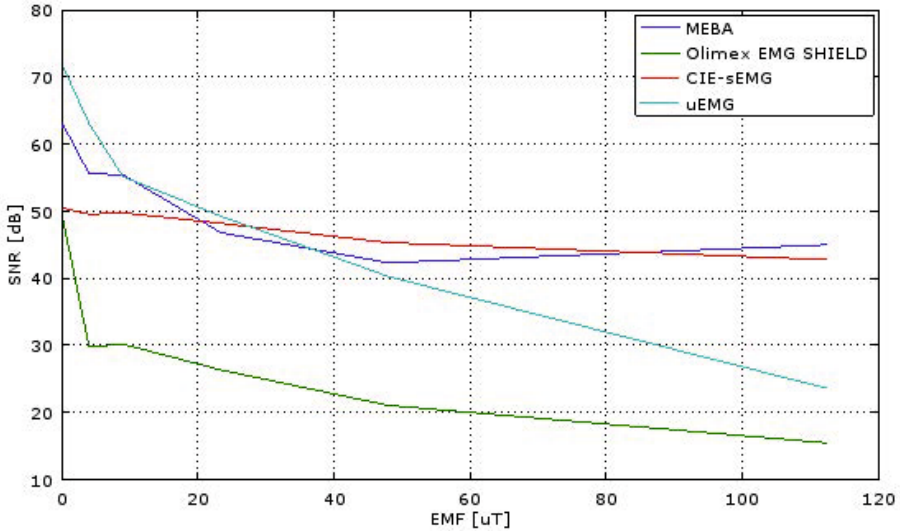


Fig. 4. Signal-to-noise ratios as function of EMF intensity in mains interference resistance test

In case of strong interference ($120 \mu\text{T}$), the SNR levels for CIE-sEMG and MEBA are similar to those recorded during intermediate interference, while the SNR for μ EMG and EES decreased greatly (respectively 21.4 and 29.5 dB lower than MEBA's SNR value).

It can be observed that the relative change of SNR induced by increase of EMF interference is the lowest for CIE-sEMG device (7.7 dB) and is the highest for μ EMG (48.3 dB decrease).

4 Discussion and Conclusions

In low-EMF conditions, worse performance of CIE-sEMG and EES designs is probably determined mostly by ADC converter properties. It should be stressed

that although all devices use high quality instrumental amplifiers, they can be a potential source of background noise. However, their parameters (such as amplifier noise and CMNR) which could strongly influence the SNR level have similar values (table 1). Thus obtained SNR values can not be explained by difference in amplifier parameters. In case of CIE-sEMG and EES amplifiers the EMG signal was digitized using general purpose multiplexed 12-bit ADC available in the MEBA device, which is dedicated to record the auxiliary analog inputs. To record EMG signal, the MEBA amplifier has set of separate high quality, not multiplexed, 12-bit ADCs, while the μ EMG has an integrated 8-bit ADC. It is very likely that the 8-bit ADC converter has a lower quantization noise than 12-bit one of similar class. Thus the absolute SNR values obtained for μ EMG cannot be strictly compared with the other devices. Moreover in this case the higher SNR for 8-bit ADC does not denote the better signal quality compared to 12-bit ADC.

With proposed design, signal-to-noise ratios have similar values to reference desktop amplifier for medium and high level of mains interference. Moreover, for these devices SNR decrease with increase of EMF intensity is significantly lower than for the other amplifiers. Most likely this is due to DRL circuit which compensates the common mode noise of the input signal. The DRL is used by CIE-sEMG and MEBA devices, while the others use constant-voltage reference signal. The worst parameters of EES device can be credited to long, unshielded wires between the module and all electrodes. In contrast, μ EMG was located directly over the reference electrode and the CIE-sEMG was placed directly over one of EMG electrodes, providing signal paths as short as possible.

Proposed design offers a promising solution in various myopotential acquisition applications. In terms of electromagnetic field interference resistance, it performs comparably to a reference desktop, commercial amplifier design, which utilizes two additional electrodes for improved noise removal. Filters used in the design proved to be effective in basic elimination of movement artifacts and protecting the amplifier against saturation, while maintaining necessary EMG bandwidth. Active DRL system, not available in open-source EES and μ EMG, has proven its worth as the best method of mains interference elimination.

Provided guidelines of amplifier design can be successfully used in developing a trustworthy sEMG acquisition system. This set of rules, while seemingly basic and easy to implement, proved to be crucial in achieving desired amplifier performance.

References

1. Liu, C., Wang, X.: Development of the system to detect and process Electromyogram signals. *IEEE Int. Conf. of the Eng. IEEE Int. Conf. of the Eng. in Med. and Biol. Soc.* 6627–6630 (2006)
2. Cram, J.R.: The History of Surface Electromyography. *Appl. Psychophysiology and Biofeedback* 28(2), 81–91 (2003)
3. De Luca, C.J., Gilmore, L.D., Kuznetsov, M., Roy, S.H.: Filtering the surface EMG signal: Movement artifact and baseline noise contamination. *J. Biomech.* 43(8), 1573–1579 (2010)

4. Devanandan, M.S., Eccles, R.M., Westerman, R.A.: Single motor units of mammalian muscle. *J. Physiol.* 178(2), 359–367 (1965)
5. Fraser, G.D., Chan, A.D.C., Green, J.R., Abser, N., MacIsaac, D.: CleanEMG - Power line interference estimation in sEMG using an adaptive least squares algorithm. *Conf. Proc. IEEE Eng. Med. Biol. Soc.*, 7941–7944 (2011)
6. Fraser, G.D., Chan, A.D.C., Green, J.R., MacIsaac, D.T.: Automated Biosignal Quality Analysis for Electromyography Using a One-Class Support Vector Machine. *IEEE Trans. on Instr. and Meas.* 99, 1–11 (2014)
7. Fraser, G.D., Chan, A.D.C., Green, J.R., MacIsaac, D.T.: Biosignal quality analysis of surface EMG using a correlation coefficient test for normality. In: *IEEE Int. Symp. on Med. Meas. and Appl. Proc.*, pp. 196–200 (2013)
8. Fuglevand, A.J., Winter, D.A., Patla, A.E., Stashuk, D.: Detection of motor unit action potentials with surface electrodes: influence of electrode size and spacing. *Biol. Cybern.* 67(2), 143–153 (1992)
9. Gomez-Clapers, J., Serrano-Finetti, J., Casanella, E., Pallas-Areny, R., R.: Can Driven-Right-Leg Circuits Increase Interference in ECG Amplifiers? In: *33rd Ann. Int. Conf. of the IEEE EMBS* (2011)
10. Li, H., Xu, S., Yang, P., Chen, L.: A Research and Design on Surface EMG Amplifier. *Int. Conf. on Meas. Tech. and Mech. Autom.* 1, 306–309 (2010)
11. International Commission on Non-Ionizing Radiation Protection: Guidelines for limiting exposure to time-varying electric and magnetic fields (1 Hz - 100 kHz). *Health Physics* 99(6) (2010)
12. Konrad, P.: *The ABC of EMG: A Practical Introduction to Kinesiological Electromyography*. Scottsdale (2005)
13. Matsuzaka, Y., Ichihara, T., Abe, T., Mushiake, H.: Bio-amplifier with Driven Shield Inputs to Reduce Electrical Noise and its Application to Laboratory Teaching of Electrophysiology. *J. Undergrad. Neurosci. Educ.* 10(2), 118–124 (2012)
14. Merritt, C.R., Nagle, H.T., Grant, E.: Fabric-based active electrode design and fabrication for health monitoring clothing. *IEEE Trans. Inf. Technol. Biomed.* 13(2), 274–280 (2009)
15. Moritani, T., Muro, M.: Motor unit activity and surface electromyogram power spectrum during increasing force of contraction. *Eur. J. Appl. Physiol. Occup. Physiol.* 56(3), 260–265 (1987)
16. Moritani, T., Stegeman, D., Marletti, R.: Basic Physiology and Biophysics of EMG Signal Generation. In: Merletti, R., Parker, P. (eds.) *Electromyography: Physiology, Engineering, and Non-Invasive Applications*. Wiley (2004)
17. Redfern, M.S., Hughes, R.E., Chaffin, D.B.: High-pass filtering to remove electrocardiographic interference from torso EMG recordings. *Clinical Biomechanics* 8(1), 44–48 (1993)
18. Shimomura, Y., Iwanaga, K., Harada, H., Katsuura, T.: Evaluation and design of a small portable EMG amplifier with potential RMS output. *Appl. Human Sci.* 18(2), 61–67 (1999)
19. Spinelli, E.M., Pallás-Areny, R., Mayosky, M.A.: AC-Coupled Front-End for Biopotential Measurements. *IEEE Trans. on Biomed. Eng.* 50(3) (2003)
20. Tenmars Electronics, C.: LTD: TM-192 TM-192D 3-axis EMF Meter, <http://www.tenmars.com/web1s-en-us/TM-192TM-192D.html> (accessed November 6, 2014)

Electromagnetic Protection in High Precision Tri-axial Thermometric AC Bridge

Aleksander A. Mikhal¹ and Zygmunt L. Warsza²

¹ Institute of Electrodynamics, National Academy of Science of Ukraine, Kiev, Ukraine

² Industrial Research Institute of Automation and Measurement (PIAP) Warszawa,
zlw@op.pl

Abstract. The effective protection against electromagnetic influences in the measuring circuit of thermometric AC bridges is discussed. The equivalent AC circuit of the SPRT sensor when connected to the bridge is discussed. The capacitance C of the connection cable and output capacitance of the bridge inductive divider can change impedance of this circuit from the serial RL to parallel RC one. The tangent of the impedance phase angle as a criterion of the type of equivalent circuit is proposed. The precision AC thermometric bridge with the double shielding technique is designed. Bifilar connections by two-axial concentric cables with two shields and equipotential protection is used. Circuit is automatically balanced and has advantages of the coaxial bridges and the equipotential protection. The term tri-axial bridge is proposed for it. The detail analysis of this automatically balanced circuit resulted on its high immunity to interferences and over 100 times smaller impact of the capacitive leakage. The efficiency of solution is verified experimentally in a few high accuracy (10^{-7} – 10^{-8}) AC bridges.

Keywords: standard platinum resistance thermometer SPRT, equivalent circuit, coaxial bridge, double shielding technique, tri-axial bridge.

1 Introduction

The laboratory posts of standard temperature control points, maintained by NMI and other metrological and research laboratories, as the rule, are now equipped with a 6–8 decades AC automatic transformer bridges and standard platinum resistance thermometers (SPRT). High precise measurements of temperature in a wide range (-260 – 1100) °C are obtained. To measure the relative changes of the SPRT resistance these AC bridges should have the relative error of the order of 0.1–0.01 ppm – see e.g. data of some actually offered the high precision thermometric bridges in [8].

The main unit of the AC bridge is a inductive coupling voltage divider (IVD). It defines the metrological characteristics of the AC bridge and also its errors and non-linearity. When a multi-stage transformer is used we can get the large input impedance of IVD operating on the low frequency. As a result the non-linearity (integral and differential error) of the AC bridge measurement circuit becomes comparable to the value of LSB or less. Analysis of the properties of the basic schemes of bridges

has been reported in [1–5, 8–10]. Further improvement of the accuracy and resolution of bridges is associated with a reduction of the influence of the noise and parasitic shunting admittances. To solve this problem, there are solutions associated with the narrowing of the bandwidth, the stabilization of the environment temperature and use of operational amplifiers with optimal noise parameters of voltage and current. The capabilities of these methods are now practically exhausted. Another option is the structural and constructive methods. The design of modern high-precision instrument should provide high noise immunity and protect from the impact of spurious signals due to electric and magnetic fields, as well as from leakage currents.

To reduce the magnetic coupling in circuit of any measuring device it is necessary to minimize the effective area of signal loops. Structurally, this is achieved through the use of twisted-pair wires and coaxial cables. Then magnetic fields of the forward and reverse current compensate each other. Bridges of circuits with coaxial elements are called coaxial bridges. Their theory and use is described in detail in [2, 3].

However in the most precision AC bridges the normal shielding method is not satisfactory enough. The equipotential protection and a special coaxial cable, called the tri-axial cable is used [5, Fig. 3.16]. This cable connects the bridge measuring circuit and the detector of its balance. Its second internal shield is connected to a source of the protective voltage. In the monograph [5] only the principle of such protection in the most general form is given. Methods for the formation of protective voltage and modes of operation are not specified.

The main purpose of this paper is to identify in detail circuit operating and shielding problems of the automatic AC bridge. The thermometric precision AC bridge with the inductive voltage divider (IVD) was the object of this study. The option, how to generate the voltage protection for inner shield of the tri-axial cable, is also described.

2 AC Equivalent Circuit of SPRT Sensor

Tested temperatures are obtained indirectly through measurement the resistance of the SPRT sensor. To understand the AC bridge circuit balancing process and its protection from electromagnetic influences, the equivalent circuit of SPRT sensor is needed. In AC circuit it is a complex impedance Z with four leads of resistances r_1 – r_4 and parallel equivalent capacitances C_1 , C_2 of the bridge circuit and connection cables, all shown together in Fig. 1a. Parameters of this scheme depend on many factors. This complicates the automation of the balancing process and calibration procedure of the bridge. The detail knowledge about that is very useful for designers and users.

Overall analysis of the circuit from Fig. 1a is made in [6] and [7]. It was found that with an acceptable error (0.1–0.01) ppm it is possible to use successfully the simplified model of the equivalent circuit given in Figure 1b. The total parasitic capacitance $C = C_1 + C_2$ takes into account capacities on both the current and voltage bridge terminals. Stray capacitance is determined by the length of the cable and by the capacitance between the turns of the IVD. In some laboratories, the distance between the bridge and thermostats of temperature reference points is 5–30 m long. Therefore, the capacity of the cable can be in the range of 500 pF to (3–5) nF. Output capacity of

IVD with the strong inductive coupling can reach (1.5–2) nF. It is determined by the density of twisting the wirings from which IVD is made.

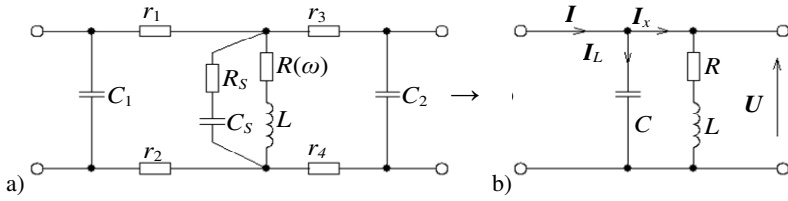


Fig. 1. Equivalent AC circuits of SPRT sensor connected to the bridge: a – full circuit, b – simplified version; $R(\omega)$ and L elements takes into account the skin effect [6] and inductance of the SPRT, R_S , C_S – lumped shunting resistance and capacitance at high temperatures [7]; r_1 – r_4 – lead resistances; C_1 , C_2 – capacitances of cable and bridge in current and voltage circuits

The problem: how capacitances C effect the measurement result should be analyzed. The simplified model of the circuit of SPRT sensor, when is connected to the bridge terminals, given in fig.1b will be used. The equivalent impedance Z_x of that circuit can be expressed as

$$Z_x = \frac{R}{(1 - \omega^2 LC)^2 + \omega^2 R^2 C^2} + j\omega \frac{L - R^2 C - \omega^2 L^2 C}{(1 - \omega^2 LC)^2 + \omega^2 R^2 C^2} \equiv R_x + j\omega L_x \quad (1)$$

Components of this formula with the parameter ω^2 are much less than unity and can be neglected. After this simplification we obtain Z_x expressed as

$$Z_x \approx R + j\omega (L - R^2 C) \quad (2)$$

The ratio of the active and reactive components of Z_x is tangent of its phase angle φ

$$\operatorname{tg} \varphi = \frac{\operatorname{Im}(Z_x)}{\operatorname{Re}(Z_x)} = \frac{\omega (L - R^2 C)}{R} \quad (3)$$

From formula (3) and Fig. 1b two such conclusions follow:

- for $L > R^2 C$ we have $\operatorname{tg} \varphi > 0$, i.e. the reactive component of Z_x is inductive and the equivalent circuit can be of the structure of two RL elements in series;
- for $L < R^2 C$, $\operatorname{tg} \varphi < 0$, i.e. the reactive component is capacitive and the equivalent circuit can be better represented by two parallelly connected RC elements.

Therefore, the change of $\operatorname{tg} \varphi$ sign is the criterion of the equivalent scheme transition.

3 Experimental Data of SPRT Sensor

The main AC characteristics of the platinum thermal resistance sensors were measured. In experiment the precision SPRT sensor and industrial sensors are tested. Some obtained parameters of the serial RL equivalent circuit are given in Table 1.

Table 1. Measured parameters of three temperature sensors at $f = 100$ Hz

Parameters	Type of SPRT ¹		
	TCPH-5V (TCIIH-5B)	PTS-10M (ИТС-10М)	VTS (Рус. BTC)
$R_{r,0}(0^{\circ}\text{C})$	100 ohm	10 ohm	0.6 ohm
$\text{tg}\varphi$	0.00052	0.00034	0.0013
L/C	90 μH	29 nH/ 19 nF	1.3 μH

In the second experiment to current terminals of each sensor the additional parallel capacitor C_E was connected – see Fig. 2. Values of $\text{tg}\varphi$ at different capacitances C_E were measured. For all above sensors the common general trend is existing. If the additional capacity is increased then the parameter $\text{tg}\varphi$ will decrease. Change in the sign of $\text{tg}\varphi$ for all types of temperature sensors is observed, which occurs in the range of parasitic capacitance (500–2000) pF. Experimental results confirmed theoretical considerations.

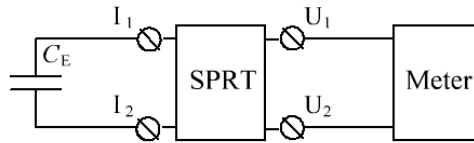


Fig. 2. Simplified circuit of $\text{tg}\varphi$ measurements

4 Selecting the Structure of AC Bridge Circuit

Figure 3 shows a generalized diagram of the AC bridge measuring circuit.

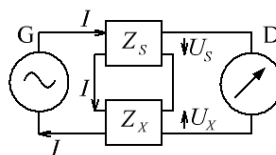


Fig. 3. Generalized block diagram of the bridge

The block diagram in Fig. 3 consists the AC generator G, two branches: the branch of the variable reference measures Z_S and of the object Z_X and the balance detector D.

¹ All tested types of SPRT sensors are made by company "Etalon" in Vladimir, Russia, i.e.:
 - High temperature resistance thermometer WTS (BTC): range (692.73–1358) K, length 675 mm, outer diameter 8 mm, sensing element – platinum PL0 wire diameter 4 mm, weight 110 g
 - Model PTS-10M (Рус. ИТС-10М): range (90–273.15) K – type A, range (273.15–903.9) K – type B, length 658 mm, outer diameter 6.3 mm, the sensing element – platinum PL0 wire diameter 0.1 mm, weight 150 g.
 - Low-temperature model TCPH-5V (Рус. TCIIH-5B): range (3.81–273.15) K, length 39 mm, an outer diameter of 3.7 mm, weight 2 g.

Both branches are presented as two-ports and their inputs and outputs are connected in series. The detector D controls the difference of output voltages. Its output signal is used for automatic adjustment of the value of Z_S components to obtain the balance of the bridge: $U_S - U_X = 0$. Then in the balance voltages on branch outputs have opposite signs. Branches have the following coefficients of transmission (transmittances):

$$Z_S = U_S / I = Z_{mS} \Psi_1(p_S, q_S) \quad (4)$$

$$Z_X = U_X / I = Z_{mX} \Psi_1(p_X, q_X) \quad (5)$$

where: Z_{mS} and Z_{mX} – the normalized parameters of the object and measure branches; Ψ_1 and Ψ_2 – characteristic functions in complex numbers of both above branches; p_S , q_S , and p_X , q_X – normalized values of two adjustable and two measured parameters.

To get the best performance of AC bridges a number of requirements is necessary to satisfied [7, 8], i.e.:

- A) Ability to obtain the circuit balance separately for active and reactive component.
- B) The sensitivity of the measuring circuit should be constant.
- C) Lack of mutual influence of control loops for active and reactive parameters.

This is possible when the characteristic functions Ψ_1 of the branch of measures and Ψ_2 of the object branch will be isomorphic with respect to each other. The simplest form of these functions is preferable, for example:

$$\Psi(p, q) = p + j \frac{\omega}{\omega_0} q, \quad (6)$$

where: $\omega = 2\pi f$, f – operating frequency ; ω_0 – coefficient depend on the ratio of the normalized parameters of active and reactive components of Z_S or Z_X .

However, each type of SPRT input equivalent circuit requires the bridge measuring circuit of the different structure. A two simplified versions of this circuits for Z_X of the positive and negative reactance component are shown in Fig. 4a and Fig. 4b. Both schemes are only partly similar. The circuit of Fig. 4b must possess additional properties, i. e.:

- to avoid the loading of coil m_1 by resistance R_1 , the operation amplifier OP was used to establish the open circuit mode of work,
- transmitter U performs two functions: shifting the phase by 90° (as on Fig. 4a) and summarizing the real and reactive components of the balancing signal. Methods of the precision calibration of the phase quadrature shifter are known. However, a calibration methods of block U on Fig. 4b are not yet established and approved.
- Ratio of resistances R_2/R_1 is included in the measurement result of the bridge. This ratio should be as accurate as a voltage divider T_1 .
- For the comparison of voltages and effective minimization of the leads' resistances influence, the additional transformer T_2 has to be used.

Errors of T_2 transformation ratio are included in the measurement result.

Thus, it is necessary to establish conditions for which only the bridge circuit structure given in Fig.4a should be satisfied enough. Also to work with short measuring cables it is necessary, but this not always can be done. Some realizations of reference

temperatures (in induction furnaces, cryostats) need a considerable distance. Other solution is to provide the equipotential protection of bridge measuring circuit.

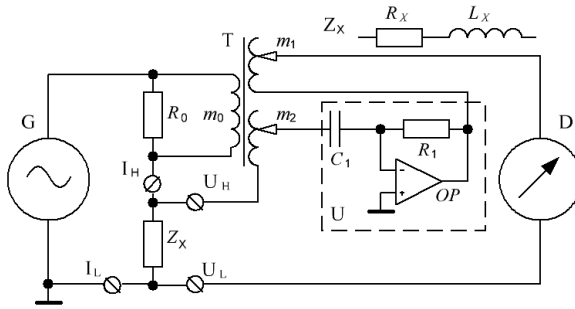


Fig. 4a. Bridge measuring circuit for the serial $R_x L_x$ equivalent circuit of SPRT

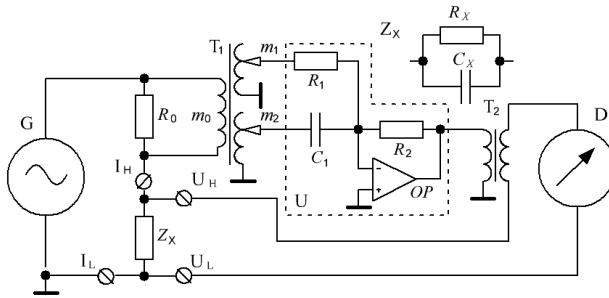


Fig. 4b. Bridge measuring circuit for the parallel capacitive equivalent circuit of SPRT

5 Equipotential Protection and Its Implementation

The AC equivalent circuit of the SPRT sensor connected to bridge terminals may be changed from the serial inductive to parallel capacitive circuit. It depends from the sum C of leakage capacitances of cables and inductive divider. In such measurements of the SPRT resistance in automatic mode require the quick switching of the bridge measurement circuit structure from the scheme of Fig. 4a to scheme of Fig. 4b. The implementation of these possibility in AC bridges of the accuracy 0.1–0.01 ppm is the serious technical problem. In this case to provide the calibration of bridge internal modules is almost impossible and such transition of the circuit must be avoided.

It is impossible to reduce the leakage capacitance C , but the effect of its impact can be minimized. The portion of cable in which the operating current flows to the measuring object Z_x , is shown on Fig. 5. It has a cylindrical shield. Normally, the shield is connected to ground (common). To provide an equipotential protection the shield is connected to the output of the voltage follower F. Then the primary leakage current I_{L1} through the parasitic capacitance C (switch in position S1) with the equipotential protection by amplifier F falls down to the current I_{L2} . Let us calculate them.

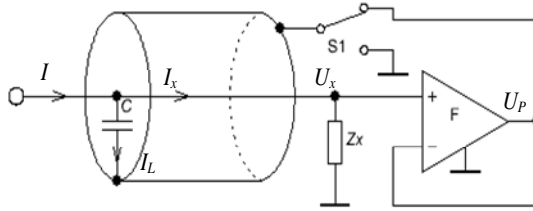


Fig. 5. Scheme of the equipotential protection

Leakage currents I_{L1}, I_{L2} are determined by expressions:

$$I_{L1} = U_x j\omega C, \quad I_{L2} = (U_x - U_P) j\omega C \equiv U_x j\omega C_E \quad (7a, b)$$

where: C_E – the virtual equivalent capacitance.

If there is an equipotential protection, the leakage current decreases by ratio

$$I_{L1}/I_{L2} = U_x / (U_x - U_P) = C/C_E \quad (8)$$

It is proportional to ratio of capacitances C_E/C . Theoretically, this gain is limited only by the amplification of the open circuit operational amplifier F. It is important for the real bridge, as the small equivalent capacitance C_E do not change the sign of $tg\varphi$ in (3) and the change of serial equivalent circuit to parallel one is not necessary.

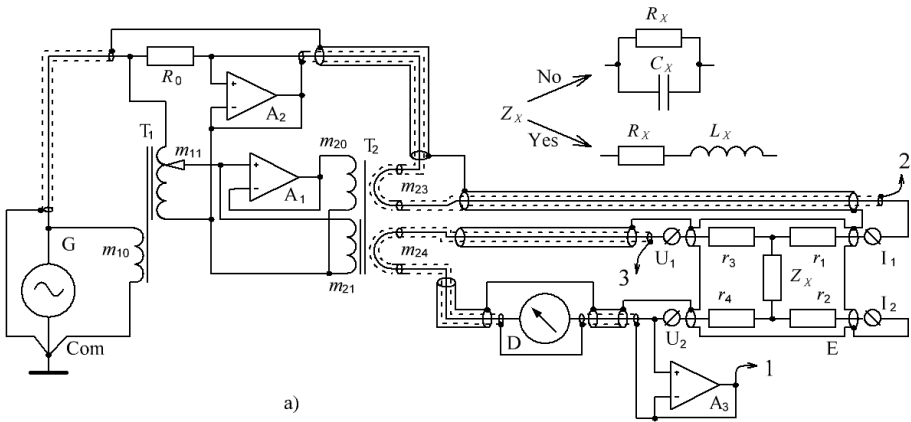
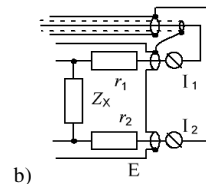


Fig. 6. a) Measurement circuit of coaxial bridge with three types of equipotential protection; b) other variant of protection type 2: G – voltage generator of the operating frequency f ; T_1 – two-stage voltage transformer with close inductive coupling between windings (acts as voltage divider); T_2 – a two-stage intermediate transformer; A_1, A_2, A_3 – voltage followers (buffer amplifiers); R_0 – resistance of the standard measure; D – detector of the bridge balance; Z_x – impedance of the SPRT sensor



In Fig. 6a diagram of the measuring circuit of thermometric bridge is given. This circuit has two multi-coil transformers T_1 , T_2 . Also three types of the equipotential protection (marked on Fig. 6a as 1–3) and bifilar winding are implemented. The additional two-step transformer T_2 is a very important feature of this scheme. Secondary windings m_{23} and m_{24} of T_2 use the shielded wire. Winding m_{23} with the operating current is wound on the single core of transformer T_2 (the coarse channel). The voltage from coil m_{24} is taken for compensation.

Connections of the measurement object and secondary windings of the transformer T_2 is made by tri-axial cable (the center conductor and two isolated shields) [3]. For the equipotential protection of center conductor the internal shield is used. The "reverse" current is flowing back in the external shield. On Figures 6a,b all internal shields are marked by dotted lines and the outer shields – by solid lines, respectively.

The shields of both secondary windings of the transformer T_2 are connected to the internal shield of the tri-axial cable. Central wire of communication line from the standard R_0 to the winding m_{23} of the transformer T_2 , central wire of winding m_{23} and the central wire of communication line from winding m_{23} to the measurement object Z_X constituted the path of the operating current in forward direction.

The external shield of communication line between the measured object and winding as well as an external shield of communication line between the coil m_{23} and the standard measure R_0 constituted a path of the reverse current. Such flow path of forward and reverse current, as used for the particular circuit in Fig. 6a, created the type of construction known under name coaxial bridge [2, 3]. The standard measure and SPRT sensor are considered as a four-terminal two-port elements.

The internal shield of the communication line from the measure R_0 to the winding m_{23} of transformer T_2 , central conductor of the secondary winding m_{23} and of the communication line from winding m_{23} to the measurement object Z_x , forms the equipotential protection circuit. It is used to reduce the influence of capacitive leakage currents. The protection circuit is located between the loops of forward and reverse current (Fig. 6a). This is a new configuration of the measuring circuit. In analogy to the term "tri-axial cable" [3], such measuring circuit as can be call "tri-axial bridge".

It is necessary to pay attention on several aspects of this new type scheme, i.e.:

- Series connection of two transformers T_1 and T_2 on Fig. 6a may cause the bridge nonlinearity. This is the deterministic (systematic) component of the error. It can be evaluated and used to correction purposes. Causes of the non-linearity and the original method of its control are considered in [8, 9].
- Shield E of the measurement object is connected in Fig. 6a to the second external shield of current loop. Potential of the shield and potential of the circuit "common" point will close each other. It is typical for coaxial bridges. But the shield E can be also connected to the portion of the chain at the points 1, 2, or 3 in Fig. 6a. In each case potentials of the shield are different. the alternative of point 2 connection is shown in Fig. 6b. For the complete equipotential protection (when resistances $r_1 - r_4$ cannot be neglected) the proper protective potentials should be find inside the measured object. Then a new type of the measurement object has to be design for that. This can be called e.g. as a four-terminal-triple

element. A rigorous approach of that subject needs description in a separate publication.

- Levels of equipotential protection in a potential and in current loop are different.

Let us consider the latter aspect. In the potential loop is implemented almost the complete equipotential protection. In the center conductor coil m_{23} and the shield the same voltage will be induced. At balance the potentials of the circuit inner conductor and shield are equal. Capacity C_E in a potential loop can be reduced by 5–6 orders. Therefore, the leakage currents are practically absent.

In the current loop the equipotential protection is difficult to implement, see Fig. 7. Parasitic resistances r_{01} , r_{02} , r_1 , r_2 , r_T are distributed parameters. Operating current creates a voltage drops across these resistors.

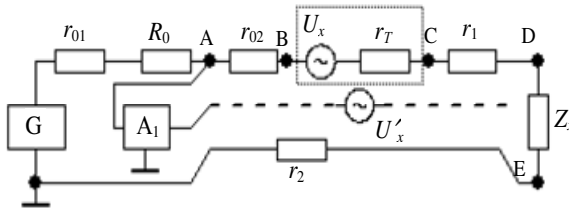


Fig. 7. Current loop of the bridge measurement circuit: r_{01} , r_{02} – resistances of standard R_0 leads; r_1 , r_2 – resistances of the connection line; U_x – voltage source (voltage of the transformer T_2 windings n_{22}); U'_x – a similar source in the shield circuit; r_T – resistance of windings n_{22}

Obviously, the leakage current I_L will depend on the voltage between the central conductor and its surroundings (see Fig. 5). In the absence of the inner shield the central wire is surrounded only by the outer shield (conductor with reverse current). The maximum voltage between them is defined as:

$$\Delta U_1 = I(R_X + r_1 + r_2 + r_{02} + r_T) \quad (6)$$

When using the inner shield with the corresponding potential (see Fig. 7), this voltage will be considerably less: $\Delta U_2 = I \cdot (r_1 + r_{02} + r_T)$. Hence using equipotential protection a leakage current decreases approximately K times:

$$K = \frac{\Delta U_1}{\Delta U_2} = \frac{R_X + r_1 + r_2 + r_{02} + r_T}{r_1 + r_{02} + r_T} \quad (7)$$

The presence of the insulation on the wire shield 2 (Fig. 6) allows to twist the winding m_{23} (i.e. reduce the inductive coupling) and eliminate galvanic contact between the shields. As a rule, values of resistances (Fig. 7) are in the following ranges: $r_{01} \approx r_{02} \approx (5-10) \text{ m}\Omega$, $r_T \approx (30-50) \text{ m}\Omega$, $r_1 \approx r_2 \approx (0,1-1) \Omega$. With these values we obtained reduction of the equivalent capacitance C to C_E above 100 times. This allows for the measurement of the SPRT resistance with connection cables up to 100 m long.

6 Conclusions

The sum of capacitances of cables and of the bridge inductive divider output, of value 1–3 nF, connected parallelly to the SPRT sensor, can change the AC equivalent circuit from the serial inductive circuit to the parallel capacitive circuit. It happens as well for high precision SPRT sensors as for industrial sensors.

Such change of the equivalent circuit complicates the calibration of internal nodes of the AC bridges, reduce their accuracy and complicates automation of the balancing process. Equipotential protection of the current and voltage bridge loops eliminates these drawbacks.

In the proposed scheme of AC bridge the structural and constructive techniques are used to reduce influences of electrical and magnetic fields on properties of the measuring circuit. These methods are based on an additional transformer application. The secondary windings of this transformer are made from the shielded wire. Such scheme unified advantages of the coaxial bridge balanced circuit and the equipotential protection. The AC bridge with such scheme implemented is proposed to call as tri-axial bridge.

References

1. Quinn, T.J.: *Temperature*. Academic Press Inc. London. – (1983)
2. Kibble, B.R., Rainer, G.H.: *Coaxial alternative current bridges*. Adam Hilder, Bristol (1984)
3. Awan, S., Kibble, B.R., Schurr, J.: *Coaxial electrical circuits for interference-free measurements*. The Institution of Engineering and Technology, London (2011)
4. Novik, A.I.: *Systems of automatic balancing of digital extreme bridges of alternating current*. Naukovaja dumka, Kiev 1983, p. 224 (1983) (in Russian)
5. Grinevich, F.B., Surdu, M.N.: *High-precision variation measuring systems of alternating current*. Naukovaja dumka, Kiev, p. 192 (1989) (in Russian)
6. Meleschuk, D.V., Mykhal, A.A.: *Error of platinum resistance thermometers caused by surface effect in a wire of sensitive element*. Tekhnichna elektrodinamika. Ukrainian Academy of Science 2, 69–71 (2004) (in Russian)
7. Mykhal, A.A., Meleschuk, D.V.: *Impedance model of precision platinum resistance thermometers in the field of high temperatures*. Tekhnichna elektrodinamika 4, 73–79 (2012) (in Russian)
8. Mikhal, A.A., Warsza, Z.L.: *Simple methods to control the accuracy of precision thermometric bridges (Part 1). Historical review, parameters and circuit operation of AC bridges, new method of its zero control*. *Pomiary Automatyka Robotyka* 2013 9, 92–96 (2013) (in Russian)
9. Mikhal, A.A., Warsza, Z.L.: *Simple Methods to Measure the Additive Error and Integral Nonlinearity of Precision Thermometric Bridges*. In this book
10. Mikhal, A.A., Meleschuk, D.V., Warsza, Z.L.: *Application of double-shielding technique in thermometric AC bridges*. *Pomiary Automatyka Kontrola* 11 (2014) (in Polish)

Simple Methods to Measure the Additive Error and Integral Nonlinearity of Precision Thermometric Bridges

Aleksander A. Mikhal¹ and Zygmunt L. Warsza²

¹ Institute of Electrodynamics, National Academy of Science of Ukraine, Kiev, Ukraine

² Industrial Research Institute of Automation and Measurement (PIAP) Warszawa
z.l.w@op.pl

Abstract. Determination of the accuracy of AC bridges with the high precision adjustable transformer voltage dividers based on the strongly magnetic coupling coils is referred in this paper. Metrological model of the temperature measurements by resistive sensors connected to these bridges is presented. The additive, multiplicative and linearity components of error in temperature measurement are considered. Method for determining the zero of the bridge error is developed. It is based on the non standard connection mode of the equipotential pairs of current and voltage terminals of standard resistance to the bridge. It is estimated that up to 1 M Ω of this resistance, the effective resistance obtained on the bridge input is less than 10⁻¹⁰ Ω . Four-terminal standard resistors of 0.1 Ω up to 1 M Ω are used in experiments to find bridge zero readings. Results indicate that the additive error of the tested precision bridge is about 0.5 LSB and is independent from the nominal standard resistance value. The conditions under which in temperature measurements remains only the linearity bridge error are formulated. Proposed is the unconventional method of measure and estimating the bridge nonlinearity named as dichotomy method. It applies algorithm based on the division of the measurement range and then obtained subsequent intervals always in half. Graphical interpretation and the analytical expression for the nonlinearity error are given. Sets of paired four terminal reference standard resistors are proposed for use in control. The resistance of each of them separately and of the given serial physical connection of them both has to be measured by tested bridge. The reasons affecting the accuracy of the physical realization of resistance summation is discussed. By calculations and experimental verification is find that in measurements by dichotomy method the bridge linearity error of 0.1 ppm or less can be discovered. Conclusions and final remarks are included. Both methods are simply and can be easily implemented in any metrology lab and be used also in automatic calibrators.

Keywords: Precision AC thermometric bridge, resistance standard, additive error, modeling of zero resistance, nonlinearity, dichotomy method.

1 Introduction

In roadmap for electrical and magnetic measurements for the years from 2012 [1] provided as a priority the development of commercial metrology systems based on

quantum phenomena. This will lead to a significant, more than 10-time reduction of uncertainty of the highest precision temperature measurements. Already the development of impedance-based quantum bridge, which allows to compare two resistance with the uncertainty of 0.2 ppm has been reported [2]. Some financial limitations of many national metrology institutes (NMI) make that transition to this new measurement technology will follow gradually. However, the temperature measurements in the international environmental monitoring and in controlling environmental conditions extensively are used. The basis of the credibility of these studies requires that high precise temperature standard measurements consequently must be also developed. It is after the opinion given in [3]: "Better monitoring of Global Warming would be effected through strengthening traceability links to national standards." Control and the continuous monitoring of basic metrological parameters of these measuring systems is required.

Already the temperature standards, which are maintained by NMI and some other metrological laboratories, in the most cases are equipped with a 6–8 decade AC transformer bridges. The first such AC bridges have been developed in the 60–70 of the last century. Technology continuously was improved and measurement process is now automated by the use of digital electronics. Metrological parameters of precision thermometric bridges are subject to periodic verification and certification. It is an important task in metrological practice. Technical data of AC impedance bridges and of the current quantum bridge are now very near each other but bridges need external calibration. However it is anticipated that in the near future in stands for the reproducing of standards of a various quantity, quantum instruments will be applied [2] and external calibration not be required.

Measurements of the temperature by the high precision thermometric bridges have its own specific features, which includes:

1. Level of the precision of AC bridges is so high that the limited relative measurement error is very small. It is unit of the lowest decade (1 LSB) and is 0.5–0.01 ppm. Random errors or uncertainties are smaller on the order than the determined systematic errors. The adjustable standard resistors to check the AC bridge with this level of accuracy are not available, so special methods and equipment was created.
2. For the calculation of the temperature of the MTS90 scale the W coefficient is measured. It is the ratio of two resistances of the standard platinum sensor – at the tested and at reference standard temperature.
3. Model of the measurement error of the AC bridges contains three components: additive, multiplicative and linearity error. The analysis shows that in such as above relative measurements the influence of the component multiplicative can be eliminated. The necessary condition is that the additive component of error was either zero or have to be removed by the calculation after the bridge calibration.

One of the basic metrological parameters of thermometric bridge is the value of their linearity error. In few of IMEKO or TEMPMEKO conferences presented are works on reducing the uncertainty of the reference temperature measurement by monitoring and taking into account the bridge non-linearity [4, 5]. The work of recent

years is addressed on the automation of the calibration procedure and the possibility of integration the bridge and the standard temperature system equipment used for this purpose. These tasks are important for the companies producing temperature bridges, but mainly for users as temperature measurements can be easily performed. T. Quinn wrote in [6] «They do not, however, absolve users from the need to have calibrations from a national metrology institute or properly accredited calibration laboratory to provide formal traceability to ITS-90 and the World's measurement system ».

In the manual of temperature measurements [7], two types of non-linearity are defined: the integral and differential. To designate both types of nonlinearities the special methods are developed [8]. However, its implementation requires highly specialized equipment – unique 30-bit inductive voltage divider and special high sensitivity detector of the circuit balance. The calibration method also been proposed [9, 10]. Essential to this is the low contact resistance commutator used to a series-parallel connection of four standard resistors. The explanation of this switch operation is described in [11]. It has been shown empirically that in connecting stage of the commutator its resistance is less than 1 nΩ. However, information, what is the geometry of electrodes, what the spatial symmetry is needed, what is the influence of surface phenomena and proximity to current and voltage circuits, is not given. For the self-realization of this control instrument additional purchase of a license of "know how" is required.

Methods to control the linearity of precise bridges, which are based on the use of stable resistors connected in series/parallel [9, 10], may be subject to systematic errors. These errors are negligible for the two simple original methods presented below. This paper is an expanded and enriched synthesis of authors' partial works. It may be of interest to professionals in the field of high accuracy thermometry.

2 Method of Rescaled Median Deviation

In the Fig. 1 shows the equivalent circuit of the precision AC bridge.

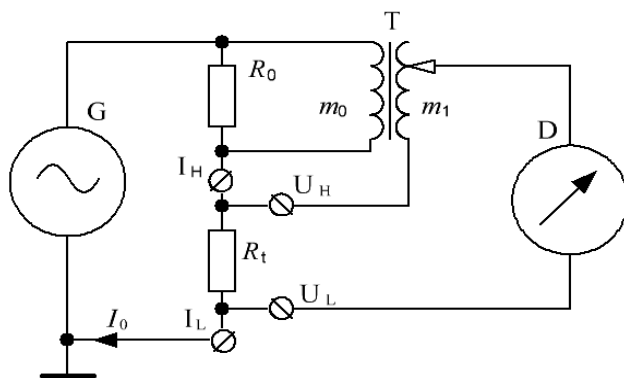


Fig. 1. Equivalent circuit of the AC measurement bridge

From the condition of the bridge equilibrium (which occurs at detector D indicating zero), the equation of measurement is:

$$R_t = R_0 m_1/m_0 \quad (1)$$

$$y = x \quad (2)$$

where: $x=R_t/R_0$ – the ratio of the measured resistance R_t of a platinum thermometer and of the bridge standard resistance R_0 , $y = m_1/m_0$ – the equivalent ratio of the numbers of turns of the divider T coils.

Eq. (2) is an ideal relative transfer function of the bridge and is a straight line with the slope equal to 1. Results of the resistance measurement are affected by the bridge error of components: additive (zero error), multiplicative and nonlinearity error. The actual characteristic is therefore the non-linear function expanding in a series

$$y = \sum_{i=0}^n a_i x^i = x (1 + \delta_m)(1 + \delta_l) + \Delta_a \quad (3)$$

where: a_i – expansion coefficients, $\Delta_a = a_0$ – additive component (zero error), $\delta_m = a_1 - 1$ multiplicative error and δ_l – linearity error described by series terms as

$$\delta_l = \frac{1}{a_1} \sum_{i=2}^n a_i x^{i-1}.$$

The coefficients a_i are complex and usually unknown functions of the deterministic (for systematic errors) and random components. They depend on a variety of influencing factors such as: leakage field of signal circuits, transformers and of measurement network inside the bridge, inaccurate value of the reference resistance R_0 and bypassing of it by the input impedance of transformer T (Fig. 1), non-ideal characteristics of the magnetic core, the impact of the supply source and of the output and load resistance of decades, etc. Further discussion of the accuracy of precision bridges is applied only to systematic errors, because the random errors are much smaller.

The technical data of precision thermometric bridges usually do not contain the multiplicative error. This is due to the algorithm (4) used for calculation of the temperature, which is measured in sub-ranges between control points of ITS 90 scale. This temperature is determined from the value of the W parameter. It is the ratio of bridge readings y/y_V for resistances of the standard sensor Pt immersed in the measured and reference temperature, e.g. the triple point of water. On the basis of Eq. (3) from such two measurements ratio W is obtained

$$W = \frac{y}{y_V} = \frac{x(1 + \delta_m)(1 + \delta_l) + \Delta_a}{x_V(1 + \delta_m)(1 + \delta_{lV}) + \Delta_a} \quad (4)$$

Eq. (4) shows that the multiplicative component δ_m of the systematic error does not affect the coefficient W , when the additive error component Δ_a is equal to zero. In such case the greater accuracy can be achieved. So, there are two possibilities:

- error Δ_a is less than 0.5 LSB of the bridge indication and can be omitted,
- Δ_a must be known and taken into account when measurement results are calculated.

The additive and linearity errors are the basic metrological parameters of precision thermometric bridges. Simple methods of their determination will be considered.

3 Method of Measurement of the Bridge Zero Error

The circuit for modeling the value of measured resistance equal to zero can be obtained by connecting the standard resistance R_0 to the bridge input in unconventional way given in Fig. 2.

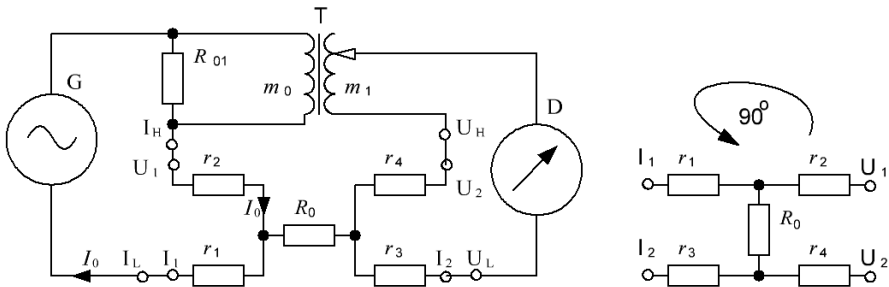


Fig. 2. Connection of the standard resistor R_0 when zero value of resistance is measured

Almost any four-terminal standard resistor can be used for that. In the circuit of Fig. 2 it is connected to bridge terminals after rotation of resistor leads on 90° with respect to the classical connection given in Fig. 1. The equipotential leads U_1, I_1 of this resistor are connected to current terminals I_H, I_L of the bridge input, and the second pair U_2, I_2 – to its voltage terminals U_H, U_L . Then the bridge current I_0 flows only through the lead resistances r_2, r_1 . The resistance R_0 acts as the jumper connecting voltage and current circuits of the bridge. In this case the bridge display should be zero. However, in the real bridge that may not occur.

The AC bridge measures the resistive component R_x of the ratio of voltage on the bridge voltage terminals to a current flowing through bridge current terminals. Value R_x , which should be indicated on the bridge display, can be estimated from the equivalent scheme given in Fig. 3.

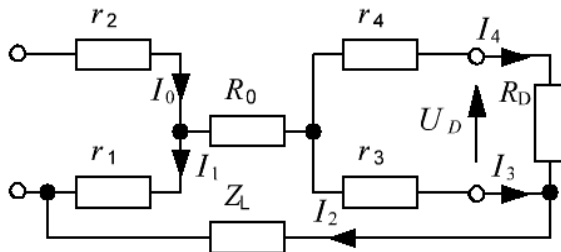


Fig. 3. Circuit for calculation the equivalent resistance R_x in zero calibration mode

The influence of resistances: of the lead wires r_1, \dots, r_4 , of the detector input resistance R_D and the impedance Z_L of the leakage through insulation to the common circuit mass have been considered. In this circuit, the following relationships occur

$$I_0 = I_1 + I_2, \quad I_2 = I_3 + I_4, \quad I_3 r_3 = I_4 (r_4 + R_D) \quad (5-7)$$

which gives:

$$R_X = \frac{r_1 r_3}{\left[R_0 + Z_L + r_1 + \frac{r_3 (1 + r_4 / R_D)}{1 + (r_3 + r_4) / R_D} \right] \left[1 + \frac{r_3}{(R_D + r_4)} \right]} \quad (8)$$

Eq. (8) can be simplified by assuming that all lead resistances r_i are the same and equal to r . The unknown leakage isolation impedance Z_L can be substituted by a isolation resistance R_i as parameter given usually in the technical data of electrical devices. Due to the security of service should be $|Z_L| \geq R_i \geq 100 \text{ M}\Omega$. If $r/R_D \leq 10^{-5}$, then

$$R_X \leq \frac{r^2}{R_0 + R_i + 2r} \quad (9)$$

After taking into account the resistances of the real measuring devices, the Eq. (9) shows that for a four-lead resistances $r < 0.1 \text{ }\Omega$ with a nominal value of standard resistance of $R_0 < R_i$ the equivalent resistance R_X does not exceed $10^{-10} \text{ }\Omega$.

4 Reasons for Nonlinearity of AC Bridge Characteristics

These reasons will be discussed on the example of the typical AC multi-decade thermometric bridge. Figure 4a shows the simplified main part of the bridge circuit with 12-bit inductive voltage divider (IVD) including T_1 and T_2 transformers.

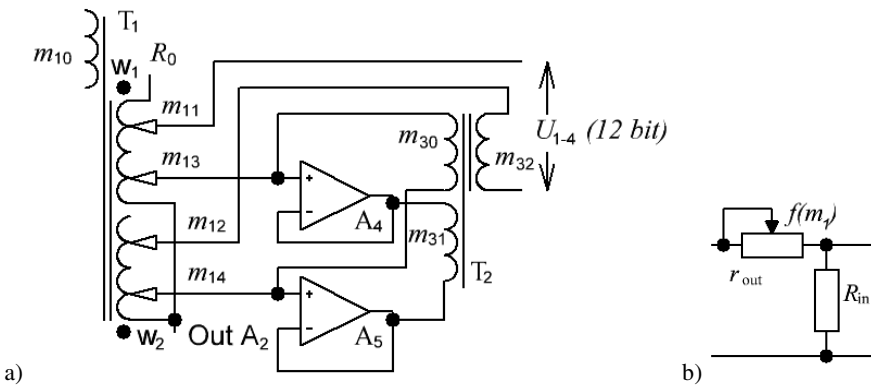


Fig. 4. a) Simplified circuit of the 12 bit IVD (equivalent to transformer T on Fig. 1), b) source of the bridge integral nonlinearity

To reduce the quantization error two-stage transformer voltage dividers with a strong magnetic coupling are used. The secondary winding m_1 of the inductive divider T_1 has several coils. To create the desired ratio of voltages it can be of the decimal or binary format. In binary format, as a rule, the adjustable coils with eight (triadic system) or sixteen (tetradic system) leads is used. Transformers T_1 and T_2 are made on core ring of the amorphous cobalt. Few such transformers are connected in series as cascade. This results in adding of voltage settings of all decades. However, there is also the negative effect of a mutual cooperation of the connected decades. Leakage coil inductances are negligible, but resistance of wires – not. For example, the output resistance r_{out} of m_{13} , m_{14} winding and input resistance R_{in} of transformer T_2 form a voltage divider (Fig. 4b). Output resistance r_{out} of the decade T_1 depends on number of turns m_{13} , m_{14} and is changed when its setting is switched, i.e. $r_{out} = f(m_{13}, m_{14})$. If the transformer cores are made from modern magnetic materials with relative permeability $\mu = (1-2) \times 10^5$, then the input impedance

$$R_{in} \approx (j\omega L)^2 / R \quad (10)$$

where: R – primary coil resistance for DC current, L – inductivity of that coil, $\omega = 2\pi f$ – pulsation of AC current of frequency f .

Input resistance R_{in} is (10–20) M Ω , and r_{out} may change in the range 0 to (3–4) Ω .

The linearity errors are usually defined as the distance between the real bridge transfer function $y = f(x)$ and the straight line through points 0, f_m of the bridge range.

In general, the nonlinearity of transfer characteristics of the transformer divider may be described similarly as for other analog-to-digital converters, by integral and differential linearity errors. If transfer coefficients of the decades are changed because of their loadings then the smoothed transfer characteristics of the bridge will be a convex monotonic function, as shown in Fig. 5a. Non-linearity of this function was intentionally exaggerated. For given input and output resistances of the oldest decades of the AC bridge the integral linearity error can reach values (0.1–0.2) ppm.

Differential non-linearity (called DLN) of the transformer bridge is existing due to differences of inducing electromotive force in each coil winding of the regulated inductive divider. It manifests itself as a non-uniformity of quantization. Differential non-linearity is observed, for example, when replacing all turns set on the lower order decade by one coil of the earlier decade (decade replacement effect). Examples of such differential non-linearity of the binary induction divider are given in Fig. 5b. The second type of differential non-linearity is manifested in unequal voltages of winding section of a the same decade – Fig 5c. In particular, the greatest impact have such differences in the oldest decade. Differential nonlinearity arises mainly due to the heterogeneity of the parameters of magnetic cores and other performance imperfections. This type of nonlinearity is checked in the process of production of transformer dividers using the standard winding or reference divider [8] according to the procedure generally unavailable to users. Differential non-linearity of AC bridges is at least on order lower than the integral non-linearity and for high precision bridges it does not exceed 0.25 LSB.

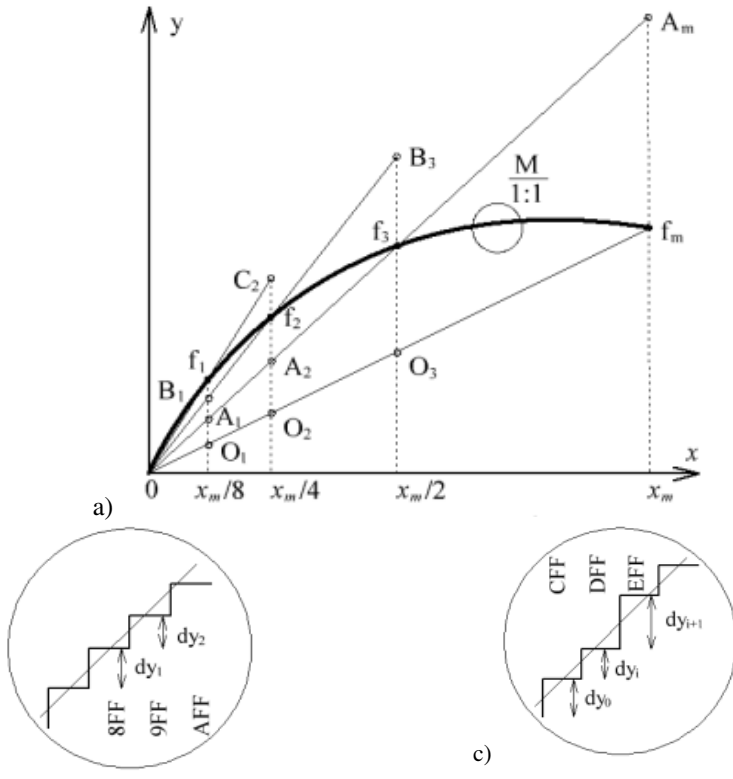


Fig. 5. Nonlinearities of the transformer divider: a) Graphical interpretation of the integral nonlinearity and the idea of the dichotomy method. Examples of differential transformer nonlinearities of binary divider: b) $dy_1 \neq dy_2$ – from exchange of decades (8FF \rightarrow 9FF) during regulation: c) dy_i -var – from difference of weight coefficients of the steps of single decade, e.g. of the older one (9FF the FFF) of above divider.

Direct testing the integral linearity error of the precision AC bridges with the highest resolution of 7–8 digits needs of the same level of accuracy set of the standard resistances, including values other than 10 nΩ. Such standards resistors are not yet available. It is the accuracy level of the cryogenic Hall Effect resistance standard. This difficulty can be avoided in method used for a temperature measurements by AC bridge. These measurements are relative and based on the coefficient W as the ratio of the sensor resistance at two temperatures.

5 Numerical Example

The method here presented is used to determine the integral linearity errors of the bridge characteristics. Its idea is based on the verification that the characteristics fulfills the principle of additively

$$f(x_1) + f(x_2) = f(x_1 + x_2) \tag{11}$$

If the bridge function is nonlinear, the relation (10) for measuring the resistance does not occur. The difference between the right and left side of (11) can be taken as integral nonlinearity. For monotonic functions a univocal result is obtained. Understanding the algorithm of method proposed here should be easier if explanation of the Fig. 5a is used.

The values x_i of the measured resistance are on x axis and the measurement results are y_i ordinates laying on the curve $y = f(x)$, i.e. of points $0, f_1, f_2, \dots, f_m$. As an ideal, a linear transfer function of the bridge (excluding the additive and multiplicative error component) has to be taken. The easiest way is to take the straight line connecting the end points 0 and f_m of the range. Then all integral linearity errors will be of the same sign. On such virtually adopted the perfectly linear bridge curve are lying points $0, O_1, O_2, \dots, f_m$. The essence of the linearity test is to measure the differences between the corresponding values of y coordinates of points on the curve $y = f(x)$ and points of the same ordinate x of the ideal characteristics of the bridge span. Then all integral linearity errors will be of the same sign. Other ideal characteristics, such as optimum straight line with slope calculated by accepted criteria as minimum square error, Chebyshev criterion and others could be also used. But such characteristics would have had the individual character for any bridge and can be find if linearity errors are known or a priori estimated.

The accuracy of determining the values of the linearity error does not need to be too large (1 or 2 digits only). For this purpose the course of nonlinear characteristics of the bridge in the relevant range can be roughly described as piece of a parabola. Then the greatest linearity error occurs in the middle of this range.

To determine the non-linearity in the middle of the range, i.e. in the point $x_m/2$, two resistors of the equal resistances R_{11} and R_{12} are used. The measurement results of both resistance bridges should be the ordinate of point f_3 . It is also assumed that these resistors are connected so that their resistances add up perfectly (reasons of non-ideal summation are examined below). From the additivity of summation given by the Eq. 10, follows that for measurement of the resistance $R_{11} + R_{12} \equiv R_{1C}$, their intercept point A_m should lay on the line passing through the points 0 and f_3 . From the similarity of the triangles $0 A_m f_m$ and $0 f_3 O_3$ is, that length of $f_3 O_3$ segment is equal to the linearity error of the bridge characteristics and is half the length of the $A_m f_m$. The point corresponding to the mid-range value of the linearity error related to the measuring range R_{max} is described by the expression

$$\delta_1 = \frac{R_{1C} - (R_{11} + R_{12})}{2R_{max}} \tag{12}$$

where: R_{1C} – measured resistance of R_{11}, R_{12} physically connected in series.

Similarly, the linearity error at the point $x_m/4$ corresponding to 0.25 range, is equal to the length of the $f_2 O_2$, consisting of sections $f_2 A_2$ and $A_2 O_2$. Based on the similarity of the respective triangles, the sections are equal to half the sections $B_3 f_3$ and $f_3 O_3$. Since the ordinate of point f_2 is determined by the resistances R_{21}, R_{22} , and the ordinate of the B_3 by their sum, the error at the point $x_m/4$ is the sum of the two segments

and for $x_m/8$ will be a total of three sections. In general, for the k -fold division of the range, linearity error of $(1/k)$ part of the range is:

$$\delta_k = \frac{1}{R_{\max}} \sum_{i=1}^k \frac{R_{iC} - (R_{i1} + R_{i2})}{2^{k-i+1}} \tag{13}$$

The presented algorithm of the determination of the maximum integral linearity error of each range is related to the division of the whole range of measurement and subsequently received subranges in half. In the mathematics this algorithm is called the dichotomy method.

6 Double Resistance Standard for the Dichotomy Method

The implementation of the dichotomy method in the measuring practice needs to create a set of several standard resistors of connected two equal resistances. Resistance of each pair should be precisely their sum. The accuracy of the resistance value is not too critical, but only its stability. Structurally, each double standard resistor consists of two identical four-terminal standard resistors connected in one system with the scheme shown in Fig. 6.

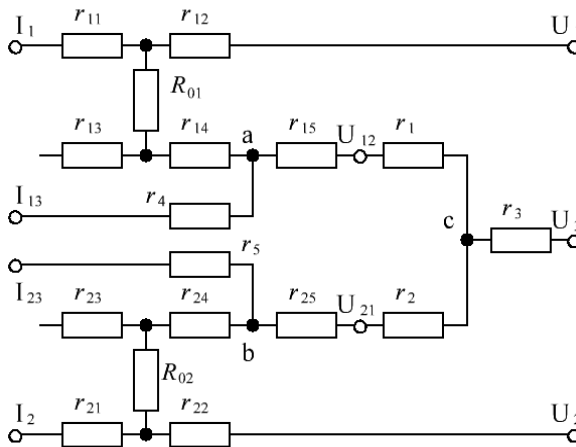


Fig. 6. Circuit of resistances of the standard double resistor

It presents the resistances R_{01} and R_{02} and leads resistances r_{11}, \dots, r_{15} and r_{21}, \dots, r_{25} . Equipotential current r_{11} and voltage r_{12} lead resistances and as well r_{21}, r_{22} are connected respectively to terminals I_1, U_1 and I_2, U_2 . Lead resistances r_{15}, r_{25} are connected to the additional voltage terminals labeled as U_{12} and U_{21} . These terminals are shorted with a jumper with a total resistance $r_1 + r_2$. At about the middle of it the pin is made (with resistance r_3) to terminal U_3 . Cable from the voltage point of standard resistance R_{01} has resistance $r_{14} + r_{15}$. It is divided roughly in half and from its center

connection is made with a resistance r_4 , to be attached to the terminal I_{13} . The same is applied to the voltage lead of standard resistance R_{02} which has resistance $r_{24} + r_{25}$.

The results of measurement R_{01} and R_{02} depend on their lead wire resistance r_{14} , r_{15} , r_{24} , r_{25} and the jumper resistance r_1 , r_2 , i.e.

$$R_{11} = R_{01} + r_{14} + r_{15} + r_1, \quad (14 \text{ a})$$

$$R_{12} = R_{02} + r_{24} + r_{25} + r_2 \quad (14 \text{ b})$$

And the measured resistance of the double R_{1C}

$$R_{1C} = R_{01} + R_{02} + r_{14} + r_{15} + r_{24} + r_{25} + r_1 + r_2 \quad (15)$$

A comparison of sums of Eq. (14a), (14b), and Eq. (15) shows that the method based on the assumption of a linear function additivity given by Eq. (11) works in full for a double standard resistance. It remains to examine the accuracy of the resistance of the resistor R_{1C} double as the physical implementation of the summation of $R_{11}+R_{12}$ components. The accuracy depends on the stability of all resistances included in Eq. (15) and is determined by the influence of several factors indicated below.

1. Effect of the finite dimensions of the connection points indicated in Fig. 4 as a, b, c and heterogeneity of the electric field therein. The strict approach would need to be based on Maxwell's equations and solving the electric field distribution. The practical experience shows that when measuring resistances R_{01} , R_{02} , R_{1C} , non-linear distribution of the electric field at these points does not change if the lengths of the resistors r_{15} , r_{25} , r_1 , r_2 are much larger than their diameters.
2. Effect of time instability of standard resistance R_{01} and R_{02} . The stability of resistors depends on their technology. Among types used in Ukraine the best performance have resistors MR3000 produced by ZIP Krasnodar – Russian factory of measuring instruments with rich experience. The specification contains the annual relative variation of resistance of 5×10^{-6} . Studies have shown that daily volatility is about two orders of magnitude less than the annual. Therefore, at the time of checking the bridge linearity error by the presented method (including averaging) their time instability is below the threshold sensitivity of the bridge. An alternative to the resistors MR3000 are standard resistors made by companies: Vishay (S102C, VHP 4, 247 VPR) and Powertron (UNR4-T220, USR4-3425).
3. Effect of temperature instability resistance value involved in the measurement. Jumper and cables are made of copper wire of the resistance temperature coefficient $\alpha_r \approx 4 \times 10^{-3} \text{ } \Omega/\text{deg}$. The combined effect of temperature coefficients of standard resistance and jumper resistance shows the maximum permissible jumper resistance:

$$r_1 + r_{14} + r_{15} \leq R_{01}(\alpha_R/\alpha_r) \quad (16)$$

For example, for the standard resistance $10 \text{ } \Omega$ from Eq. (16) is obtained that the copper jumper resistance should not exceed $2.5 \text{ m}\Omega$.

Effect of thermal instability can be eliminated satisfactorily by other ways. Simplest one is to place a double standard in passive air thermostat. However, much better is to use an active thermostat with temperature control within ± 0.01 °C. In this case the effect of temperature instability fall down below the sensitivity of the bridge AC highest resolution.

The presented dichotomy method does not include points of the upper half of the range and of each upper successively obtained sub-ranges. In most cases, however it is enough to find the maximum linearity errors occurring in their centre. Only in some of the most accurate temperature measurements values of errors are need to make corrections in some other points. Now we are developing a method for measuring the linearity error of AC bridges that allows control over the whole measuring range. It is a upgrading of the dichotomy method described herein for measurements in the upper half of each tested range and sub-range. It is a development of the methods described herein dichotomy measurements in the upper half of each test range and sub-range.

7 Experimental Verification of Both Methods

The object of this study was one of the high precise thermometric AC bridges type CA 300 developed by A. Mikhal and others. They have been produced individually by company "Specavtomatika" Kyiv, Ukraine. Simplified its circuit and principle of its work was in short described in [13]. Views of the instrument and of double resistance standard is also given there. The double-shielding technique applied in this AC bridge is analyzed in details in [14].

Bridge CA 300 has a measuring range of 0-125 Ω , LSB 10^{-5} Ω and noise bandwidth for a single measurement – 1 Hz. The measurement process was automated. Its metrological parameters are nearly similar as the previous version of the precision AC bridge of ASL of symbol F18. Few copies of the bridges CA 300 runs in metrology labs on Ukraine and few other countries of the former Soviet Union.

Readings of the bridge at the measured resistance unconventional connection equal to zero mode (Fig. 2) and the bridge integral linearity of to dichotomy method, are experimentally verified. To check zero of the bridge CA 300, standard resistors with nominal value of 0.1 Ω to 1 M Ω has been used. The measurements were made in a bridge-enabled mode averaging. Measuring samples of at least 10 observations, whose corresponds to the noise band width of 0.1 Hz have been used. Fig. 7 shows the measurement results obtained for several standard resistors of different nominal values.

Each series of about 25 measuring observations has almost the same average value $+5.5$ $\mu\Omega$. It is equal to half of the decade with the lowest indicated resistance value (1 LSB) and is an additive component of the bridge systematic error. Obtained value can be used for correction of measured temperature.

Therefore obtained is the experimental confirmation that after joining four-lead resistance R_0 by an unconventional way the bridge display will show value corresponding to zero resistance. In such a simple, fast and effective way is identified one of the main metrological parameters of the precision thermometric bridges – an additive component of the systematic error. Its determined value is independent in a wide range on value of the standard resistance R_0 used in testing, i.e. from 0.1 to 1 M Ω .

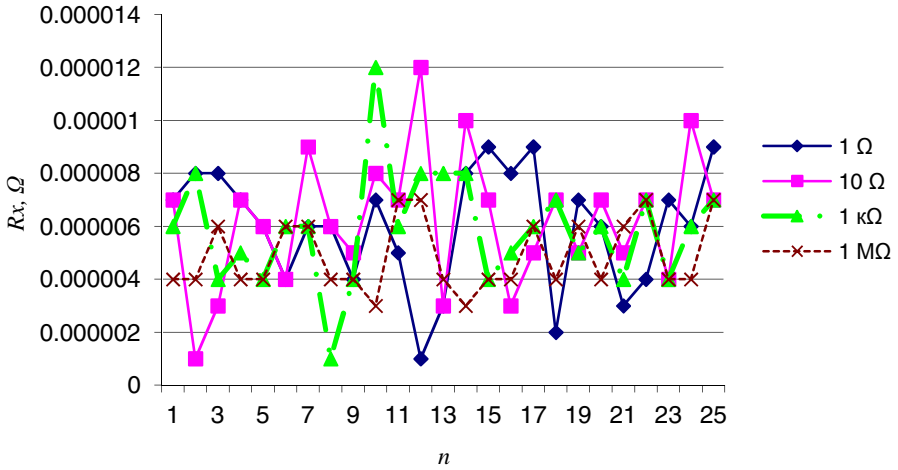


Fig. 7. Experimental results obtained for bridge CA 300 with different nominal values of four-terminal standard resistors connected to modeling the resistance equal to zero

Integral non-linearity of the CA 300 bridge was examined by the dichotomy method [13]. For the measuring range 0–125 Ω it is enough (in practice) to use only three standard double resistors (62+62) Ω , (31+31) Ω , (15.5+15.5) Ω . Tested are several units of the precision AC thermometric bridges of the smallest 1 LSB relative resolution is less than $6.2 \cdot 10^{-8}$. Integral linearity errors related to measurement ranges were within the range of $(0.5-2.1) \cdot 10^{-7}$ with a standard deviation not exceeding 3×10^{-8} at 0.05 Hz band noise.

The resulting experimentally obtained error values almost coincide with estimated ones based on metrological parameters of bridges listed in their technical data. Measured biases of any bridge can be eliminated by corrections – automatically or in calculations.

Determination of the type B standard uncertainty in the measurement of standard temperatures by bridges, of the estimated, but not possible to delete components of systematic errors are discussed in [7].

8 Summary

1. This paper presents two original methods for testing bridges used in the precision temperature measurements. First one is for measurement the additive component of the bridge error. It allows to test with the highest precision the bridge reading for resistance equal to zero. The method how to test the integral bridge nonlinearity by use the original dichotomy is also given.

2. It has been shown theoretically and experimentally verified that using any of the four-terminal resistor having a value below the standard 100 M Ω unconventional attached to the bridge as shown in Fig. 2, may implement a value of resistance less than 10^{-10} Ω for controlling the bridge zero.
3. It was also confirmed experimentally that by the proposed dichotomy method for measuring the total non-linearity (called also integral nonlinearity), you can detect a very small non-linearity of high precision AC bridges, i.e. at level 0.1 ppm and below.
4. Both methods are simple and inexpensive to implement for almost any control metrology lab having precision AC bridges and are also suitable for automated procedures of measurement.

References

1. TC-EM Roadmap: Innovative calibration means in electricity/magnetism, <http://www.euramet.org/index.php?id=roadmaps>
2. Palafox, L.: PTB Develop Quantum-Based Impedance Bridges. *Measure* 7(1), 4 (2012)
3. Machin, G., et al.: A European roadmap for thermometry, EURAMET TCT (2012), <http://www.euramet.org/index.php?id=roadmaps>
4. Joung, W., Gam, K.S., Yang, I., Kim, Y.-G.: Uncertainty assessment of resistance thermometry bridges. In: XX IMEKO World Congress, September 9-14, Busan, Republic of Korea (2012)
5. Walker, R.: Automatic linearity calibration in a resistance thermometry bridge. *TEMPMEKO & ISHM Book of Abstracts*, 217 (2010)
6. Quinn, T.: Temperature Scales from the early days of thermometry to the 21st century IMEKO-TC12-2004-PL-001.pdf (2004)
7. Uncertainties in the realization of the SPRT Subranges of the ITS-90, CCT-WG3 on Uncertainties in Contact Thermometry, CCT/08-19/rev (July 10, 2009), http://www.bipm.org/cc/CCT/. /24/D19_rev_WG3_Doc_rev_10July2009.pdf
8. Avramov, S., Oldham, N., Gammon, R.: Inductive voltage divider calibration for a NASA flight experiment. In: *NCSL Workshop & Symposium, Session 3C*, pp. 225–232 (1993)
9. White, D.R.: A method for calibrating resistance thermometry. In: Torino, P., Marcarino, L., Bella, T. (eds.), pp. 129–134 (1996)
10. White, D.R., Jones, K., Williams, J.M., Ramsey, I.E.: A simple resistance network for calibrating resistance bridges. *IEEE Trans. Instr. Meas* 46(5), 1068–1074 (1997)
11. Riley, J.C.: The accuracy of series and parallel connections of four-terminal resistors. *IEEE Trans. of Instrumentation and Measurement* 16(3), 258–268 (1967)
12. Awan, S., Kibble, B., Schurr, J.: *Coaxial Electrical Circuits for Interference-free Measurements*, vol. 350, p. 321. The Institution of Engineering and Technology, London (2011)
13. Mikhal, A.A., Warsza, Z.L.: Simply calibration methods of the precision AC thermometric bridges (2) Measurement of integral nonlinearity by the dichotomy method. *Pomiary Automatyka Robotyka* 10, 130–137 (2013) (in Polish)
14. Mikhal, A.A., Meleshchuk, D.V., Warsza, Z.L.: Application of double-shielding technique in thermometric AC bridges. *Pomiary Automatyka Kontrola (Measurement Automation Monitoring)* 11 (2014) (in Polish)

Study on Graphene Growth Process on Various Bronzes and Copper-Plated Steel Substrates

Tadeusz Missala¹, Roman Szewczyk¹, Marcin Kamiński¹, Marek Hamela¹,
Wojciech Winiarski¹, Jakub Szałatkiewicz¹, Jan Tomasiak², Jacek Salach²,
Włodzimierz Strupiński³, Iwona Pasternak³, and Zdzisław Borkowski⁴

¹ Industrial Research Institute for Automation and Measurements PIAP,
Al. Jerozolimskie 202, 02-486 Warszawa, Poland
tmissala@piap.pl

² Warsaw University of Technology, Faculty of Mechatronics,
św. A. Boboli 8, 02-525 Warszawa, Poland

³ Institute of Electronic Materials Technology,
ul. Wólczyńska 133, 01-919 Warszawa, Poland

⁴ Zakład Mechaniki Maszyn s.c., ul. Otyńska 6, 54-426 Wrocław, Poland

Abstract. The paper presents the aim, way of proceeding and results obtained during the research made in the project GRAPHTRIB to determine the metallic substrates, other than copper, to realize graphene growth process. The various silicon and silicon free bronzes were the objects of investigations. The obtained results presented in the paper aren't encouraging.

Keywords: graphene, graphene growth process, substrates for graphene.

1 Introduction

There are instruments and drives in which components made of steel or other ferromagnetic metals or alloys cannot be used, because they should be unsusceptible to strong magnetic fields. One may point to a compass as an example of instrument like that. Unfortunately, bearings and gears made of metals other than steel are not sufficiently resistant to wear and tear and represent poor tribological performance.

The first information on graphene mechanical properties [1–3] has created an opportunity to improve tribological performance of the non-steel components. To verify if this possibility is real or not, the project GRAPHTRIB – graphene-based coating of special gear-wheels and bearings has been founded [4].

2 Research Aim and Parameters

The assumed research aim of the project was to find such a metallic substrate for the graphene layer deposition, that suitably formed would enable introduction of the graphene into other applications such as electronics and measuring elements, using graphene layers deposited on copper or monocrystalline silicon carbide.

The assumed investigation parameters are:

- substrate material that, enforced by the graphene layer, could be an interesting alternative in mechanism building, especially for elements sensitive to magnetic fields – therefore testing of various metals was planned;
- smoothness and state of the substrate surface – therefore various kinds of manufacturing processes were applied (milling, grinding, polishing and surface galvanic coating) followed by appropriate measurements.

3 Planned Research Activities and Logistic Procedure

To fulfill the project objectives, the following research activities were planned:

- experiment of graphene layer deposition on specimens of silicon bronzes;
- experiment of graphene layer deposition on specimens of other bronzes;
- experiment of graphene layer deposition on specimens of copper covered steel;
- experiment of graphene layer deposition on selected machine elements.

To conduct the experiments the logistic procedure as shown in Fig. 1 was adopted.

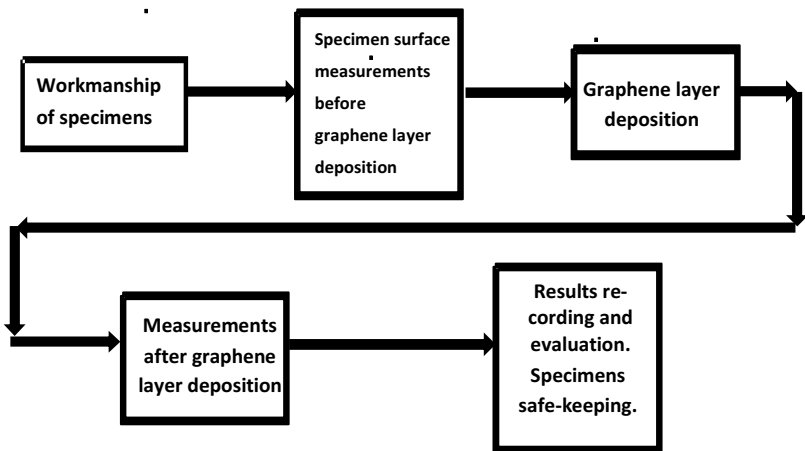


Fig. 1. Logistic procedure

4 Methodology of Specimen Surface Microgeometry Measurements before Graphene Deposition

Measurements were made of surface microgeometry of all specimens intended to have a graphene coating put on. The preliminary measurements were performed in order to evaluate surface texture and, as a result, choose a proper number of measurements to be carried out for each specimen. Then, representative measurements of

standard parameters: amplitudes (R_a , R_z , R_v , R_p) and material ratios (Mr_1 , Mr_2), were conducted using the sampling lengths which were chosen in the preceding step. The peak and valley parameters mentioned above are perceived to be crucial for outlining differences between surface texture properties before and after application of the graphene coating. In addition, values of those parameters were calculated as a mean value of three measurement results obtained for each specimen. Then, the uncertainties of all measurement results were estimated with influence of calibration artefacts from deviations and repeatability of measuring instruments indications taken into account. It is also worth mentioning that a comparative research of measurement results was carried out as two different metrological devices were used: Form Talysurf PGI 830 profilometer (tactile method) and CCI SunStar (non-contact method).

5 Graphene Layer Deposition on Silicon Bronzes

In all experiments concerning graphene layer deposition the epitaxial method of graphene grow, elaborated in the Institute of Electronic Materials Technology, was used. The manufacturing process of graphene has been performed under carefully arranged conditions, taking into account the physical properties of silicon bronze. Graphene films were synthesized in a 6-inch Black Magic system by the CVD method. The process is divided into few steps. At first, the samples were pretreated under an Ar gas flow and then H_2 gas flow at the pressure of 100 mbar. The purpose of this step was to improve the quality of substrates. Afterwards, both CH_4 and H_2 gas were introduced into the reactor for few minutes. Finally, the substrates were cooled down to room temperature in an Ar atmosphere. To ensure optimal temperature conditions, thus preventing bronze substrates from melting, the temperature was chosen in the range between 960 °C and 980 °C. During the process of graphene deposition the pressure of 20 mbar was sustained.

Various silicon bronzes presented in Table 1 were used as substrates. Because the first experiments with use of standard bronzes gave negative results, some special bronzes were melted to determine the impact of silicon content on graphene deposition.

Table 1. Silicon bronzes used in experiments

Item	Alloy	Chemical composition [%]	Melting Temperature [°C]	Reference Standard (w/ alloy identifier) [5]
1	CuSi3 Mn1	Si – 3; Mn – 1; Cu – rest	971	EN 12166: 2011; CW116C
2	CuSi1	Si – 1.00; Zn – <0.01; Mn – 0.10; Pb – <0.01; Fe – <0.01; Cu – rest	1032	EN12166:2011; CW115C
3	CuSi05	Si – 0.45; Cu – rest	1032–1083	Special
4	CuSi03	Si – 0.35; Cu – rest	1032–1083	Special
5	CuSi01	Si – 0.12; Cu – rest	1032–1083	Special

The results of experiments are presented in Figs. 2–6.

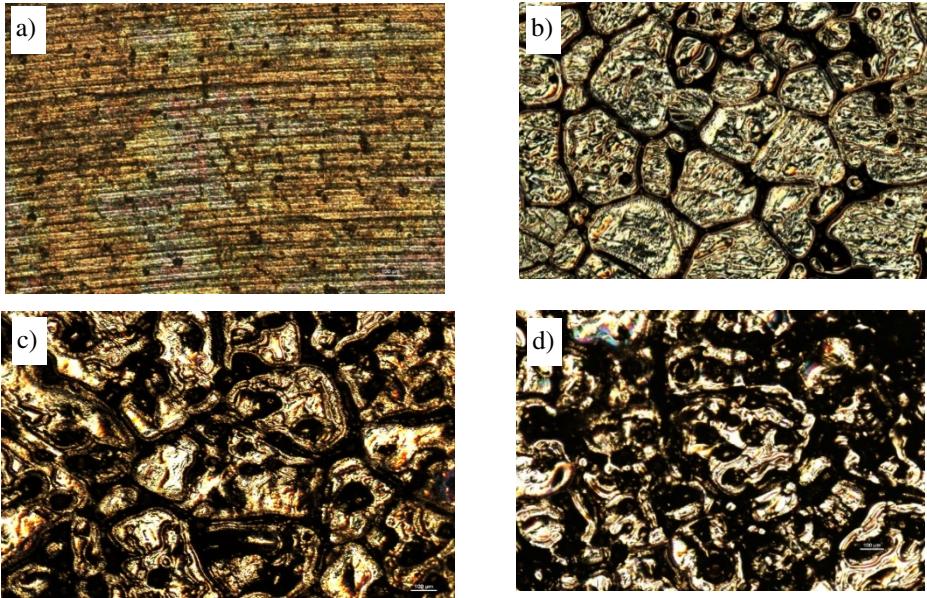


Fig. 2. Images of surfaces of specimens of bronze CuSi3Mn1: a) before the epitaxial process, after the epitaxial process b) in 950 °C, c) in 970 °C, d) in 980 °C

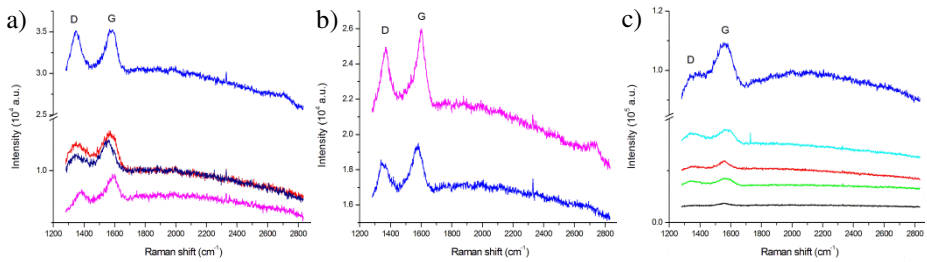


Fig. 3. Raman spectra of CuSi3Mn1 specimen after processes of graphene layer deposition in temperature, a) 950 °C, b) 970 °C, c) 980 °C

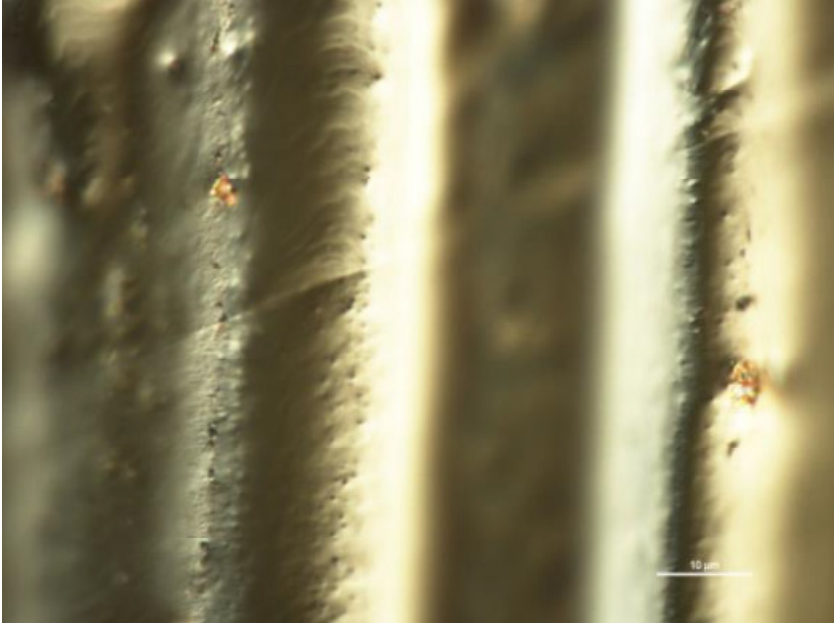


Fig. 4. Image of CuSi1 specimen surface after epitaxial process in temperature 1000 °C and duration of 10 minutes

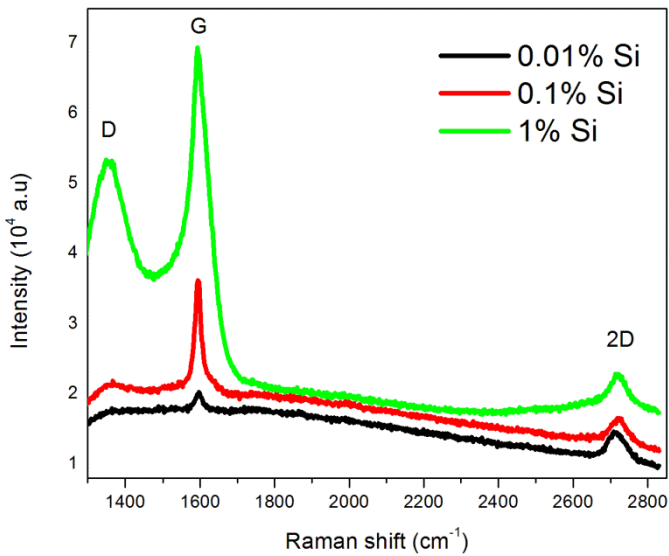


Fig. 5. Raman spectra of layers deposited on copper with various silicon contents

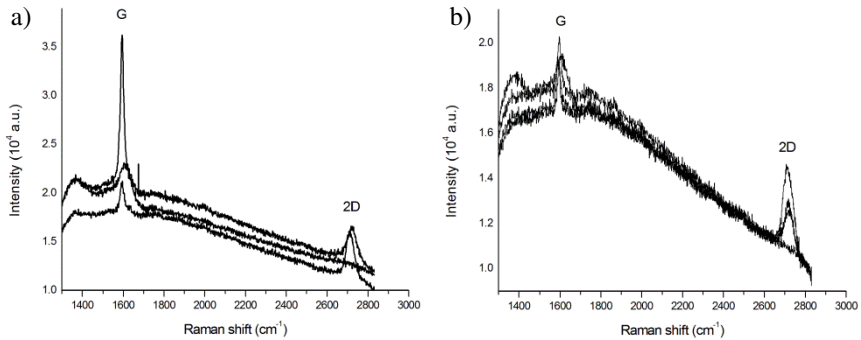


Fig. 6. Raman spectra after graphene deposition process a) 0.1% Si, b) 0.01% Si

The figures presented above clearly show that graphene layer was grown on the copper with silicon content 0.01%, that is, only on the copper with a very small admixture of silicon. **The following conclusion can be stated: any significant content of silicon prevents graphene layer from deposition.**

6 Graphene Layer Deposition on Other Bronzes

As in previous experiments the epitaxial method of graphene grow, elaborated in the Institute of Electronic Materials Technology, was used. In these experiments, we expanded the range of applied temperatures between 950 °C and 1000 °C.

As shown in Table 2, this time various bronzes, other than silicon bronzes, were used as substrates. Apart from the standardized bronzes, additionally some special bronzes were included, to extend the scope of experiments. The results of experiments are presented in Figs. 7–12.

Table 2. Bronzes, other than the silicon bronzes, used in the experiments

Item	Alloy	Chemical composition [%]	Reference Standard (w/ alloy identifier) [5]
1	CuAl10Fe3 Mn2	Al – 10; Fe – 3; Mn – 2; Cu – rest	EN 12166:2011 – CW306G
2	CuAl6Si2	Al – 6; Si – 2; Cu –rest	Special
3	CuSn10P	Sn – 10; P – 1; Cu – rest	EN 12166:2011 – CW305G
4	CuAl5	Al – 5; Cu – rest	Special
5	CuSn2	Sn – 2; Cu – 98	Special
6	CuNi2Be	Ni – 2; Be – 1; Cu – rest	EN 12166:2011 – CW110C
7	CuBe2	Be – 2; Cu – rest	EN 12166:2011 – CW101C
8	CuCo10	Co – 10; Cu – rest	Special



Fig. 7. Images of the surface of CuAl₆Si₂ bronze specimen: a) before the process, b) after the process, c) Raman spectra – absence of the graphene layer



Fig. 8. Images of the surface of CuNi₂Be bronze specimen: a) before the process, b) after the process, c) Raman spectra – absence of the graphene layer

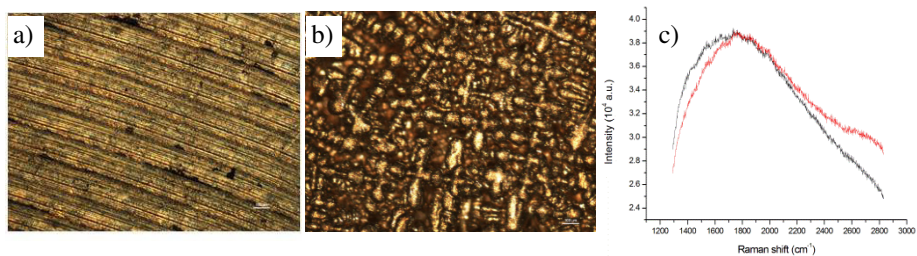


Fig. 9. Images of the surface of CuBe₂ bronze specimen: a) before the process, b) after the process, c) Raman spectra – absence of the graphene layer

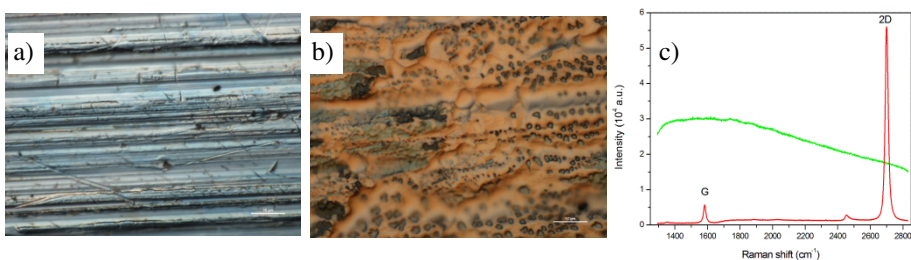


Fig. 10. Images of the surface of CuCo₁₀ bronze specimen: a) before the process, b) after the process, c) Raman spectra – absence of the graphene layer

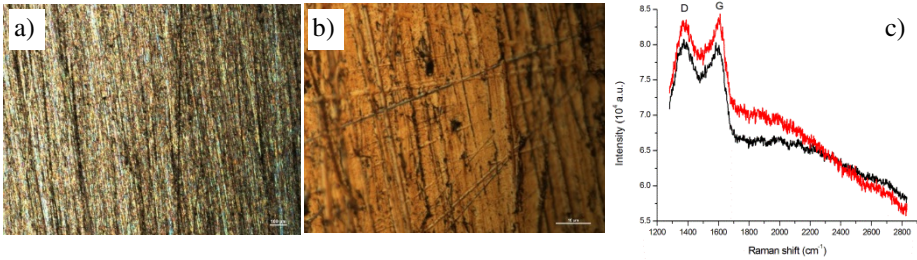


Fig. 11. Images of the surface of the CuAl15 specimen: a) before the process, b) after the process, c) Raman spectra – absence of the graphene layer

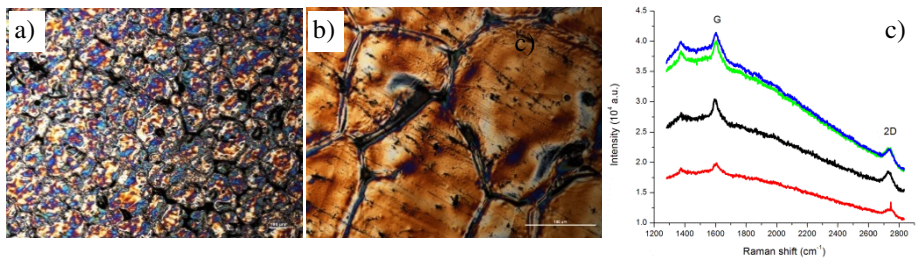


Fig. 12. Images of the surface of CuSn2 bronze specimen: a) before the process, b) after the process, c) Raman spectra – presence of the graphene layer

7 Graphene Layer Deposition on Steel Substrates Covered with Copper

To secure a possibility of conducting investigations of tribology properties and environment immunity of the graphene layer planned in the project [4], in case of failure of experiments with bronzes, the experiments of graphene layer deposition on steel substrates covered with copper layer were foreseen. Parameters of steels used for the substrates are presented in Table 3. Summary of the obtained results is given in Table 4 and the detailed results are shown in Figs. 13–15.

Table 3. Steels used for substrates

Item	Type of steel	Chemical composition [%]
1	45	C – 0.42 ÷ 0.50; Mn – 0.50 ÷ 0.80; Si – 0.17 ÷ 0.37
2	40HM	C – 0.38; Mn – 0.40; Si – 0.17; Cr – 0.90; Ni – <0.30; Mo – 0.15
3	35HGS	C – 0.32; Mn – 0.80; Si – 1.10; Cr – 1.10; Ni – <0.30

Table 4. Summary of results

Specimen identifier	Type of steel	Kind of surface process used	Coating	Presence of the graphene layer
G11-G14	45	Grinding	Electrolysis copper layer	YES
AA11-AA14	40HM-T	Grinding	Electrolysis copper layer	YES
BB11-BB14	35HGS	Grinding	Electrolysis copper layer	YES

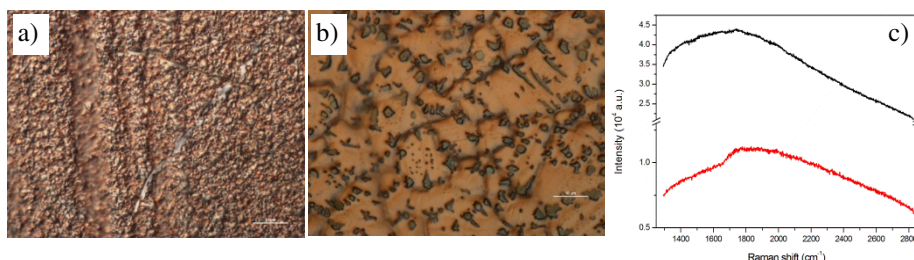


Fig. 13. Images of the surface of steel specimen covered with “acid copper”: a) before the process, b) after the process, c) Raman spectra – absence of the graphene layer

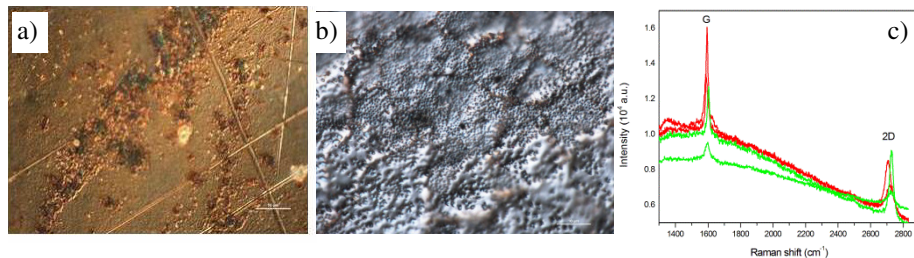


Fig. 14. Images of the surface of steel specimen covered with “electrolytic copper”: a) before the process, b) after the process, c) Raman spectra – presence of the graphene layer

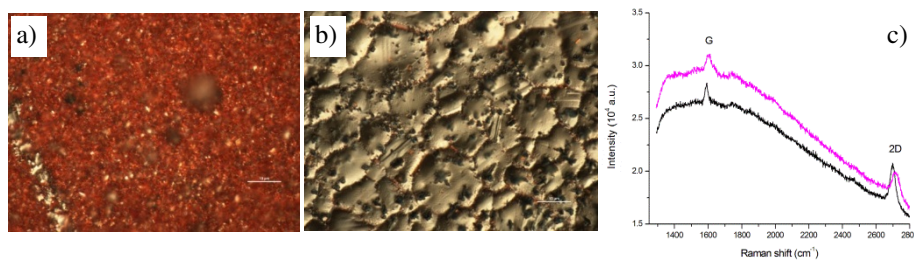


Fig. 15. Images of the surface of steel specimen covered with “cyanide copper”: a) before the process, b) after the process, c) Raman spectra – presence of the graphene layer

8 Alternative Experiments

To complete the investigations, additional experiments of graphene layer deposition on bronzes plated with copper layer are planned. The bronzes without silicon, aluminum, cobalt and nickel are selected for those experiments. In case of positive results, the way to obtain non-magnetic mechanical elements covered with graphene layer will be open.

9 Conclusions

The presented results indicate that deposition of the graphene layer on substrates other than copper or monocrystalline silicon carbide is practically impossible. Only the experiments of graphene layer deposition on specimens made of steel plated with copper were successful.

References

1. Money.pl>Technologie>Grafen. Materiał 100 razy mocniejszy od stali
2. NIST. Researches Quantyfynthe Friction of Graphene
3. Finnish researches plan to unravel the mechanical properties of atomically thin films, http://www.electronics-eetimes.com/_includes/print.php?lg=en&cmp_id+17&safe_m.
4. Project GRAPHTRIB – Graphene-based coatings of special gear-wheels and bearings. NCBR Contract No GRAPH – TECH/NCBR/05/13/2012
5. EN 12166:2911, Copper and copper alloys – Wire for general purposes

Study on Tribological Properties of Lubricating Grease with Additive of Graphene

Tadeusz Missala¹, Roman Szewczyk¹, Wojciech Winiarski¹, Marek Hamela¹,
Marcin Kamiński¹, Szymon Dąbrowski¹, Dawid Pogorzelski¹,
Małgorzata Jakubowska², and Jan Tomasiak²

¹ Industrial Research Institute for Automation and Measurements PIAP,
Al. Jerozolimskie 202, 02-486 Warsaw, Poland

{tmissala, rszewczyk, wwiniarski, mhamela,
mkaminski, sdabrowski, dpogorzelski}@piap.pl

² Institute of Metrology and Biomedical Engineering, Warsaw University of Technology,
Św. Andrzeja Boboli 8, 02-525 Warsaw, Poland
{maljakub, j.tomasik}@mchtr.pw.edu.pl

Abstract. This paper presents results of study on coefficient of friction of surfaces in case of lubrication with use of lubricating grease with 2% graphene additive, same grease without graphene additive and in case of no lubrication. Besides differences in coefficient of friction there are also shown differences in wear of specimens used in experiment. Results indicate that additive of graphene in lubricating grease decreases coefficient of friction as well as wear of friction pairs.

Keywords: graphene, tribology, grease.

1 Introduction

It is estimated that more than 30% of generated energy is wasted because of phenomena related to friction of interacting surfaces [1]. These phenomena cause additionally wear of these surfaces and in consequence lead to loose of functional properties of kinematic pairs and to damage them. A way to limit these very adverse effects is application of lubricating substance between cooperating surfaces which results in replacing external friction of these surfaces with internal friction of lubricating substance. Depending on thickness of lubricant film friction can be fluid (when this thickness is much higher than roughness of surfaces) or mixed (thickness is lower than roughness or both are close to each other – besides fluid friction there are also places on interacting surfaces where friction is boundary or even dry). It means that only first case (fluid friction) ensures full separation of surfaces. Thickness of lubricant film depends not only on viscosity of base oil (which is function of temperature) but also (most of all) on relative velocity and press between surfaces. Increasing of load causes decreasing of lubricant film thickness while increasing of speed means its increasing. It is not always possible to fulfill requirements to get fluid friction. Higher

level of viscosity results in higher internal friction which is disadvantage especially by high speeds. Working mode of machine can also be too slow or generate too big load and in practice mixed friction often occurs (especially by starting up). In this case decrease of wear and coefficient of friction depends on ability of base oil to create boundary layers which prevent surfaces from direct contact. Similar effect can be achieved by use of extreme pressure (EP), anti-wear (AW) and/or solid greases (graphite, molybdenum disulfide) additives. Application of these additives lets decrease base oil viscosity and in result increases performance of lubricated kinematic pair and whole machine.

Graphene consists of one atomic carbon layer with hexagonal layout. That's why it is considered as a two dimensional structure. Besides very good properties from the point of view of application in electronics, graphene has also high mechanical strength (approximately 100 times better strength tensile than by hardened steel) and thermal conductivity on a level of 5000 W/mK [2]. These properties as well as results of previous studies on influence of graphene on tribological properties of various lubricating fluids (see [3–5]) result in described in this paper experiment of adding graphene to lubricating grease, which potentially can improve its lubricity.

As a base to create lubricating grease with additive of graphene a commercially available lithium grease was chosen. Basic parameters of that grease were: mineral base oil with kinematic viscosity of 100 mm²/s (at 40 °C) and NLGI consistency number of 2 [6]. It didn't have any extreme pressure, anti-wear etc. additives in order to get grease where the only lubricity additives are graphene platelets (in described case 2% of weight of prepared grease).

2 Measuring Stand and Research Process

Main goal of research described in this paper was to examine the influence of graphene additive in lubricating grease on coefficient of friction and wear of interacting surfaces. For this purpose a measuring stand was built. It provides relative movement between surfaces forming a friction pair as well as measurement of coefficient of friction of this pair. Main part of this stand is shown on Fig. 1.

The stand (Fig. 1) consists of rotating in vertical axis replaceable track (1) which is ring-shaped. There are also three holders (2) to keep specimens (3) to be tested. Specimens are pressed to track (1) by the gravity with use of shield (4), pin (5) and loads (6). In order to have equal press on each one specimen there are two rotational degrees of freedom (in X and Y axis) between holders (2) and shield (4) and between shield (4) and pin (5). Thank to these there is parallelism between specimens (3) and track (1). Third degree of freedom (in vertical axis) between shield (4) and pin (5) is taken by force sensor (7). Force measured by this device is reaction to friction forces between track (1) and specimens (3). This force is recorded with numbers of pulses from rotation sensor (8) and after a few basic computations coefficient of friction characteristics can be shown.

Kinematics of the above described stand was formed in a way to get mixed friction with domination of boundary friction between interacting surfaces of track (1) and specimens (3). It is because the aim of the experiment was to test the influence of graphene on tribological properties of grease and not to test influence of base oil.

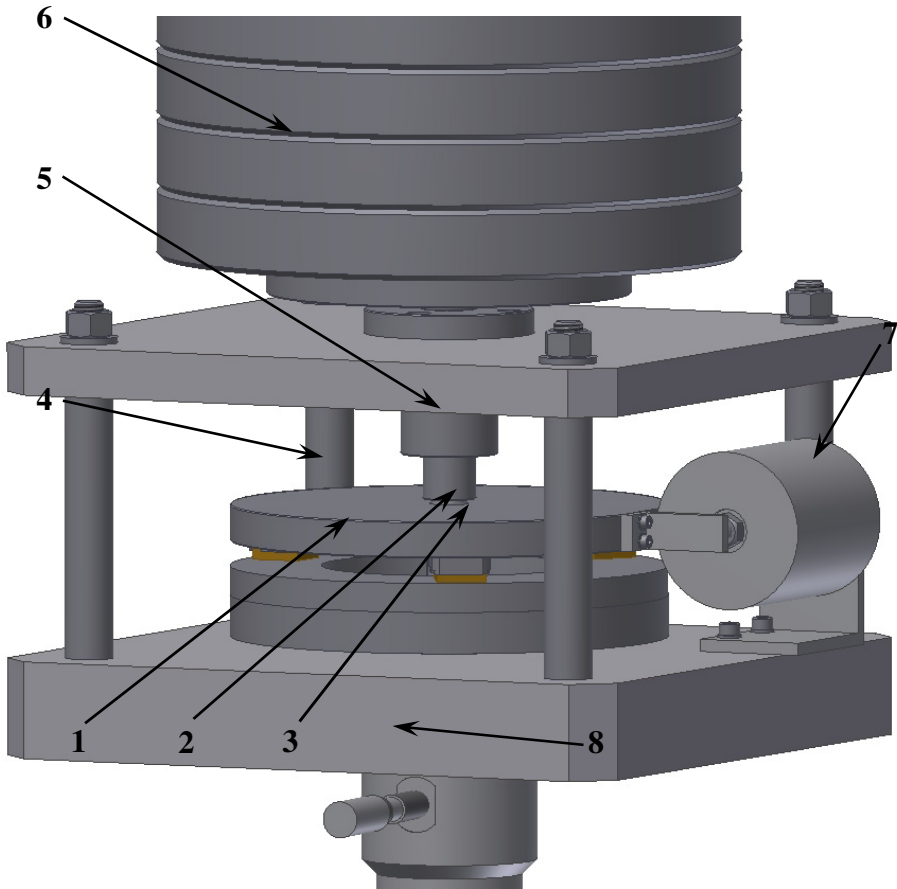


Fig. 1. Main part of the stand for tribological properties of graphene grease testing

Main parameters of the experiments carried out on the above described stand are: sort of grease, press, linear velocity, distance, materials of friction pairs and roughness of their surfaces. Three of the experiments are described in this paper. Since their goal was to determine influence of graphene on tribological properties of grease, only sort of grease was changed during these experiments: (a) described in p. 2 lithium grease with additive of graphene, (b) same grease without graphene additive, (c) no grease – experiment with (technical) dry friction. Values of other parameters of experiments are shown in the table 1.

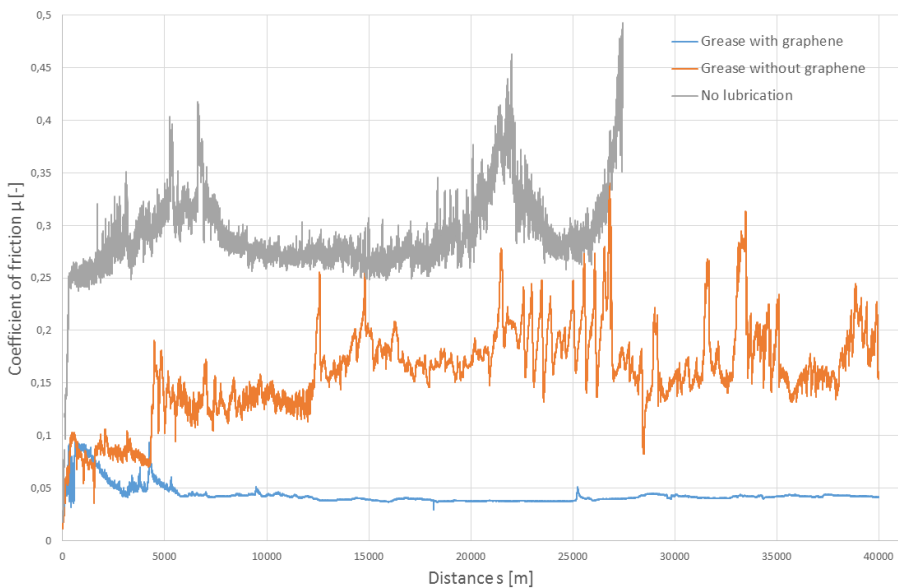
Table 1. Common values of parameters of tests

Parameter	Value
Press [MPa]	2.2
Velocity [m/s]	0.53
Distance [m]	40 000
Specimen material	Bronze CW306G (CuAl10Fe3Mn2)
Track material	Steel 41Cr4
Specimen surface roughness [μm]	~ 0.4 (see tab. 3)
Track surface roughness [μm]	~ 0.3 (see tab. 3)

Although working of the built stand causes wear of specimens, quantity description of this wear was determined on the other stands in two ways: by measurement of mass of specimens before and after experiment (scales RADWAG PS 600.R2) and as a result of measurement of roughness of surfaces before and after experiment (profilometer Taylor-Hobson Talysurf PGI830) with application of guidelines described in [7].

3 Results

Results of the experiments described in section 3 are shown for better clearness on the Fig. 2 as diagrams of coefficients of friction μ versus distance s .

**Fig. 2.** Diagrams of coefficients of friction μ versus distance s

According to expectations the highest value of coefficient of friction occurred in experiment with no use of lubrication (Fig. 2, grey diagram) and it generally laid in range of 0.25–0.3. Described investigation was finished after approximately 27 000 m because of too high wear of specimens and related to this increase of coefficient of friction which caused that reaction force on force sensor ((7) on Fig. 1) exceeded its limit. Application of lubricating grease without any EP/AW additives (Fig. 2, orange diagram) decreased coefficient of friction in first 5 000 m below 0.1. In remaining part of experiment (5 000 m to 40 000 m) coefficient was about 0.15–0.2, but this value was very unstable. It can be connected with variable conditions of lubrication, appearing on areas with dry lubrication and tear particles of surfaces. Enhancing grease with 2% of graphene platelets additive brought an expected result (see Fig. 2, blue diagram). Although at the beginning of the experiment coefficient of friction laid on level of 0.1, after short distance it reached stable value of 0.4, which didn't change during the whole experiment. Initial higher value was probably consequence of running in of surfaces and of their warming up. Further results indicate that after remove highest peaks layer of graphene was durable enough to prevent surfaces from appearance of dry friction areas and as a result from adhesion and removing particles of surfaces.

Table no. 2 shows mean values of mass of specimens before and after experiments.

Table 2. Mean mass loss of specimens as a result of experiments

Lubrication	Mean mass before experiment [g]	Mean mass after experiment [g]	Mean mass loss [g]
Grease with graphene additives	12.6068	12.6053	0.0015
Grease without graphene additives	12.6167	12.6049	0.0118
No lubrication	12.6008	8.8721	3.7287

Results of mass loss measurements shown in table no. 2 can be explained in a quite similar way as results of measurement of coefficient of friction. The least mass loss in case of lubrication with graphene additive grease is effect of acting of graphene which creates a layer that limits direct contact between track and specimens. Boundary layer created by same grease without graphene platelets is much weaker and that's why adhesion is more intensive and material loss is bigger. Lack of boundary layer (from technical point of view) in case where no lubrication is applied causes catastrophic wear of surfaces. These phenomena can also be confirmed by the measurement of roughness of specimens layer before and after experiments (Tab. 3). It is worth noticing that in case of use of graphene grease roughness after the experiment is much lower than before. It is the result of running in the surfaces at the beginning of

experiment. By use of grease without graphene platelets there also can be seen improvement of surface quality but it is not as big because of bigger adhesion between specimens and track.

Table 3. Changes in roughness of surfaces as a result of frictional experiments

Lubrication	Specimens		Track	
	Mean roughness R_a before experiment [μm]	Mean roughness R_a after experiment [μm]	Mean roughness R_a before experiment [μm]	Mean roughness R_a after experiment [μm]
Grease with graphene additives	0.4159	0.1685	0.3549	0.2657
Grease without graphene additives	0.4006	0.3192	0.2709	0.3051
No lubrication	0.4093	5.1003	0.2273	4.0319

4 Conclusion

Results of studies presented in this paper confirm usefulness of graphene platelets as additives decreasing coefficient of friction and wear of friction pairs. Two percent of this ingredient caused four-time-decrease of coefficient of friction in conditions of mixed lubrication and almost eight-time-decrease of wear (weight). Results like these induce to expand studies on this kind of greases on searching for optimal content of graphene additive. Durability of graphene platelets layer as well as their influence on coefficient of friction in conditions of fluid lubrication should also be investigated.

Acknowledgements. This work has been supported by the National Centre for Research and Development (NCBiR) within the GRAF-TECH programme (no. GRAF-TECH/NCBR/05/13/2012).

References

1. Hebda, M., Wachal, A.: Trybologia. Wydawnictwa Naukowo-Techniczne, Warszawa (1980) ISBN 83-204-0043-0
2. Balandin, A.A., Ghosh, S., Bao, W., Calizo, I.: Superior Thermal Conductivity of Single-Layer Graphene. *Nano Letters* 8(3), 902–907 (2008)
3. Berman, D., Erdemir, A., Sumant, A.: Few layer graphene to reduce wear and friction on sliding steel surfaces. *Carbon* 54, 454–459 (2013)
4. Kinoshita, H., Nishina, Y., Alias, A., Fujii, M.: Tribological properties of monolayer graphene oxide sheets as water-based lubricant additives. *Carbon* 66, 720–723 (2014)

5. Lin, J., Wang, L., Chen, G.: Modification of graphene platelets and their tribological properties as a lubricant additive. *Tribol Lett* 41, 209–215 (2011)
6. Datasheet Shell Gadus S2 V100 2, http://www.epc.shell.com/docs/GPCDOC_Local_TDS_United_Kingdom_Shell_Gadus_S2_V100_2_en-GB_TDS.pdf
7. Tomasik, J., Rudziński, R.: Wpływ odstępu próbkowania na wartości wybranych parametrów chropowatości powierzchni. *Pomiary Automatyka Robotyka* 11, 5–7 (1998)

Resistance of MAX 6325 Reference Voltage Source on Operating Temperature Variation

Paweł Nowak¹, Andrzej Juś¹, and Roman Szewczyk²

¹ Industrial Research Institute for Automation and Measurements,
Al. Jerozolimskie 202, 02-486 Warsaw, Poland

² Warsaw University of Technology, Faculty of Mechatronics,
sw. A. Boboli 8, 02-525 Warsaw, Poland
{pnowak, ajus}@piap.pl

Abstract. The article presents the problem of the Zener diode based reference voltage sources resistance to changes in operating temperature. The test stand, measurement methodology and results are presented. Reference voltage sources are crucial elements of analog-to-digital systems. They set the standard to which the measured voltage is compared to. Therefore, the stability of their work is critical for many areas of precision metrology.

Keywords: voltage references, temperature coefficients, electrical measurements, FPGA, ADC.

1 Introduction

Many industrial systems are based on precision measurements. High-tech production lines require reliable and high-resolution measurements systems. The highest accuracy is achieved in electrical measurements, so even the non-electric values (like strain, pressure or temperature) are measured by transforming them to voltage, and measuring them [9, 10]. All precise analog to digital converters operate on the principle of differential measurement [8]. Measured voltage is compared with the standard, which is the reference voltage source. The stability of this standard is crucial for the stability and accuracy of measurements. The greatest impact on the standard stability have: supply voltage change (line regulation) [4], variation of the output current (load regulation) and variation of operating temperature. Measurement systems are supposed to work and being reliable in variable environmental conditions, therefore the standards should be resistant to temperature change in the operating temperature range.

2 Temperature Drift of the Reference Sources Utilizing Zener Diodes

Temperature drift is described as average value of small changes in reference's output voltage, caused by changes in temperature ($\Delta V_{\text{out}}/\Delta T$), and is expressed in ppm/°C.

In precise applications temperature drift is considered as the second (after initial accuracy) most important specification. In some solutions (for example in balances) initial accuracy can be compensated, which makes thermal resistance even more crucial. Ideally, the output voltage should not change by any measurable value in the whole operating temperature range. In reality, the output voltage will change in a way depending on reference quality. References based on buried-Zener technology have the lowest temperature coefficients in range from between 0.5 to 8 ppm/°C. [1] Highest thermal stability is achieved by temperature-compensation circuits in reference designs. The elements are also measured during the production, and some crucial elements (like thin-film resistors) are precisely trimmed with laser.

Temperature coefficients are commonly given in datasheets as single value, which assumes and suggests that temperature drift is linear. In most cases the $\Delta V/T$ function is described by 2nd or even 3rd degree function which are presented on graphs.

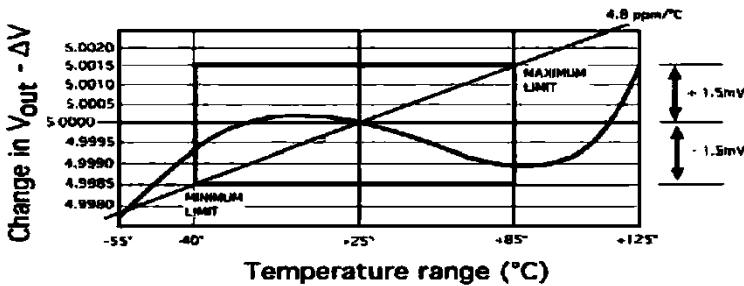


Fig. 1. Thermal characteristic of voltage reference [1]

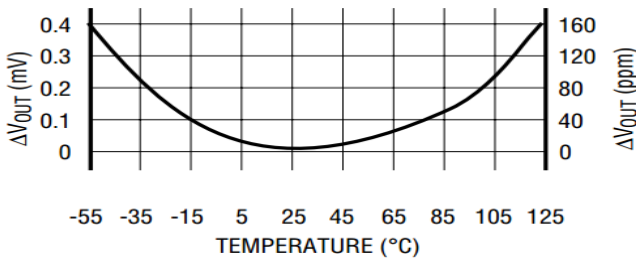


Fig. 2. MAX 6325 normalized output voltage in temperature function [2]

As presented in Fig. 1 and Fig. 2, manufacturers are using two methods for providing high stability references. First one (presented in Fig. 1) is to achieve constant temperature coefficient in typical operating range (in laboratory equipment it's typically 15–35 °C). This method is extremely useful when device utilizing reference has internal temperature measurement system – continuous corrections can be easily implemented in device software. Second method (as presented in Fig. 2) is to achieve

minimal output variation in operating temperature range. This method provides higher reference stability around operating point (typically 25 °C), but can be source of serious measurement errors, when device/circuit is operating in extremal temperatures.

3 Test Stand

3.1 General Idea

Schematic block diagram of designed test stand is presented in figure 3.

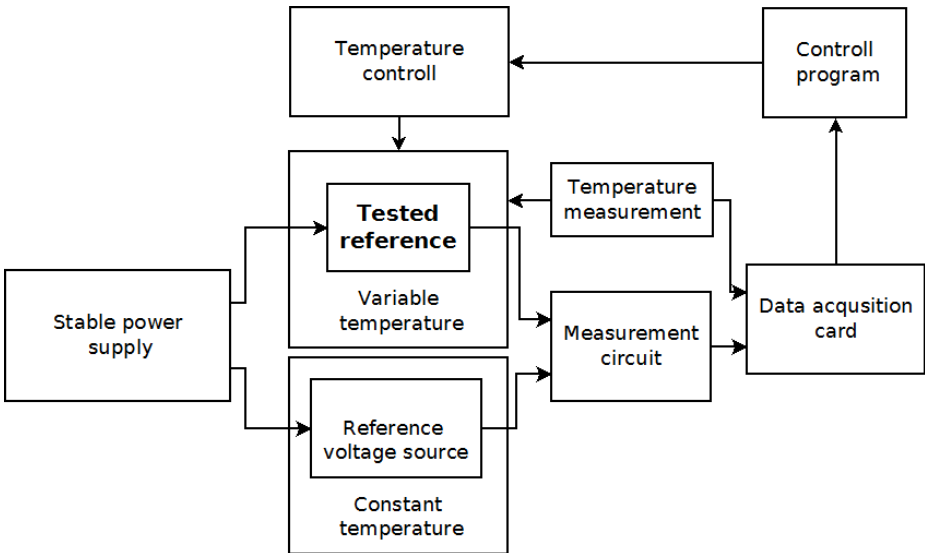


Fig. 3. Schematic block diagram of the test stand

The main idea of the utilized test stand is based on high accuracy differential voltage measurement. The tested source is operating in changing environmental conditions. The output voltage is compared with a reference voltage source operating in constant temperature. The difference of these voltages is amplified and then measured by a data acquisition card and stored along with operating temperature of the tested reference.

3.2 Variable Operating Temperature System

Change of operating conditions was achieved, by placing tested reference to copper block. Block was drilled, so liquid (water) could flow through. Due to the copper thermal conjunction, temperature of the liquid is transferred on tested reference source. Thus by controlling liquid temperature (by heating water with immersion heater), temperature variation was achieved.

3.3 Voltage Variation Measurement Circuit

To acquire highest accuracy of measurement, it was decided to design differential measurement circuit. The wiring diagram of measurement circuit is presented in Fig. 4.

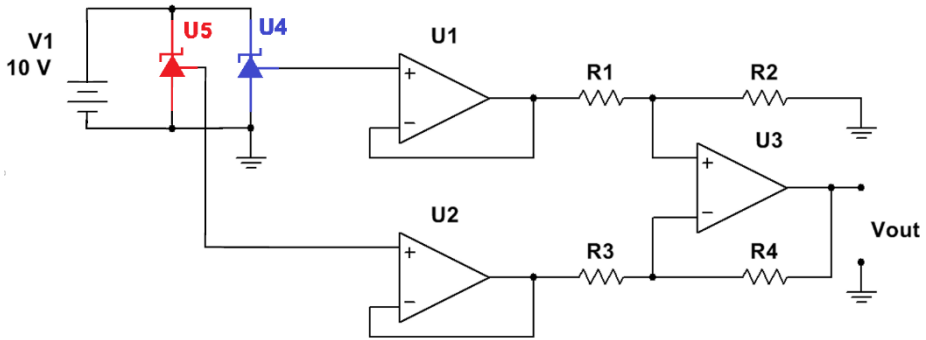


Fig. 4. Wiring diagram of measurement circuit

Both references, tested (U5) and standard (U4), are powered by the constant voltage from stabilized power source. Operational amplifiers (U1 and U2) work as a voltage followers. Their main function is to provide high and constant impedance for voltage references. The next element of circuit is a differential amplifier built on U3 and R1, R2, R3, R4 highly accurate resistors. As it can be proven [4–6], when following requirement $\frac{R_2}{R_1} = \frac{R_4}{R_3} = k$ is fulfilled, voltage held on the output of U3 is given by following dependency:

$$V_{out} = (V_1 - V_2) \cdot k \quad (1)$$

Where V_1 and V_2 are output voltages held on operational amplifiers U1 and U2. Output voltage of measurement circuit is measured by the data acquisition card, and processed by software using (1) in order to give information about tested voltage reference output change.

3.4 Temperature Measurement System

The measurement of temperature is conducted with K-type thermocouple placed in between the copper block and the tested reference. Thermocouple is connected to the programmable temperature-voltage converter with internal cold junction compensation, based on Pt 100 resistor [3]. On converter's output, voltage proportional to hot junction temperature, is held. This voltage is measured by data acquisition card and calculated by software to temperature value. The value of temperature is used for creation of $\Delta V(T)$ dependency.

4 Measurement Methodology

Test were performed on three different sources. Operating temperature of the tested source was changing in the 10–38 °C range, with approximated speed of 10 K per hour. Standard reference, as well as measurement circuit was held in stabilized temperature 25 °C.

5 Measurement Results

On the following figures the results of the measurements conducted according to the methodology described above are presented. Additionally, on each characteristic there is a black line marking the maximum allowable deviation according to [2].

The results obtained have significant repeatability. In addition, all of the results are below the curve created on the basis of catalog data [2]. Individual disorders are caused by noise in the measurement system. The second degree nature of the voltage deviation change in function of temperature is clearly seen. In order to better determine the nature of the changes, a second degree curve fit was carried out:

$$f(T) = aT^2 + bT + c \quad (1)$$

Fitted (using the least squares method) curves are presented on figures 5, 6 and 7 and are marked in red. The parameters of curves, together with R^2 match coefficients and parameters of maximal allowable deviation curve are shown in following table.

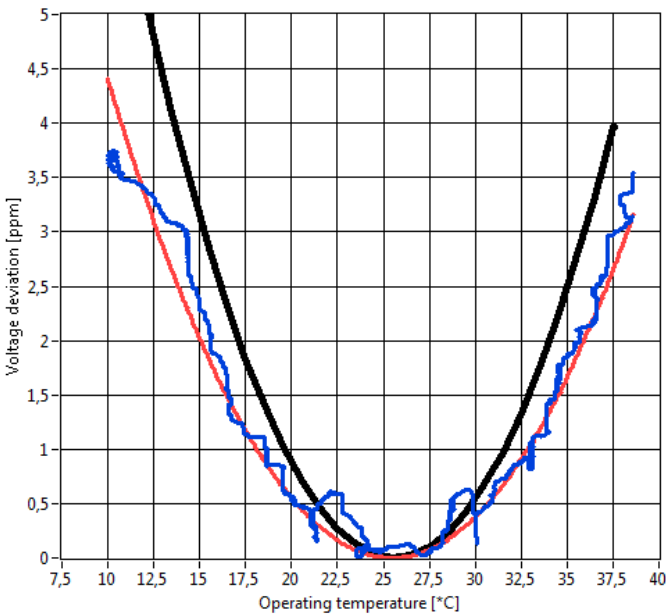


Fig. 5. Results of tested reference no.1

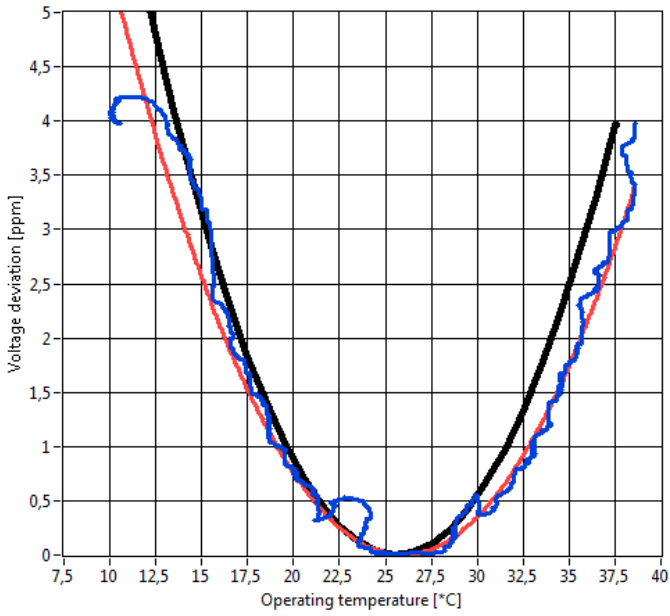


Fig. 6. Results of tested reference no.2

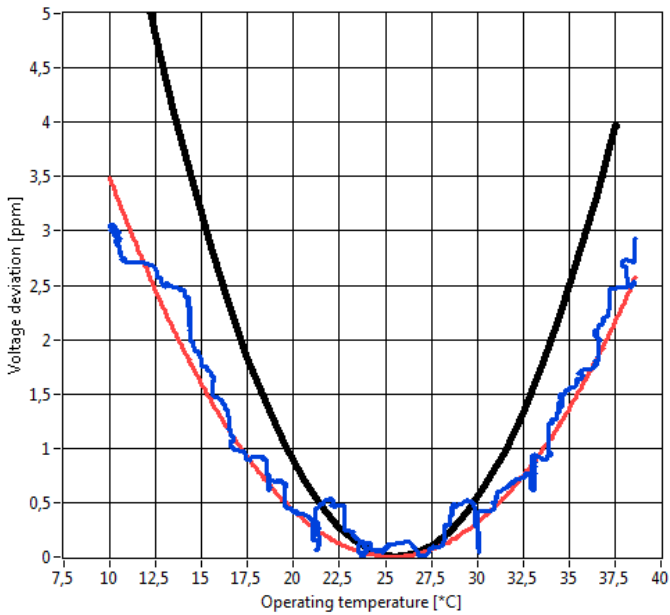


Fig. 7. Results of tested reference no. 3

Table 1. Comparisons of fitting parameters

Number of tested source	Parameters			
	a	b	C	R ²
1	0.0183	-0.9362	12.6224	0.966
2	0.0213	-0.9673	15.2382	0.952
3	0.0147	-0.7482	10.0495	0.965
Maximal allowable Deviation	0.0279	-1.4319	18.3237	0.998

Due to the high (between 0.95 and 0.99) R² coefficient it was decided not to carry out further statistical tests [7] in order to confirm the nature of the temperature changes impact on the reference sources characteristics.

Results of measurements are beneath the maximum allowable deviation curve, which is also confirmed by the comparison of parameters of fitted curves.

Thermal coefficient of tested reference can be calculated as a derivative of V(T) function. With assumption of second order nature of characteristics, it can be calculated as:

$$TC(T) = \frac{\partial f(T)}{\partial T} = 2aT + b \quad (2)$$

Analyzing (2) leads to simple conclusion, that thermal coefficient varies depending on the temperature. Table 2 presents calculated coefficients for boundary test temperatures, and in recommended operating temperature.

Table 2. Comparisons of calculated thermal coefficients

Number of tested source	TC [ppm/ °C]			
	Temperature [°C]	10	25	38
1		-0.5702	-0.0212	0.4546
2		-0.5413	0.0977	0.6515
3		-0.4542	-0.0132	0.369
Maximal allowable deviation		-0.8739	-0.0368	0.6885

All calculated thermal coefficients are in the range declared by manufacturer (± 1 ppm/°C) [2]. All tested sources have minimum of temperature characteristic around 25 °C. This result with high stability in typical operating temperature.

In typical laboratory environment temperature changes does not affect voltage output significantly. On the other hand, they depend on temperature and may increase outside declared limit while operating in extreme temperature.

6 Conclusion

Test stand for measuring temperature characteristics of reference voltage sources is presented. Methodology and the results are shown, and they confirm both the literature and sheet data. Second degree polynomial curve fit of test results is presented.

Results preset high repeatability of thermal characteristics of tested reference voltage sources. All characteristics have minimum around 25 °C, which should be recommended operating temperature. Measurements confirmed, that all

Effective way of calculating thermal coefficient in operating temperature is described, and data from reference voltage source manufacturer are confirmed in wide temperature range.

Acknowledgments. This work was partially supported by The National Center for Research and Development with PBS Program – Grant no. PBS 1/B3/8/2012.

References

1. Harrison, L.T.: Current sources and voltage references. Elsevier Inc. (2005)
2. MAX 6325 datasheet provided by Maxim Integrated
3. Kerlin, T.W., Johnson, M.: Practical Thermocouple Thermometry, 2nd edn. Research Triangle Park, ISA (2012)
4. Nowak, P., et al.: Resistance of MAX 6325 Reference Voltage Source on Supply Voltage Variation. In: Mechatronics-Ideas for Industrial Application, pp. 337–344. Springer International Publishing (2015)
5. Nowak, P., Juś, A., Szewczyk, R., Pijarski, R., Nowicki, M., Winiarski, W.: Test Stand for Temperature Characteristics of Ultra-Precise Resistors. In: Awrejcewicz, J., Szewczyk, R., Trojnecki, M., Kaliczyńska, M. (eds.) Mechatronics: Ideas for Industrial Applications. AISC, vol. 317, pp. 345–352. Springer, Heidelberg (2015)
6. Horowitz, P., Hill, P.: The art of electronics, 2nd edn. Cambridge University Press, Cambridge (1989)
7. Dobosz, M.: Wspomagana komputerowo statystyczna analiza wyników badań, EXIT (2004)
8. Korytkowski, J.: Monolityczne układy konwerterów sigma-delta do pomiaru wartości skutecznej napięcia i ich porównanie ze scalonymi konwerterami klasycznymi. Pomiary, Automatyka, Robotyka 16, 84–89 (2012)
9. Korytkowski, J.: Układ elektroniczny cyfrowej syntezy rezystancji do dokładnej symulacji rezystancyjnych czujników temperatury. Pomiary Automatyka Robotyka 5, 86–92 (2013)
10. Warsza, Z.L.: New approach to the accuracy description of unbalanced bridge circuits with the example of Pt sensor resistance bridges. Journal of Automation Mobile Robotics and Intelligent Systems 4, 8–15 (2010)

Magnetic Thermogravimetric Analysis of CuCo and CuFe Amorphous Alloys

Michał Nowicki¹, Peter Švec Sr.², Dorota Jackiewicz³, and Roman Szewczyk³

¹Institute of Metrology and Biomedical Engineering,
Warsaw University of Technology, Warsaw, Poland
m.nowicki@mchtr.pw.edu.pl

²Institute of Physics, Slovak Academy of Sciences
Peter.Svec@savba.sk

³Industrial Research Institute for Automation and Measurements,
Al. Jerozolimskie 202, PL-02-486, Warsaw, Poland
szewczyk@mchtr.pw.edu.pl

Abstract. In the paper the investigation of the temperature dependent magnetic weight change of the $\text{Cu}_{100-x}\text{Co}_x$, $x = [10, 15, 20]$ and the $\text{Cu}_{90}\text{Fe}_{10}$ amorphous alloys is presented. The idea and the test stand of the magnetic thermogravimetry analysis is described. The results of the measurements for investigated CuCo and CuFe amorphous alloys, as well as discussion of the results are given.

Keywords: TGA, amorphous alloys, CuCo, GMR.

1 Introduction

The thermogravimetric analysis is a widely used method of materials investigation. It is used as a technique to characterize materials used in various environmental, food, pharmaceutical, and petrochemical applications. The definition of the method states that it is a technique in which the mass of a substance is monitored as a function of temperature or time as the sample specimen is subjected to a controlled temperature program in a controlled atmosphere. An alternate definition: it is a technique in which, upon heating a material, its weight increases or decreases [1].

The thermogravimetric analyzer is an essential laboratory tool used for material characterization. An TGA consists of a sample pan that is supported by a precision balance. That pan resides in a furnace and is heated or cooled. The mass of the sample is monitored during the experiment. A sample purge gas controls the sample environment. This gas may be inert or a reactive gas, that flows over the sample and exits through an exhaust. These instruments can quantify loss of water, loss of solvent, loss of plasticizer, decarboxylation, pyrolysis, oxidation, decomposition, weight % filler, and weight % ash. All these quantifiable applications are usually done upon heating, but there are some experiments where information may be obtained upon cooling. The analyzers are controlled by proprietary thermal software, and have autosampler

accessories for unattended operation. The basic instrumental requirements for TGA are a precision balance, usually of the magnetomechanical type, with a pan loaded with the sample, and a programmable electric furnace [2].

Magnetic TGA is the method in which the magnetic field gradient is acting upon the sample, introducing the *magnetic weight* :

$$F = (m_a - m_b)g = m_m g \quad (1)$$

where: F – force of magnetic attraction between the sample and magnetic field gradient source, m_a – sample mass reading without the magnetic field, m_b – sample mass reading with the magnetic field gradient applied, m_m – magnetic weight.

The force F is called the Faraday Force. It is the force of magnetic attraction (or repulsion), dependent upon the sample magnetic susceptibility, shape, mass and the magnetic field gradient dH/dy . The sample of the volume V is subjected to the force depending on the magnetic dipole moment $j = \mu_0 m$ or susceptibility $\chi = \mu - 1$ [3]:

$$F = j \frac{dH}{dy} = V \chi H \frac{dH}{dy} \quad (2)$$

In situation where the magnetic field value and gradient are kept constant, the sample mass, shape and volume are constant, the resulting force and thus magnetic weight, will be directly proportional to the volume susceptibility χ (or magnetic dipole moment) of the sample. Various processes during the heating and cooling phases affect the magnetic susceptibility of the material, and are detected as the changes in the magnetic weight.

The magnetic TGA method is most often used for measurement of Curie temperature of investigated materials – it is the temperature at which rapid decrease of the magnetic weight is recorded, due to the rapid transition from the ferromagnetic (or antiferromagnetic) to the paramagnetic state. In fact, the Curie temperatures of several reference alloys (alumel, pure nickel, pure iron) are used for temperature calibration of TGA furnaces. Furthermore, the relative changes of the magnetic weight can give important clues about the temperature dependence of various phase transitions in the materials tested [2].

2 Test Stand

The test stand used for the investigation was the Perkin-Elmer TGA7 Thermogravimetric Analyzer with the magnetic field gradient source allowing for the magnetic TGA measurements. The samples can be heated in a specified atmosphere, the gas being selectable via data system control. The furnace can heat samples from room temperature to 1000 °C, at a selectable rate of 0.1 °C/min to 200 °C/min. The analytical balance of the null design is sensitive to 0.1 microgram. The amount of current needed to maintain the system in the "null" state is directly proportional to the weight change of the sample. System is controlled by the Pyris software, which allow for data logging and analysis. The schematic block diagram of the test stand is presented in Fig. 1.

The magnetic field gradient is provided by the two permanent magnets located to the sides of the furnace, below the sample. The magnets position is adjustable, to obtain vertical pulling force of certain initial value, acting upon the sample. The method itself, using the gradient fields and the analytical balance, is very similar to the Faraday balance, or the Faraday Force magnetometry [4]. On the other hand, usage of the permanent magnets with constant (during the experiment) field gradient of relatively small value make this method alike the Evans balance [5] and Gouy balance [6] methods, used primarily for the measurement of very small magnetic susceptibility values of paramagnetic and diamagnetic materials.

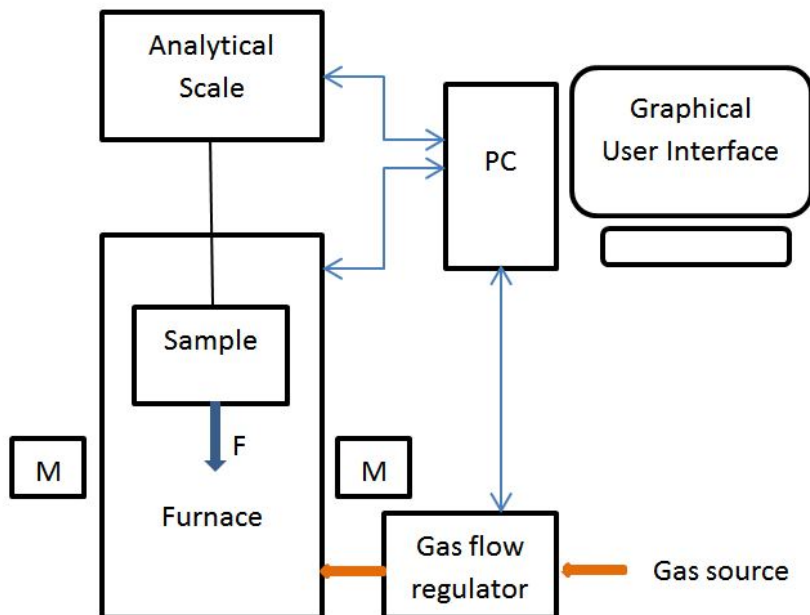


Fig. 1. Schematic block diagram of the test stand. M – permanent magnets

The apparent change in weight of the sample (the magnetic weight) is dependent upon the relative change of the magnetic susceptibility. The value of the magnetic susceptibility χ could then be calculated, knowing its initial value before the experiment. It is however irrelevant for the observation of temperature dependence of the various phase transitions in the material tested – the information can be derived from the relative change of the magnetic weight itself.

3 Investigated Materials

There were four materials investigated using the magnetic TGA method. Three of them were composed of copper and cobalt in 90–10%, 85–15% and 80–20% ratios.

The fourth, for comparison, was the $\text{Cu}_{90}\text{Fe}_{10}$ alloy. They were fabricated using the rapid quenching in the melt spun process, on specially provided wheels (as normally the casting equipment has wheels made of copper, due to its superior heat conductivity). Melt spinning is a technique used for rapid cooling of molten metals. A wheel is cooled internally, usually by water or liquid nitrogen, and fast rotated. A thin stream of liquid metal is then poured onto the wheel and instantly cooled, causing rapid solidification. This technique is used to develop materials that require extremely high cooling rates in order to form, such as metallic glasses [7]. The cooling rates achievable by melt-spinning are on the order of 10^4 – 10^7 K/s. The technique was used to cast ribbons of the CuCo and CuFe amorphous alloys. The $\text{Cu}_{100-x}\text{Co}_x$ amorphous alloys are especially interesting because of their magnetic and magnetoresistive properties. The unprocessed material behaves as almost superparamagnetic cobalt particles suspended in the diamagnetic copper medium [8, 9]. However, during the heating process, the cobalt lattices are beginning to form, changing the magnetic hysteresis of the material [10], and causing the occurrence of giant magnetoresistive effect (GMR) and giant magnetoimpedance effect (GMI) [11]. The GMI effect is typical for cobalt-rich amorphous alloys [12]. The highest reported GMR values were obtained for annealing in the 500 °C range [11, 13]. Annealing of the amorphous alloys have to be done in precisely controlled temperature and time conditions, to achieve replicable results [14]. Another interesting feature of these alloys is the remarkable complexity and non-linear behavior of the material phase transitions [15].

4 Results of Measurement

The samples were independently loaded into the measuring pan of the TGA in the absence of the magnetic field. The furnace was preheated to the 50 °C for stable measurements start point, and the balance readings were zeroed. Then the magnetic field gradient was introduced by means of the permanent magnets to achieve proper starting magnetic weight value. The samples were heated to the 800 °C at a 10 °C/min rate, and then cooled from 800 °C to 50 °C at the same 10 °C/min rate. The furnace was constantly purged with inert gas (argon), to avoid any oxidation-related readings.

In the following figures the obtained results are presented. In the Fig. 2 the magnetic weight/temperature characteristic of the $\text{Cu}_{90}\text{Co}_{10}$ amorphous alloy sample is shown. The first, heating part of the characteristic is colored in red. There is an initial slight decrease of the magnetic susceptibility up to around 218 °C, then there is a plateau up to 325 °C, where rapid increase of the magnetic weight occurs. This hint of the developing cobalt crystals in previously homogenous amorphous alloy. Then there is slight inflection point around 480 °C, and higher rate of magnetic weight increase – interesting because this is the region where highest reported GMR values were obtained (for annealing in around 500 °C, and cooling the material).

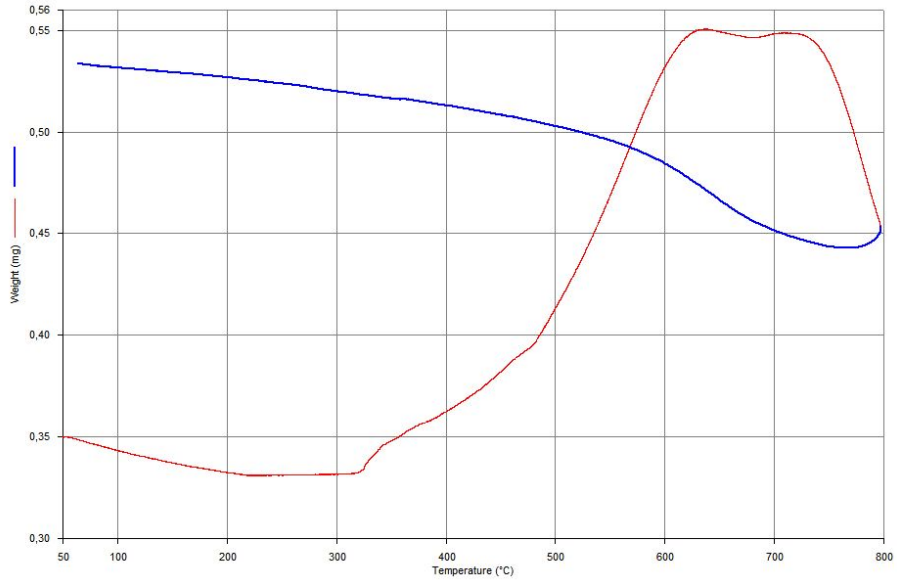


Fig. 2. The magnetic weight characteristic of the heated (red line) and cooled (blue line) $\text{Cu}_{90}\text{Co}_{10}$ amorphous alloy sample

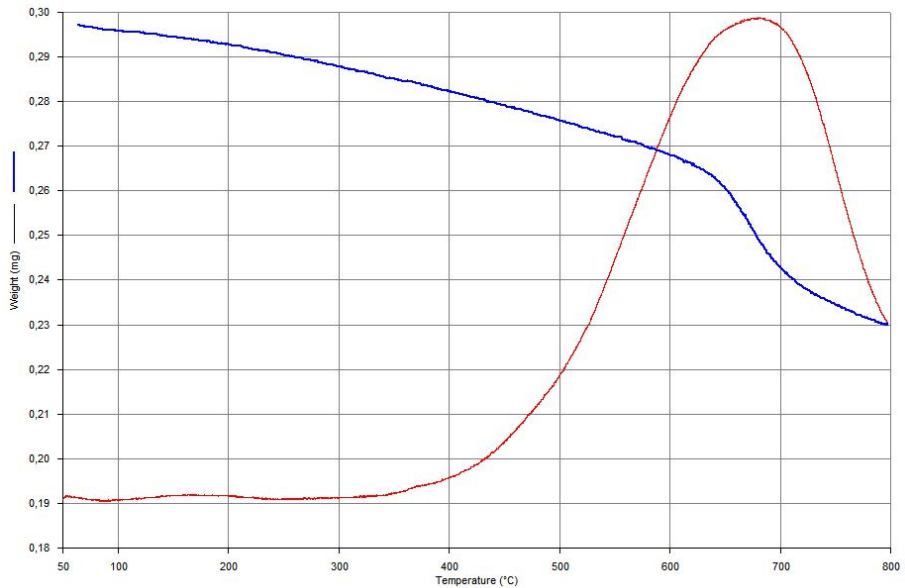


Fig. 3. The magnetic weight change of the heated (red line) and cooled (blue line) $\text{Cu}_{85}\text{Co}_{15}$ amorphous alloy sample

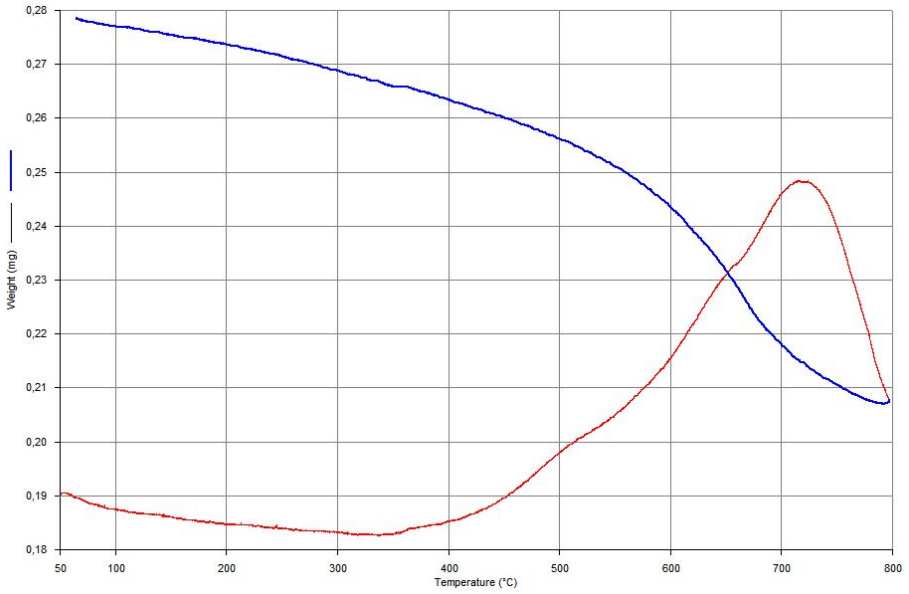


Fig. 4. The magnetic weight change of the heated (red line) and cooled (blue line) $\text{Cu}_{80}\text{Co}_{20}$ amorphous alloy sample

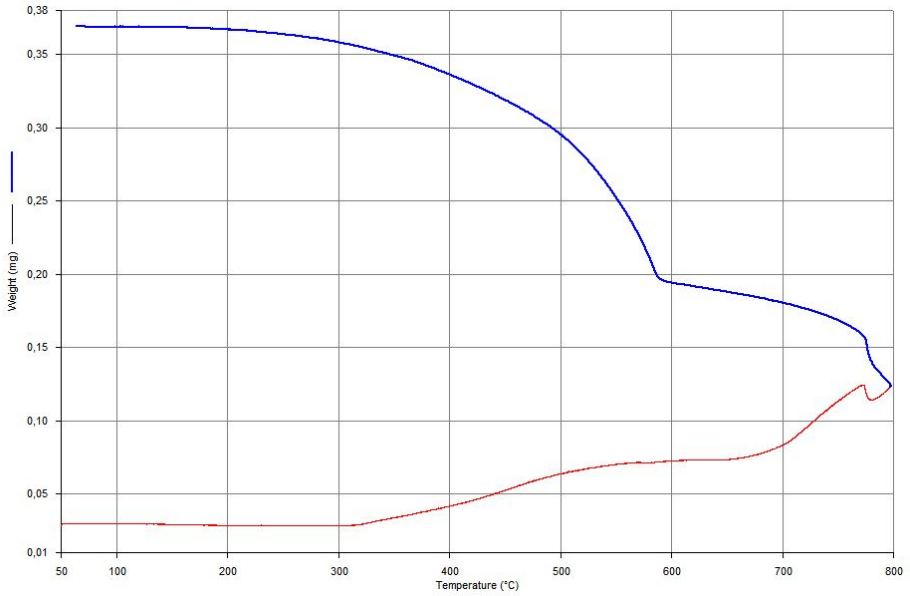


Fig. 5. The magnetic weight change of the heated (red line) and cooled (blue line) $\text{Cu}_{90}\text{Fe}_{10}$ amorphous alloy sample

From 630 °C to 725 °C there is an curious dented region with two maximum points. Then the susceptibility starts to decrease rapidly, most probably due to reaching the Curie temperature, which was above the heating range during the experiment. The blue line represents the cooling phase of the experiment – the substantial increase in the magnetic weight of the cooled sample versus the initial state is due to the ferromagnetic cobalt crystals formation.

In the Fig. 3 the characteristics of the $\text{Cu}_{85}\text{Co}_{15}$ amorphous alloy are shown. The most obvious difference to the previous characteristic is the lack of the “double maximum” in the heating phase. Additionally, the highest GMR ratio for this alloy ratio was reported to occur for annealing in 525 °C [12]. One can observe slight inflection point on the characteristic in this temperature region. In the Fig. 4 the characteristics of the $\text{Cu}_{80}\text{Co}_{20}$ are given. The overall shape is similar to $\text{Cu}_{85}\text{Co}_{15}$, the most notable difference is the much higher magnetic weight in the cooled state relative to the heating maximum.

In the Fig. 5 one can observe the characteristics of the $\text{Cu}_{90}\text{Fe}_{10}$ amorphous alloy. It is obviously different from the previous ones, even though the similarities between Fe and Co elements. The most interesting is the final part of the curve, from around 750 °C to 800 °C, during both heating and cooling phase. The overall relative permeability change was much higher than for CuCo alloys. The initial χ absolute value was also noticed to be exceptionally small (however it was not measured directly), as the applied magnetic field gave unexpectedly small magnetic weight value.

5 Conclusion

The idea of the magnetic thermogravimetric analysis of magnetic materials was described. Previously unpublished results of the TGA of $\text{Cu}_{100-x}\text{Co}_x$, $x = [10, 15, 20]$ and the $\text{Cu}_{90}\text{Fe}_{10}$ amorphous alloys are presented. Those alloys play important role in the research on the Giant Magnetoresistance (GMR) and Giant Magnetoimpedance (GMI) effects, which can be potentially utilized in design and development of novel magnetic field sensors. The results indicate at complex temperature dependent phase behavior of the CuCo and CuFe systems. Most importantly, the inflection points on the characteristics indicate the area for further, more advanced investigations of the material structure, such as the X-ray spectroscopy. Thus, the Magnetic Thermogravimetric Analysis is recommended as starting point in novel magnetic materials investigations.

Acknowledgements. The support of the bilateral project APVV-Sk-PL-0043-12 is acknowledged from the Slovak side. Polish side (Institute of Metrology and Biomedical Engineering) was supported by statutory funds within Polish-Slovak bilateral cooperation.

References

1. Coats, A.W., Redfern, J.P.: Thermogravimetric Analysis: A Review. *Analyst* 88, 906–924 (1963)
2. http://www.perkinelmer.com/CMSResources/Images/44-74556GDE_TGABeginnersGuide.pdf
3. Tumanski, S.: Handbook of magnetic measurement, 1st edn. CRC Press (2011) ISBN 978-1-4398-2951-6
4. Carlin, R.L.: Magnetochemistry, 5th edn., p. 312. Springer (1986) ISBN 978-3-540-15816-5
5. O'Connor, C.J.: In: Lippard, S.J. (ed.) Magnetic susceptibility measurements. *Progress in Inorganic Chemistry*, vol. 29, p. 203. Wiley (1982) ISBN 978-0-470-16680-2
6. Sella, A.: Gouy's Tube. Royal Society of Chemistry (2010)
7. Švec, P., Zigo, J., Nowicki, M., Jackiewicz, D., Franko, M., Hamela, M., Winiarski, W., Szewczyk, R., Skorvanek, I., Švec Sr., P.: Preparation, processing and selected properties of modern melt-quenched alloys. In: Awrejcewicz, J., Szewczyk, R., Trojnacki, M., Kaliczyńska, M. (eds.) *Mechatronics: Ideas for Industrial Applications*. AISC, vol. 317, pp. 381–396. Springer, Heidelberg (2015)
8. Hickey, B.J., et al.: Superparamagnetism in melt-spun CuCo granular samples. *Journal of Magnetism and Magnetic Materials* 147(3), 253–259 (1995)
9. Fedosyuk, V.M., et al.: Influence of composition and annealing on the criteria of superparamagnetism and the interaction of particles in granular electrolytically deposited films of CuCo. *Russian Physics Journal* 41(3), 245–247 (1998)
10. Allia, P., Coisson, M.: Magnetic hysteresis in granular CuCo alloys. *Journal of Applied Physics* 85(8), 4343 (1999)
11. Duhaj, P., Svec, P.: Giant magnetoresistance in Cu-Co ribbons prepared by planar flow casting technique. *Acta Physica Slovaca* 48, 715 (1998)
12. Poperenko, L., Manko, D.: Elevated giant magneto-impedance in amorphous metallical Co-dased alloys. *Journal of Automation, Mobile Robotics & Intelligent Systems* 6,3 (4), 12–14 (2009)
13. Murillo, N., et al.: GMR effect in CuCo annealed melt-spun ribbons. *Journal of Nanoscience and Nanotechnology* 8(4), 1056–1061 (2004)
14. Kurek, J., Szewczyk, R., Salach, J., Kloda, R.: PI Control of Laboratory Furnace for Annealing of Amorphous Alloys Cores. *Journal of Automation, Mobile Robotics & Intelligent Systems* 6(4), 13–15 (2012)
15. Liu, J.: Dynamic scaling of phase separation in CuCo alloys. *Journal of Materials Science* 31(11), 2807–2818 (1996)

Advancement in Development of Graphene Flow Sensors

Marcin Safinowski¹, Wojciech Winiarski¹, Oleg Petruk¹, Roman Szewczyk¹,
Oskar Gińko¹, Krzysztof Trzcinka¹, Marek Maciąg¹, and Waldemar Łoboda²

¹Industrial Research Institute for Automation and Measurements PIAP,
Warsaw Poland

{msafinowski, wwiniarski, opetruk, rszewczyk,
oginko, ktrzcinka, mmaciag}@piap.pl

²Aparator Powogaz S.A.
waldemar.loboda@powogaz.com.pl

Abstract. This article describes the research, development and tests of prototype graphene flow sensors. The prototype sensors were checked for impact of different parameters on value of electric charge generated on the graphene's surface, such as volume flow value, flowing liquid ions concentration and liquid temperature. The information about developed transducers which convert signals from graphene sensor is presented.

Keywords: graphene, flow sensor, measurement, converter.

1 Introduction

In studies conducted in various laboratories worldwide it was shown, that the ions containing water flow in the vicinity of graphene structure causes the generation of electrical charge on the surface of graphene [1, 3–5]. The resulting potential difference is dependent on the fluid flow rate, fluid temperature and the concentration and type of ions present in the solution [2, 6].

Within the project "Graphene based, active flow sensors" studies to develop a method of graphene flow sensors manufacture were conducted. The conducted works aimed at constructing a graphene-based flowmeter. There were several demo versions of graphene sensors produced. The transducer demonstrator cooperating with the sensor was also developed.

Environmental examination of the developed demonstrator were performed, to determine what is the effect of temperature and humidity on a processing error of the device. In addition, tests were carried out to optimize the geometric construction of sensors and process of their preparation. The research aims to develop a prototype sensor, to check its work on various conditions, and possibly to investigate the parameters of the final product.

2 Methodology of Measurement

Tests of the graphene sensors were performed, among others, at the Department of Physics, University of Warsaw, and on the PIAP developed flow test stand. The test stand allows to generate fluid flow with a precise adjustment of its value. The concentration of the solution (the working fluid) and its temperature can be regulated. Control of the test stand is implemented using iFIX SCADA software. In addition, for the recording and archiving of the test results Proficiency Historian for SCADA software was used. The position can be operated in automatic mode, in which the predefined, fixed cycle operation is carried out. Semi-automatic mode is also possible. It is more flexible and the course of the test cycles can be freely defined.



Fig. 1. Measuring station for the graphene flow sensors testing

The above test station is working with the demo graphene flowmeter, developed in „Graphene based, active flow sensors” project. Communication between devices is via RS-232 interface. The test stand can register the measurement results from the graphene flow sensor. The developed demo flowmeter is composed of the graphene flow sensor and the signal transducer.

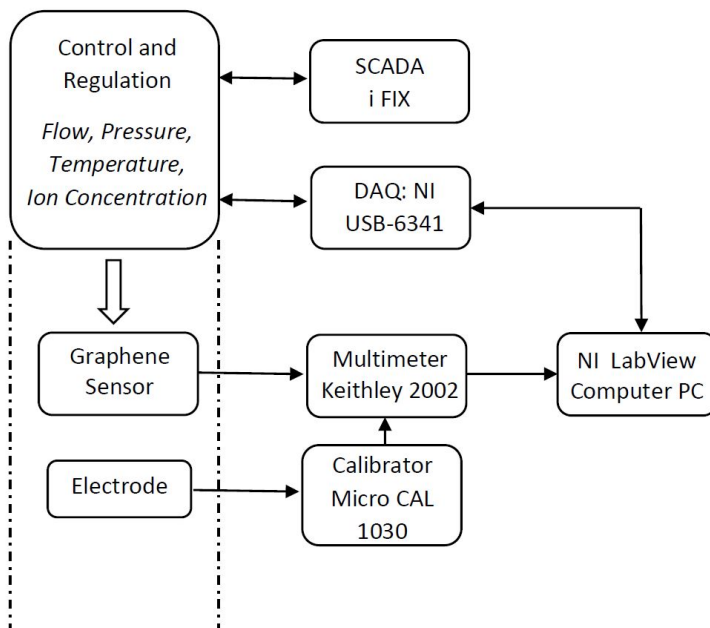


Fig. 2. The schematic block diagram of the measuring system for testing of the graphene flow sensors

For the study of the graphene sensors properties, measuring circuit has been extended by the system of direct signals measurement from the sensor. This solution was necessary to verify the operation of the developed sensor. For this purpose, Keithley 2002 multimeter was used. The source of voltage on the polarization electrode was MICRO CAL Time Electronics 1030 calibrator.

Acquisition and registration of measurement signals from the graphene sensor was carried out using NI LabVIEW environment and USB-3488A GPIB Interface card. In addition, measurements were coupled with adjustable volume flow implemented by NI DAQ USB-6341 card.

3 Graphene Sensors Demonstrators

Graphene sensor is composed of a plate made of silicon carbide with 10 mm × 10 mm dimensions, to which a layer of graphene was applied. Then on a layer of graphene gold electrodes were applied.

For the flow test, the sensor attachment system with visual observation of the flow channel has been designed and manufactured. The sensor is placed centrally in the flow channel cross-section, with a diameter of 26 mm. Polarization electrodes are also located in the flow channel. The exact electrode placement was optimized on the base of proper studies.

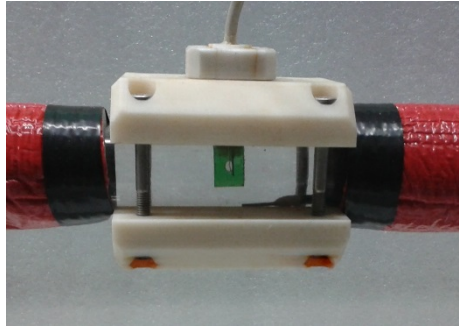


Fig. 3. Laboratory flow sensor demonstrator

Computer CFD flow simulations were performed for the graphene flowmeter demonstrator. On that basis the optimal shape of the flow channel and adequate sensor arrangement was determined. Computer simulations were performed using flow modeling software ANSYS Fluent. On the basis of the simulation results and experimental results, demonstrator transmitter housing was made. The sensor is placed against the wall of the flow channel. Channel is shaped to minimize the formation of flow disturbances.

FDM additive manufacturing technology (3D printing) was used for the housing manufacture, because it can be used to build the surfaces of any shape. The material used for the housing was acrylonitrile butadiene styrene.

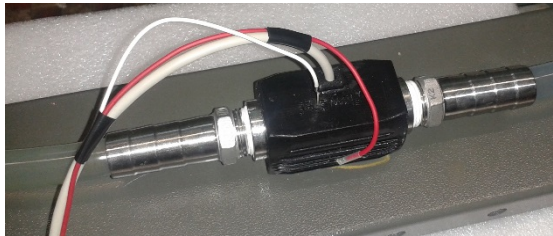


Fig. 4. Compact flow sensor demonstrator

For the research purposes, polarizing electrodes positioned parallel to, and perpendicular to the plane of the graphene was used. In addition, a possibility to adjust the length of the electrode was implemented. Housing design also allowed the use of electrodes made of other materials. The electrodes made of Pt, Ag, Cu, Sn, and 316L corrosion-resistant steel were investigated. It turned out, that the Ag electrode gave best results. The optimal electrode position was the parallel one.

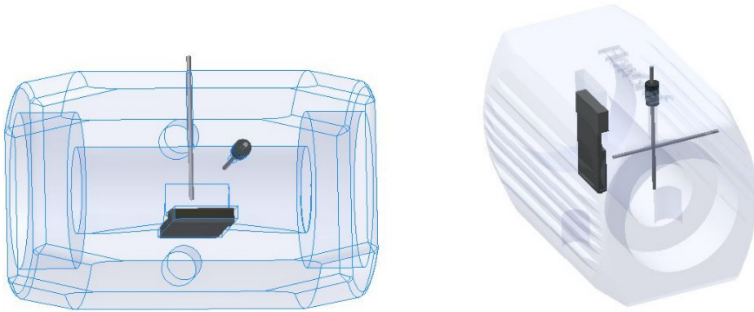


Fig. 5. Compact flow sensor demonstrator (transparent 3D view)

In the next step, work has focused on miniaturization of the sensor. The resulting housing has the input channel diameter of 6 mm that passes monotonically into the channel of 10 mm × 3 mm rectangular cross section. The sensor is located on the wall surface of the flow channel. The polarizing electrode is placed parallel to the sensor surface.

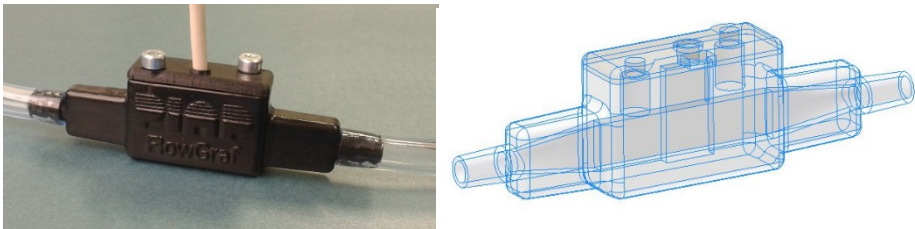


Fig. 6. Flow sensor demonstrator

4 Transducer Flow Sensor Demonstrator

In the demonstrator graphene flowmeter, liquid flow is calculated on the basis of a precise measurement of the differential voltage from the graphene sensor, and liquid conductance and temperature sensors.

The designed graphene flowmeter demonstrator contains:

- galvanically isolated analog-to-digital converter with a measuring amplifier to measure the sensor signal,
- galvanically isolated analog-to-digital converter circuit, for measuring the conductivity or concentration of the acid or salt in a liquid,
- DS18B20 digital thermometer with 1-Wire interface,
- LCD alphanumeric display.

The flowmeter demonstrator is an independent measuring device. It uses the characteristics of the graphene flow measurement sensor which were obtained in the laboratory from the flow test stand using the SCADA software.

The device enables the measurement of the volume flow taking into account the effect of temperature and concentration of the acid or salt on the characteristics of the sensor. The device indicates on the display incorrect connection of the thermometer and /or conductivity meter. The measured volume flow, temperature and solution concentration are presented on the display. They can also be read out via the demonstrator RS-232 port connected to the computer, using a "terminal" software.

The device has a service mode. After entering the service mode it is possible to read the parameters used in the calculations, and to change their value.

Display flowrate range is 0–500 l/h with a resolution of 0.1 l/h. The temperature measurement is possible in the range 1–600 °C with a resolution of 0.10 °C.



Fig. 7. Graphene flowmeter demonstrator

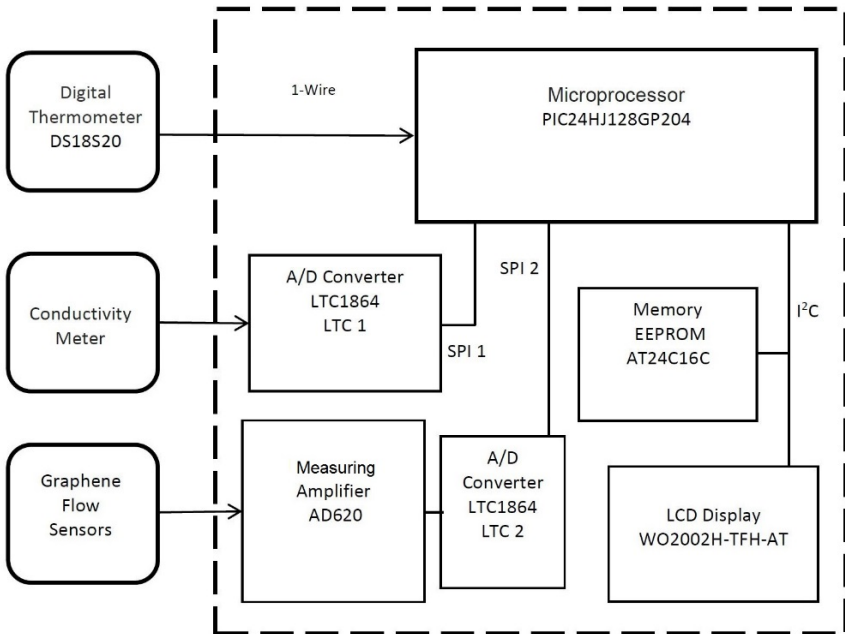


Fig. 8. Schematic block diagram of the demonstrator electronic circuit

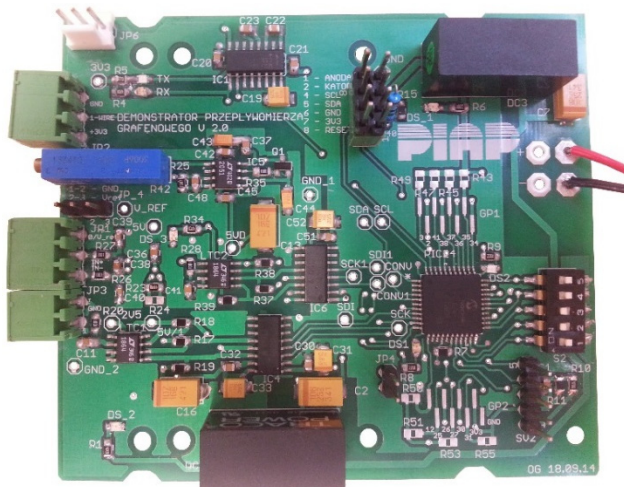


Fig. 9. Top view of the demonstrator circuit board

The signal from the flow sensor is filtered on the input and output of the measuring amplifier. Measuring amplifier is designed to measure the sensor signal, with positive and negative polarization.

Additionally, adjustment of the measuring range of the sensor signal amplitude is possible by changing the resistance in the measuring amplifier circuit.

The flowmeter demonstrator allows the output outside the sensor housing of the electrode bias voltage with the regulated value of 0 ~ 2.5 V.

Static characteristics of the AD620R measuring amplifier with 100.1 amplification were collected. Diagram of the measurement system is shown in Fig. 10.

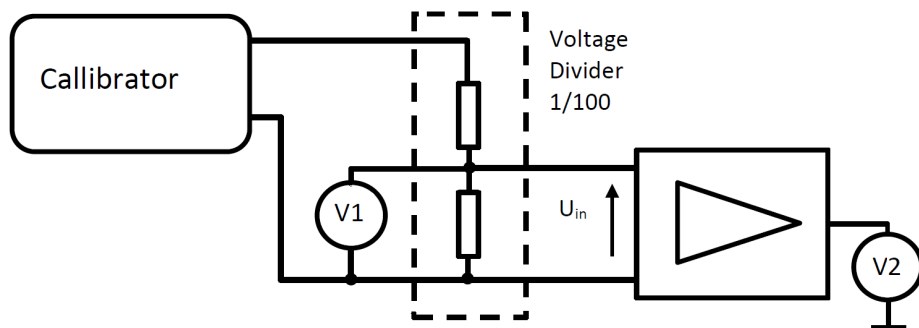


Fig. 10. Diagram of the amplifier measurement system

Tests were carried out at 22 °C and a relative humidity of 40%. Resting operating point of the measuring amplifier is 2.5 V relative to the system ground. Output voltage range was determined experimentally and is in the range of 3.9 V to 1.1 V relative to the system ground.

Figure 11 show the resulting static characteristics of the AD620R measuring amplifier. Characteristics were collected for amplification equal to 100, which has been determined using the resistor with a resistance of $499\ \Omega$ and a tolerance of $\pm 0.1\%$. The actual gain (slope approximating characteristics based on the results of measurements) was calculated as 100.1, with the coefficient of determination R^2 of 1.

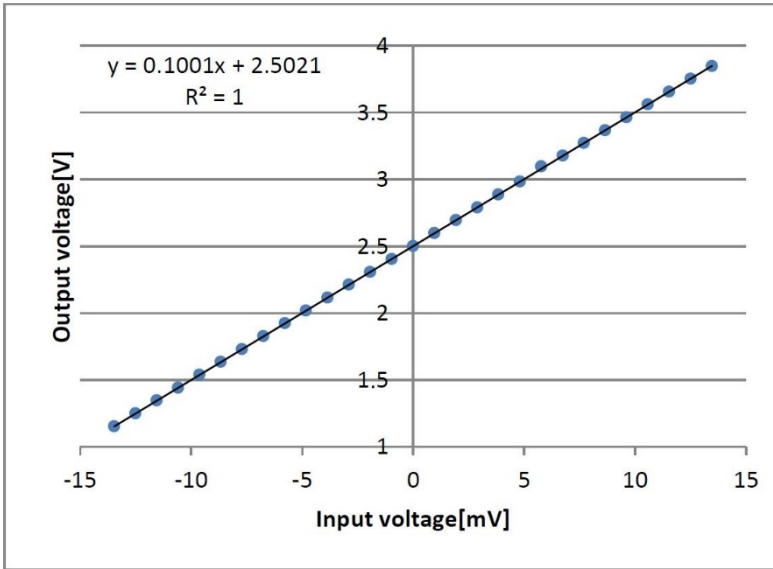


Fig. 11. AD620R measuring amp

The algorithm for flow rate and volume calculation takes into account the dependence of the flow rate on the change of temperature, solution concentration and the diameter of the pipeline.

Time base Δt for integrating the volume is 0.1 s.

5 Tests of the Graphene Flow Sensors Demonstrators

Study of the graphene flowmeter demonstrator resistance to environmental conditions was carried out. The device has been subjected to the following conditions:

- air temperature of $0\ ^\circ\text{C}$ to $50\ ^\circ\text{C}$ and a humidity of 40% to 50%,
- humidity of 40% to 85% at an air temperature of $25\ ^\circ\text{C}$.

The aim of the study was to test the stability of the flowmeter demonstrator, and to determine the effect of environmental conditions on the measurement of the following values:

- Fluid conductance/salt or acid concentration in the solution,
- Graphene flow sensor signal,
- Temperature.

The study was conducted on the test bench, the block diagram is shown in Fig. 1. During the measurements, the air temperature in the laboratory was 19–21°C and the humidity was 40–45%.

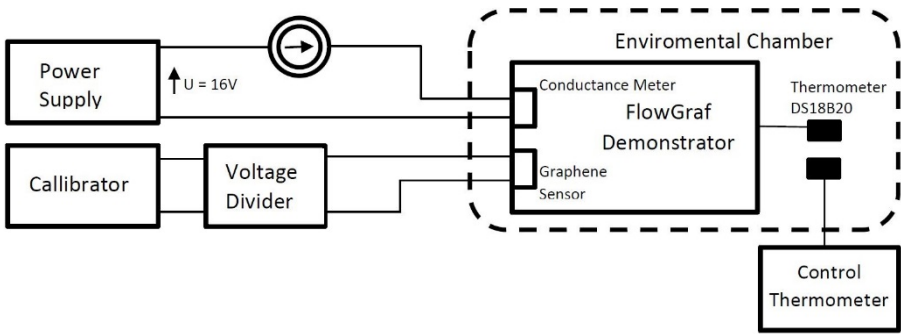


Fig. 12. Measurement test stand schematic

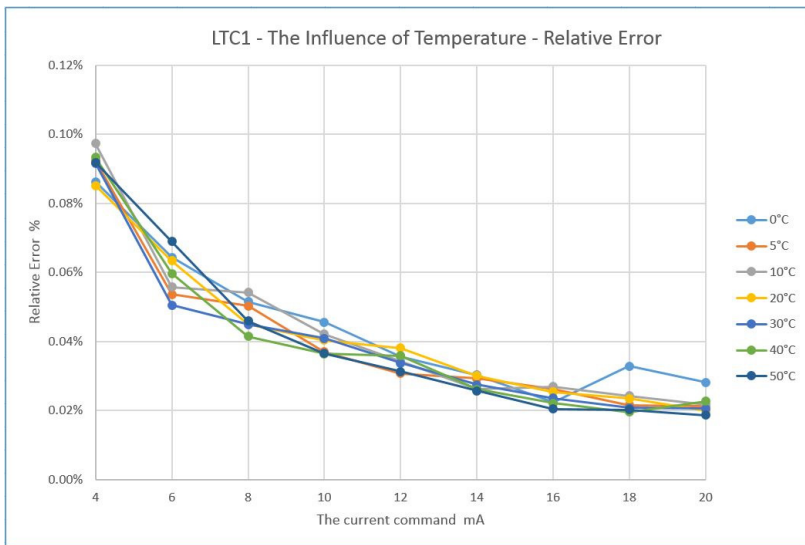


Fig. 13. LTC1 transducer relative error for temperatures 0–50 °C

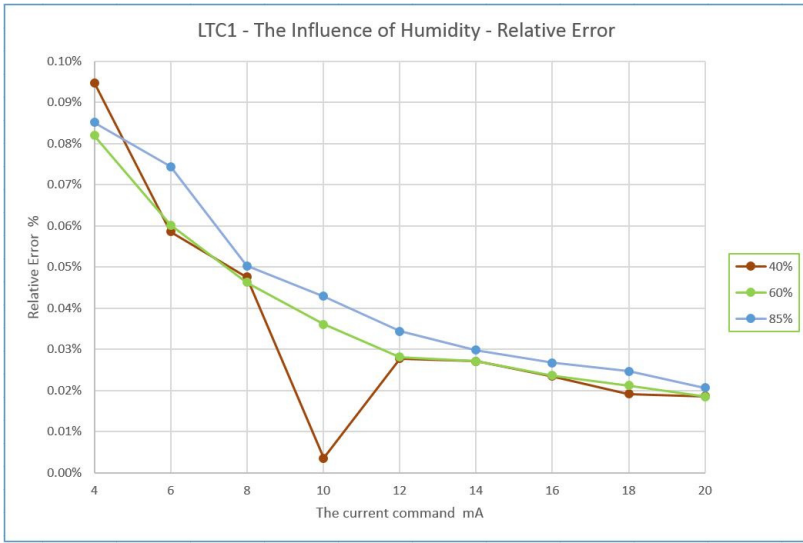


Fig. 14. LTC1 transducer relative error for humidity 40–85%

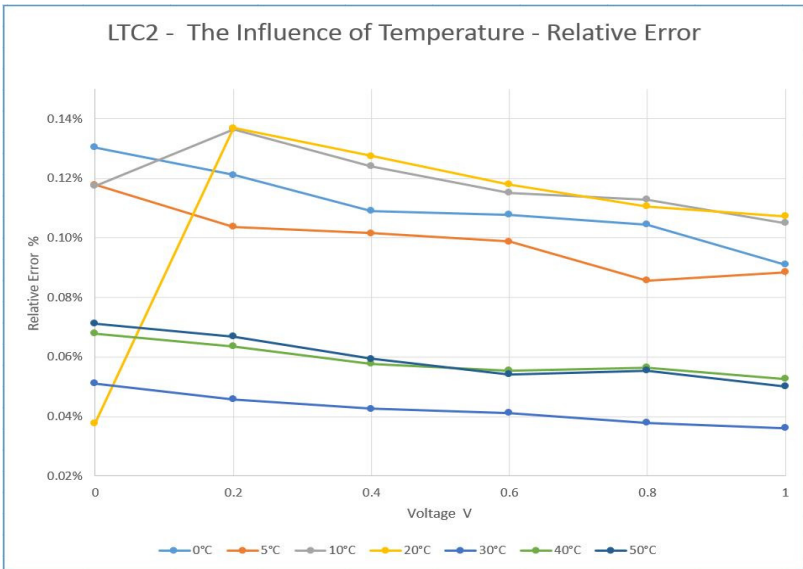


Fig. 15. LTC2 transducer relative error for temperatures 0–50°C

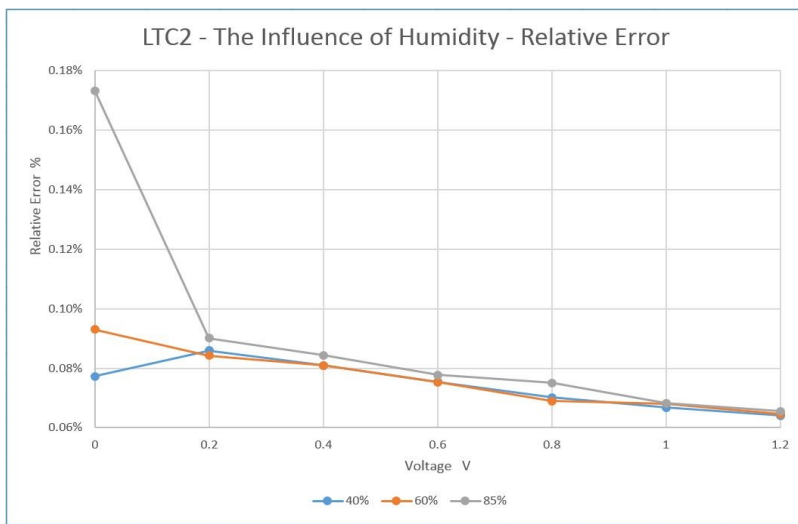


Fig. 16. LTC2 transducer relative error for humidity 40–85%

During the measurements, the temperature measurement results obtained from the flowmeter demonstrator were compared with the reference thermometer. The results are presented below in Table 1.

Table 1. The results of temperature measurement by the graphene flowmeter demonstrator

The temperature measured by the reference thermometer °C	The temperature measured by the demonstrator °C	Standard deviation °C	Error °C
0.5	0.50227	0.01887	-0.00227
5.2	5.3	0	-0.1
10	10.1	0	-0.1
19.8	19.89935	0.00804	-0.09935
29.8	29.92249	0.04176	-0.12249
40.1	39.89703	0.08663	0.20297
49.8	49.57371	0.04812	0.22629

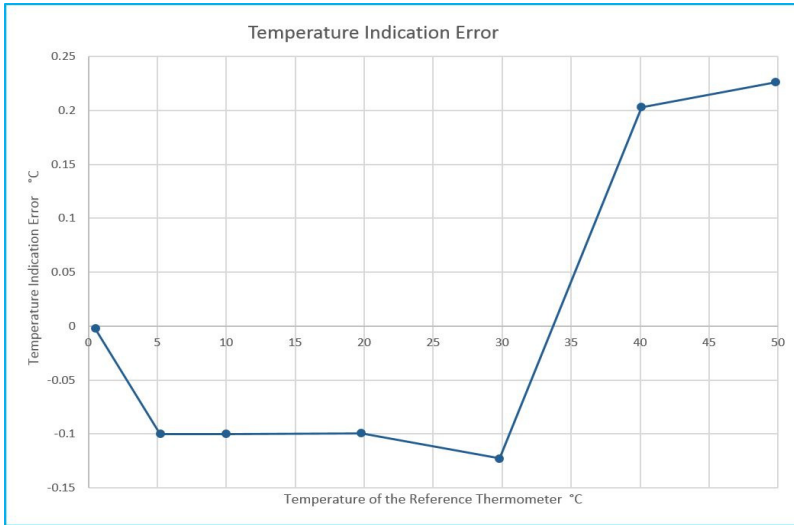


Fig. 17. Temperature indication error of the flowmeter

Examples of flow test results performed on the test bench are shown below. A block diagram of the position is shown in Fig. 2. The study was based on the measurement of the voltage on the electrodes of the graphene sensor, depending on the speed of flowing water. The measuring system uses the reference voltage sources. The polarizing electrode made of Ag wire was used. Polarization voltage was $U_p = -0.2$ V. The reference voltage source was connected to the sensor via two $R = 4.7$ M Ω resistors. Voltage was $U_{ref} = 1.25$ V.

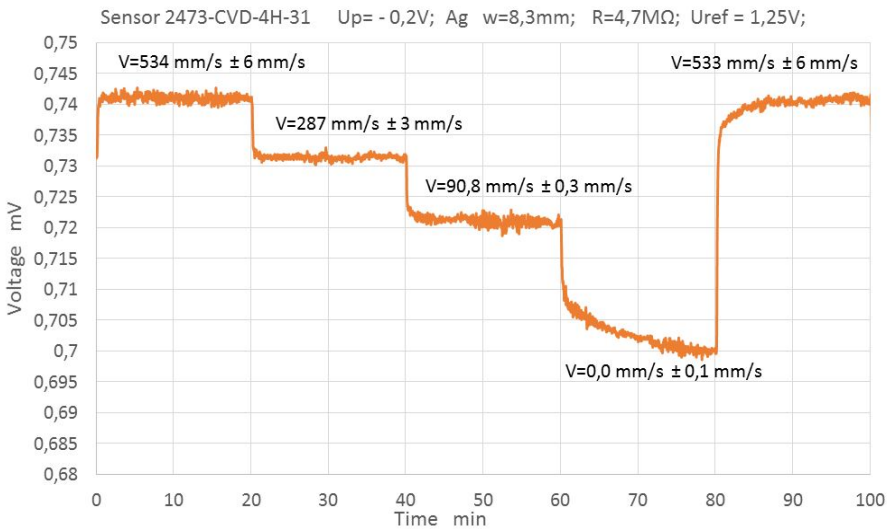


Fig. 18. Typical sensor voltage signal response on the water flow velocity

6 Conclusion

Graphene flowmeter demonstrator successfully passed the test of resistance for temperature in the range of 0–50 °C and humidity of 40–85%. During testing device worked properly. The correctness of the measured values of the input signals and the correct delivering them to the display was verified. Conductance measuring circuit showed the impact of changes in temperature and humidity at the level of 0.1% of indicated value. The voltage signal from the graphene sensor measuring circuit, including the measuring amplifier, showed the impact of temperature changes at the level of 0.18% of indicated value and the impact of changes in humidity at 0.14% of indicated value.

Given that changes in the input signal was at 40 μV , this should be considered a very good result. Demonstrator communication with a PC via RS-232 runs smoothly.

For the processing of the measurement results statistical methods were used.

The problem to solve is the repeatability of the graphene sensor signals. To solve the above problem work is underway on other graphene sensors solutions, which needs further study.

Acknowledgments. This work has been supported by the National Centre for Research and Development (NCBiR) within the GRAF-TECH programme (no. GRAF-TECH/NCBR/02/19/2012). Project "Graphene based, active flow sensors" (acronym FlowGraf).

References

1. Newaz, A.K.M., Markov, D.A., Prasai, D., Bolotin, K.I.: Graphene Transistor as a Probe for Streaming Potential. *Nano Letters* 2(6), 2931–2935 (2012)
2. Safinowski, M., Winiarski, W., Domański, K., Petruk, O., Dąbrowski, S., Szewczyk, R., Trzcinka, K.: Measuring station for testing of graphene flow sensors. In: Szewczyk, R., Zieliński, C., Kaliczyńska, M. (eds.) *Recent Advances in Automation, Robotics and Measuring Techniques*. AISC, vol. 267, pp. 649–664. Springer, Heidelberg (2014)
3. He, R.X., Lin, P., Liu, Z.K., Zhu, H.W., Zhao, X.Z.: Solution-Gated Graphene Field Effect Transistors Integrated in Microfluidic Systems and Used for Flow Velocity Detection. *Nano Letters* (2012)
4. Ghosh, S., Sood, A.K., Kumar, N.: Carbon Nanotube Flow Sensors. *Science* 299, 1041 (2003)
5. Sklyar, R.: The Microfluidic Sensors of Liquids, Gases, and Tissues Based on the CNT or Organic FETs. *JAMRIS* (February 2007)
6. Kabaciński, M., Kabza, Z., Pospolita, J.: Stanowisko laboratoryjne do badań przepływomierzy. *Pomiary Automatyka Robotyka*, pp. 53–57 (October 2010)
7. Korytkowski, J.: Układ elektroniczny cyfrowej syntezy konduktancji. *PAR*, 102–107 (September 2013)
8. Jun, S.-W., Yasutomi, K., et al.: Linearized settling error calibration for a pipeline A/D converter using non-slewing amplifiers. *JAMRIS* (April 2009)

Noise Assessment in Whitney Elements Based Forward Transformation for High Resolution Eddy Current Tomography

Roman Szewczyk¹, Jacek Salach², Juha Ruokolainen³, Peter Råback³,
Kamil Stefko², and Michał Nowicki²

¹ Industrial Research Institute for Automation and Measurements,
Al. Jerozolimskie 202, PL-02-486, Warsaw, Poland

rszewczyk@piap.pl

² Institute of Metrology and Biomedical Engineering, Warsaw University of Technology,
sw. A. Boboli 8, 02-525 Warsaw, Poland

³ CSC – IT Center for Science, Keilaranta 14, FI-20101 Espoo, Finland

Abstract. Paper presents the results of application of Whitney elements based method for performing the forward transformation in eddy current tomography. Accuracy and the noise level of such a forward transformation is the most important factor determining efficiency and metrological properties of eddy current tomography. Comparison of the experimental results of measurements on eddy current tomography test stand, and results of modelling utilizing Whitney elements indicated high accuracy of modelling. However, results of modelling present unacceptable noise level. Sources of this noise are analysed in the paper, indicating the guidelines to overcome this barrier.

Keywords: eddy current tomography, finite elements method.

1 Introduction

Eddy current tomography (ECT) is an important alternative of X-ray tomography, especially when elements have to be tested in the industrial conditions. Eddy current tomography is safe and user friendly [1]. Moreover, hardware for such tomography is not complicated, affordable, and scalable from small to quite large tested elements.

On the other side, the main barrier connected with industrial application are numerical problems connected with processing of the eddy current tomography signal and data [2, 3]. These problems are caused by the lack of sufficient theoretical background for magnetodynamics analyses utilizing finite element methods (FEM). One of the possibilities to overcome these limitations is application of Whitney edge elements methods for solving Maxwell equations in finite elements methods [4].

Recently Whitney edge elements method was implemented in the open-source ELMER FEM software [5] developed by CSC – IT Center for Science in Finland. Paper presents the results of investigation of this software usability for implementation of

forward eddy current tomographic transformation, which is the base of data processing algorithms in eddy current tomography. Such algorithm may be significant step forward concerning the recent state of the art in eddy current tomography [6–10].

2 Experimental Test Stand

To enable practical verification of proposed algorithms, experimental test stand for high resolution eddy current tomography was developed [11]. This measuring stand is suitable for spindle-shaped elements with inclusions or groves simulating defects in the material.

General view of proposed measuring test stand is presented in Fig. 1. This stand is based on two coils (2): exciting coil and detection coil. Tested, spindle-shaped object (1) is moved between the coils. Moreover, during the movement controlled by the linear actuator (3), the rotation is provided by stepper motor (4). As a result, tomographic measurements may be done with rotation resolution during the measurements of up to 1° . Simultaneously, the resolution of linear movement is up to 0.1 mm.

Due to the fact, that proposed eddy currents tomographic system test stand is controlled by the embedded microcontroller, spatial resolution of measurements may be increased or decreased accordingly to required resolution as well as requirements of tomographic data processing algorithm.

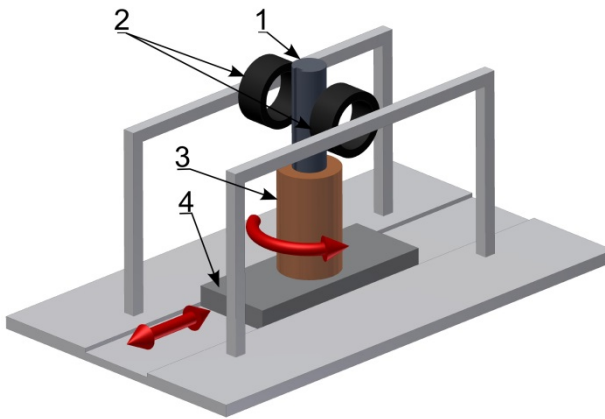


Fig. 1. Mechanical setup of eddy current tomography test stand for measurements of reference signal: 1 – element under investigation, 2 – driving and sensing coils, 3 – rotational actuator, 4 – linear actuator

The cross-section of the spindle-shaped element used for tests is presented in the Fig. 2. In the ST3 steel spindle with 30 mm diameter, the rectangular groove was made. This groove was 8 mm wide and 13 mm deep.

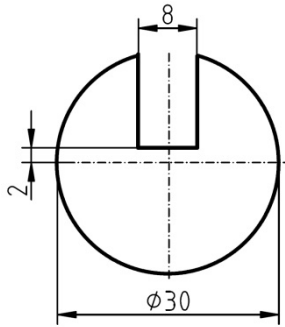


Fig. 2. Dimensions of the cylinder with the groove used as testing element

3 Principles of Eddy Current Tomography Data Processing

Schematic block diagram of data processing in the eddy current tomograph is presented in Fig. 1. The fundamental part of data processing algorithm is forward transformation. On the base of finite element model of tested element, forward transformation generates the simulated value of output signal from eddy current tomograph. Then results of modelling are compared with results of measurements in eddy current tomography test stand. Indicator of conformability between results of simulation and results of measurements is the input for optimisation algorithm, which is changing the FEM model of tested object to achieve agreement between results of experimental measurements and results of modelling. If such agreement is reached, FEM model of tested object reflects the shape of the real object.

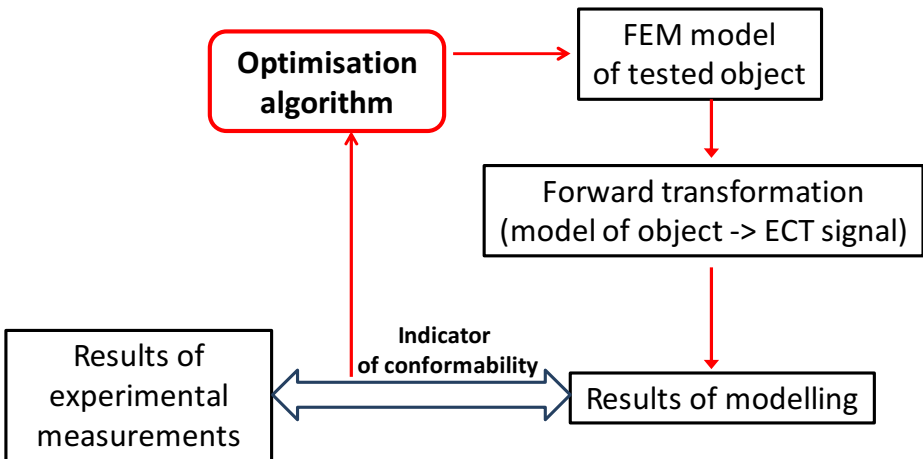


Fig. 3. Schematic block diagram of data processing in eddy current tomography

In presented investigation forward transformation for eddy current tomography was implemented as it is presented in Fig. 2. Tested object description was generated

from the OCTAVE software [12] in the form of .geo text file. Then the tetrahedral mesh was generated using NETGEN software [13]. On the base of this mesh, the finite element model was calculated on the base of the Maxwell equations, using Whitney edge element method by ELMER FEM software [4]. Then, the value of the output signal in the detecting coil of eddy current tomography was calculated by the integration of simulated distribution of flux density B in detection coil. As a result, both amplitude and phase shift of eddy current tomography signal can be calculated during the forward transformation.

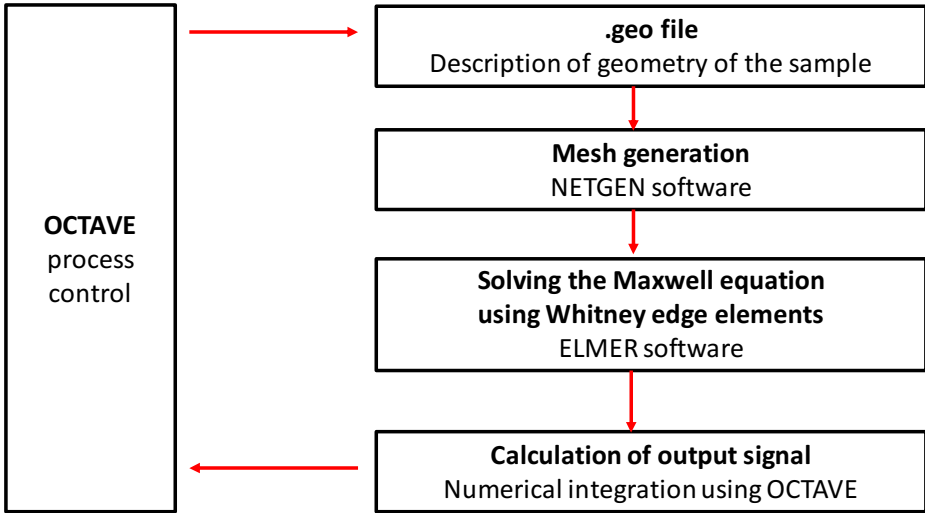


Fig. 4. Schematic block diagram of data flow during the proposed forward transformation implementation

It should be indicated, that all calculations for eddy current forward transformation were made using the open-source software. This creates the possibility of verification of achieved results by other researchers. Moreover, the improvements of proposed algorithm may be easily implemented.

4 Results of Calculation

Comparison between the results of measurements of spindle with groove presented in the Fig. 2 and results of simulation based on algorithms presented in Fig. 3 and Fig. 4 are presented in Fig. 5.

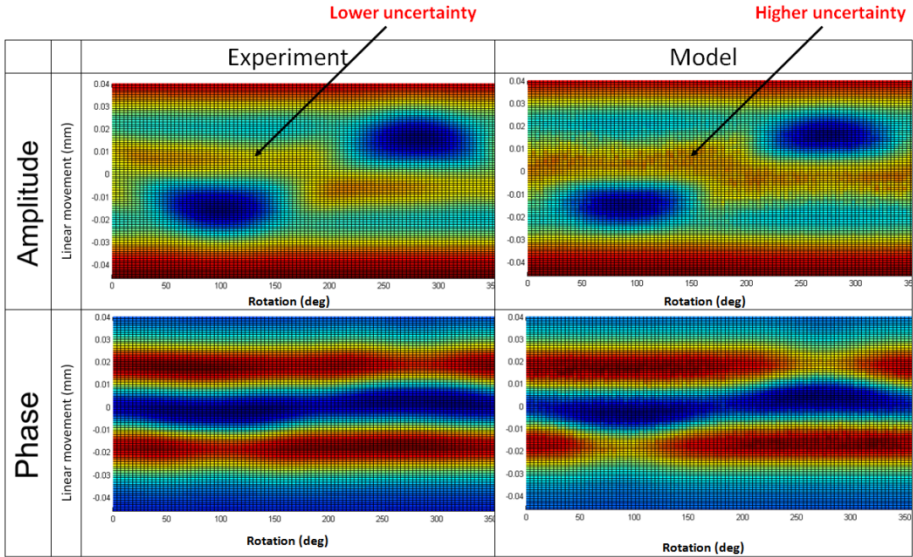


Fig. 5. The results of measurements on presented EC tomograph of sample spindle with groove (left side) and results of simulation of output signal from EC tomograph (right side). Scales are presented in arbitrary units.

It should be highlighted, that very good agreement between the results of measurements and the results of simulation was reached. This confirms the correctness of forward transformation method and opens the possibility of development of high resolution eddy current transformation based on open-source software.

However, as it is presented in Fig. 5, results of simulation exhibit higher noise level than the results of measurements. This noise will decrease the efficiency of eddy current transformation as well as will reduce the quality of tomography image.

Analysis of the source of the noise in simulation results leads to the conclusion, that it can be reduced by:

- better description of the borders of tested element,
- increasing the number of elements in FEM mesh,
- increasing quality of Whitney edge element to Cartesian space transformation,
- increasing of quality of FEM solver optimisation algorithm.

In addition it was proven, that the noise level may be reduced during the numerical filtering. However, it requires larger number of samples in the neighbourhood of each point, which increases the calculation time.

5 Conclusions

Results presented in the paper confirms that forward transformation necessary for high resolution eddy current tomography is feasible on the base of open-source software. Moreover, computing time requirements for such transformation are moderate, what makes tomographic transformation feasible on available shared memory, 48 core, computer RX900S1. Fujitsu RX900 is a rare shared memory configuration and consists of eight Xeon X7542 processors with six cores each.

On the other hand, unacceptable noise level was observed in the results of simulations. To reduce this noise, the method of forward tomographic transformation have to be developed considering increasing the mesh density, changes of tested element border definition as well as increasing of quality of FEM solver algorithm.

Acknowledgments. Calculations for the modelling were made in the Institute of Metrology and Biomedical Engineering, Warsaw University of Technology.

References

1. Prasad, J., Nair, C.G.K.: *Non-Destructive Test and Evaluation of Materials*. McGraw Hill (2011)
2. Uomoto, T.: *Non-Destructive Testing in Civil Engineering*. Elsevier (2000)
3. Grzelka, M., et al.: Accuracy of the element geometry mapping using non-invasive computer tomography method. *Journal of Automation, Mobile Robotics and Intelligent Systems* 6(3), 23 (2012)
4. Råback, P., Malinen, M., Ruokolainen, J., Pursula, A., Zwinger, T.: *Elmer Models Manual*. CSC – IT Center for Science (2014)
5. <http://www.csc.fi/english/pages/elmer>
6. Soleimani, M., Tamburrino, A.: Shape reconstruction in magnetic induction tomography using multifrequency data. *International Journal of Information and Systems Sciences* 2, 343 (2006)
7. Premel, D., Mohammad-Djafari, A.: Eddy current tomography in cylindrical geometry. *IEEE Transactions on Magnetics* 31, 2000 (1995)
8. Soleimani, M.: Simultaneous reconstruction of permeability and conductivity in magnetic induction tomography. *Journal of Electromagnetic Waves and Applications* 23, 785 (2009)
9. Tamburrino, A., Rubinacci, G.: Fast methods for quantitative eddy-current tomography of conductive materials. *IEEE Transactions on Magnetics* 42, 2017 (2006)
10. Ioan, D., Rebican, M.: Numerical model for eddy-current testing of ferromagnetic steel parts. *IEEE Transactions on Magnetics* 38, 629 (2002)
11. Salach, J., Szewczyk, R.: High resolution eddy current tomography setup and possibilities of its signal filtering. *Pomiary Automatyka Robotyka* 17, 112 (2013)
12. <http://www.octave.org>
13. <http://www.hp fem.jku.at/netgen>

A Problem of a Selection of the Stabilization Technique of False Alarm for Radar Target Detector

Ewelina Szpakowska-Peas

Institute of Aviation, Warsaw, Poland
ewelina.szpakowska@ilot.edu.pl

Abstract. In this article a few selected constant false alarm rate (CFAR) detection procedures has been presented. The various behavior of these algorithms for specific scenarios of local clutter or multiple target situations has been analyzed. Among presented algorithms one have been selected by author in order to implement it in the module of Radar Target Detector. Operations of algorithms have been simulated in Matlab.

Keywords: radar detection, constant false alarm rate, CFAR.

1 Introduction

Techniques of detection false alarm (CFAR stands. Constant False Alarm Rate) allow for detection of object which is surrounded by various disturbances. In real radar applications may appear all sorts of noises and echoes from fixed objects. Generally speaking, detection could to be an easy task if the echoing object would be located in front of a clear or empty background. In this case, the echo of objects would be located on a homogeneous background noise.

In real situations, however, the target is always in front of clutter. Usually the location of the clutter is dependent on the change in time and location. This fact requires an adaptive signal processing techniques operating with variable threshold detection in order to be adapted to the level of local clutter. In order to obtain the necessary information about the local constant echo, certain environment defined by the window around the radar test cell must be analysed. The design of signal processing systems is assumed that clutter is evenly distributed throughout the entire environment. The signal processing is designed in a way to obtain the detection of useful targets not the background reflections.

For the objects that are appearing on the plan of a constant echoes a complete picture of the situation encountered at the observation site must be created. In existing CFAR systems decision is usually made based on the technique of sliding windows. The algorithm of the decision threshold consists of data available in the reference windows. These procedures are nearly the same in all systems CFAR and they are depicted in figure 1. It shows two reference window and

signal processing structure for detection techniques. In order to avoid energy leakage signal from the test cell to the adjacent cells, which may consequently have an impact on the estimate of the noise power level of the reference windows. Therefore, shown in Figure guard cells are ignored. [3]

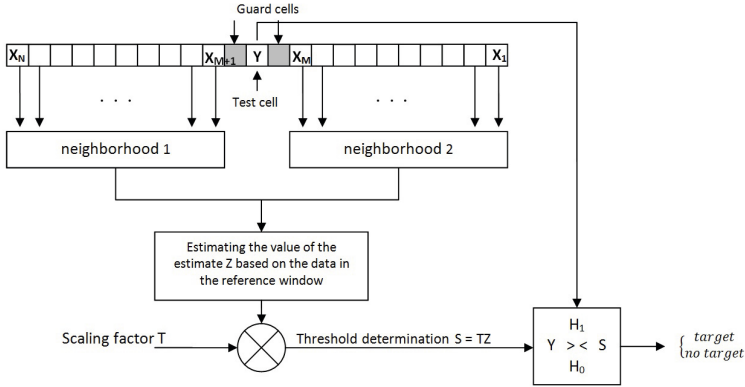


Fig. 1. The general scheme of the CFAR algorithm

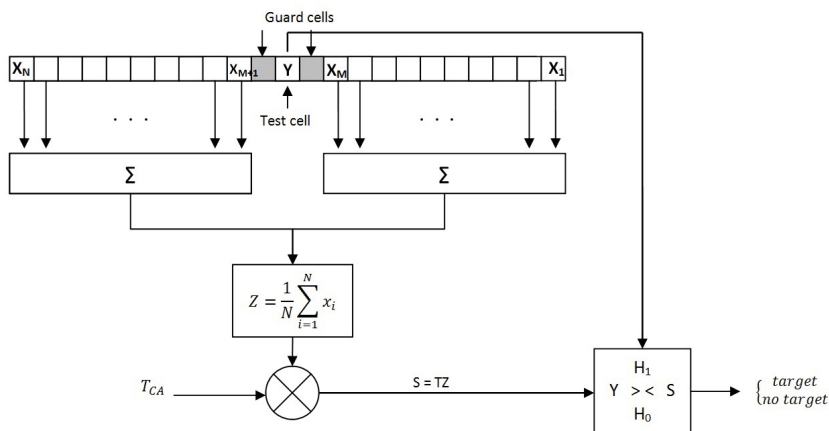
The first step is to measure the mean power level of background Z . Then Z value is multiplied by a scaling factor T selected depending on the version of the algorithm and the assumed probability of false alarm. The result of multiplication $S = TZ$ is directly used as the threshold value. [3]

Common CFAR systems usually used in estimation techniques, which are mainly based on the arithmetic averaging. There is also another procedure, which is based on ordered statistics (ordered- statistic - OS [3]). The rest of the signal processing algorithm remains almost unchanged. The next sections present a comparison of different versions of the CFAR algorithms for non-stationary noise.

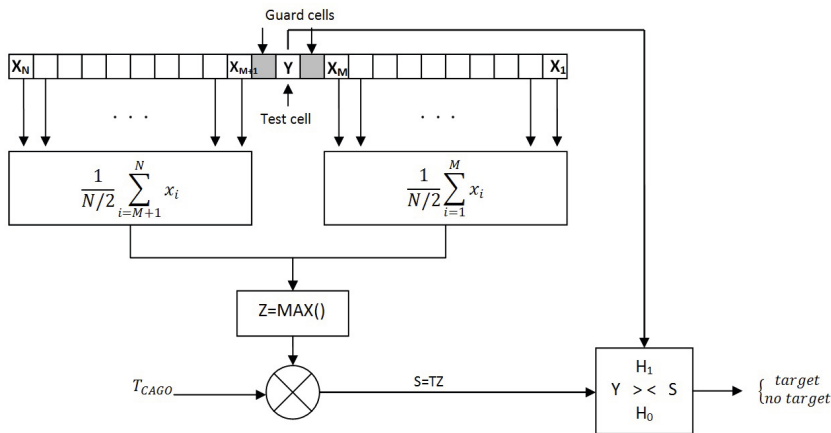
2 Analysis of Selected Detection Techniques

2.1 Cell Averaging Techniques

Firstly, two methods of detection will be discussed: by averaging cells called cell averaging CFAR (CA CFAR) and cell averaging with greatest of CFAR (CAGO CFAR). Differences in the processing of these algorithms are shown schematically in figure 2.



(a) CA CFAR



(b) CAGO CFAR

Fig. 2. Comparison of the block diagrams CA CFAR and CAGO CFAR algorithms

Arithmetic averages of amplitudes are calculated from each of the two adjacent areas. Two values of the constant echo are estimated and then combined into a single value by subsequent averaging them or selecting the greatest of numbers. The main difference between the CA CFAR and CAGO CFAR is that the first one is clearly based on the establishment of a single clutter situation, and the second takes into account the edges of the clutter appearing in the reference area.

In situations where edges of clutter occur, this structure creates a temporarily better behavior of CAGO CFAR than CA CFAR, although it is known that the first performance is only slightly worse than the latter in the case where it has a sensitivity of only 0.3dB loss in signal to noise ratio (SNR).

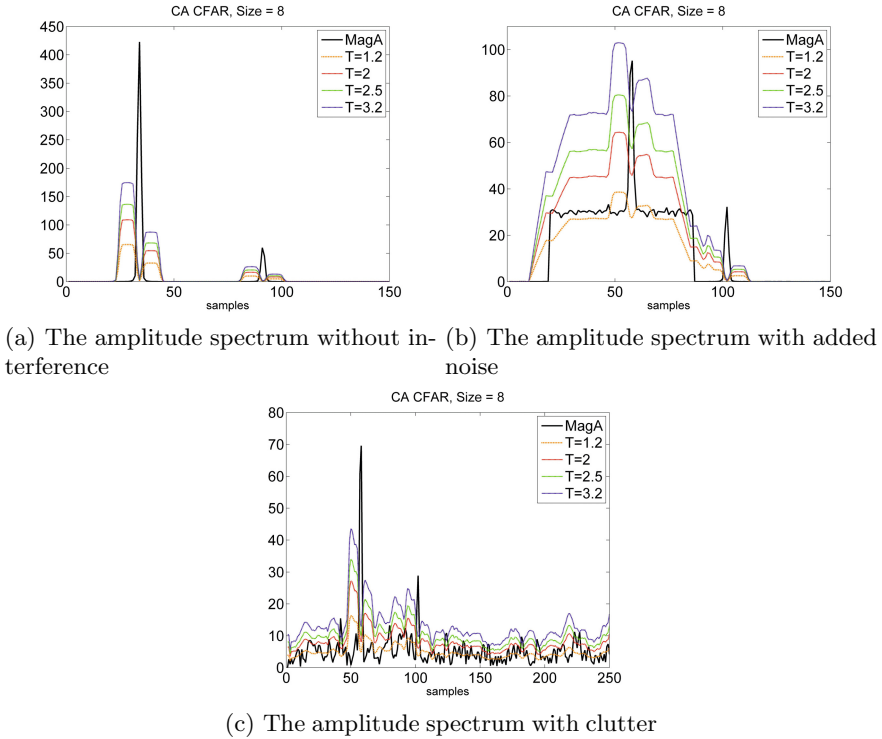


Fig. 3. CA CFAR algorithm behavior in the various situations

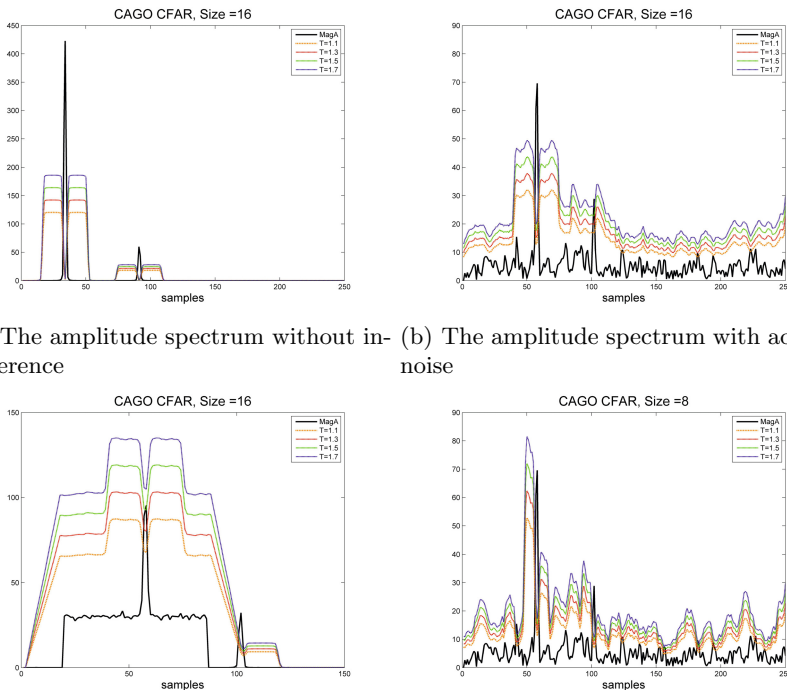
In this paragraph, the simulation results are described some techniques of target detection CA and CAGO CFAR. For a discussion on the pros and cons two different situations have been taken into account: uniform (stationary) and heterogeneous (edges) in the clutter reference. These are two selected, idealized examples of the many various situations that may occur in practice, and they are not sufficient for a comprehensive assessment of adaptive procedures in the processing of the radar signal. In this context, the analysis of the behavior of both CFAR methods is focused on situations of a multiple targets.

The amplitude spectrum of the simulated signal from transceiver module is shown in figures 3 and 4. It is assumed that within the radar range there are two objects with known distance and velocity: 120 m, 10 m/s and 180 m, 25 m/s, respectively. Three different situations are depicted: a signal without interference, with additional noise and clutter. The noise vector consists of pseudo-random numbers from Gaussian distribution function and it is added to the vector comprised of the signal samples. In each situation, the chosen detection technique is based on 16-element a reference window and one cell protection on both sides of the test cell.

The behavior of the detection threshold with four fixed values of the scaling factor T has been presented on a discussed figure. The figure 3(c) indicates that

certain values of the scaling factor T algorithm detects the edges of the clutter. There are objects that are not really there. The width or the size of the reference windows or value of the scaling factor T could be manipulated, but as it is shown in figure 3(c) does not always can improve the quality of the whole algorithm.

The behavior of the detection threshold for CAGO CFAR technique is shown in the next set of figures 4. In this case, the procedure methodology is similar to the previous one. Figures 4(c) and 4(d) shows the situation with a clutter and two stripes. One peak is located in the background noise and the other in the vicinity of the clutter edge. The difference between graphs is the size of the sliding window. The second peak has been found, but with a very low T coefficient. By comparing these results with the previous figures (4(a) and 4(b)) it can be concluded that unwanted stripes are selected in noised signal for a small scaling factor T . Even when the signal is noise-free (fig. 4(a)) are found adjacent bands. To obtain the best results the proposed solution is to reduce the sensitivity of the threshold and to reduce the number of cells in the reference window. Nevertheless, it can't be guaranteed that this algorithm will be successful with different situations.



(a) The amplitude spectrum without in- (b) The amplitude spectrum with added
 terference noise

(c) The amplitude spectrum with clutter (d) The amplitude spectrum with clutter
 with different reference window size

Fig. 4. CAGO CFAR algorithm behavior in the various situations

2.2 Ordered Statistic Techniques

Secondly, another methods of detection will be discussed. They are based on ranking elements in the array. The main idea of the OS CFAR process is the selection of a value of X $X_{(n)}$, $k \in \{1, 2, \dots, N\}$ from the series and it is used to estimate the Z value. The adverse result is a longer processing time of this kind of algorithm, but it has some valuable advantages.

$$X_{(1)} \leq X_{(2)} \leq \dots \leq X_{(N)} \tag{1}$$

The general diagram of the operation of these algorithms is depicted in figure 5.

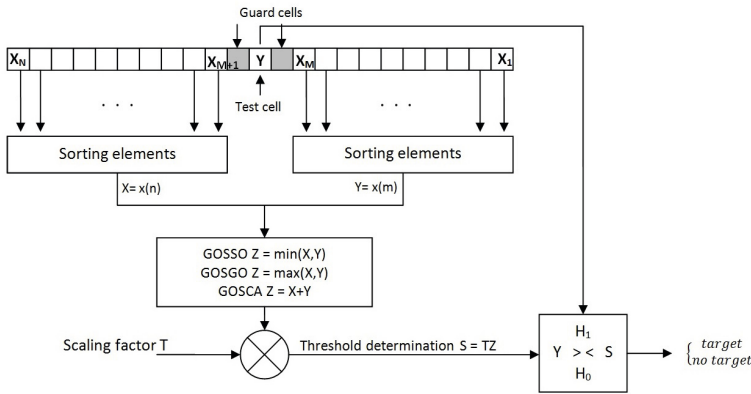
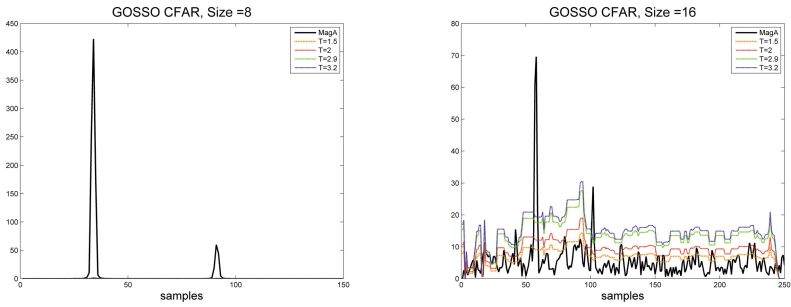


Fig. 5. The general scheme of the CFAR algorithm

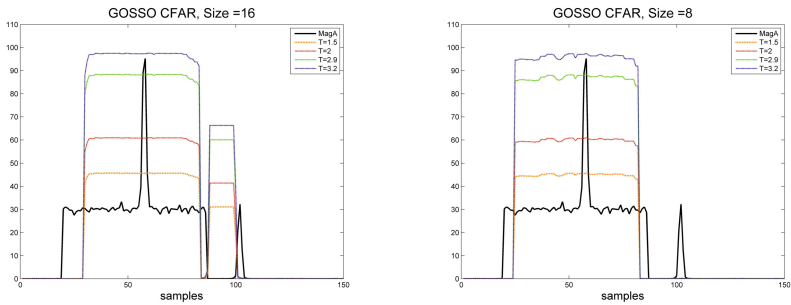
In each of the two adjacent areas are serialized elements from the smallest the largest value. Then, the selected n -th value of both series and the Z value is estimated depending on the method has been used. In the considered cases, the value of n will be $\frac{3}{4}$ the width of the reference window. The next steps are the same as in these previous techniques (2.1).

The first type of algorithm is GOSSO CFAR (Generalized order statistics smallest of CFAR).The method is based on the selection of a smaller value between values indicated from reference windows ($Z = \min (X, Y)$).

Another technique for detecting objects, GOSGO CFAR (generalized order statistics greatest of CFAR), is shown in figure 7. The Z value is a higher value of previously selected X and Y (figure 5). This technique works best in those situations as compared to the previously discussed methods. It does not detect the edge of the clutter and detects only the peaks containing information about the targets. Similarly behaves another algorithm, GOSCA CFAR (Generalized order statistics averaging cell CFAR), where the value of the parameter Z is the sum of the selected values of X and Y . The different situations for GOSGA CFAR algorithm are shown in figure .



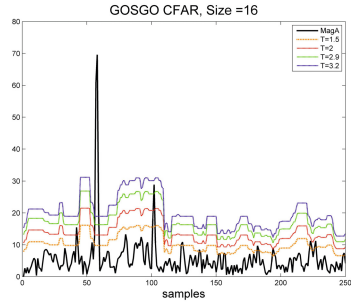
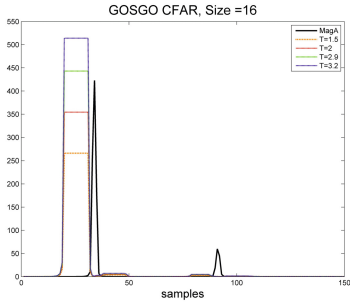
(a) The amplitude spectrum without in- (b) The amplitude spectrum with added interference noise



(c) The amplitude spectrum with clutter (d) The amplitude spectrum with clutter with different reference window size

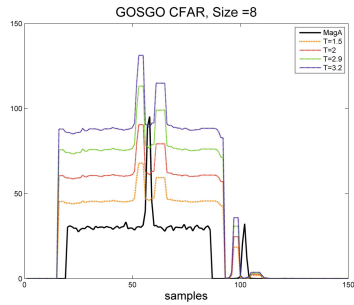
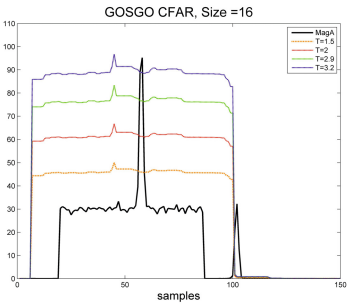
Fig. 6. GOSSO CFAR algorithm behavior in the various situations

The selected variants of the test signal are shown in figure 6. Just as in section 2.1, figures present three situations where different values of scaling factor T were considered. The algorithm does not work well in situations the appearance of an object on a background of clutter (figures 6(c) and 6(d)). Detection detects not only the two objects, but also the edges of the interference. Despite the reduction in the number of cells in the reference window (fig. 6(d)), the problem does not go away.



(a) The amplitude spectrum without interference

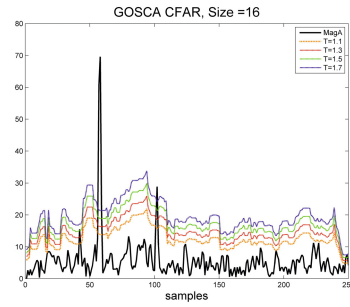
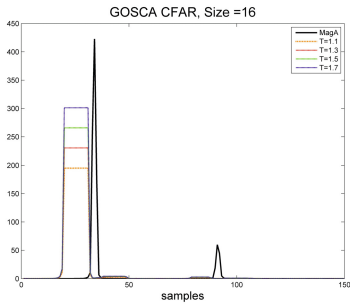
(b) The amplitude spectrum with added noise



(c) The amplitude spectrum with clutter

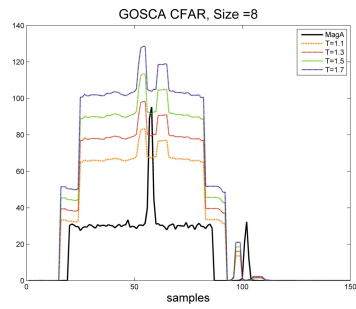
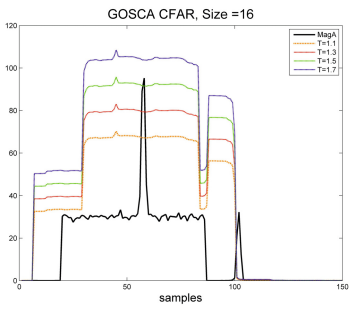
(d) The amplitude spectrum with clutter with different reference window size

Fig. 7. GOSGO CFAR algorithm behavior in the various situations



(a) The amplitude spectrum without interference

(b) The amplitude spectrum with added noise



(c) The amplitude spectrum with clutter

(d) The amplitude spectrum with clutter with different reference window size

Fig. 8. GOSCA CFAR algorithm behavior in the various situations

3 The Measurement Results

Laboratory tests of the Radar Target Detector (RDP) module system have static nature(no RDP movement and obstacles). It was necessary for selecting the parameters when comes to choosing a correct peak in the amplitude spectrum of the signal. Moreover, it was mandatory to verify the accuracy of the distance measurement to the static obstacles. Laboratory experiments were carried out in various environments. In this paper would be presented two of them. In figure 9(b) and table 1 show the simple situation. The algorithm correctly detects peaks responsible for the information storage on detected objects.

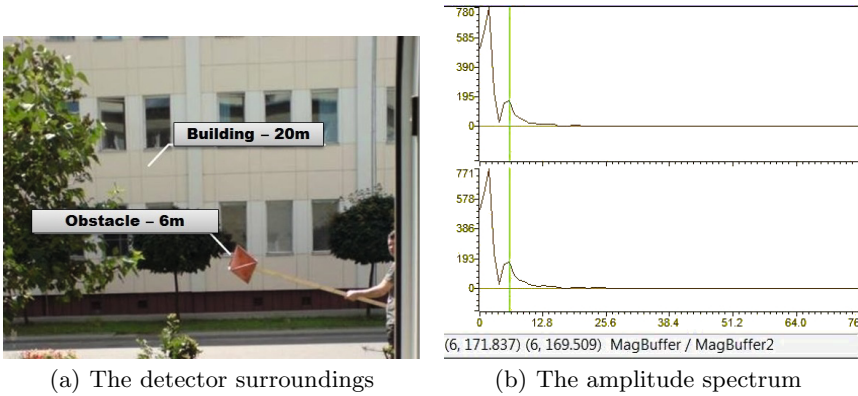


Fig. 9. Static measurements

Table 1. Signal analysis

Target number	Peak number	R [m]	V $\frac{m}{s}$
1	2	05.8	0.1
2	6	18.3	-0.5

The table 1 summarizes the results of the experiment. The figure 9(b) shows the course of the amplitude spectrum of the signal. You can see two characteristic peaks. These peaks has indexes 2 and 6 and they have been correctly selected by the algorithm. Based on peaks it has been obtained information about the distances and velocities of detected obstacles. The table shows the results of these measurements. They are consistent with the actual measurement results.

Another experiment, that was conducted, is shown in figure 10. In this case, the algorithm also correctly detected targets. The results of measured distance and velocity referred to obstacles are correct.

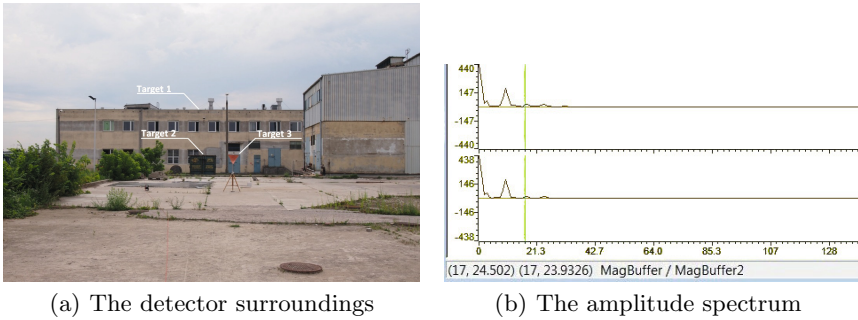


Fig. 10. Static measurements

Table 2. Signal analysis

Target number	Peak number	R [m]	V $\frac{m}{s}$
1	10	33.3802	-0.1304
2	18	51.7361	1.3659
3	24	73.7747	0.9021

4 Summary

The comparison of different techniques of stabilization of a false alarm in various situational models clearly demonstrated OS CFAR superiority over standard methods of CA CFAR and CAGO CFAR. The main advantage of the algorithm with the orderly elements is its behavior in the case of heterogeneous and multi target situation. Whereas, a large disadvantage is a longer processing time, due to the sorting algorithms of samples values in the reference windows. The proper work of chosen technique was presented in this paper.

References

- [1] Panzhi, L., Chendong, D.: Distributed GOSCA-CFAR Detection based on Automatic Censoring Technique (2010)
- [2] You, H.: Performance of some generalised mmodified order statistics CFAR detectors with automatic censoring technique in multiple target situation (1994)
- [3] Rohling, H.: Radar CFAR thresholding and multiple target situations (1983)
- [4] di Cenzo, A.: Analysis of some modified ordered statistic CFAR: OSGO and OSSO CFAR
- [5] Szpakowska-Peas, E.: Algorytm detekcji obiektów dla Radarowego Detektora Przeszkód (2013)

Investigation of the Functional and Environmental Characteristics of Elements with Graphene Coating

Krzysztof Trzcinka¹, Tadeusz Missala¹, Iwona Pasternak²,
Włodzimierz Strupiński², Wojciech Winiarski¹, Marcin Kamiński¹,
Roman Szewczyk³, and Michał Nowicki³

¹ Industrial Research Institute of Automation and Measurements PIAP,
Al. Jerozolimskie 202, Warsaw, 02-486, Poland
{ktrzcinka, tmissala, wwiniarski, mkaminski}@piap.pl

² Institute of Electronic Materials Technology, ul. Wólczyńska 133, Warsaw, 01-919, Poland
{iwona.pasternak, wlodek.strupinski}@itme.edu.pl

³ Institute of Metrology and Biomedical Engineering, Warsaw University of Technology,
Warsaw, Poland
{r.szewczyk, m.nowicki}@mchtr.pw.edu.pl

Abstract. This paper presents environmental and functional tests to determine the areas for graphene coated element application. The researches were held for the following environmental testing of samples with graphene: cold, dry heat, rapid temperature changes and sinusoidal vibrations.

Keywords: graphene, graphene coating, environmental testing.

1 Introduction

Graphene is a new material created in the field of nanotechnology, discovered in 2004 by Andre Geim and Konstantin Novoselov-Kon (awarded the Nobel Prize in 2010). It consists of single layer of carbon atoms [1].

This material is shaped like a honeycomb, and because it has a monoatomic thickness it is considered as a two-dimensional structure. Graphene is the object of interest of the industry, due to various characteristics, including electrical and mechanical properties. Many of these properties have not been verified by laboratory tests, so now all over the world intensive studies on the properties of graphene are being carried out [2, 3].

Industrial Research Institute for Automation and Measurements PIAP (Przemysłowy Instytut Automatyki i Pomiarów PIAP) is the coordinator of the research project *Graphene – based coatings of special gear-wheels and bearings* (acronym Graphtrib) for the applicability of graphene plating on gears. Such plating is intended to provide much higher mechanical strength and better tribological properties of gears.

One of the stages of the Graphtrib project is to perform environmental testing of samples made of graphene covered material. The tests were performed on samples of graphene-coated copper to identify possible areas of application in industry, which is the topic of discussion in this article [4–6].

2 The Preparation of the Samples for Research

The graphene covered samples for environmental research were prepared in the Institute of Electronic Materials Technology ITME (Instytut Technologii Materiałów Elektronicznych ITME). The samples are made of copper foil having a 35 μm thick graphene layer applied on one side. For each type of environmental testing 10 pieces of the foil samples with graphene cover, 30 mm \times 30 mm each, were prepared.

2.1 Process of Graphene Coating

Graphene films were synthesized by the CVD method in a prototype system made by Seco-Warwick. 35 μm thick copper foils with the size of 30 mm \times 30 mm were used as substrates. The capacity of the chamber of the coating system is 50 cm \times 50 cm, as a result of which more than one hundred samples at one run were able to be prepared. The process of graphene manufacturing was divided into a few steps. At first, the samples were pretreated under Ar gas flow and then H₂ gas flow at the pressure of 100 mbar. The purpose of this step was to improve the quality of substrates and increase the size of copper grains. Afterwards, both CH₄ and H₂ gases were introduced into the reactor for a few minutes. Finally, the substrates were cooled down to room temperature in an Ar atmosphere. To ensure optimal temperature conditions, the chosen temperature was in the range between 1020 °C and 1040 °C. During the process of graphene deposition the pressure of 20 mbar was sustained [7].

3 Environmental Research of Graphene Covered Samples

Environmental tests were carried out in the Industrial Research Institute for Automation and Measurements PIAP. The main purpose of the environmental research carried out on samples of graphene coated copper was to test the durability of graphene layers on copper obtained in a variety of environmental conditions, simulated in the laboratory. Parameters which were considered during the tests are temperature and sinusoidal vibration. The effect of temperature on the metal causes the formation of expansion stresses which might cause damage to the connection between the metal and graphene, resulting in risk of graphene coating damage.

The vibrations from the rotating machines are sinusoidal, which can have a negative effect on the graphene plating, and may result in loss of graphene adhesion to the material subjected to vibration.

The choice of environmental conditions was made on the grounds of the document standards PN-EN 60654-1:1996 [8], according to the specified exposure occurring at specific locations, e.g. indoor and outdoor. This will help to identify possible areas of application of graphene for industrial applications. Graphene plating may improve metallic materials properties, such as increasing the mechanical strength, increasing the resistance to corrosion or oxidation.

The study was divided into two main stages. In the first stage of the environmental conditions which can be typically met in the spaces within the industrial buildings, for

example in warehouses, office space or factory production spaces were simulated. These conditions are characterized in a following way:

- Temperature range of + 5 °C to +40 °C,
- Humidity up to 85%,
- Sinusoidal vibration parameters: the amplitude of the displacement was 0.035 mm, 4.9 m/s² acceleration, the vibration frequency range was from 10 Hz to 150 Hz.

In the second stage environmental conditions which are typical in industrial spaces outside buildings were simulated that were characterized in following way:

- Temperature range from -25 °C to +55 °C,
- Humidity up to 100%,
- Sinusoidal vibration parameters: the amplitude of the displacement of 0.075 mm, the acceleration of 9.8 m/s² and the vibration frequency range from 10 Hz to 150 Hz.

This article does not include the results of the research for humidity changes.

Additional environmental tests were made, with more extreme exposures compared to the test in the first stage and the second, which to some way are characteristic for the aerospace industry. Each series of samples were subjected to one of the environmental tests, after which they were subjected to a specialized laboratory analysis.

The first stage of the environmental studies were performed in following research [9–12]:

- Test A – cold: temperature +5 °C, time 16 h,
- Test B – dry heat: temperature +40 °C, time 16 h,
- Test Fc – sinusoidal vibration, displacement A = 0.035 mm, acceleration a = 4.9 m/s², with frequency changes from 10 Hz to 150 Hz, 5 cycles.

In the second step research with more stringent exposures were made:

- Test A – cold: temperature -25 °C, time 16 h,
- Test B – dry heat: temperature +55 °C, time 16 h,
- Test Fc – sinusoidal vibration, displacement A = 0.075 mm, acceleration a = 9.8 m/s², with frequency changes from 10 Hz to 150 Hz, 5 cycles.

Additional research of characteristic environmental exposure for application in the aerospace industry:

- Test A – cold: temperature -50 °C, time 16h,
- Test N – rapid temperature changes [13]: a) from -25 °C to +55 °C,
b) from -50 °C to +55 °C,
- Test Fc – sinusoidal vibration, displacement A = 0.075 mm, acceleration a = 9.8 m/s², with frequency changes from 10 Hz to 2000 Hz, 5 cycles.

4 Research of Graphene Coating after Environmental Exposure

The samples were examined before and after the environmental exposures by optical microscopy and Raman spectroscopy. The optical analysis revealed no changes on the graphene/copper surfaces. We did not observe any spots which could suggest cracked graphene layers or show oxidized copper substrates.

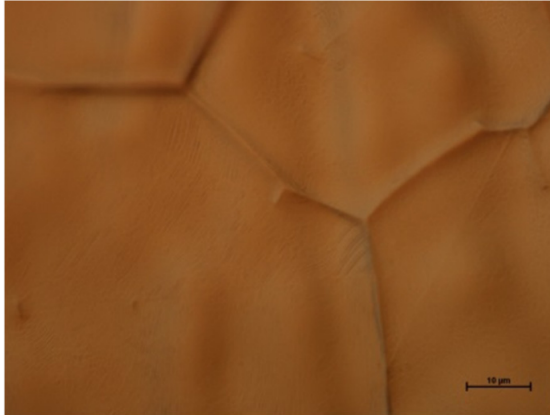


Fig. 1. Optical image of selected graphene/copper surface – reference sample

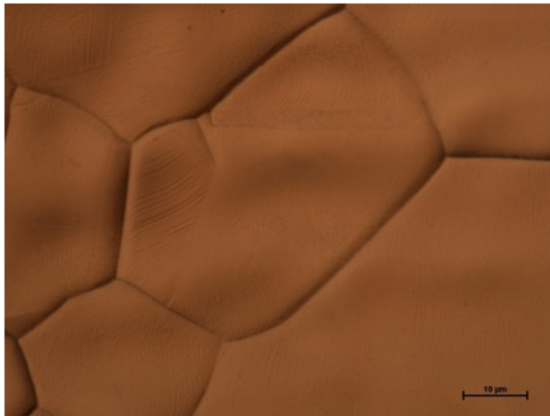


Fig. 2. Optical image of selected graphene/copper surface after test +40 °C, 16 h

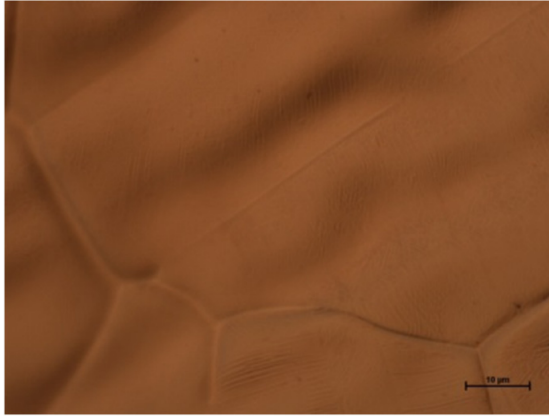


Fig. 3. Optical image of selected graphene/copper surface after test -50 °C, 16 h

The microstructural characterization of the properties of graphene just after its fabrication on reference samples as well as after having performed the investigation was done by Raman spectroscopy using a Renishaw system with a 532 nm Nd:YAG laser as an excitation source. The laser spot diameter on the sample surface was approximately 0.3 μm.

Figures 4, 5, 6 and 7 present the Raman spectra of graphene films after being exposed to 4 groups of environmental test conditions, cold, dry heat, rapid temperature changes and sinusoidal vibration in relation to the reference sample respectively.

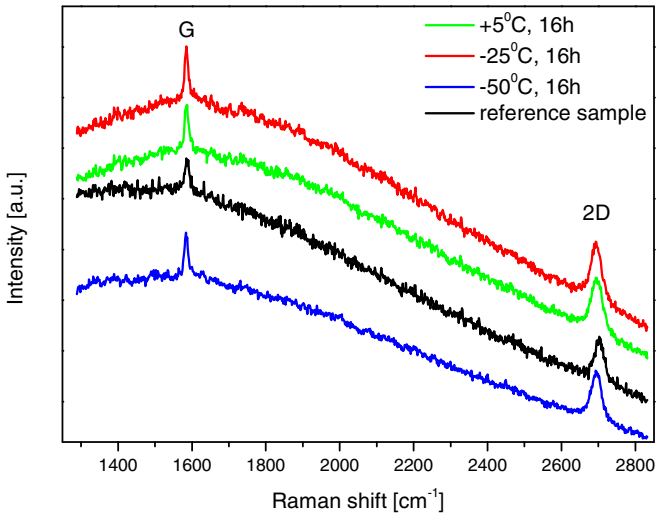


Fig. 4. Raman spectra of graphene films after cold tests

One can observe the presence of G and 2D peaks, characteristic for graphene layers, in the case of all spectra. Moreover, it is clearly visible that these peaks did not change their positions or widths after the performed treatments. This suggests no changes in the graphene structure. The curved shape of the spectra is caused by strong copper luminescence and is usually observed in graphene/Cu Raman spectra.

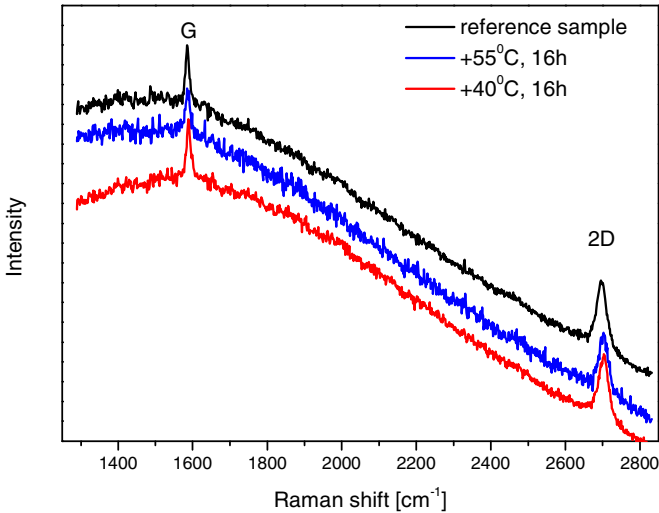


Fig. 5. Raman spectra of graphene films after dry heat tests

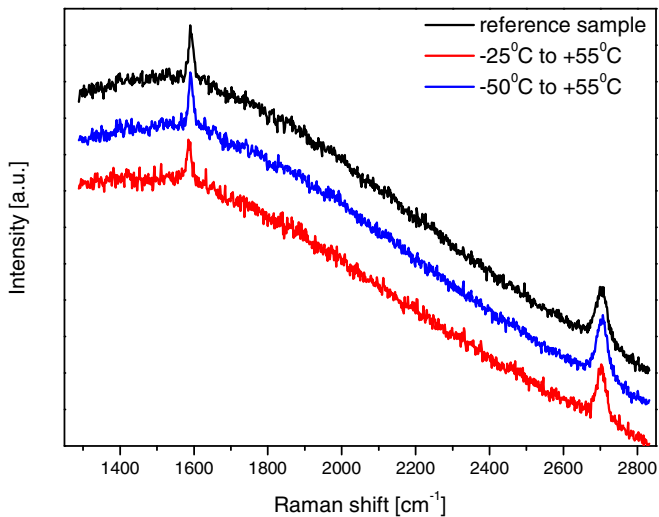


Fig. 6. Raman spectra of graphene films after rapid temperature changes

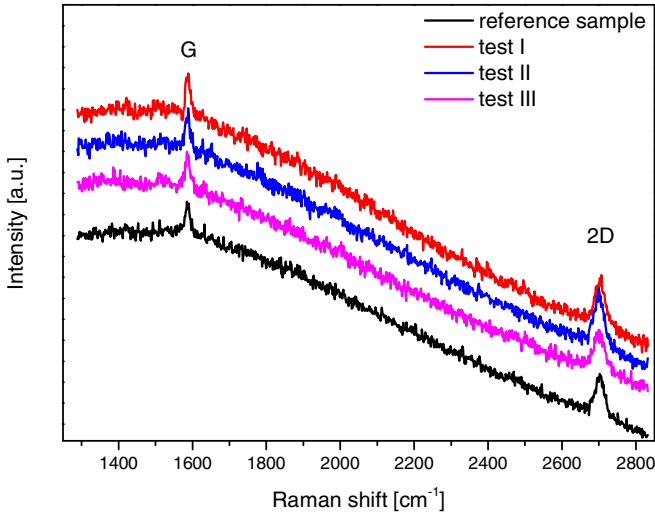


Fig. 7. Raman spectra of graphene films after vibration tests: test I – acceleration of $4,9 \text{ m/s}^2$, frequency range from 10 Hz to 150 Hz, test II – acceleration of $9,8 \text{ m/s}^2$, frequency range from 10 Hz to 2000 Hz, test III – acceleration of $9,8 \text{ m/s}^2$, frequency range from 10 Hz to 150 Hz

5 Conclusions

Positive results of environmental exposure of graphene samples mean that the adhesion between copper and graphene is very strong and is not damaged as a result of the influence of temperature and sinusoidal vibration. The samples covered with graphene are resistant to temperatures down to $-50 \text{ }^\circ\text{C}$ and up to $+55 \text{ }^\circ\text{C}$, rapid temperature changes from $-50 \text{ }^\circ\text{C}$ to $+55 \text{ }^\circ\text{C}$, and sinusoidal vibrations with frequency range up to 2000 Hz, which is a very important information for industrial applications. Knowing the target application, one will need to do more research on other levels of exposure.

In summary, we proved that graphene films on copper foils are stable during environmental exposure. Graphene layers withstood different treatments, which means that we did not notice any changes on their surface and in their micro-composition.

Acknowledgements. This work has been supported by the National Centre for Research and Development (NCBiR) within the GRAF-TECH programme (no. GRAF-TECH/NCBR/05/13/2012). Project "Graphene – based coatings of special gearwheels and bearings" (acronym Graphtrib).

References

1. Shimizu, S., Okada, M., Inoue, Y., Neo, Y., Kume, H., Aoki, T., Mimura, H.: Growth and application of ultra-long multi-walled carbon nanotube. 3(4), 163–165 (2009)
2. Tokarczyk, M., Kowalski, G., Mozdzonek, M., Borysiuk, J., Stepniewski, R., Strupinski, W., Ciepielewski, P., Baranowski, J.M.: Structural investigations of hydrogenated epitaxial graphene grown on 4H-SiC (0001). Applied Physics Letters 103, 241915 (2013)

3. Urban, J.M., Dąbrowski, P., Binder, J., Kopciuszyński, M., Wysmołek, A., Klusek, Z., Jałochowski, M., Strupinski, W., Baranowski, J.M.: Nitrogen doping of chemical vapor deposition grown graphene on 4H-SiC (0001). *Journal of Applied Physics* 115, 233504 (2014)
4. Pasternak, I., Krajewska, A., Grodecki, K., Jozwik-Biała, I., Sobczak, K., Strupinski, W.: Graphene films transfer using marker-frame method. *Aip Advances* 4, 97133 (2014)
5. EN 12166:2911, Copper and copper alloys – Wire for general purposes
6. Project GRAPHTRIB – Graphene-based coatings of special gear-wheels and bearings. NCBR Contract No GRAPH – TECH/NCBR/05/13/2012
7. Lorenc, M.: Measurement system of temperature layout in large buildings. *Pomiary Automatyka Robotyka* 14(12), 69–72 (2010)
8. PN-EN 60654-1:1996, Urządzenia do pomiarów i sterowania procesami przemysłowymi – Warunki pracy – Warunki klimatyczne
9. PN-EN 60068-1:2014-06E, Badania środowiskowe - Część 1: Postanowienia ogólne i wytyczne
10. PN-EN 60068-2-1:2009, Badania środowiskowe - Część 2-1: Próba A: Zimno
11. PN-EN 60068-2-2:2009P, Badania środowiskowe - Część 2-2: Próba B: Suche gorąco
12. PN-EN 60068-2-6:2008E, Badania środowiskowe - Część 2-6: Próba Fc: Wibracje (sinusoidalne)
13. PN-EN 60068-2-14:2009E, Badania środowiskowe - Część 2-14: - Próba N: Zmiany temperatury

Influence of Electromagnetic Pulse Disturbance on the Functional Properties of Ultra-High Resolution Analog to Digital Converter

Krzysztof Trzcinka and Roman Szewczyk

Industrial Research Institute of Automation and Measurements PIAP,
Al. Jerozolimskie 202, Warsaw, 02-486, Poland
{ktrzcinka, rszewczyk}@piap.pl

Abstract. This paper presents the results of the research on electromagnetic pulse disturbances impact on the performance of the 31 bit resolution analog-to-digital converter. The research was held for the following operating conditions of the AD converter: with and without the galvanic isolation through the signal lines. The results of measurements were calculated as the standard deviation in the number of the ADC's elementary divisions. Standard deviation was used to quantify the impact on the accuracy of the AD converter measurements.

Keywords: analog to digital converter, ultra-high resolution, EMC, pulse disturbance.

1 Introduction

Analog to digital converters are used to convert the analog signal to a digital form. By converting the analog signal by the ADC to its digital form it is possible to form a digital signal processing using microprocessor systems. The advantage of digital signals is that they can be very easily processed using advanced methods and algorithms, one can filter, record, analyze and transmit them over long distances [1–2].

Wide availability of analog-to-digital converters of high resolution makes it possible for measuring systems of high precision to be built more often. Precise measuring instruments can work not only in the laboratory environment, sometimes they need to be installed in industrial environments [3–5]. And industrial environment is characterized by, for example, difficult electromagnetic conditions.

For this reason, the design and implementation process for the production of equipment resistant to industrial conditions is very difficult. This requires a lot of experience and knowledge from the constructors in the field of design and software solutions, providing immunity to electromagnetic interference [6–9]. For example, the general requirements of resistance to the disturbances of EMC for operating devices in industrial conditions are described in the PN-EN 61000-6-2 [10].

This paper describes the impact of disturbances of nanosecond pulses (Electrical Fast Transient Burst) [11] on the work of the most important element of a measuring device, which is the analog-to-digital converter, using galvanic isolation in the data

line, and without it. Galvanic separation is one of the examples of design solutions which increase the level of immunity to the electromagnetic pulse disturbances. For this purpose an electronic circuit with ADS1281 analog-to-digital converter was designed and manufactured. Its block diagram is shown below in Fig. 1 on the left side. The latest products from Texas Instruments, which appeared on the market recently, were considered. This includes the ADS1281 analog-to-digital delta-sigma converter, specified by the manufacturer to have a 31-bit resolution. ADCs with such a high resolution are new to the market, so it was decided to examine the quantitative impact of impulse disturbances on the deterioration of effective resolution (ENOB) for the ADS1281 converter, which is the issue of the presented work.

2 Electronic System with Analog-to-Digital Converter ADS1281 for Testing

2.1 PCB with ADS 1281 (ADC 31bit)

In Fig. 1 on the left side, indicated by the dashed line, a block diagram of the electronic circuit with ADS1281 analog-to-digital converter designed for testing is presented. On the analog input of the ADC, a very stable and precise voltage V_{TEST} (2.048 V) was given. Power supply of the whole electronic system with the ADC was carried out using a 9 V battery to exclude the impact of disturbances coming from the power source. Data lines (SPI) from the converter to the microprocessor were connected through the galvanic isolation system with the possibility of omission (short circuit).

2.2 PCB with Microprocessor

The microprocessor which supports the ADC was built on separate printed circuit board. It was powered by a separate power supply which was a switching-mode power supply connected to the mains. The microprocessor circuit is equipped with a LED diode, which during the work of the ADC flashes at a constant rate. LED's actuation is performed in a loop of the program that supports the ADC, a flash in the LED's work is a simplified information of a proper operation of the microprocessor and the implemented program.

2.3 Coupling Disturbances

Pulse disturbances EFT/B were given on the 230 V switching mode power supply input [3], where through the microprocessor circuit and then via the data lines, disturbances enter the ADC. The best place to easily filter disturbances in the test system shown in fig. 1 is the input and output of the switching-mode power supply. However, to examine the effect of the disturbances on the ADC, no filtration in the power supply circuit was used. It was assumed that the disturbances were limited (separated) in the data transmission circuit (SPI), through the use of a galvanic isolation.

2.4 Registration and Processing of Data

The results of measurements were recorded on a computer connected to the microprocessor system using a RS-232 to USB converter with galvanic isolation. In addition, in order to protect the computer from EFT/B disturbances, on both ends of the cable connecting the computer to the microprocessor, ferrite cores were installed.

The information of the measured voltage on the analog input of the ADC was set to the smallest possible frequency of 250 samples per second (250SPS). Each case consisted of about 20,000 measurements, then the data were subjected to analysis and filtering using MATLAB software.

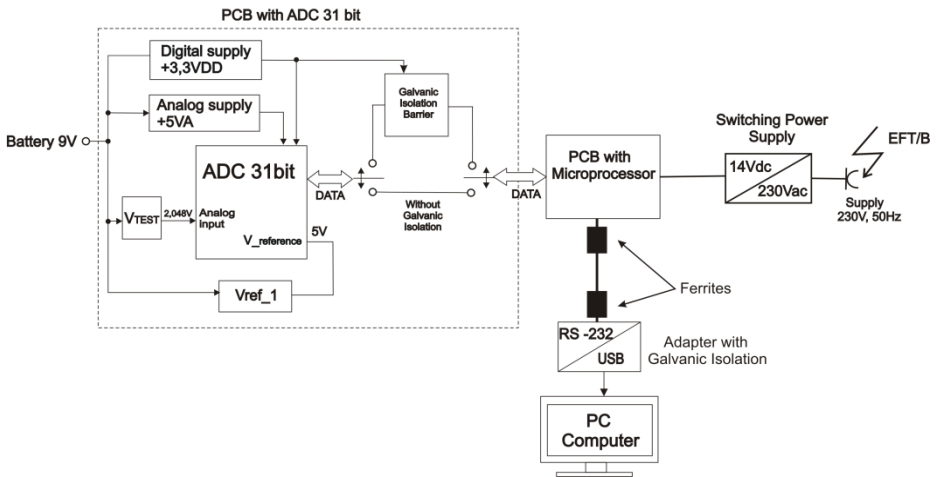


Fig. 1. Block diagram of electronic system with ADS1281, a 31 bit analog-to-digital converter

2.5 System Parameters

Below are shown the most important parameters of the electronic systems with the ADS1281 converter. To efficiently exploit the resolution of an ADC, any electronic part should be carefully selected.

Parameters of analog-to-digital converter ADS 1281, 31 bits sigma-delta [12]:

Resolution (Bits) : 31,

Interface: Serial SPI

Output data rate : selectable 250SPS to 4kSPS,

Signal-to-noise ratio SNR: 130 dB ($f_{DATA} = 250SPS$)

Analog input ($\pm V_{ref}/2$): $\pm 2,5$ V,

Offset error after calibration: $1 \mu V$

Offset drift: $0,06 \mu V/^{\circ}C$,

Gain drift: 0,4 ppm/°C
Temperature range: -40 °C to +125 °C,
24-lead TSSOP package.

Parameters of reference voltage source ADR445 – Vref_1 [13]:

Input Voltage: 5,5 – 18 V
Output Voltage, Vout: 5 V
Voltage noise (0,1 Hz – 10 Hz): 2,25 μ Vp-p
Temperature coefficient: 3 ppm/°C
Temperature range: -40 °C to +125 °C
Precision: 0.04%

Parameters of researched voltage sources LTC6655 - VTEST [14]:

Input Voltage: 3-13,2 V
Output Voltage, Vout: 2,048 V
Voltage noise (0,1 Hz – 10 Hz): 512nVp-p
Temperature coefficient: 2 ppm/°C
Temperature range: -40 °C to +125 °C
Precision: 0.025%

Parameters of galvanic isolation barrier HCPL091J [15]:

Propagation delay: 15 ns max.
High speed: 100 MBd
Barrier Impedance $10^{14} \Omega \parallel 7$ pF
Common mode rejection: 15 kV/ μ s min.
Isolation: 2500 V RMS

3 Impact of Electromagnetic Pulse Disturbances

EFT/B (Electrical Fast Transient Burst) pulse disturbances were chosen for testing the converter, because in practice they are the most common disturbances in the mains. The characteristic features of this test are: high amplitude pulses, short rise time, high repetition rate and low energy transients. EFT/B test is designed to demonstrate the immunity of electrical and electronic equipment when they are exposed to transient disturbances, which are formed during switching transients, such as disconnecting inductive loads and the effect of the relay contact bounce, etc. Figure 2 presents a series of EFT/B pulses. A characteristic attribute of these disturbances is that they are a ‘packs’ of pulses with burst duration of 15 ms (pulse frequency 5 kHz) repeated every 300 ms (see Fig. 2).

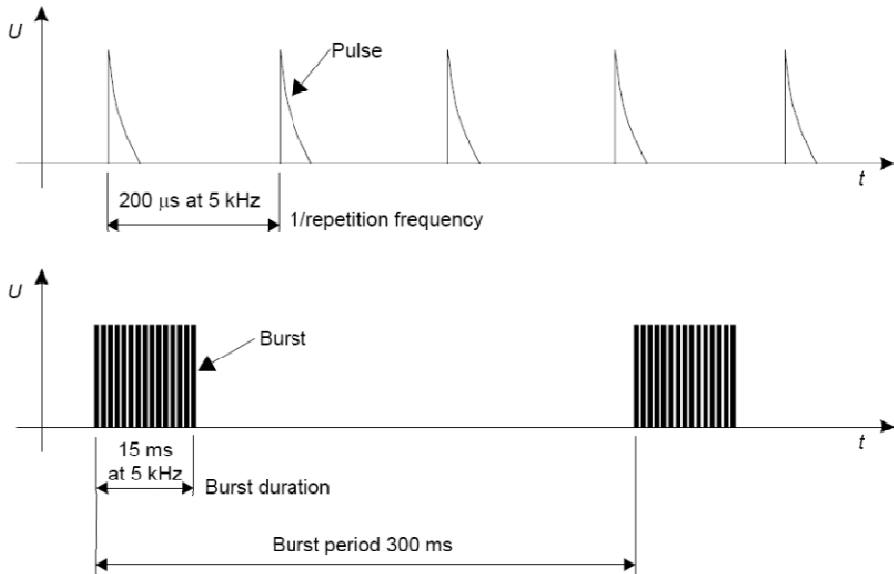


Fig. 2. Electrical Fast Transient Burst (EFT/B) [11]

EFT/B disturbances were introduced to the ADC system through the power supply of the microprocessor to the data lines (SPI). The results are presented in Table 1, where the standard deviation in elementary plots of the AD converter is given.

Table 1. The results of the measurements as the standard deviation in the ADC plots, dependant on the EFT/B disturbances level

EFT/B Level disturbances	σ – standard deviation for analog-to-digital converter	
	ADC without galvanic isolation	ADC with galvanic isolation
None	769.73	752.6
+200 V	1091	765.5
-200 V	47148	758.56
+300 V	177350	806.87
-300 V	8.7221×10^7	754.4
+400 V	9.885×10^7	752.71
-400 V	1.1955×10^8	9.6878×10^4
+500 V	9.6219×10^7	1.1156×10^5
-500 V	1.7186×10^8	4.2336×10^7

A dissection of the results was required to identify how different are the results from the mean value. For this purpose, measurements were divided into ranges of values and it was studied how many measurements belonged in a given interval. Detailed results of the measurements presented for the configuration without electrical isolation can be found in Table 2, and the configuration with galvanic isolation in Table 3. Fig. 3 and Fig. 4 show these results graphically, with the results of the ranges modified in accordance with the signatures of the drawings.

Table 2. The number of measurements for the selected range values dependant on the level of EFT/B disturbances (system work without galvanic isolation)

Range in which are the measurements of results (the difference from the average results of the measurement series)	Occurrences of measurements in given range for disturbance levels							
	+200 [V]	-200 [V]	+300 [V]	-300 [V]	+400 [V]	-400 [V]	+500 [V]	-500 [V]
Higher than mean values in the range of 10 000 ÷ 100 000	0	8	2	9	17	32	135	473
Lower than mean values in the range of 10 000 ÷ 100 000	0	6	10	20	22	276	214	826
Higher than mean values in the range of 100 001 ÷ 1000 000	0	0	0	0	11	29	17	34
Lower than mean values in the range of 100 001 ÷ 1000 000	0	0	0	0	1	12	12	52
Higher than mean values by at least 1 000 001	0	0	7	5	3	15	8	118
Lower than mean values by at least 1 000 001	0	1	11	71	86	147	107	276

Table 1 and 2 shows that for the operation of the AD converter without electrical isolation for all levels of disturbances EFT/B of ± 200 V to ± 500 V, negative effect of disturbances on the measurement results were observed. With the increase of the disturbance voltage, the standard deviation of measurement results also increases.

Negative polarity of disturbance voltage causes more problems for the system under study, resulting in higher values of the standard deviation of measurements than for positive polarity of the disturbances. Only for +200 V results are satisfactory, the standard deviation is 1091 plots and is higher by 41% than when the ADC is working without problems. In contrast to -500 V obtained standard deviation was about $1,72 \times 10^8$ which covers 80% of the measuring range of the ADC.

Table 3. The number of measurements for the selected range values dependant on the level of EFT/B disturbances (system with galvanic isolation)

Range in which are the measurements of results (difference from the average results of the measurement series)	Occurrences of measurements in given range for disturbance levels							
	+200 [V]	-200 [V]	+300 [V]	-300 [V]	+400 [V]	-400 [V]	+500 [V]	-500 [V]
Higher than mean values in the range of 10 000 ÷ 100 000	0	0	2	0	0	0	0	4
Lower than mean values in the range of 10 000 ÷ 100 000	5	0	3	0	0	0	0	28
Higher than mean values in the range of 100 001 ÷ 1000 000	0	0	0	0	0	1	0	5
Lower than mean values in the range of 100 001 ÷ 1000 000	0	0	0	0	0	1	0	11
Higher than mean values by at least 1 000 001	0	0	0	0	0	0	1	0
Lower than mean values by at least 1 000 001	0	0	0	0	0	3	4	33

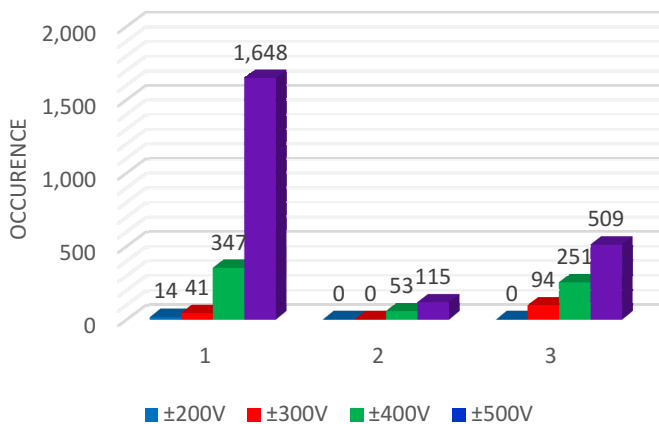


Fig. 3. The number of measurement results in data numerical ranges depending on the level of EFT/B disturbances in the system without electrical isolation: 1 – the results of measurements in the range ± (10 000 to 100 000) from the mean value, 2 – the results of measurements in the range of ± (100 001 to 1000 000) from the mean value, 3 – the results of measurements in the range ± (1 000 001 to ∞) from the mean value

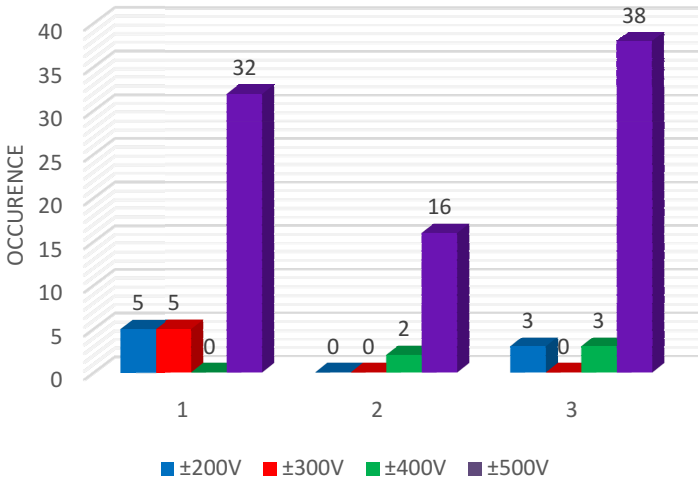


Fig. 4. The number of measurement results in data numerical ranges depending on the level of EFT/B disturbances in the system with galvanic isolation: 1 – the results of measurements in the range $\pm (10\ 000 \text{ to } 100\ 000)$ from the mean value, 2 – the results of measurements in the range of $\pm (100\ 001 \text{ to } 1000\ 000)$ from the mean value, 3 – the results of measurements in the range $\pm (1\ 000\ 001 \text{ to } \infty)$ from the mean value

Fig. 5 presents a graph of the recorded measurement data in which pulses of EFT/B disturbances of +300 V level are visible (in the operation without galvanic isolation). Fig. 6 zooms on the effect of one of the packs of EFT/B pulses.

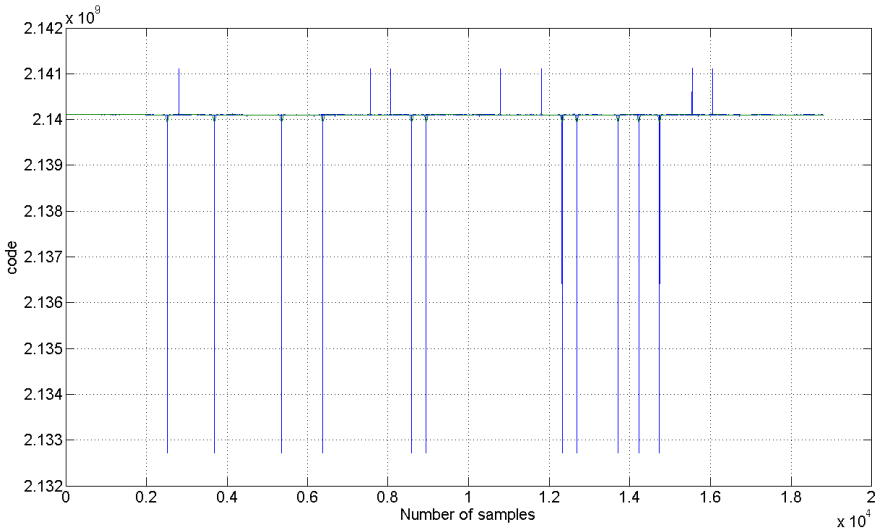


Fig. 5. The measurement results of the level of disturbance pulse exposures of +300 V in the system work without galvanic isolation

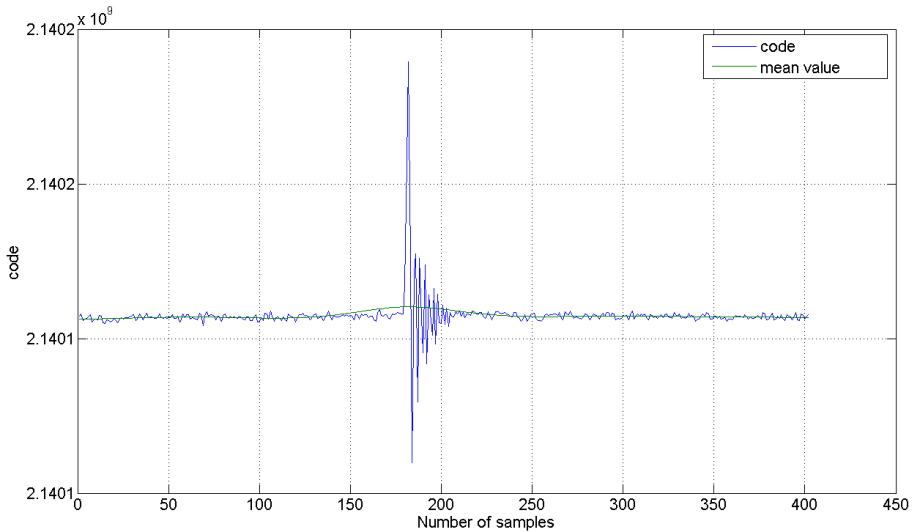


Fig. 6. The measurement results of the level of disturbance pulse exposures of +300 V (enlarged) in the system work without galvanic isolation

For the AD converter with galvanic isolation, the negative polarity of the pulses also causes interference in its work, though the system works correctly for the levels of EFT/B disturbances of ± 200 V to +400 V. The standard deviation of results in this case increases, but this increase does not exceed 10% compared to results without EFT/B disturbances. At voltages of -400 V and ± 500 V the results contain a big measurement error, the standard deviation of the results increases more than 100-times for -400 V and much more for ± 500 V.

According to the results presented in Table 3, for the worst case being converter's work with EFT/B disturbances on the level of -500 V for the system work with galvanic isolation, about 0.4% of the results were classified as bad. For the work without electrical isolation (see Table 2) at disturbances level of -500 V approximately 9% of the results were classified as bad. The criterion of describing a measurement as bad was defined as when the difference between the mean value of all measurements and the measurement result exceed 10,000 plots of AD converter.

4 Conclusions

Research described in this paper clearly show that the use of galvanic isolation in the analog-to-digital converter's system increases the level of immunity to electromagnetic pulse disturbances. This is a very important practical information. Galvanic isolation systems should be applied to electronic circuits with AD converters which are connected to the mains.

In practice, the filtration of disturbances should primarily be used close to the power connection as to reduce the disturbances that can engage with the circuit board sensitive measuring devices to a minimum level. Knowing the characteristics of pulse disturbances and the response of the measuring system under their effect, as a complementary solution one can digitally filter the pulse disturbances.

Acknowledgment. This work was partially supported by The National Center for Research and Development within PBS Program, grant no: PBS1/B3/8/2012.

References

1. Marcel, J.M.: Pelgrom Analog-to-Digital Conversion Hardcover (December 11, 2012)
2. Jun, S.-W., Yasutomi, K., et al.: Linearized settling error calibration for pipeline A/D converter using non-slewing amplifiers. JAMRIS 4, 204–206 (2009)
3. Trzcinka, K., Szewczyk, R., Ginko, O.: Influence of operating conditions on functional properties of high resolution analog to digital converter. Springer 267, 697 (2014)
4. Trzcinka, K.: Conducted disturbances of switching power supply. *Pomiary Automatyka Robotyka* 16(12), 192–195 (2012)
5. Jakubiec, J.: Measurement process in Sigma-Delta AD converter. *Pomiary Automatyka Robotyka* 54(6), 343–346 (2008)
6. Korytkowski, J.: The present monolithic sigma-delta converters for root-mean-square voltage measurement and their comparison to classic monolithic integrated RMS converters. *Pomiary Automatyka Robotyka* 16(7-8), 84–89 (2012)
7. IEEE Standard for Terminology and Test Methods for Analog-to-Digital Converters, IEEE Std 1241TM (2010)
8. Williams, T.: EMC for Product Designers, 4th edn. Paperback (2007)
9. Haasz, V., Pistinek, F.: Influence of disturbance on measurement precision using AD plugin boards. *Measurements* 28, 115–122 (2000)
10. IEC 61000-6-2 ed2.0 Electromagnetic compatibility (EMC) – Part 6-2: Generic standards – Immunity for industrial environments
11. IEC 61000-4-4 ed3.0, Electromagnetic compatibility (EMC) – Part 4-4: Testing and measurement techniques – Electrical fast transient/burst immunity test (2012)
12. <http://www.ti.com/lit/ds/symlink/ads1281.pdf>
13. http://www.analog.com/static/imported-files/data_sheets/ADR440_441_443_444_445.pdf
14. <http://cds.linear.com/docs/en/datasheet/6655fe.pdf>
15. http://www.avagotech.com/pages/en/optocouplers_plastic/plastic_digital_isolator/hcpl-091j/

Influence of Operating Conditions on the Functional Properties of Ultra-high Resolution Analog to Digital Converter

Krzysztof Trzcinka¹, Roman Szewczyk², Tomasz Charubin¹,
Wojciech Winiarski¹, Marek Maciag¹, and Michał Nowicki²

¹ Industrial Research Institute of Automation and Measurements PIAP,
Al. Jerozolimskie 202, Warsaw, 02-486, Poland

{ktrzcinka, tcharubin, wwiniarski, mmaciag}@piap.pl

² Institute of Metrology and Biomedical Engineering, Warsaw University of Technology,
Warsaw, Poland

{r.szewczyk, m.nowicki}@mchtr.pw.edu.pl

Abstract. This paper presents the results of measuring the impact of disturbances on the properties of a 31 bit resolution analog-to-digital converter. The researches were held for the following AD converter operating conditions: with battery supply or with switching power supply, for different ambient temperatures, with the galvanic isolation of the signal lines. The results of the measurements were calculated using standard deviation in the number of scale intervals. Standard deviation was used to quantify the impact on the accuracy of the measurements of an AD converter.

Keywords: analog to digital converter, ultra-high resolution, operating conditions.

1 Introduction

Analog-to-digital converters are fundamental elements of electronic measurement systems, as they are the link between analog and digital signals. Thanks to the conversion of an analog signal by an ADC to its digital form, it is possible to reshape a digital signal through the usage of a microprocessor system. The advantage of digital signals is that they are very easily converted through the usage of advanced methods and algorithms. One can filter, monitor, analyze and transmit them through great distances [1–2].

Common availability of high resolution analog-to-digital converters contributes to creation of measurement systems of increasing accuracy. The need of high accuracy measurement causes a constant work on improving the architecture of existing ADCs that are already on the market (on the manufacturer's side), and minimizing the existing measurement error sources – disturbances (on the user's side), as to obtain maximal ADC resolution. From the user's point of view the essential error sources are the

environmental and electromagnetic conditions during the work of an ADC, as well as the schematic of the electronic system [3].

Delta-sigma type analog-to-digital converters offer high resolution signal processing, reaching up to 24 bits. Among others, Analog Devices, Texas Instruments, Linear Technology and Maxim Integrated have such devices in their offers. One of the newest Texas Instruments products that has appeared on the market recently is a delta-sigma ADC named ADS1281 that, as the manufacturer declares, achieves 31 bit accuracy. Analog-to-digital converters of such high resolution are new on the market, so a study of the impact of external factors on the decrease of effective number of bits (ENOB) of the ADS1281 was made. This is the thesis of the paper.

In practice, the declared resolution presented in the manual of an ADC is very rarely or never reached. It is related to the signal-to-noise ratio (SNR), which describes the level of noise in the electric circuit of the converter. The noise causes reduction in the achieved resolution, it renders the least significant bits (LSB) of the result useless. To efficiently exploit the resolution of an ADC, one should minimize noise level, which is a huge challenge on the level of high resolution measurements [4–6]. This paper studies the impact on decrease of the resolution of the ADC caused by external factors like:

- the occurrence of disturbances emerging in the supply lines,
- the occurrence of disturbances transferred through signal lines,
- ambient temperature changes.

For this purpose an electric system including ADS1281 ADC was designed and build. Fig. 1 presents the block diagram of the said system.

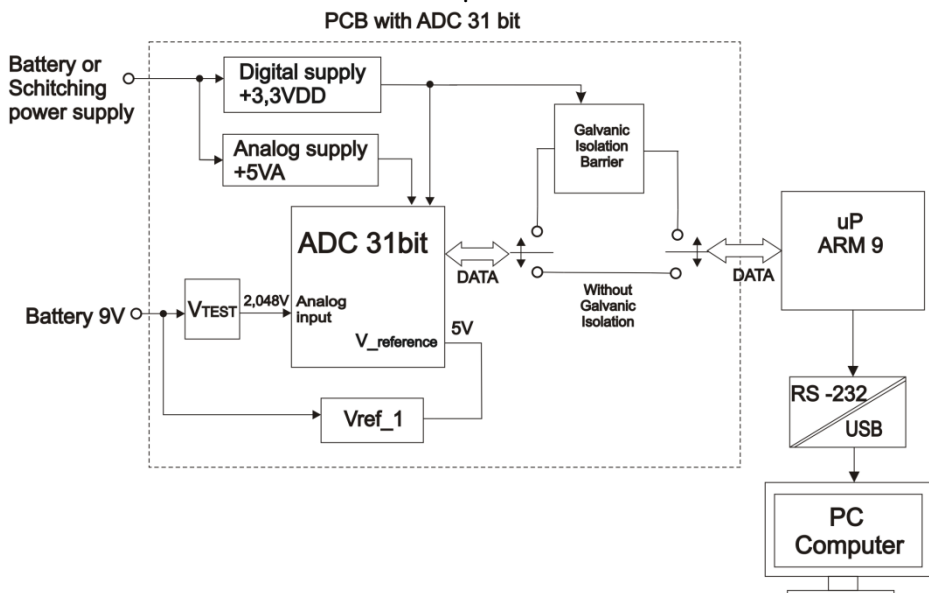


Fig. 1. Block diagram of electronic system with 31 bits analog-to-digital converter ADS1281

2 Electronic System with ADS1281 Analog-to-Digital Converter

Figure 1 presents block diagram of the electronic system with ADS1281, a 31 bit analog-to-digital converter. The analog input of the converter was supplied with VTEST voltage (2.048 V), which was measured and converted by the ADC to digital signal, which then was recorded on a PC. Reference voltage source V_ref1 (5 V) and measured voltage source VTEST were both powered by a battery, as to minimize the noise coming from the power source. The microcontroller handling the ADC was installed on a separate circuit board and powered by a separate battery. The SPI data lines linking the microcontroller to the ADC were connected through a galvanic isolation, with the option to bypass it. The information regarding the measured voltage from the analog input of the ADC was read with the least possible sampling rate of 250 SPS, which ensured maximum resolution. The recording on the PC consisted of approx. 100,000 measured samples for each case. The data were analyzed and filtered using MATLAB software.

2.1 System Parameters

Below are shown the most important parameters of the electronic systems with the ADS1281 converter. To efficiently exploit the resolution of an ADC, any electronic part should be carefully selected.

Parameters of analog-to-digital converter ADS 1281, 31 bits sigma-delta [7]:

Resolution (Bits) : 31,
 Interface: Serial SPI,
 Output data rate : selectable 250SPS to 4kSPS,
 Signal-to-noise ratio SNR: 130 dB (fDATA=250SPS)
 Analog input ($\pm V_{ref}/2$): $\pm 2,5$ V,
 Offset error after calibration: 1 μ V
 Offset drift: 0,06 μ V/ $^{\circ}$ C,
 Gain drift: 0,4 ppm/ $^{\circ}$ C
 Temperature range: -40 $^{\circ}$ C to +125 $^{\circ}$ C,
 24-lead TSSOP package.

Parameters of reference voltage source ADR445 – Vref_1 [8]:

Input Voltage: 5,5 – 18 V
 Output Voltage, Vout: 5 V
 Voltage noise (0,1Hz – 10Hz): 2,25 μ Vp-p
 Temperature coefficient: 3 ppm/ $^{\circ}$ C
 Temperature range: -40 $^{\circ}$ C to +125 $^{\circ}$ C
 Precision: 0.04%

Parameters of researched voltage sources LTC6655 - VTEST [9]:

Input Voltage: 3-13,2 V
 Output Voltage, V_{out} : 2,048 V
 Voltage noise (0,1 Hz – 10 Hz): 512nVp-p
 Temperature coefficient: 2 ppm/°C
 Temperature range: -40 °C to +125 °C
 Precision: 0.025%

Parameters of galvanic isolation barrier HCPL091J [10]:

Propagation delay: 15 ns max.
 High speed: 100 MBd
 Common mode rejection: 15 kV/μs min.
 Isolation: 2500 V RMS

3 Research of Efficiency of Ultra-high Resolution Analog-to-Digital Converter

The measurements results were converted to decimal system value, so that in the result was the number of elementary divisions. The results were subjected to filtration in MATLAB software using third order digital Butterworth filter with 25 Hz cut-off frequency. From the obtained (filtered) signal values the standard deviation was determined, which showed the dispersion of the results from mean value. The calculated standard deviation is used to qualify the impacts on measurements made by AD converter.

3.1 Impact of Disturbances from the Power Supply

To measure the impact of the disturbances coming from the power sources, the ADC circuit has been powered with three different power sources, that is a battery and two different switching-mode power supplies.

A battery is a stable source of voltage that has little to no output voltage ripple and very low impedance, while switching-mode power supplies have noticeable voltage ripple and characteristic frequency of switching, that produces disturbances of harmonic frequencies which negatively influence the work of powered electrical system. [11] In this study particularly, they could worsen the conditions of work of the ADC, which would decrease its effective resolution.

Power supply no. 1 has 12 V output voltage, 450 Hz switching frequency and output voltage ripple of 100 mV_{p-p}. Figure 2 presents the level of conducted disturbances in the low voltage circuit of the supply, with the ADS1281 circuit board as a load.

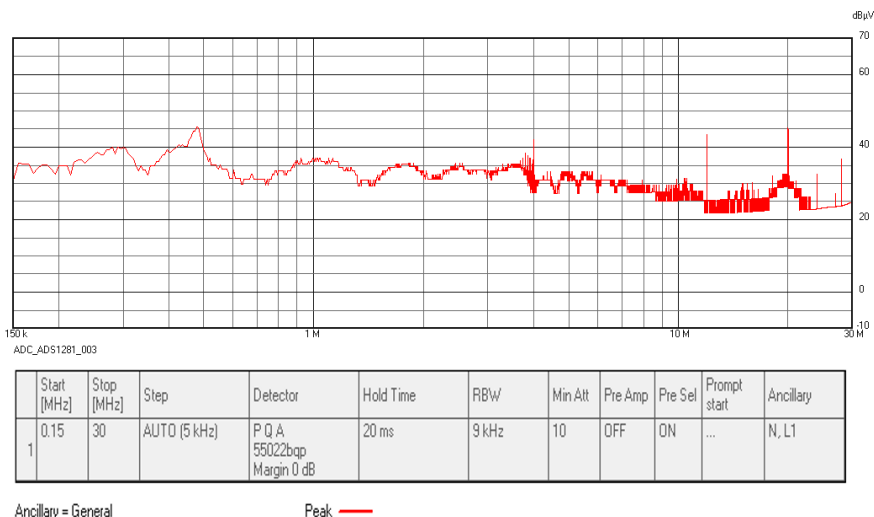


Fig. 2. Level of conducted disturbances measured in the output circuit of power supply no. 1

Table 1. Maximum levels of conducted disturbances in the output voltage of power supply no. 1

	Frequency [MHz]	Level [dBµV]
1	0.3	40.06
2	0.435	40.78
3	0.475	45.61
4	0.925	36.95
5	2.555	35.63
6	3.8	38.26
7	4	42.17
8	12	43.50
9	20	45.34
10	28	36.81

Power supply no. 2 has 9 V output voltage, 52,5 kHz switching frequency and output voltage ripple of 350 mV_{p-p}. Figure 3 presents the level of conducted disturbances in the low voltage circuit of the supply, with the ADS1281 circuit board as a load.

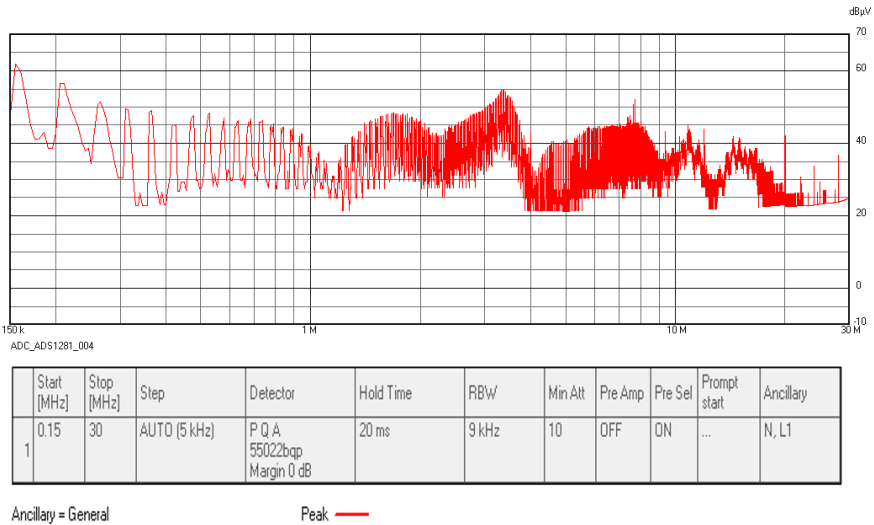


Fig. 3. Level of conducted disturbances measured in the output circuit of power supply no. 2

Table 2. Maximum levels of conducted disturbances in the output voltage of power supply no. 2

	Frequency [MHz]	Level [dBµV]
1	0.155	61.93
2	0.205	56.46
3	3.22	52.41
4	3.27	53.44
5	3.32	54.56
6	3.375	54.65
7	3.415	54.26
8	3.515	52.74
9	3.57	51.62
10	7.74	52.11

From Fig. 2 & 3, and Tables 1 & 2, one can conclude, that the switching-mode power supply no. 2 is a power supply of much worse quality parameters, as it has bigger output voltage ripple and emits greater conducted disturbances than power supply no. 1. To ensure the repeatability of the research, each time the power supply was connected to the mains, it was bypassed by a mains filter (EMI filter 1-phase type 2010). During every measurement the environmental conditions existing in the lab were recorded. The measurement results are presented in Table 3.

3.2 Impact of Interference of the Signal Lines, Galvanic Isolation

The connection of the ADS1281 converter with the microcontroller system was made through a galvanic isolation system using a magnetic coupling barrier. The galvanic isolation on the data lines causes a restrain on the disturbances transmitted through the signal lines of the microprocessor, which is a source of noise on high frequency level.

Research was made for two configurations: with and without the magnetic decoupling barrier in the data lines. As the ADC's power supply three options were measured: battery power supply and two different switching-mode power supplies. Table 3 presents the measurement results.

Table 3. Standard deviation of the AD converter measurement results depending on the application of galvanic isolation of the signal line

Configuration	6 – standard deviation for analog-to-digital converter		
	Battery powered	Switched-mode power supply powered type 1	Switched-mode power supply powered type 2
Galvanic isolation (1)	751.14	796.97	933.45
Absence of galvanic isolation (2)	753.85	864.13	1297.8
Difference between 1st and 2nd	2.71	67.16	364.35

As expected, minimal standard deviation was obtained for the battery power supply configuration with galvanic isolation on the data lines. In this case the result being 751.14 ADC nodes. It is the most precise acquired result (with the least dispersion of the results).

While supplying the ADC with the switching-mode power supplies, the obtained dispersion of the results was bigger than with the battery operation, which means a decrease in the measurement precision. While using the galvanic isolation barrier on data lines, the results of using switching-mode power supply no.1 as opposed to battery power supply show a 45.83 node standard deviation increase, while using switching-mode power supply no. 2 as opposed to battery power supply show a 182.31 node standard deviation increase. However, while working without the galvanic isolation, using switching-mode power supply no. 2 show a 543.95 node standard deviation increase as opposed to battery power supply operation.

The use of galvanic isolation in the data lines for every case of power supply (battery and switching-mode power supplies) causes a decrease in the dispersion of measurement results, as opposed to operation without the galvanic isolation. In the case of using battery power supply, the use of galvanic isolation causes a decrease in the standard deviation of the measurement by 2.71 nodes as opposed to operation without the galvanic isolation. In the case of using switching-mode power supply no. 1 the

difference in standard deviation of the measurement amounts to 67.16 less nodes, while for the switching-mode power supply no. 2 it is 364.35 nodes less than in the case of not having galvanic isolation.

3.3 Impact of Ambient Temperature

The circuit with the ADC was subjected to an ambient temperature change in the range of 0–50 °C. It is the working temperature range for measurement devices used indoors. Table 4 and Fig. 4 present the results of the research. The results can be very useful in practice for correcting the impact of the temperature on the results of an ADC converter measurements.

Table 4. The standard deviation of the AD converter measurement results depending on the temperature

Temp. [°C]	σ – standard deviation for analog-to-digital converter
0	719,68
10	730,11
20	747,3
30	748
40	759
50	781

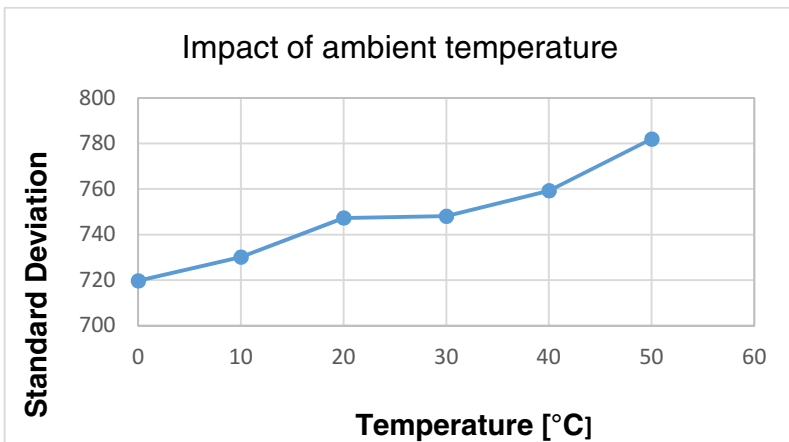


Fig. 4. The standard deviation of the AD converter measurement results depending on the temperature

The results of the research presented in Table 4 show, that ambient temperature significantly influence the measurement results obtained from the ADS1281 analog-to-digital converter in the configuration presented on Fig. 1. The measurements were held while supplying the ADC with a battery and using the galvanic isolation in the data lines. The least obtained standard deviation was for the ambient temperature of 0 °C, while the biggest for the ambient temperature of 50 °C. The difference between 0 °C and 50 °C was 61.32 ADC's nodes.

4 Conclusions

Research done in this paper covers only a part of the factors that have influence on the work of a 31-bit analog-to-digital converter. The impact of the power source type, the usage of a galvanic barrier and the changes in ambient temperature on the ADC's resolution has been shown. Obtained results prove, that the factors mentioned above are very significant and affect the useful resolution of the tested ADS1281 converter. A conclusion that the biggest influence on the standard deviation of measurement results comes from the power supply type has been shown. That's why, the power supplies for measurement applications should be carefully selected in terms of generated disturbances.

In the case of switching-mode power supply no. 2 (the worst case scenario, biggest transmitted disturbances) the worst results (biggest standard deviation of results) have been obtained. The standard deviation of the measurement of the ADC with galvanic isolation and battery power supply, as opposed to switching-mode power supply no. 1 is 110.28 nodes smaller and opposed to switching-mode power supply no. 2 is 543.95 nodes smaller. This is a very meaningful difference.

If possible, for high accuracy measurements one should use batteries as power supply. It is also important to use galvanic isolation on the data lines, especially while supplying the ADC circuit with switching-mode power supply. Obtained results show, that while using switching-mode power supply no. 2 to supply the ADC circuit, the standard deviation difference of results between using and not using the galvanic isolation reach 364.35 nodes.

Ambient temperature change also has a big influence, the difference in standard deviation of measurement results between temperatures of 0 °C and 50 °C amounts to 61.32 ADC's nodes. Knowing the characteristics of the results of measurements of temperature change, one can compensate its influence.

It is worth mentioning, that obtained results should be related to the measuring range of the ADS1281, which is $2^{31} = 2\,147\,483\,648$ nodes at maximum input voltage level.

Acknowledgment. This work was partially supported by The National Center for Research and Development within PBS Program, grant no: PBS1/B3/8/2012.

References

1. Marcel, J.M.: Pelgrom Analog-to-Digital Conversion Hardcover (December 11, 2012)
2. Jun, S.-W., Yasutomi, K., Itoh, S., Kawahito, S.: Linearized settling error calibration for pipeline A/D converter using non-slewing amplifiers. 3(4), 204–206 (2009)
3. Haasz, V., Pistinek, F.: Influence of disturbance on measurement precision using AD plug-in boards. *Measurements* 28, 115–122 (2000)
4. Korytkowski, J.: The present monolithic sigma-delta converters for root-mean-square voltage measurement and their comparison to classic monolithic integrated RMS converters. *Pomiary Automatyka Robotyka* 16(7-8), 84–89 (2012)
5. Trzcinka, K., Szewczyk, R., Ginko, O.: Influence of operating conditions on functional properties of high resolution analog to digital converter. *Springer* 267, 697 (2014)
6. Jakubiec, J.: Measurement process in Sigma-Delta AD converter. *Pomiary Automatyka Robotyka* 54(6), 343–346 (2008)
7. <http://www.ti.com/lit/ds/symlink/ads1281.pdf>
8. http://www.analog.com/static/imported-files/data_sheets/ADR440_441_443_444_445.pdf
9. <http://cds.linear.com/docs/en/datasheet/6655fe.pdf>
10. http://www.avagotech.com/pages/en/optocouplers_plastic/plastic_digital_isolator/hcpl-091j/
11. Trzcinka, K.: Conducted disturbances of switching power supply. *Pomiary Automatyka Robotyka* 16(12), 192–195 (2012)

Flowmeter Converter Based on Hall Effect Sensor

Michał Urbański¹, Michał Nowicki², Roman Szewczyk², and Wojciech Winiarski¹

¹ Industrial Research Institute for Automation and Measurements, Warsaw, Poland
{murbanski, rszewczyk, wwiniarski}@piap.pl

² Institute of Metrology and Biomedical Engineering, Warsaw University of Technology,
Warsaw, Poland
m.nowicki@mchtr.pw.edu.pl

Abstract. This paper presents results of research on the Hall effect sensor as a converter for single- and multi-jet water meters. The research was carried out on industrial single- and multi-jet water meter. The analysis of magnetic field simulations based on finite elements method and studies of magnetic field distribution provide guidelines for utilization of Hall effect sensor in flowmeters applications in order to improve sensing abilities, such as resolution and sensitivity.

Keywords: Hall effect sensor, single-jet, multi-jet, water meter, magnetic field converter.

1 Introduction

The two most common approaches to measurement of flow are displacement and velocity, each using a variety of technologies. Velocity type meters measure the velocity of flowing liquid through a determined internal capacity. The speed of the flow is then converted into the flow volume. Designs based on velocity measurement include single- and multi-jet meters and turbine flowmeters. The basic problem with velocity measurement lies in providing an output signal from sensor.

The current solutions of multi-jet meters apply either mechanical coupling (gear-box) or magnetic coupling with registers, which generates a friction of sensing element such as turbine or impeller. This creates a problem in measuring very low flow rates, as the kinetic energy of the flow is not able to cause rotation of sensing element, causing underflow of measurement. In addition, in common water meters applications, rotating magnet generates 1 impulse per revolution, which results in low resolution at lower flow rates [1, 2].

The aim of this paper is to present alternative method for detecting rotation of sensing element, which will not be affected by listed problems, providing high resolution measures at low flow rates.

2 Working Principle of the Investigated Single- and Multi-jet Water Meter

For the research purpose a WSK-NKP Vane-Wheel Multi-Jet Dry Water Meter (DN20) and JS SMART+ – Vane-Wheel Single-Jet Dry Water Meter (DN20) produced by APATOR POWOGAZ has been chosen. Both of the flow meters are magnetic coupled through a gearbox to flow register. The cases of given flow meters are made from bronze. The impellers, and elements if internal chamber are made from non-magnetic plastic.

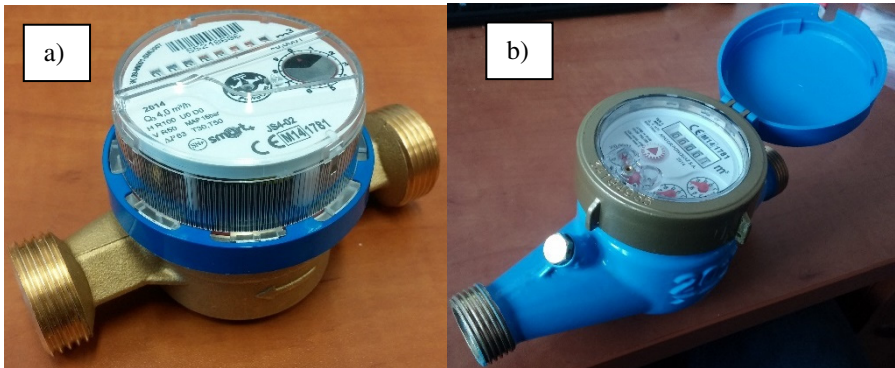


Fig. 1. a) JS SMART+ – Vane-Wheel Single-Jet Dry Water Meter (DN20); b) WSK-NKP Vane-Wheel Multi-Jet Dry Water Meter (DN20)

Researched flowmeters are based on the flow velocity measurement , which is determined by rotational speed of sensing element – turbine or impeller. The velocity of the flow is then converted to the volume of the flow. Conversion factor is determined in the process of calibration, and is mainly related to the internal capacity of the meter.

Single-jet flowmeter design are most commonly used in small residential applications. Single inflow port into chamber creates single jet of water against the impeller.

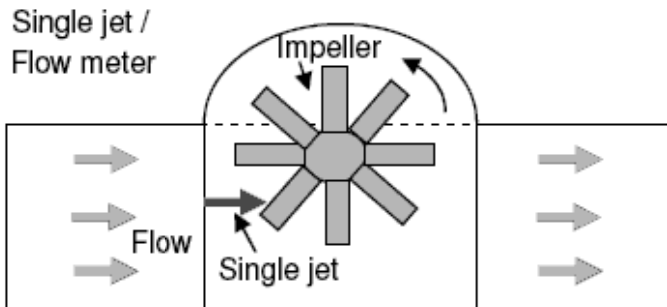


Fig. 2. Schematic design of a single-jet meter [1]

Single-jet water meter is less accurate than multi-jet. On the other hand, the flow of water is not obstructed, which results in possibility of measuring higher flow rates.



Fig. 3. JS SMART+ – Vane-Wheel Single-Jet Dry Water Meter with visible inflow port

Multi-jet flow meters (Fig. 4) are most commonly used for residential and small commercial application. In the researched most common multi-jet flowmeter design multiple ports surround an internal chamber in order to create multiple jets of water against the impeller.

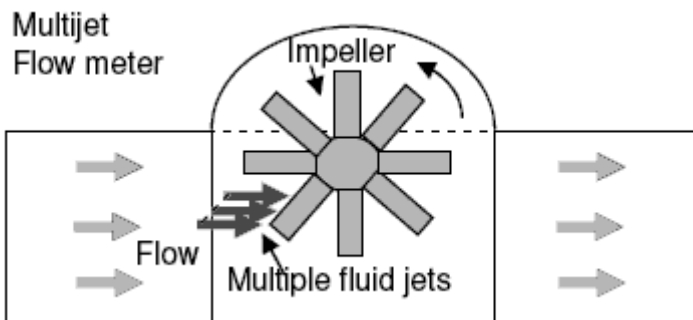


Fig. 4. Schematic design of a multi-jet meter [1]

Multi-jet meters work accurately at low flow rates, but their usage is restricted to diameter of flow path – high rate flows require higher straight-through path.

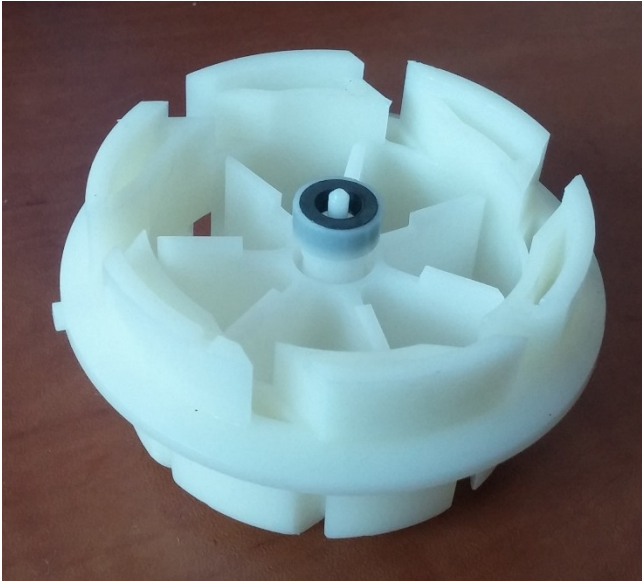


Fig. 5. Multiple ports of multi-jet water meter internal chamber

‘Starting flow rate’ parameter presented in Table 1. is a result of friction present in bearings as well as gearshift. For overcoming resistance forces, minimal value of flow has to be reached to initiate rotation of sensing element. This problem concerns meters with magnetic coupling as well.

Table 1. Parameters of researched water meters

Parameter		JS SMART+ Single-Jet	WSK-NKP Multi-Jet
Nominal diameter	mm	20	20
Continuous flow rate	m ³ /h	4	4
Max flow rate	m ³ /h	5	–
Minimum flow rate	dm ³ /h	40 (cold water)	–
Starting flow rate	dm ³ /h	15	–

The idea behind this paper is to present the possibility of unnecessary elements elimination in measurement processing chain, that may prevent free rotation of sensing element. In addition, this paper may provide a guideline for increasing resolution of tachometric measurement [3], by integrating small-size magnets into paddles of impeller as well as turbine.

3 Hall Effect Sensor

Hall effect sensor is an analog transducer in which output voltage varies in response to the magnetic field strength. Hall sensors are most commonly used for proximity switching, positioning and current sensing applications [5].

The principle of the Hall effect is that current flowing through the conductor, in the presence of magnetic field perpendicular to direction of current, deflects to the side of the conductor, due to the Lorentz law. The asymmetric distribution of charge density in conductor generates an electrical potential. The measured voltage is corresponding to the strength of the magnetic field. [4]

For the purpose of research a Toshiba THS119 hall effect sensor (Table 2.) was used. It is most commonly used as a high stability crank shaft position detector.

Table 2. Parameters of Toshiba THS119 Hall effect sensor

CHARACTERISTIC	SYMBOL	TEST CONDITION	MIN.	TYP.	MAX.	UNIT
Internal Resistance (Input)	R_d	$I_C = 5\text{mA}$	450	—	900	Ω
Residual Voltage Ratio	V_{HO} / V_H	$I_C = 5\text{mA}$, $B = 0 / B = 0.1\text{T}$	—	—	± 10	%
Hall Voltage (Note 1)	V_H	$I_C = 5\text{mA}$, $B = 0.1\text{T}$	55	—	140	mV
Temperature Coefficient (Note 2)	V_{HT}	$I_C = 5\text{mA}$, $B = 0.1\text{T}$ $T_1 = 25^\circ\text{C}$, $T_a = 125^\circ\text{C}$	—	—	-0.06	% / $^\circ\text{C}$
Linearity (Note 3)	ΔK_H	$I_C = 5\text{mA}$, $B_1 = 0.1\text{T}$, $B_2 = 0.5\text{T}$	—	—	2	%
Specific Sensitivity (Note 4)	K^*	$I_C = 5\text{mA}$, $B = 0.1\text{T}$	—	27	—	$\times 10^{-2} / \text{T}$
Internal Resistance (Output)	R_{OUT}	$I_C = 5\text{mA}$	580	—	1350	Ω

4 Simulation Model

The idea behind increasing resolution and eliminating of unnecessary elements in measurement processing chain is to integrate small-size neodymium magnets into paddles of the impeller. For this paper a neodymium 3 mm \times 1 mm magnet was attached to each paddle of the impeller, with parameters showed in Table 3.

Table 3. Parameters of neodymium magnet

Material	Neodymium Iron Boron (NdFeB) Nickel plated
Distance (mm) at which magnets measure 1000 gauss	4.1
Surface flux measurement (gauss)	1500
Grade/Energy density	Grade N30H, max. energy density 30 MGOe ($2387 \cdot 10^6 \text{ A/m}$)

To simulate distribution of magnetic field in single- and mulit-jet water meters ElmerFEM software was used. ElmerFEM is free and open-source Finite Element Method software, subject to the requirements of the GNU General Public License (GPL), developed by Finnish IT Center for Science.

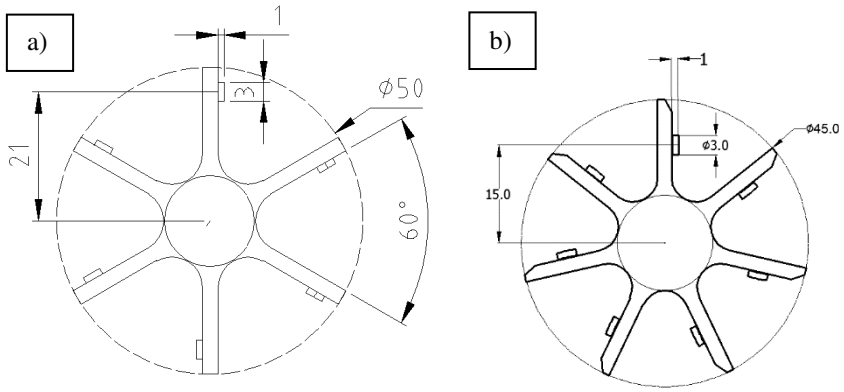


Fig. 6. Geometry of: a) single-jet impeller, b) multi-jet impeller

For the purpose of magnetic field simulation an Elmer Magneto Dynamics procedure was used, along with WhitneyAVSolver [6]. Meshes (Fig. 7) for simulation were created in NETGEN 5.3 open-source software, based on the LGPL, based on geometry shown on Fig. 6.

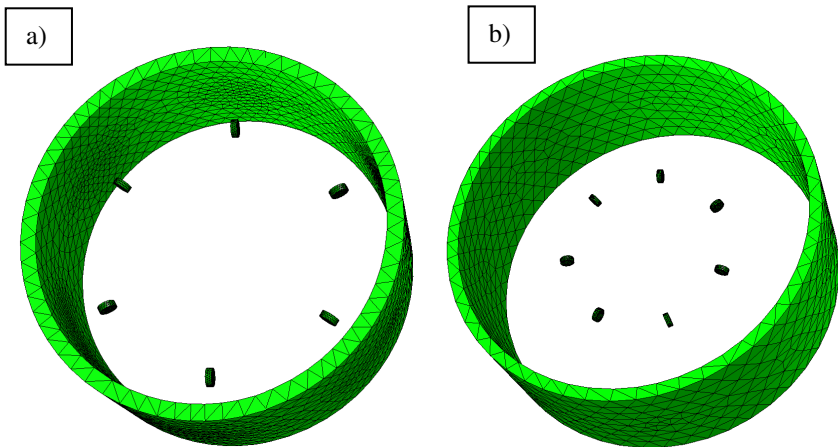


Fig. 7. Meshes of: a) single-jet impeller, b) multi-jet impeller

The aim of the simulation is to determine the distribution of the magnetic field on the external surface of water meter’s cases. Given the results it is possible to confirm if each of magnet peaks would be detectable, as well as to choose optimal placement point for Hall sensor.

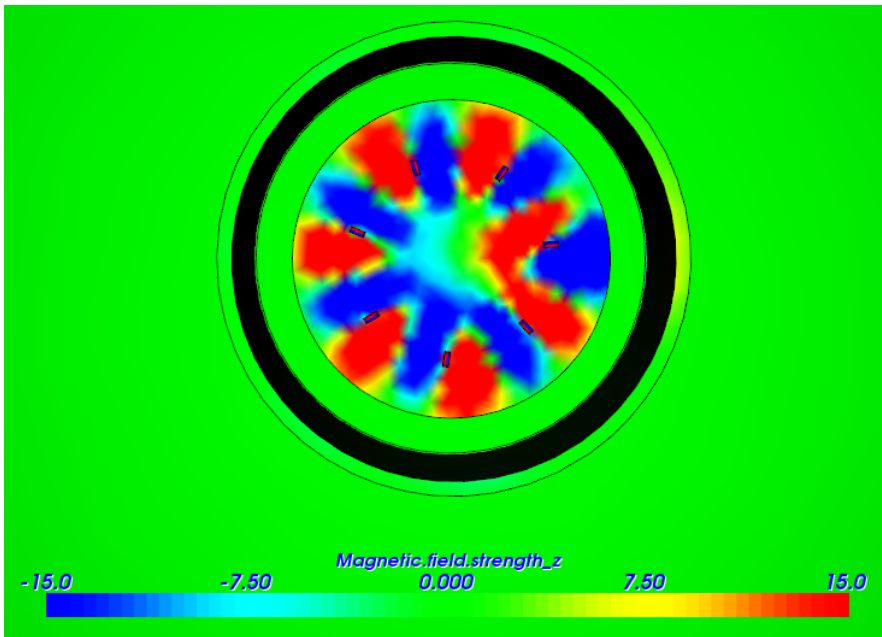


Fig. 8. Distribution of magnetic field on XY plane in WSK-NKP Multi-Jet Water Meter

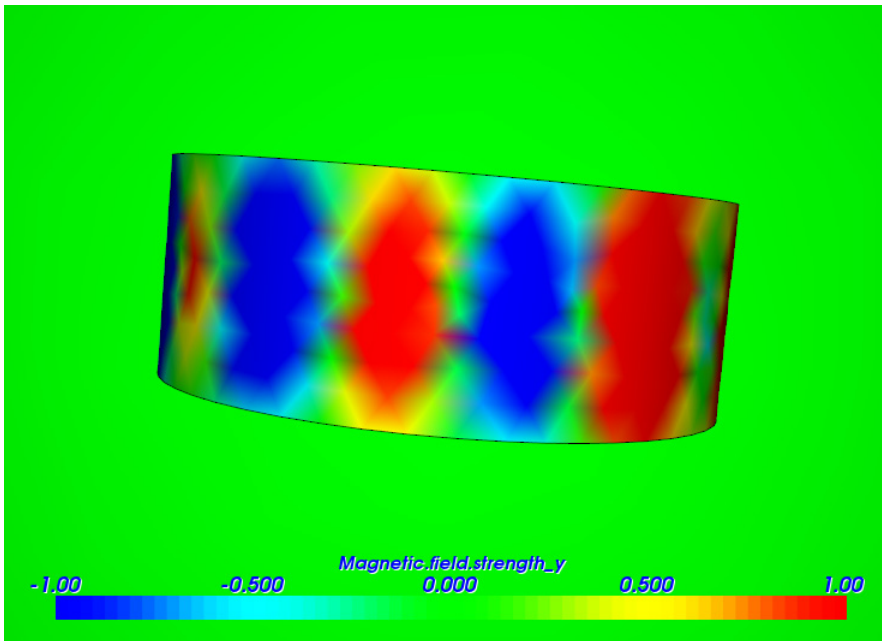


Fig. 9. Distribution of magnetic field on side of case in WSK-NKP Multi-Jet Water Meter

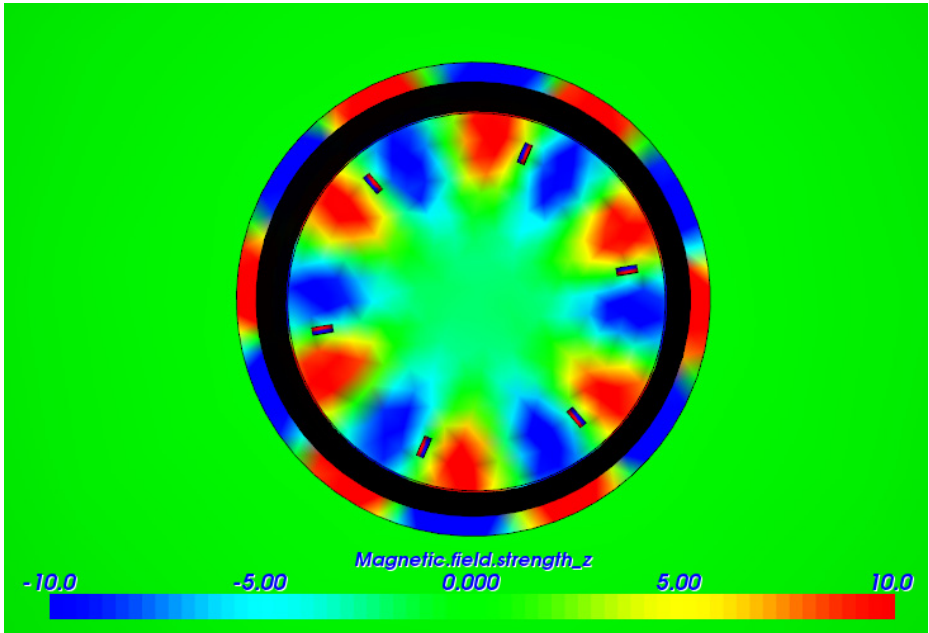


Fig. 10. Distribution of magnetic field on XY plane in JS+ Single-Jet Water Meter

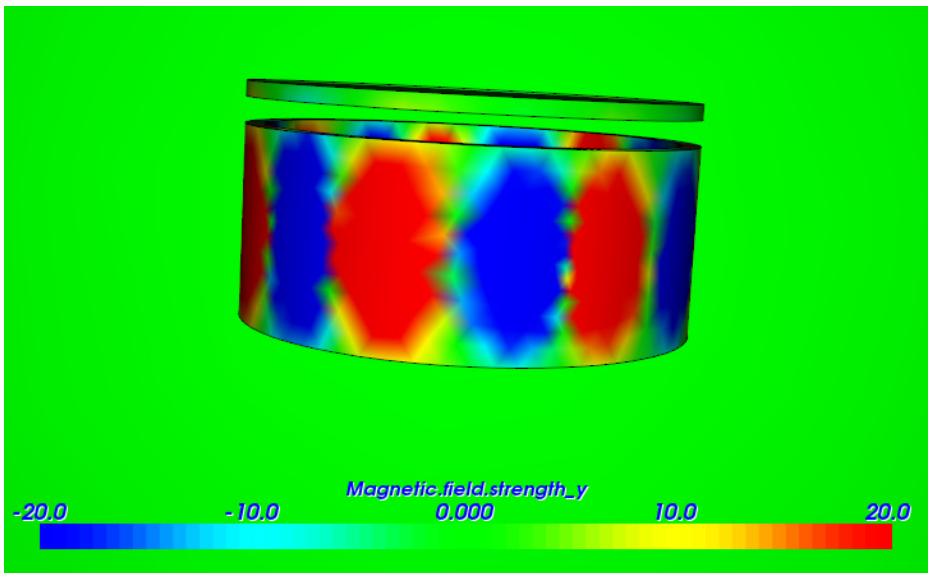


Fig. 11. Distribution of magnetic field on side of case in JS+ Single-Jet Water Meter

As presented on Figures 8–11 it is possible both to install Hall effect sensor on the outer case of the flow meter, as well inside the water meter – between the internal flow chamber and the register mechanism. In the investigated Multi-Jet Water Meter

the optimal position is inside – because of the internal multiport chamber the distance between the impeller paddle and outside case is significantly longer than between the impeller paddle and field strength, as seen of Fig. 8 and Fig. 9.

On the contrary, in the investigated Single-Jet Water Meter the better position of hall effect sensor would be on the side of case. Again, it depend on the distances between possible positions, what is presented on Fig. 10 and Fig. 11.

5 Measurements

In order to confirm simulation results, and give them exact values of magnetic field density measurements with Toshiba THS119 Hall Effect sensor were performed for both of given water meters. The results are presented on Figures 12–14.

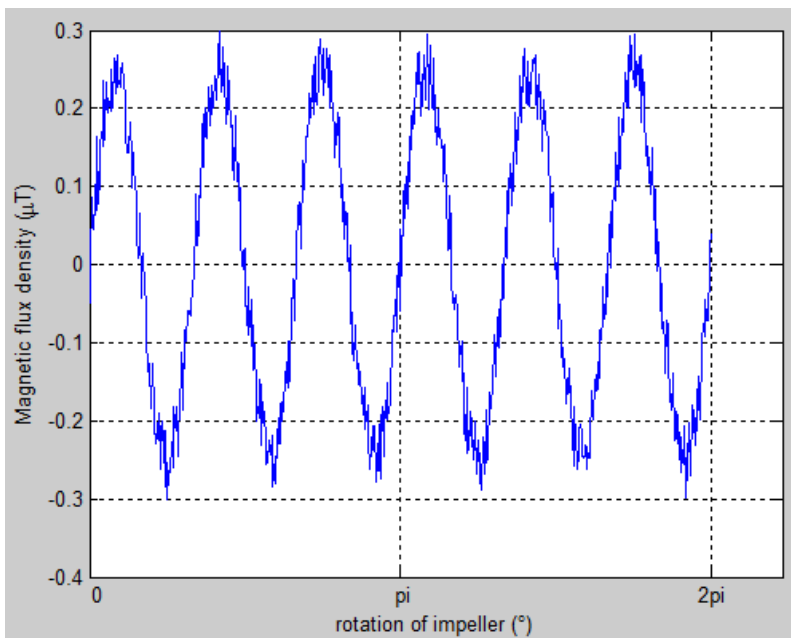


Fig. 12. Magnetic flux density measurement on the side of Single-Jet Water Meter

In the case of investigated Single-Jet Water Meter the difference between signal acquired on the side (Fig. 12) and above the internal chamber, or XY plane (Fig. 13) is relatively small. It results from the geometry of given Water meter, especially from the lack of internal multi-port chamber, as is the case of Mutli-Jet Water Meter.

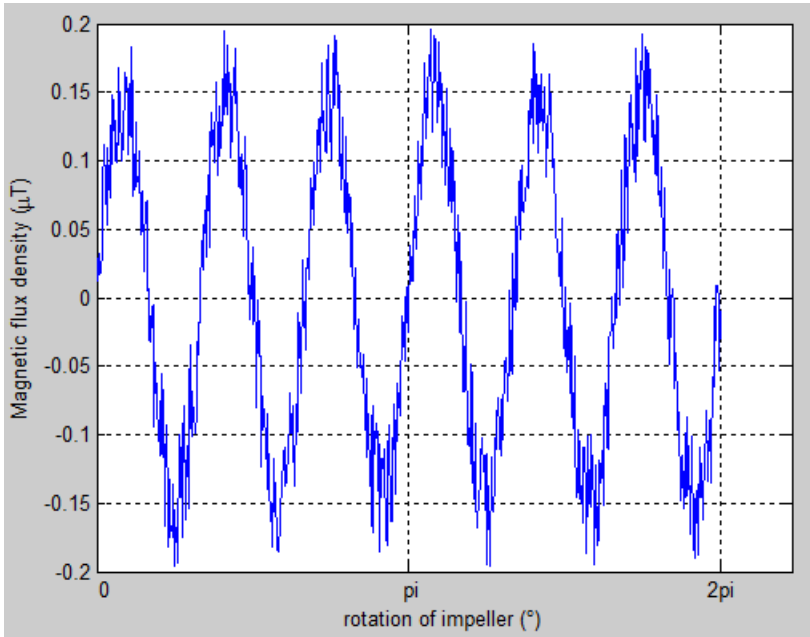


Fig. 13. Magnetic flux density measurement on XY plane of Single-Jet Water Meter

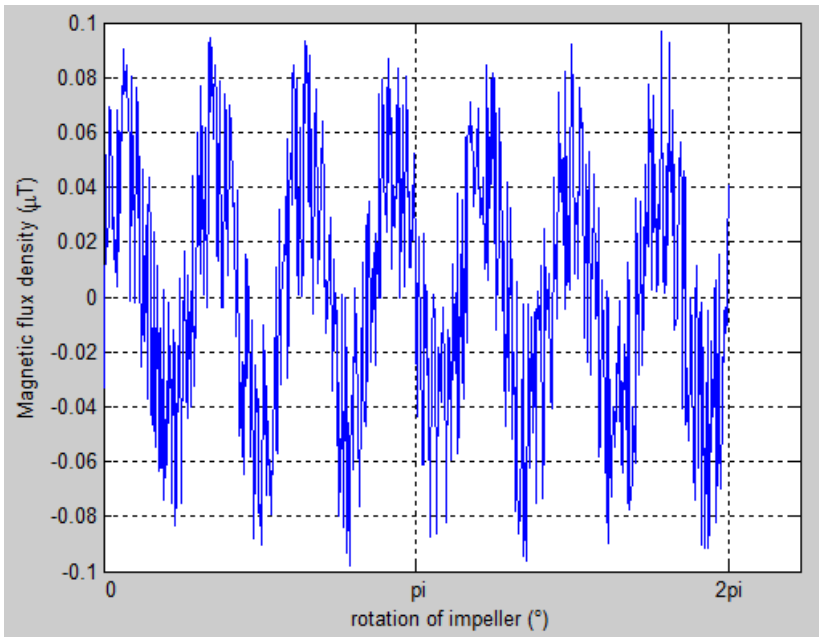


Fig. 14. Magnetic flux density measurement on the side of Multi-Jet Water Meter

In the case of investigated Multi-Jet Water Meter there is more significant discrepancy of signal between measurements on the side case (Fig. 14) and on XY plane (Fig. 15) It confirms the simulation model presented before.

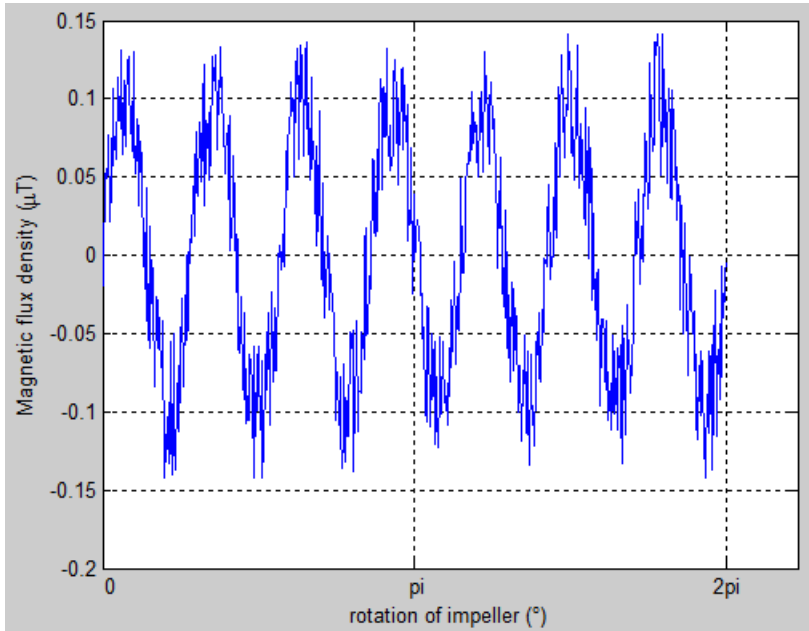


Fig. 15. Magnetic flux density measurement on the XY plane of Multi-Jet Water Meter

6 Conclusion

As presented in the paper, it is possible to utilize a Hall effect sensor as converter for both single- and multi-jet flowmeters. The magnetic field provided by low-size neodymium magnet is strong enough to be detected outside of the internal chamber. It gives the possibility of enhancing sensing resolution by installing magnet on each of impellers paddles. Hall sensor, being magnetically neutral does not provide additional friction in measurement chain, which results in wider sensing range. It allows also for the digital output from water meter, with data ready to be postprocessed without additional converting steps.

The research opens the possibility for graphene Hall sensor to be utilized, enhancing the sensitivity, thus allowing more arbitrary placement of sensor, and even contactless measurements of the flow [7].

Acknowledgments. This work has been supported by the National Centre for Research and Development (NCBiR) within the GRAF-TECH programme (no. GRAF-TECH/NCBR/02/19/2012). Project " Graphene based, active flow sensors " (acronym FlowGraf).

References

1. Zyl van, J.E.: Introduction to Integrated Water Meter Management (Water Research Commission) (2010)
2. Bartyś, M.: Inteligentny przetwornik strumienia objętościowego. *Pomiary Automatyka Robotyka* 14, 74–78 (2010)
3. Niewiatowski, J.: Algorytm tachometru. *Pomiary Automatyka Robotyka* 16, 73–77 (2012)
4. Ramsden, Hall-effect sensors: theory and applications (2006)
5. Barczyk, J.: Hallotronowe sensory położenia. *Pomiary Automatyka Robotyka* 5 (1998)
6. Reddy, J.N.: An Introduction to the Finite Element Method, 3rd edn. McGraw-Hill (2005)
7. Petruk, O., Szewczyk, R., Ciuk, T., et al.: Sensitivity and Offset Voltage Testing in the Hall-Effect Sensors Made of Graphene. AISC. Springer (2014)

Analysis of Response Time of Carbon Dioxide Sensor in Chemical Sensor System for Mobile Robot

Michał Urbański¹ and Roman Szewczyk²

¹ Industrial Research Institute for Automation and Measurements PIAP, Warsaw, Poland
murbanski@piap.pl

² Institute of Metrology and Biomedical Engineering, Warsaw University of Technology,
Warsaw, Poland
r.szewczyk@mchtr.pw.edu.pl

Abstract. The aim of this paper is analysis of NDIR carbon dioxide sensor response time. The NDIR sensor is part of chemical sensor system designed for mobile robot PIAP-GRYF made by Industrial Research Institute for Automation and Measurement PIAP. This paper presents analysis of response time of an CO₂ Engine K30 NDIR sensor, manufactured by SenseAir, both as the analog voltage signal and digital text output. This will help to determine the time inertia of sensor in presence of a rapid concentration increase of carbon dioxide.

Keywords: CBRN defense, NDIR, carbon dioxide, mobile robot.

1 Introduction

With the increasing risk of chemical, biological, radiological and nuclear threats (CBRN) there is a need to ensure safety of uniformed service workers on their place of operation. With that in mind, a system of chemical sensors for detecting such threats for mobile recon robot PIAP – GRYF was designed. The system is developed as a support for analyzing the scene of operations in presence of CBRN threats [1, 2].

One of the sensors implemented on platform of chemical sensor is Carbon Dioxide sensor. Carbon Dioxide (CO₂) is scentless, colorless gas dissolvable in water. It is a product of complete combustion of carbon and all organic compounds. In fresh air, the concentration of Carbon dioxide is 400 ppm (parts per million) what equals to 0.04%. In low concentration carbon dioxide is safe for human. In contradiction to other gases like, carbon monoxide (CO) or hydrogen sulfide (H₂S), carbon dioxide poisoning is a simultaneous stat of hypoxia and hypercapnia (increased partial pressure in blood). It results in shortness of breath and feeling of anxiety. Further increase of concentration of carbon dioxide in air results in headache and dizziness, perceptual distortions and increased heart rate. Concentrations above 10% may result in death in few minutes. Effects of carbon dioxide concentration in air are shown in Table 1.

Table 1. Carbon Dioxide – Physiological effects [3]

CO ₂ volume in air (%)	Likely effects
1–1.5	Slight effect on chemical metabolism after exposures of several hours
3	The gas is weakly narcotic at this level, giving rise to deeper breathing, reduced hearing ability, coupled with headache, an increase in blood pressure and pulse rate.
4–5	Stimulation of the respiratory centre occurs resulting in deeper and more rapid breathing. Signs of intoxication will become more evident after 30 minutes exposure.
5–10	Breathing becomes more laborious with dizziness, headache, visual and hearing dysfunction.
10–100	When the carbon dioxide concentration increases above 10%, unconsciousness will occur in under one minute and unless prompt action is taken, further exposure to these high levels will eventually result in death.

Carbon dioxide also indicates of oxidation processes (especially combustion), as well as fermentation processes. Monitoring of carbon dioxide concentration in air allows to detect such threats in advance, and prepare an adequate response.

In this paper a testing platform for NDIR K30 carbon dioxide sensor is prepared. The response time proposed by the manufacturer, SenseAir, is a value of 20 s, and is restricted by diffusion time of air into chamber. Sensor measures concentration every 2 seconds. Proposed research method aim to confirm this information in different cases.

2 System of Chemical Sensors

The system of chemical sensors is designed for mobile recon robot PIAP-GRYF. It is developed by Industrial Research Institute for Automation and Measurement, and shown on Fig. 1. The system of chemical sensors, shown on Fig. 2 consists of following sensors:

1. Radiological
2. Hazardous gases (chloride, chlorine, hydrogen sulfide)
3. Carbon dioxide

Given sensor work under the control of ARM NXP LPC1114 microprocessor, that collects and processes measurement data. During measurements for purpose of this paper digital data collected by microprocessor were processed to a Desktop Computer through RS-232 interface. Simultaneously analog measurement data was collected directly from sensor through a National Instruments USB 6341 Data Acquisition Device.



Fig. 1. Mobile robot PIAP-GRYF

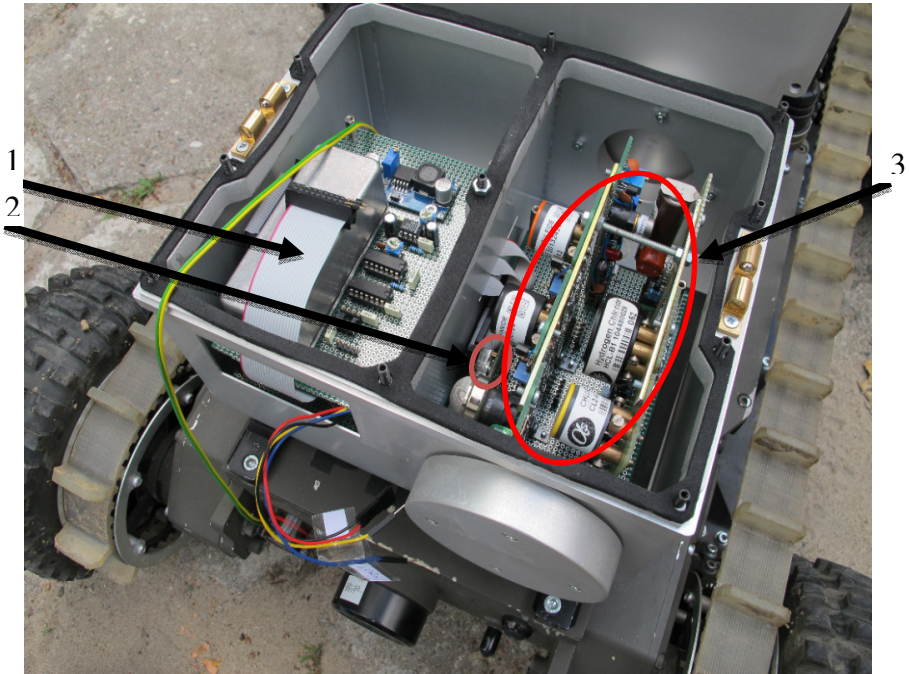


Fig. 2. Chemical sensor platform – sensors: 1) Radiological, 2) CO₂, 3) Hazardous gasses

Carbon dioxide K30 Engine is a NonDispersive InfraRed sensor (NDIR). It is a simple spectroscopic sensor. Infrared light is directed through the sampling chamber of sensor. According to Beer-Lambert law (1) [4], the gas in the chambers absorb specific wavelengths. Infrared filter present before the detector narrows down detected wavelengths to a single value, proper for detected gas. The detector measures the intensity of passing wavelength, and on that basis the concentration of gas in sample chamber is determined (Fig. 3). The parameters of this sensor are presented in Table 2.

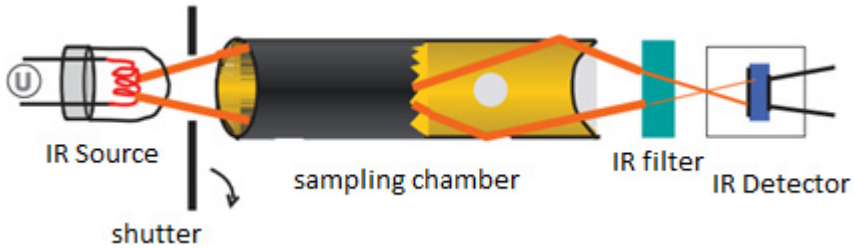


Fig. 3. Schematic NDIR sensor [4]

$$I = I_0 e^{-kP} \tag{1}$$

where: I – intensity of light striking the NDIR detector, I_0 – intensity calibrated for zero point, k – proportionality factor, P – concentration of measured gas.

Sampling in chosen sensor is based on diffusion, hence the necessity to measure response time. Digital signal from sensor is acquired through UART interface with MODBUS protocol.



Fig. 4. Engine K30 Carbon Dioxide sensor by SenseAir

Table 2. Parameters of Engine K30 Carbon Dioxide sensor

Input Voltage	4,5 V – 14 V DC
Average current consumption	~40 mA
Start-up time	<1 min
Analog output	0–4 V – 0...2000 ppm 1-5 V – 0...2000 ppm
Digital Interface	UART Interface MODBUS open protocol

3 Measurement Method

For purpose of this paper a testing system was designed in order to acquire measurements in digital (text) and analog (voltage) form (Fig. 5).

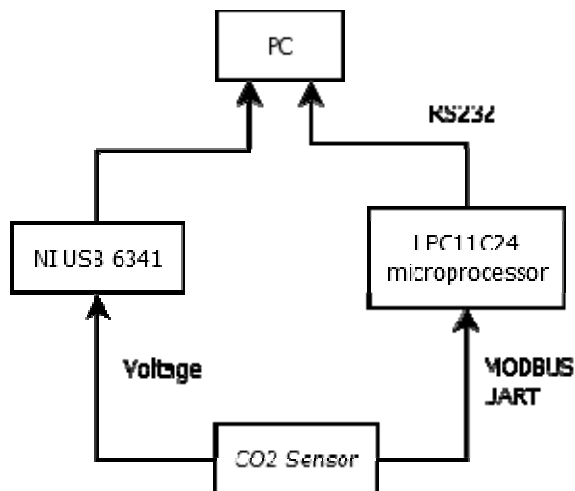


Fig. 5. Flowchart of data acquisition

The increase of carbon dioxide concentration was triggered with a compressed gas from tank. After each measurement the testing chamber was ventilated and calibrated to fresh air value of 400 ppm/ The measurements were made for two cases:

1. Increasing the concentration of CO₂ around the sensor
2. Placing sensor inside the area of high CO₂ concentration

The testing conditions were set to near normal:

- Temperature: 20 °C
- Pressure: 101.3 Pa
- Humidity: 50%

4 Results

The results of measurement are presented on Figures 6–8. Sampling rate for analog signal was set to 100 Hz, and the digital signal was acquired every 2 s (sensor own measurement time and conversion/transmission time to PC was accounted for).

On Fig. 6 a response for increasing concentration of investigated sensor is presented. Red line marks the moment of applying Carbon Dioxide inside testing chamber, black dotted line presents the when the value of concentration has stabilized. The difference in response between the analog and digital output is negligibly small in that case.

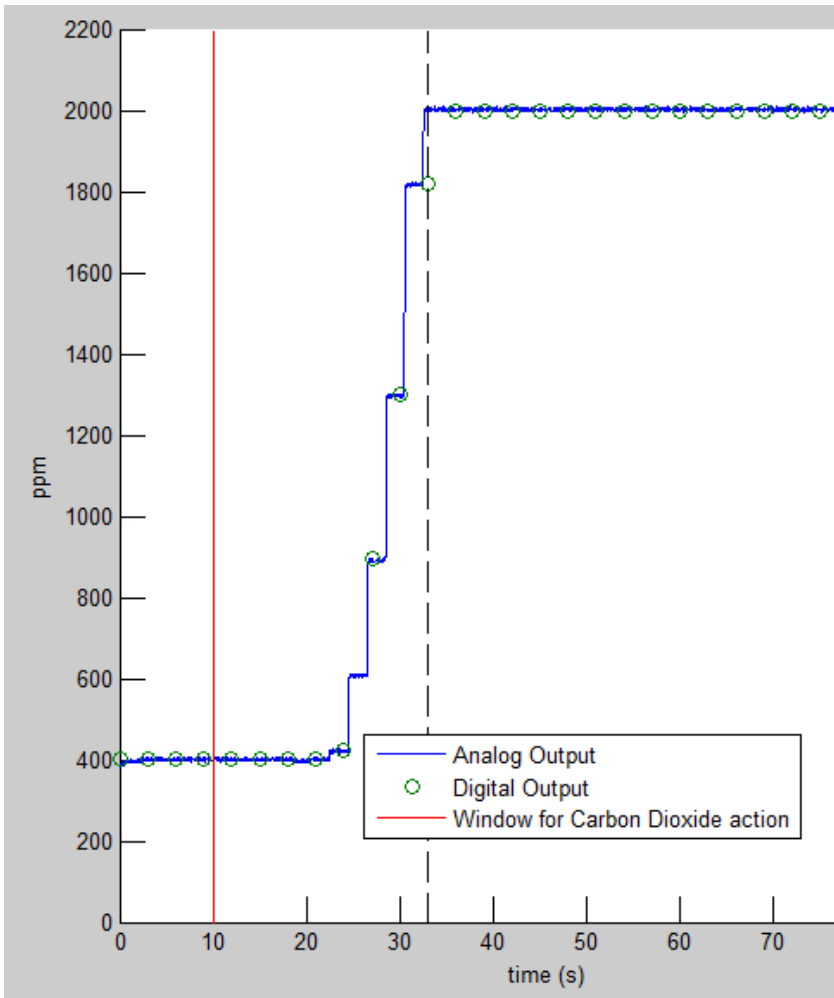


Fig. 6. Analog and digital response of sensor at increase of CO₂ concentration

The time span between applying Carbon Dioxide and first reaction of sensor is 12 seconds, and another 10 seconds till stabilizing, sums up to 22 seconds of time response for analog signal. For digital output it took another 2 seconds to set down at given value. The difference may result from software part of measuring setup and slow communication between controller and PC.

The decrease of concentration of Carbon dioxide seen on Fig. 7 is triggered by ventilation of testing chamber. That results in much slower change of analog and digital output. The indication of digital and analog signal stabilized in ~110 seconds. There is a significant difference in response time of digital and analog signal at the sloping part of waveform, but stabilizing time is approximately the same. The discrepancy may be a result asynchronous sampling of the microcontroller and sensor.

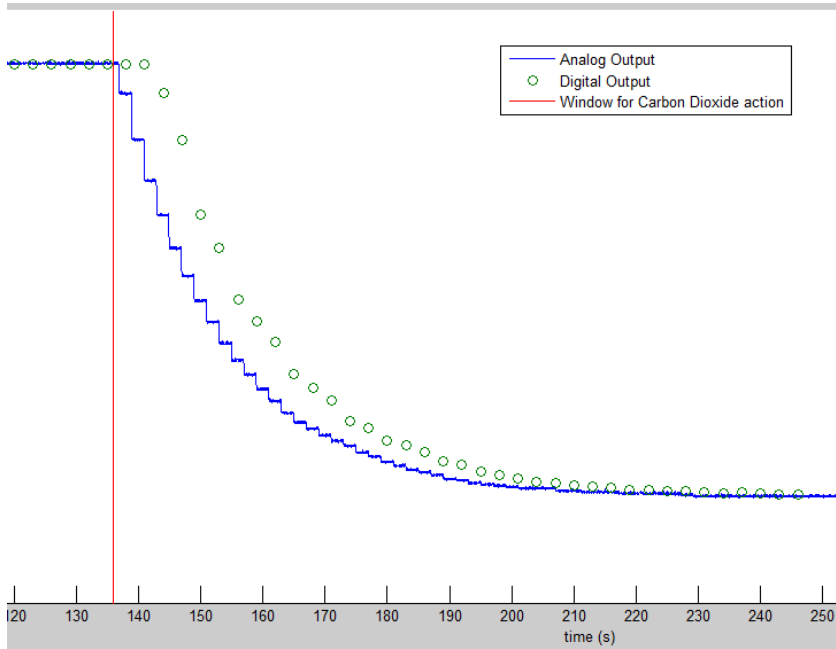


Fig. 7. Analog and digital response of sensor at increase of CO₂ concentration

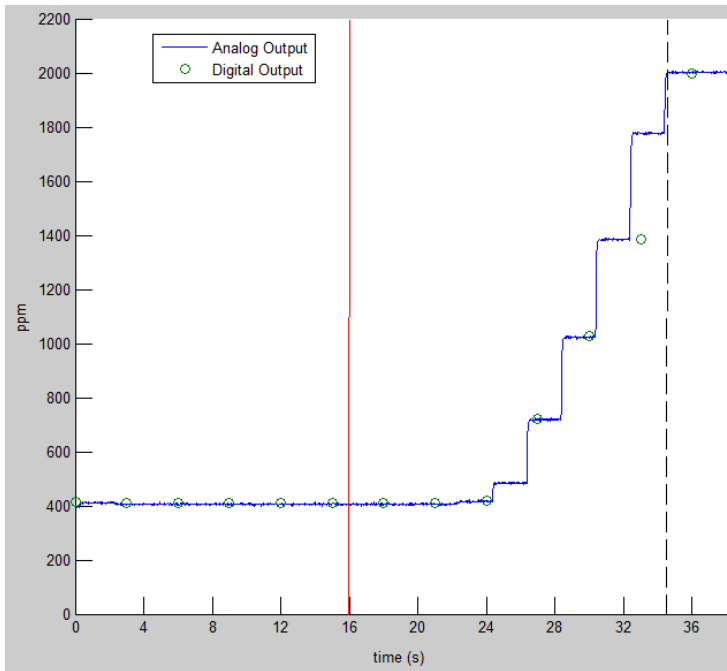


Fig. 8. Analog and digital response of sensor at placing sensor in high concentration CO₂

In second case, sensor was placed inside testing chamber with already high concentration of Carbon Dioxide. The red line on Fig. 8 marks the approximate moment of placing sensor inside testing chamber. While the reaction time of sensor was similar to case investigated before (~10 seconds), the time it for acquiring stable digital and analog output was shorter – 14 seconds. This may be the result of more precise control of CO₂ concentration, than in the case given before. The digital signal received by microcontroller tends to fall behind on rapid changes of gas concentration, as it may be the case of trying to read a frequently updated value register. It may even result in data loss, when the read-out and write-in procedures come simultaneously.

5 Conclusion

Time constant of the sensor was measured to a value of approximately 20 seconds, as declared by the manufacturer. The reason for that is the method for gas sampling used in given sensor, as well as time between measures which for this sensor is equal to 2s. Given that the role of K30 Engine SenseAir CO₂ sensor in chemical sensor system as level indicator for of carbon dioxide, the nature of the gas itself measurements were conducted under worst-case scenario conditions, the chosen sensor is sufficient for given application.

Acknowledgments. This work was supported by Polish National Centre for Research and Development (No. 0015/R/ID1/2011/01).

References

1. Kasprzyczak, L., Trenczek, S., Cader, M.: Robot for Monitoring Hazardous Environments as a Mechatronic Product. *Journal of Automation, Mobile Robotics & Intelligent Systems* 6(4) (2012)
2. Kasprzyczak, L., Trenczek, S.: Górniczy mobilny robot inspekcyjny do monitorowania stref zagrożonych wybuchem. *Pomiary, Automatyka, Robotyka* 15, 431–440 (2011)
3. EIGA, Carbon Dioxide Physiological Hazards. Not just an asphyxiant! *Safety Info* 24/11/E (2011)
4. Ingle, J.D.J., Crouch, S.R.: *Spectrochemical Analysis*. Prentice Hall, New Jersey (1988)
5. Szuba P.: Pomiar dwutlenku węgla, a układy klimatyzacji i wentylacji, *Pod Kontrolą* (January 2008)

Examples of Robust Estimation with Small Number of Measurements

Evgeniy T. Volodarsky¹ and Zygmunt L. Warsza²

¹ State Technological University - Kiev Politehnika, Ukraine
vet-1@ukr.net

² Industrial Research Institute of Automation and Measurement (PIAP) Warszawa Pl
zlw@op.pl

Abstract. Two robust methods of assessing the value and the uncertainty of the measurand from the samples of small number of experimental data are presented. Those methods should be used when some measurements results contain outliers, i.e. when the values of certain measurement significantly differ from the others. They allow to set a credible statistical parameters of the measurements with the use of all experimental data. The following considerations are illustrated by the numerical example of the interlaboratory measurement data key comparison. Compared are the results obtained by a classical method with rejection of outliers with two robust methods: a rescaled median absolute deviation MAD_s and an iterative two-criteria method.

Keywords: robust statistics, outliers, uncertainty of measurements, interlaboratory comparisons.

1 Introduction

In many experimental studies in various fields, including the technical and scientific research, interlaboratory comparison and laboratory proficiency testing the measurement samples can contain few number of elements only. This occurs because of the high costs of measurements, the use of destructive methods, the poor availability of objects for testing, or the inability of multiple tests due to long or limited time of their execution. For small samples the measurement result and its uncertainty u_A evaluated by the GUM recommendations [1], significantly depends on the outliers. Therefore the obtained values sometimes may be even unreliable or unrealistic. Removing one observation only from a small sample significantly reduces the credibility of the evaluation results. For example for a very small sample of 4 elements the relative standard deviation of uncertainty $s(u_A)/u_A$ is as high as 42%, and for $n=3$ it will increase even up to 52% (GUM [1], Table E.1 in Appendix E.1). The removal of only one observation from a such small sample increases the relative standard deviation of uncertainty approximately on 24%. So the general tendency for small samples with outliers is to use the robust statistical methods, which applying all data obtained experimentally, including outliers. These methods are developed and to be used from the late 70's of

the twentieth century. They are highly resistant to the influence of outliers. Such data considered before in conventional methods as to be "bad" can be successfully used now. Literature on these methods is quite rich. An overview of the basic items are in the bibliography of [5] - [8]. Robust methods provide less than conventional methods the impact of too high errors caused by different usually unrecognized sources. The term *robust* means resistance immunity to irregularities and inhomogeneities of the sample data.

In the robust statistics the outlier data are not removed, but are used different ways to modify their values, or their participation in procedures to estimate the statistical parameters of the sample. A number of robust statistical methods, (among others) are programmed in MatLab. Two of them are recommended in ISO 13528-2 [3] for proficiency testing by interlaboratory comparisons. These methods should be added in the new upgraded GUM. Various data processing tasks appear constantly in the new applications of robust statistical methods including such one as calibration of multi-parameter measurements in chemometrics. One of the areas where robust methods could also be usefully applied is estimation of accuracy of results obtained by the some measurement method in inter-laboratory comparison experiments [6] - [8].

2 Method of Rescaled Median Deviation

In the simplest robust method for a sample of n elements used is the Median Absolute Deviation

$$\text{MAD}_n = \text{med}\{|x_i - M_n|\} \quad (1)$$

where: x_i - i -th element of the sample, $M_n = \text{med}\{x_i\}$ - the median.

This simple robust procedure is as follows:

- for all n data x_i ordered by values determined is the median *med* and considered to be the estimate of the measurement result value,
- the deviations of the sample data sets from this median the median absolute deviation MAD is calculated,
- standard uncertainty $s(x)$ of the measurand is considered the rescaled median deviation MAD_s

$$s(x) \equiv \text{MAD}_s = \kappa(n) \text{MAD} \quad (2)$$

For a normal distribution the value of $\kappa_\infty=1,483$ is the asymptotic limit of the ratio of $s(x)/\text{MAD}$ when $n \rightarrow \infty$, i.e. for the general population. Use of κ_∞ for samples with a finite number n of measurements gives too low the assessment of uncertainty, as $s(x_n) > s(x_\infty)$. Then for the more accurate estimation coefficient $\kappa(n)$ as dependent on the number of elements n in the data sample has to be applied. Randa of NIST published values of the coefficient $\kappa(n)$ in internet [4].

3 The Robust Iterative Method

More reliable statistical parameters than by above method can be obtained by an iterative robust methods. In the method of robust statistics considered here the outlier data is downloading to positions closer to the center of the distribution. This operation is called winsoryzation after the name of American mathematician Winsor. Samples with the outlier data should not be simulated by a model of single normal distribution and the least squares method (LSM) is not useful, as shares of single data in it increases with the square of its distance from the center of concentration. More resistant to large deviations is the criterion of minimum modules (LMM) given by Laplace. So, in robust methods many ways of both criteria "symbiosis" are used. It is assumed that only the central part of the PDF (Probability Density Function) of sample data distribution, i.e. for small deviations from the estimate of measurand value, does not differ from the normal distribution. Only for them the least-squares criterion LSM can be used. Beyond the limits of this range the criterion of minimum module LMM is used to reduce the impact of outliers. After Tukay and Huber [5] works it is possible to apply for data processing the iterative robust method under acronym IRLS (iteratively reweighted least squares). In this method the following functional is used for the sensitivity

$$\sum_{i=1}^n \rho(x_i - \mu) \tag{3}$$

where: $\rho(x_i - \mu)$ - function depended on the selected parameter c .

For observations of the deviation values of $|\varepsilon| < c\sigma$ (where σ is the standard deviation, c - factor) a square function is used and for larger deviations the modules $|\varepsilon| = |x_i - \mu|$ are minimized. So the function $\rho(\varepsilon)$ is "more mild" for data outliers with values $|\varepsilon| > c\sigma$ from the center of the sample distribution. Constant c determines the degree of "robustness". The value of the constant c depends on the percentage of "contamination" of the sample distribution. For 1% $c=2$, and for the 5% $c=1.4$. Commonly $c=1.5$ is used. Experimental data are modified in accordance with the selected criterion as follows

$$x_i^* = \begin{cases} x_i & \text{for } |x_i - \hat{\mu}| \leq c\sigma \\ \hat{\mu} - c\sigma & \text{for } x_i < \hat{\mu} - c\sigma \\ \hat{\mu} + c\sigma & \text{for } x_i > \hat{\mu} + c\sigma \end{cases} \tag{4}$$

where $\hat{\mu} = med\{x_i\}$ from data x_i ranked in ascending order.

"Treatment" of the data by (4) is one of the ways of winsoryzation. As resistant to outliers the estimate of the sample data grouping center $\hat{\mu}$ the median $med\{x_i\}$ shall be preliminary adopted. Huber [5] finds that the best assessment of the distribution center is the midrange between the lower first ($p=1/4$) and the higher third ($p=3/4$) of the sample quartiles (inter-quartile midrange) - Fig 1.

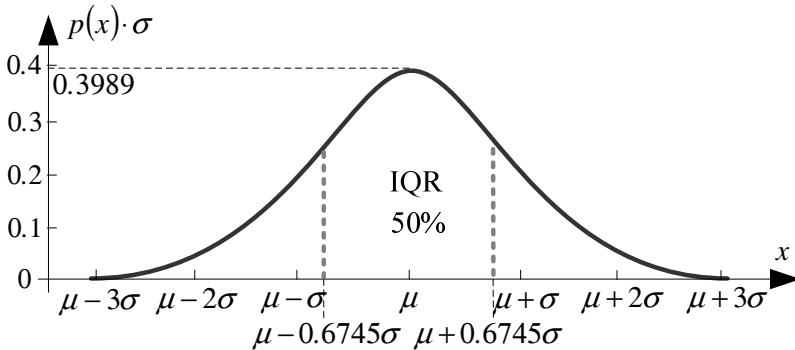


Fig. 1. Definition of inter-quartile mid-range: dotted lines – ordinates of first and third quartile $a = \mu - 0.6745$, $b = \mu + 0.6745$

The iterative procedure starts after arranging the elements of the sample according to their values x_1, x_2, \dots, x_n . Then the center of grouping data is

$$x^* = med\{x_i\}, i = 1, \dots, n \tag{5}$$

In this case the standard deviation is

$$s^* = 1,483 MAD_n \tag{6}$$

Then for $c=1,5$ with $\varphi = 1,5s^*$ can be determined boundaries of the range $x^* \pm \varphi$ to which are compared the original data x_i . Data protruding beyond this range are pulled on this boundaries and whole procedure is repeated. In any step (j) of an iterative procedure, after the modified value from the step ($j-1$) according to the conditions (4), is in turn fined a new mean value and new standard deviation of the sample

$$\bar{x}_{(j)} = \sum_{i=1}^n x_{i(j)}^* / n; \tag{7}$$

$$s_{(j)} = 1,134 \sqrt{\sum_{i=1}^n (x_{i(j)}^* - \bar{x}_{(j)})^2 / (n-1)} \tag{8}$$

Factor 1.134 is used when $c = 1.5$.

The resulting value s_j is used to calculate a new distance $\varphi_j = 1.5s$ to boundaries of inter-quartile interval and again data coming off as outliers are pulled on them, and the procedure as above is continued. Convergence of the algorithm is determined by comparing the calculated values \bar{x}_j^* and \bar{x}_{j-1}^* of the current and the previous iteration step. The procedure is repeated until changes of \bar{x}_j and s_j between successive steps will be minimal. The procedure is stopped after $j=m$ steps, where the difference of standard deviations $s_{(m)} - s_{(m-1)}$ for two successive steps is acceptably small.

Robust iterative double-criteria method IRLS has no defects of the median method. It allows in the calculation of the standard deviation of the sample also to include the outliers, i.e., data of the maximum absolute deviation, bringing them to the borders of the inter-quartile diapason of normal probability distribution of the data. An example of use this procedure in the inter-comparison measurements are presented in section 4. Numerical example of the data homogeneity conditions test and determination of limits of extreme deviations for small samples are given in [8].

4 Numerical Example

In this example, the mean value of measurement results of nine laboratories and its estimated uncertainty are calculated by two classic and two above robust methods. Results will be compared. Measurement data is taken from [2]. Nine laboratories conducted a joint experiment involving comparative measurements by a tested method to assess its accuracy. It was assumed initially that the credibility of all laboratory measurements are the same. From measurements made by tested method in $n = 9$ laboratories received are mean values $x_1 \dots x_9$ ordered below

17.570 19.500 20.100 20.155 20.300 20.705 20.940 21.185 24.140.

Two underlined results x_1 and x_9 are the significant outliers. Results obtained by various methods are shown in Table 1

Table 1. Comparison of the results obtained by four methods

Method	For all data	Rejected x_1, x_9 by Grabb's crit.	Robust MAD _s	Robust iterative
Result value	$\bar{x}_0 = 20.511$	$m = 20.4$	$med = 20.3$	$\bar{x}_5^* = 20.412$
Std. uncertainty	$s_0 = 1.727$	$s = 0.501$	$s(x_9) = 1.045$	$s^* = 1.039$

For the all 9 initial data $x_i = x_{i(0)}$ the mean value $\bar{x}_0 = 20,511$ and the sample standard deviation $s_0 = 1,727$. In the traditional model (cross-contamination) it is assumed that only valid observations are derived from a normal distribution. A consequence of that is to use the proper test, e.g. Grubbs test to find the outliers

$$G_{n \max} = (x_n - \bar{x}) / s \tag{9}$$

After rejection outliers $x_{1(0)} = 17.570$ i $x_{9(0)} = 24.140$, for the remaining data is obtained the average value $\bar{x} = 20,41$ and much lower than previous the standard deviation $s = 0.50$ as results common to the whole experiment. Both are calculated from measurements in 7 laboratories only. These assessments are of the lower statistical reliability.

In the classical approach the average values \bar{x}_0 , m calculated by both methods differ relatively little. Standard uncertainty s_0 of the data of all nine laboratories is very high. After elimination of two outliers by the Grubbs criterion, the uncertainty

calculated for seven laboratories is almost 3.5 times lower. However, measurements are unreasonably idealized here. The reliability of the averaged data for 7 labs is decreasing as the formula $s(u_A)/u_A = 1/\sqrt{2(n-1)}$ (Table E.1 GUM [1]) showed that the relative standard deviation of the measurement uncertainty will increase from 25% to 29%.

For both robust methods values of the data grouping center are nearly similar.

Their uncertainties differ each other only by 9% and are between these two of the classical method. For the iterative method achieved is $s^* = 1.039 > s$. The mean value and standard deviation determined by this method is based on the data of all laboratories and seems to be as closer to the data which would be for a larger number of independent measurements treated as general population.

5 Summary

The rescaled median deviation method given in section 2, is very simple but it does not give correct results when the outlier is far from the rest of the data.

Iterative method of section 3 is more complicated, but easier to automate the algorithm. With the introduction of the threshold $\pm c\sigma$ decreasing sensitivity to data outliers, oriented is mainly to determine robust assessment of uncertainty.

Carried out in section 4 results of calculation showed the usefulness of the application of two criteria iterative robust method resistant to determine the statistical parameters of samples with a small number of data when they are taken from the general population of the assumed normal distribution, but include the results significantly different from the others. It allows you to more objectively assess the value of the result and the accuracy of the test methods.

The analysis shows that for the evaluation of results presented in controlled laboratories, should take into account the number of samples n obtained for the investigated objects. When a sample is of a small number of items, to evaluate the performance of results you can use the robust method of an iterative process of data with winsorization of outliers. In this case received is a much smaller variance and greater credibility than by the standard methods.

References

1. Guide to the Expression of Uncertainty in Measurement GUM. BIPM JCGM 100 (2008)
2. ISO 5725-2:1994 -Accuracy (trueness and precision) of measurement methods and results
3. ISO 13528-2005 Statistical methods for use in proficiency testing by interlaboratory comparisons. Annex C 1
4. Randa, J.: Update to Proposal for KCRV & Degree of Equivalence for GTRF Key Comparisons. NIST, GT-RF / 2005-04 Internet (2005)
5. Huber, P.J., Ronchetti, E.M.: Robust Statistics, 2nd edn., p. 380. Wiley (2011)

6. Wilrich, P.T.: Robust estimates of the theoretical standard deviation to be used in inter-laboratory precision experiments. *Accred. and Quality Assurance* 5, 231–240 (2007)
7. Belli, M., Ellison, S.L.: Implementation of proficiency testing schemes for a limited number of participants. *Accreditation and Quality Assurance* 2, 391–398 (2007)
8. Volodarski, E., Warsza, Z.: Applications of the robust statistic estimation on the example of inter-laboratory measurements, pp. 260–267 (2013) (in Polish)

Statistical Properties of Skewness and Kurtosis of Small Samples from Normal and Two Other Populations

Zygmunt L. Warsza¹ and Marian J. Korczyński²

¹ Industrial Research Institute of Automation and Measurement PIAP, Warsaw
zlw@op.pl

² Lodz University of Technology
jerzykor@p.lodz.pl

Abstract. Statistics of skewness and kurtosis distributions and their basic parameters for a set of samples of certain small numbers of elements are found. These distributions were determined using the Monte Carlo method. The samples were repeatedly taken at random from a normally distributed population and for comparison from the population of a two other simple distributions. Knowledge about statistics of skewness and kurtosis should allow to obtain a more reliable estimate of the standard deviation and the uncertainty of the measurand value estimator from samples of a small number of measurement observations, when range of their value distribution is known.

Keywords: handling of samples, skewness, kurtosis, data modelling.

1 Introduction

The experimental data collected for further handling might be symmetrically or asymmetrically and in many ways distributed. They may contain trends or be without trends and each observation carries with it imperfection of used instrumentation. For instrument or measuring system with sensors of different quantities a collection of readings or output value in the form of samples in time. The uneven spreading concerns not only the samples from a population of non-symmetrical probability distributions. However, in many cases it occurred in practice, that we can collect only a small number of measurement observations for various reasons. Then also samples from a normally distributed population and other symmetric distributions can be asymmetric. The asymmetry of these samples increases with decreasing the number of elements in collected samples. A reason of small measurement sample might be:

- The lack of a larger number of objects to be tested (eg. for the validation of the method used in only a few accredited laboratories),
- High cost of measurements or limited time of their execution,
- The inability to re-perform the measurements, eg. in the study of a distant terrain and in medicine.
- The limited number of collected data might be while object under investigation might be destroyed or its properties after test are changing irreversibly.

In all above mentioned cases, only a small sample might be available for further data handling. According to GUM Guide [2], in determining the result and uncertainty of measurement any sample of the data is considered as it comes from a normally distributed population. The best estimator is regarded as a mean value of collected data, and the uncertainty of type A as a parameter, which characterize data scattering, basing on calculated of the variance of the sample. It was necessary to examine to what extent it can also be a significant knowledge of other statistical parameters of small and very small samples, including skewness and kurtosis of the cases where the type of distribution of the population is a priori not known. Here, as the first step of this research will appoint the skewness and kurtosis statistics of small and very small samples taken at random from a normally distributed population and, for comparison – from a two other simple distributions: uniform and triangle. Monte Carlo simulation method was applied to analyze small samples.

2 Pearson’s Skewness Coefficients of Population and Sample

The probability density distribution (pdf) of the asymmetry of the right tail, with median, mean and mode marked, as an example is presented in Fig. 1.

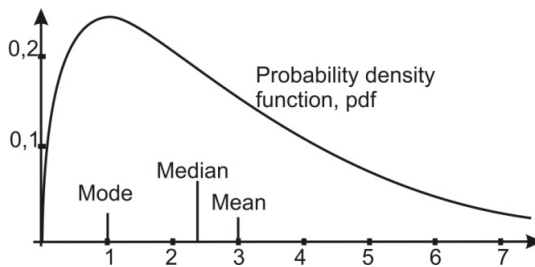


Fig. 1. Parameters of the right-asymmetric distribution function (pdf)

For asymmetric distributions of the mean value μ , mode and median do not overlap with each other. Unified description of various distributions allows asymmetry is given by Pearson’s coefficient of skewness γ_1

$$\gamma_1 = E\left[\left(\frac{X - \mu}{\sigma}\right)^3\right] = \frac{\mu_3}{\sigma^3} = \frac{E[(X - \mu)^3]}{(E[(X - \mu)^2])^{3/2}} \tag{1}$$

The Pearson’s coefficient of skewness γ_1 given by Eq. (1) is based on the central moment of μ_3 and a standard deviation σ of the data population. The coefficient equals to zero for a symmetric distribution, and is positive for right-tailed asymmetry distributions (extended right tail). Also other non-classical skewness coefficients are used.

Pearson’s skewness coefficient g_1 for a n -element sample of $x_i \in X$ population is determined by this sample central moments: $m_2 = s^2$ and m_3 as estimators of μ_2, μ_3 . Skewness coefficient of sample g_1 is given by formula

$$g_1 = \frac{m_3}{m_2^{3/2}} = \frac{\frac{1}{n} \sum_{i=1}^n (x_i - \bar{x})^3}{\left(\frac{1}{n} \sum_{i=1}^n (x_i - \bar{x})^2 \right)^{3/2}} \tag{2}$$

The skewness coefficient g_1 according (2) is biased, so that is unbiased if driven in [1]

$$g = \frac{\sqrt{n(n-1)}}{n-2} g_1 \tag{3}$$

The software supporting statistical calculation for skewness coefficient of the sample use a bit different form then given by (2) i (3) [3], like given by (4)

$$SKE = \frac{n \sum_{i=1}^n (x_i - \bar{x})^3}{(n-1)(n-2) s^3} \tag{4}$$

and use also a standardised skewness coefficient

$$SSKE = SKE \sqrt{\frac{n}{6}} \tag{5}$$

For symmetric population and $n > 150$ SSKE coefficient is of Normal distribution [3].

The differences between the values of the coefficient of skewness given by different definitions are not significant but for the very small samples should be considered.

3 Standard Deviation of the Skewness Coefficient

Variation of the skewness coefficient of g for a sample of n elements from Normal population, according to [2] is

$$D(g) = \frac{6n(n-1)}{(n-2)(n+1)(n+3)} \tag{6}$$

To estimate variance of $D(g)$ of small samples the Smirnov formula [4] is also used:

$$D(g) = \frac{6(n-2)}{(n+1)(n+3)} = \frac{6}{n} \left[1 - \frac{12}{2n+7} + O\left(\frac{1}{n^3}\right) \right] \tag{7}$$

where: $O(\cdot)$ – is a residual part $1/n^3$

Equation (7) refers to samples of $n > 25$ elements. For larger number of n a residua part in (7) becomes neglected and variance is tending to: $D(g) \rightarrow 6/n$.

4 Kurtosis of Small Samples

Kurtosis of the population is given by the ratio: μ_4/σ^4 . It serves as a measure of flattening (slenderness) of distribution, which indicates the concentration of its data. For a Normal distribution (Gaussian) kurtosis is equal to 3.

Kurtosis of the sample is a ratio of its moments: m_4, m_2 , so:

$$Kurtosis = \frac{m_4}{m_2^2} = \frac{\sum_{i=1}^n (x_i - \bar{x})^4}{(n-1) s^4} \quad (8)$$

To compare other distributions with Normal distribution, the excess kurtosis coefficient of the population defined as: $K=Kurtosis-3$ is used, and comparison of samples, for $n \geq 4$ the formula from [3] given below is applied

$$K(n) = \frac{n(n+1) \sum_{i=1}^n (x_i - \bar{x})^4}{(n-1)(n-2)(n-3)s^4} - \frac{3(n-1)^2}{(n-2)(n-3)s^4} \quad (9)$$

and the standardised Kurtosis coefficient also is used

$$SK(n) = K \cdot \left(\frac{24}{n} \right)^{\frac{1}{2}} \quad (10)$$

5 MC Modeling of Skewness and Kurtosis of Small Samples

The authors noticed that consideration related to distribution of skewness coefficient g and excess kurtosis coefficient K of very small samples of number of elements below 25 ($n < 25$) might be of worth of analysis. Such samples are analysed using Monte Carlo method. Skewness coefficient g and excess of kurtosis coefficient K for samples of $3 < n < 25$ elements are calculated and results in function of n are presented.

To determine distributions of the Pearson skewness coefficient for samples with n elements drawn from the population of X with normal distribution (Gaussian) was used unencumbered value of $p(x_i)$ the standard deviation of the sample. From (2)

$$g = \frac{m_3}{s^3} = \frac{\sum_{i=1}^n (x_i - \bar{x})^3}{n \left(\sqrt{\frac{\sum_{i=1}^n (x_i - \bar{x})^2}{n-1}} \right)^3 \quad (11)$$

where: m_3 – the sample third central moment, s – sample unbiased standard deviation. The samples of number of elements $n = (3, 4, 5, \dots)$ were extracted from the Normal distribution population and 100 000 such samples were analysed. In Fig. 2 selected results are presented. The larger sample, the shape is closer to Gaussian distribution.

For samples of $n \geq 3$ the mean of modulus of skewness coefficient $\overline{|g|}$ and its variance $D\overline{|g|}$ and standard deviation $s\overline{|g|} = \sqrt{D\overline{|g|}}$ were calculated. Results are presented in Fig 3 as relations vs. the number of sample elements n . In addition the standard deviation $s(g) = \sqrt{D(g)}$ from the Smirnov formula (7) is also derived. Mean value of modulus of skewness $\overline{|g|}$ and its standard deviation $s(g)$ for the small n -element sample has a maximum for ca. $n = 6$ and then is declining when n decreases.

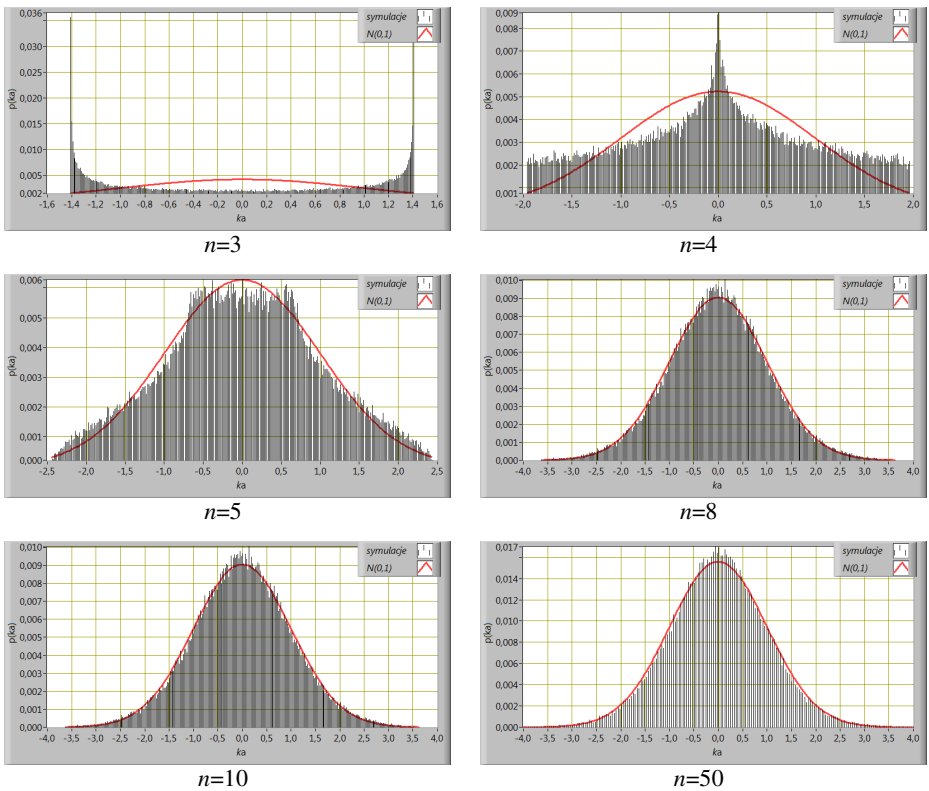


Fig. 2. Some distributions of skewness coefficient $k_a \equiv g$ for samples of low number elements n

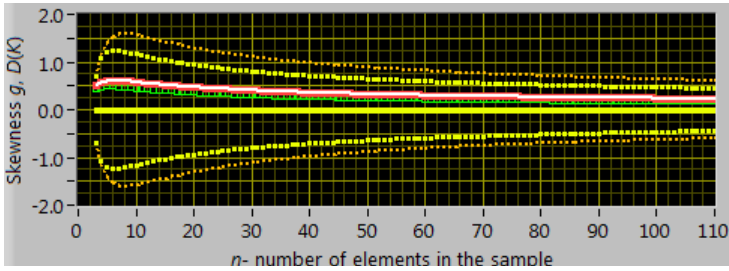


Fig. 3. Skewness g as a function of the small number n of elements of samples extracted from Gauss population with a marked dispersions at level of confidence 0.95 and 0.99 respectively.

– mean value of g , – dispersion at $p = 0.95$, – dispersion at $p = 0.99$
 – modulus of average $|g|$, – SD of mean; – $D(K)$ Smirnov eq. (7).

Using the Monte Carlo simulation with sets of 100 000 of n -element samples from a normally distributed population, the excess of kurtosis coefficient K were analyzed. Some histograms of them are in Fig. 4 and the variance of their mean value and other statistical parameters as a function of n are presented in Fig. 5.

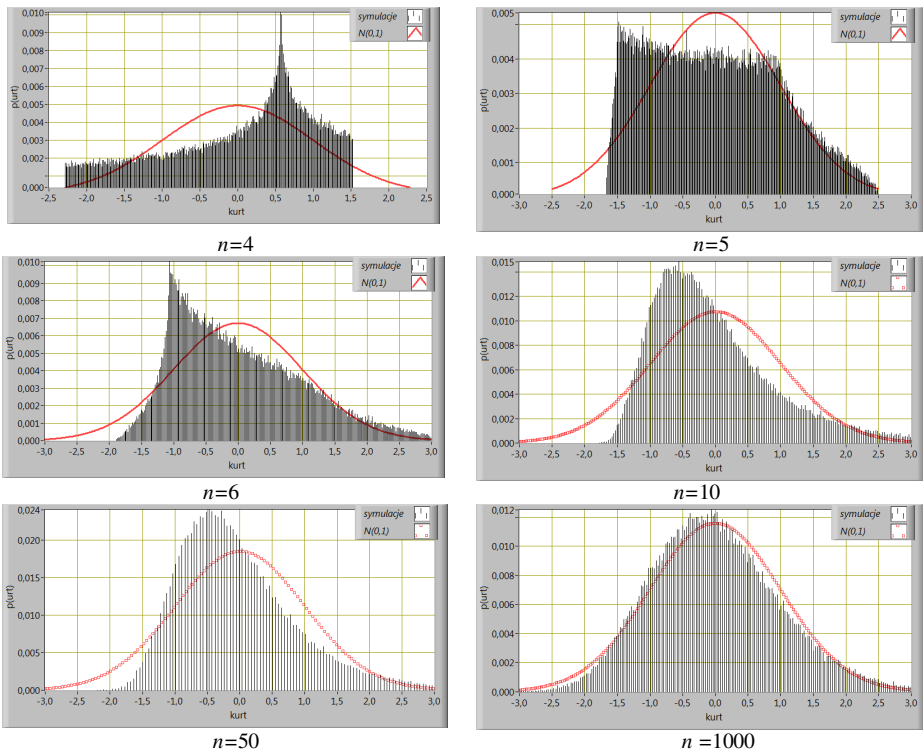


Fig. 4. Histograms of kurtosis excess $K-3$ of n -element samples from Gauss population

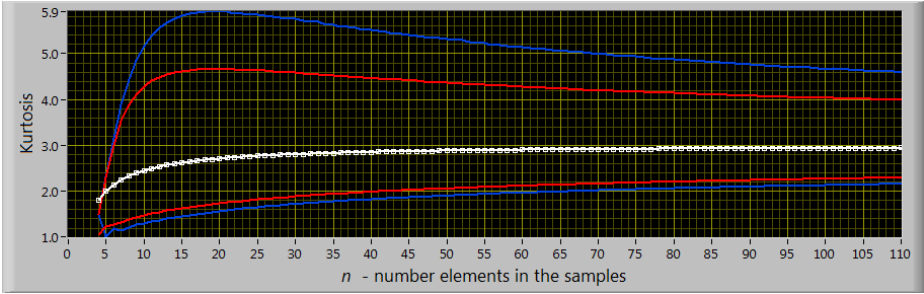


Fig. 5. Statistical parameters of kurtosis K as function of number of elements n of sample from Gauss population: – mean value, – dispersion at $p = 0.9$; – dispersion at $p = 0.99$

6 Comparison of Skewness of Samples from a Normal, Uniform and Triangular Distributions

The mean value of skewness coefficient module $|\bar{g}|$ for n -element samples derived from: a normal, an uniform and a triangular distributions and variance D are in Fig. 6. Standard deviations $s = \sqrt{D|\bar{g}|}$ and according to Smirnov equ. (7) are shown in Fig. 7.

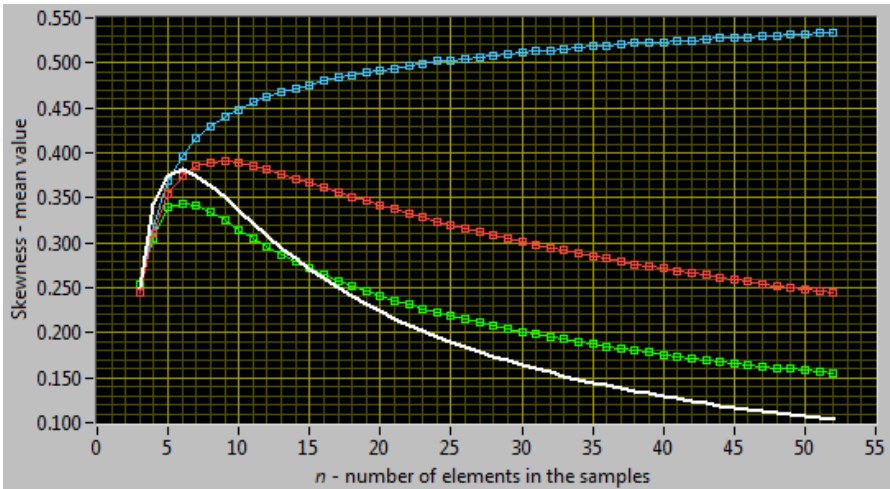


Fig. 6. Skewness $|\bar{g}|$ of n -element samples from 3 different populations: – $D(g)$, eq. (7), – Normal, – triangular, – uniform

Results presented in Fig. 6 and Fig. 7 allows us to conclude, that samples from a population with uniform distribution are “less” skewness, triangular – more. Number of measurements n_{max} , at which occurs the maximum average skewness is also greatest for the triangular distribution.

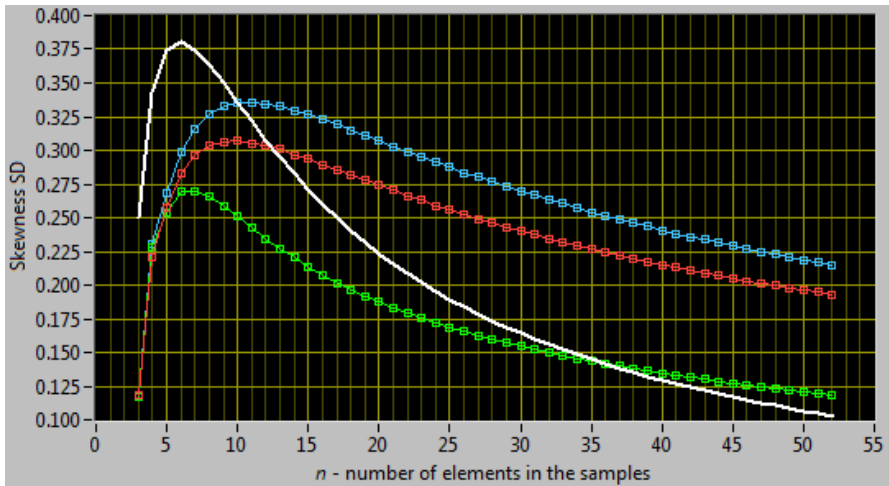






Fig. 7. Variance $D(g)$ and standard deviations $SD(g)$ of the skewness of n -element samples from population:  – $D(g)$,  $SD(g)$ – Normal;  – triangular;  – uniform

7 Conclusions

For the collection of small samples from a normally distributed population, mean value of the coefficient of skewness deviates significantly from zero, and the kurtosis – from the value of 3 for this population. The skewness is a maximum for the number n of elements of the sample about 6, and excess of kurtosis – n approx. 20. Then, with increasing n , both parameters slowly decreases to 0 and to 3 for the population.

Shapes of distributions of both parameter histograms for small n are also very different from Gaussian pdf.

The skewness and kurtosis are not yet taken into account in determining whether the value of the sample mean as an estimator of the measurement result and its uncertainty as a measure of assessing the accuracy (precision) of the measurement result.

For samples from a population of distributions other than normal, e.g. uniform, trapeze and triangular the average value is not the best estimator of the measurement result [7–9]. The skewness and kurtosis functions versus n are also different than for a Normal pdf.

It is intended to reproduce the data of small samples by resampling method and examine whether the skewness and kurtosis of these data enable a more precise estimate the measured value and its expanded uncertainty, e.g. by Monte Carlo method [8].

References

1. Benjamin, J.R., Cornell, C.A.: Probability, Statistics and Decision. Mc-Graw Hill Inc. (1970)
2. Guide to the Expression of Uncertainty in Measurement GUM. BIPM JCGM 100 (2008)

3. Dobosz, M.: Statistical analysis of experimental results. Exit Warszawa (2004) (in Polish)
4. Bolshev, L.N., Smirnov, N.V.: Tables of mathematical statistics. Nauka (1983) (in Russ)
5. Warsza, Z.L.: One component estimators of measurand value of data samples of some non-Gaussian PDF-s. PAK (Measurement Automation and Monitoring) 1, 101–104 (2011) (in Polish)
6. Warsza, Z.L.: Effective Measurand Estimators for Samples of Trapezoidal PDFs. JAMRIS (Journal of Automation Mobile Robotics & Intelligent Systems) 6(1), 35–41 (2012)
7. Kubisa, S., Warsza, Z.L.: Mid-range as estimator of samples from uniform and flattened-Gaussian distribution. In: Proc. of 20th IMEKO TC4 Symposium, Benevento, Italy, September 15–17 (2014)
8. Propagation of distributions using a Monte Carlo method, Suppl.1 to Guide to the Expression of Uncertainty in Measurement GUM. BIPM JCGM, G1 –101 (2007)

About a Certain Way of the Membrane Kinetic Energy Transformation into Electric Energy

Aleksandra Waszczuk-Młyńska and Stanisław Radkowski

Institute of Vehicles, Faculty of Automotive and Construction Machinery Engineering
Warsaw University of Technology, Warsaw, Poland
awm@mechatronika.net.pl, ras@simr.edu.pw.pl

Abstract. The paper outlines the way of vibration energy recovery of continuous systems. The research object was a circular membrane with a piezoelectric element. Vibrations were described analytically and verified by the experiment using laser vibrometer. Force input function was set by acoustic wave with different frequencies. The results obtained in the laboratory experiments confirmed the need of taking into account the changes in system parameters in direct energy efficiency evaluation of the mechanical and electric transformation.

Keywords: energy harvesting, vibrations of the membrane, laser vibrometer, modeling continuous systems.

1 Introduction

We all live in times when renewable energy sources are much sought for, be it for ecological, economic, or political reasons. The wind power is used nowadays – in wind power plants, the power of water – in hydroelectric power plants, the sun rays – in solar panels, the earth warmth – in geothermal pumps and similar appliances, but new solutions need to be found and the old ones developed together with the development of technologies.

An important notion in new technologies are intelligent materials which can serve as the most important element in energy harvesting systems [1–4]. The systems of that kind have the purpose of harvesting energy to supply the devices in their working environment. One of the examples of traditional solutions are mechanical watches, which wind themselves up as a result of a natural hand's movement. A new application using intelligent polymers consists in supplying personal electronic devices with electric current via active fabrics or elements in the soles of our shoes [5].

Using intelligent materials will enable creation of miniature generators. With their help, retrieving energy from vibrations, or charging batteries of portable electronic devices is possible.

The team supervised by R.D. Kornbluh [6] created in 2012 the so called “heel strike generator”, which is a type of generator based on dielectric elastomers, enclosed in shoe heels, that were able to generate about 1 W of power. A mobile phone during the call uses about 1.4 W, and on stand-by 70 mW [7], so such a system, even

if the losses are considered, can reduce the need of charging with the electric current from the mains. Such a solution is light-weight, small, and does not require complicated mechanical elements.

In the article herein, we will describe the way of the membrane's kinetic energy transformation into electric energy. It will be depicted, how electric current can be obtained due to the actuation of a circular membrane to vibrate through the application of an acoustic wave, and therefore, through the application of sound.

2 Experiment

2.1 Measurement Instruments

Laser vibrometry is a new technique designed to make non-contact vibration measurements of a construction. The systems offered on the market at the moment, enable scanning the surface of the whole elements as well as registering of vibrations in three directions.

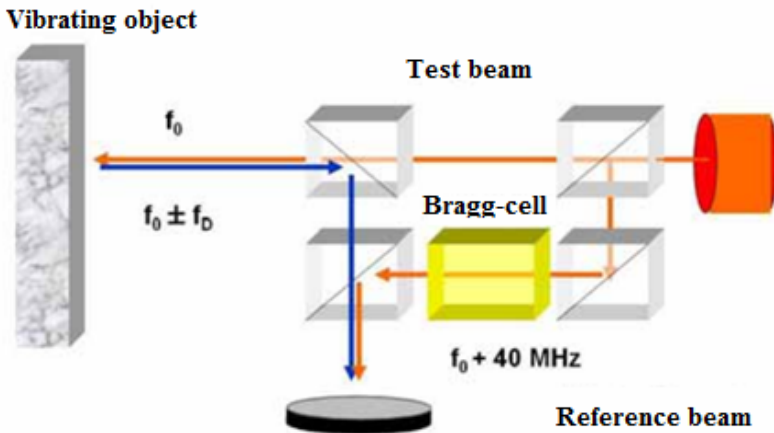


Fig. 1. Using the Doppler-effect in a laser vibrometer [8]

A laser Doppler vibrometer (LDV) is a scientific instrument the operation of which is based on the Doppler-effect. Inside the laser head is an interferometer and a set of beam splitters. It is the laser head where splitting of the beam into two components takes place. The first, the reference beam, is directed straight to the photodetector, passing on its way through the so called Bragg-cell. Due to the Doppler-effect its frequency is shifted by 40 MHz. As a result, it is possible to measure the constant component and the direction of the examined object's movement. The second part of the beam is directed on the examined object, and after being reflected by its surface, comes back to the laser head and subsequently reaching the photodetector (Fig. 1).

Due to the data collected from the reference and test beams, the signal is generated, which is then further analysed [8].

A laser vibrometer has many advantages over similar devices used to measure vibrations such as an accelerometer. It is a result of the fact that the vibrometers can be directed at objects that are difficult to access, or that can turn out to be too small or too hot to attach a physical transducer. Also, the vibrometers assure the non-contact vibration measurement, which allows for avoiding mass-loading the examined structure, which is especially important for devices in microelectromechanical systems (MEMS).

With the help of the vibrometer the analysis of construction vibrations can be conducted in relation to both: the time and the frequency. An additional merit is the possibility of visualisation and analysis of the dynamic phenomena taking place in the examined construction.

2.2 Stand and Measurements

The experimental stand consists of a loudspeaker (Fig. 2) connected with a generator, which is built in a control-measuring unit of the laser vibrometer. Due to the generator, the acoustic wave is obtained, that is further propagated through the loudspeaker to actuate the circular membrane to vibrate. The membrane diameter – 10 inches = 25.4 cm. The acoustic power obtained from the loudspeaker amounts to approximately 42 W.



Fig. 2. Mechanical Acoustic actuation

The initial enforcement was the white noise, whose aim was to actuate the membrane to vibrate and to obtain the answer in the form of the frequency spectrum. Due to the measurements conducted by means of the laser vibrometer we were able to obtain the visualisation of the results (Fig. 3).

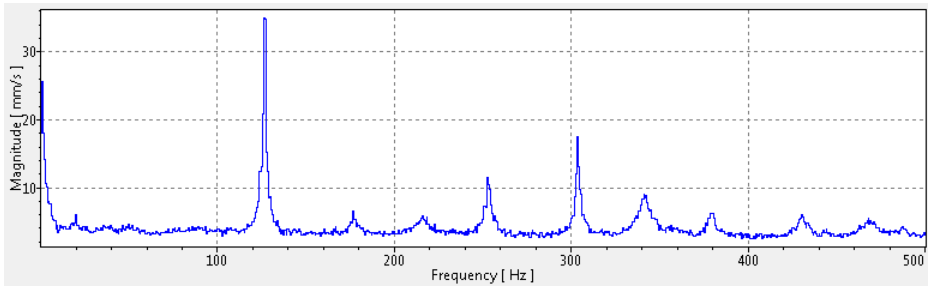


Fig. 3. Frequency spectrum of the membrane

In the given case of the circular membrane in the preset frequency band 0–500 Hz, we can observe the first form of proper vibration dominating for the 127 Hz value. Due to the unambiguous qualification of the value of the vibrations' first form and thanks to the visualisation, we can locate the maximum deflections in the centre of the membrane. At the same time, it is the place where the piezoelectric material was placed (Fig. 4), for its deflections also reach maximum value at this spot.



Fig. 4. Circular membrane with a piezoelectric material put up

As the next step there was the sine signal generated with the frequency of 127 Hz. The obtained effect is shown in the Fig. 5. It is the first form of the circular membrane vibrations. The maximum deflection, i.e. the membrane amplitude amounts to 1.4 mm, therefore the power equaled about 0.6 mW.

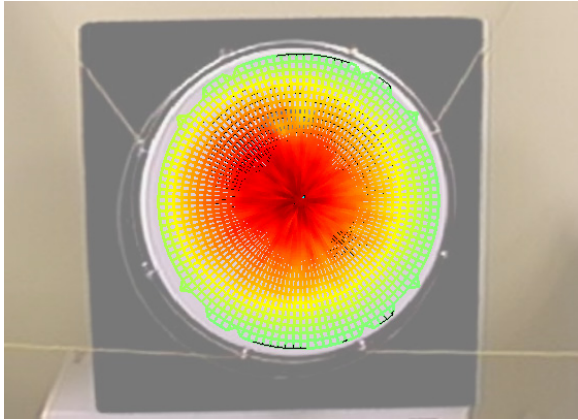


Fig. 5. The first form of membrane vibrations

The piezoelectric material deflects together with the membrane, its “work” was used to obtain electric energy. In the Fig. 6 there is the electric circuit shown, which generates electric current activating a small diode to illuminate, as a result of the membrane vibrations.

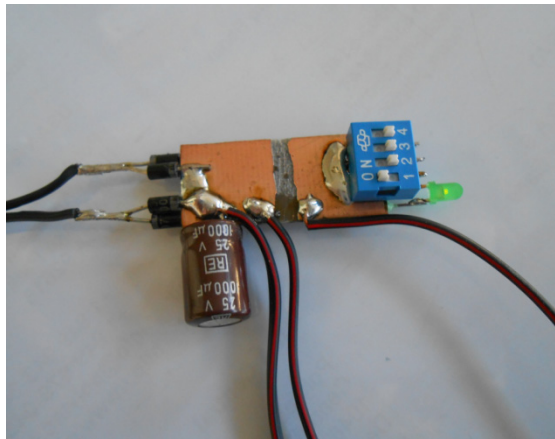


Fig. 6. Elements of the electric circuit

Measured were: the current (amperage) and the voltage. In the given case the following values were obtained: $I = 0.24 \text{ mA}$, $U = 2.1 \text{ V}$, which results in the power $P = 0.5 \text{ mW}$.

In our experiment the maximum membrane deflection amounted to 1.435 mm and the piezoelectric material deflection at the above assumptions amounted to 0.085 mm.

3 Model

The vibrations of the membrane are described by the formula [9]:

$$\rho h \frac{\partial^2 w}{\partial t^2} - N \nabla^2 w = p(r, \varphi, t) \quad (1)$$

$$w = w(x, y, t) \quad (2)$$

For the circular membrane we proceed to use polar coordinates

$$w = w(r, \varphi, t)$$

$$x = r \cos \varphi, \quad y = r \sin \varphi \quad (3)$$

Therefore, we obtain

$$\begin{aligned} \nabla^2 &= \frac{\partial^2}{\partial x^2} + \frac{\partial^2}{\partial y^2} = \frac{1}{r} \frac{\partial}{\partial r} r \frac{\partial}{\partial r} + \frac{1}{r^2} \frac{\partial^2}{\partial \varphi^2} = \\ &= \frac{\partial^2}{\partial r^2} + \frac{1}{r} \frac{\partial}{\partial r} + \frac{1}{r^2} \frac{\partial^2}{\partial \varphi^2} \end{aligned} \quad (4)$$

$$\frac{\partial^2 w}{\partial t^2} - a^2 \nabla^2 w = \frac{1}{\rho h} p(r, \varphi, t) \quad (5)$$

$$a^2 = \frac{N}{\rho h} \quad (6)$$

where: N – power per unit of circumference, membrane tension, ρ – density, h – thickness.

The membrane proper vibrations are described through solving the equation

$$\frac{\partial^2 w}{\partial r^2} + \frac{1}{r} \frac{\partial w}{\partial r} + \frac{1}{r^2} \frac{\partial^2 w}{\partial \varphi^2} - \frac{1}{a^2} \frac{\partial^2 w}{\partial t^2} = 0 \quad (7)$$

At the initial conditions

$$w(r_0, \varphi, t) = 0, \quad w(0, \varphi, t) < \infty$$

$$w(r, \varphi, t) = w(r, \varphi + 2\pi, t) \quad (8)$$

We calculate adopting the method of separated variables

$$w(r, \varphi, t) = R(r)\Phi(\varphi)T(t) \quad (9)$$

$$\ddot{T}(t) + \omega^2 T(t) = 0$$

$$\Phi''(\varphi) + \mu^2 \Phi(\varphi) = 0 \quad (10)$$

$$R''(r) + \frac{1}{r} R'(r) + \left(\frac{\omega^2}{a^2} - \frac{\mu^2}{r^2} \right) R(r) = 0$$

The solutions for the second equation:

$$\Phi^{(1)}(\varphi) = \sin\mu\varphi \quad \Phi^{(2)}(\varphi) = \cos\mu\varphi \tag{11}$$

Periodicity condition: $\mu = n = 0, \pm 1, \pm 2, \dots$

To solve the third equation we apply substitution:

$$r = \frac{a}{\omega} x, \quad R(r) = R\left(\frac{ax}{\omega}\right) = X(x) \tag{12}$$

Therefore, the equation takes the form of the Bessel equation:

$$X''(x) + \frac{1}{x}X'(x) + \left(1 - \frac{n^2}{x^2}\right)X(x) = 0 \tag{13}$$

The general solution of which is :

$$X(x) = AJ_n(x) + BY_n(x) \tag{14}$$

$J_n(x) = \sum_{k=0}^{\infty} \frac{(-1)^k \left(\frac{x}{2}\right)^{2k+n}}{k! \Gamma(k+n+1)}$ – the Bessel function of the first kind of for integer orders,

$\Gamma(z) = \frac{1}{z} \prod_{n=1}^{\infty} \frac{(1+\frac{1}{n})^z}{1+\frac{z}{n}}$ – gamma function,

$Y_n = \lim_{\gamma \rightarrow n} \frac{J_{\gamma}(x) \cos(\gamma\pi) - J_{-\gamma}(x)}{\sin(\gamma\pi)}$ – the Bessel function of the second kind of for integer orders.

For $x \rightarrow 0 \lim Y_n \rightarrow \infty$ then, what results from the second condition $B = 0$. And the first condition yields:

$$J_n(x_0) = J_n\left(\frac{\omega}{a} r_0\right) = 0 \tag{15}$$

We arrive at the solution depending on x_0 , Table 1

$$x_0 = x_{0mn}, \quad m = 1, 2, 3, \dots, \quad n = 0, 1, 2, 3, \dots$$

$$\omega_{mn} = \frac{x_{0mn} a}{r_0} = \frac{x_{0mn}}{r_0} \sqrt{\frac{N}{\rho h}} \tag{16}$$

Table 1. Zero points of the Bessel functions of the first kind for integer orders

n	m			
	1	2	3	4
0	2.4	5.52	8.65	11.79
1	3.83	7.02	10.17	13.32
2	5.14	8.42	11.62	14.79
3	6.38	9.76	13.02	16.22

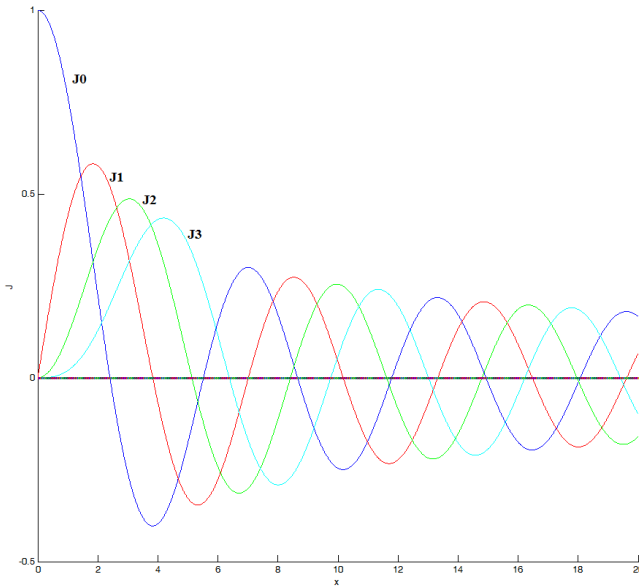


Fig. 7. Plot of Bessel function of the first kind, for integer orders

We have two types of eigenfunctions :

$$W = W_{mn}^{(1)}(r, \varphi) = J_n\left(\frac{\omega_{mn}}{a} r\right) \sin(n\varphi) \tag{17}$$

$$W = W_{mn}^{(2)}(r, \varphi) = J_n\left(\frac{\omega_{mn}}{a} r\right) \cos(n\varphi) \tag{18}$$

Main vibrations of the circular membrane have the form

$$\begin{aligned} w_{mn}^{(1)}(r, \varphi, t) &= \\ &= (A_{mn} \sin(\omega_{mn}t) + B_{mn} \cos(\omega_{mn}t)) W_{mn}^{(1)}(r, \varphi) \end{aligned} \tag{19}$$

$$\begin{aligned} w_{mn}^{(2)}(r, \varphi, t) &= \\ &= (D_{mn} \sin(\omega_{mn}t) + E_{mn} \cos(\omega_{mn}t)) W_{mn}^{(2)}(r, \varphi) \end{aligned} \tag{20}$$

In the general case we arrive at:

$$\begin{aligned} w(r, \varphi, t) &= \sum_{m=1}^{\infty} \sum_{n=0}^{\infty} w_{mn}(r, \varphi, t) = \\ &= \sum_{m=1}^{\infty} \sum_{n=0}^{\infty} (A_{mn} \sin(\omega_{mn}t) + B_{mn} \cos(\omega_{mn}t)) J_n\left(\frac{\omega_{mn}}{a} r\right) (\sin(n\varphi) + \cos(n\varphi)) \end{aligned} \tag{21}$$

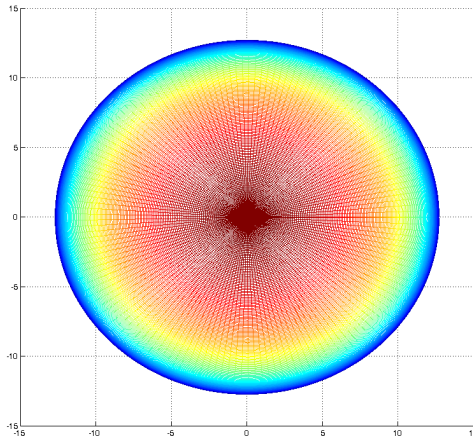


Fig. 8. The first form of the membrane vibrations

With the maximum membrane deflection assumed 1.435 mm and the diameter 254 mm, the piezoelectric material's deflection with the longer dimension of 64 mm, amounted to 0.1 mm from the above calculations. The additional assumption is that the piezoelectric material is well put up.

4 Summary

The experiment described above has shown that retrieving the energy from sound is possible, however, the efficiency is to be worked upon. A substantial part of acoustic energy is dispersed and in order to be able to utilise it to a greater extent, bigger elements and a prominent number of piezoelectric materials should be applied. In the conditions created we succeeded, though, in causing the diode to illuminate, which is a good prospect for the future research.

It is difficult to verify the analytical model against the experiment because defining the density and the membrane tension in the examined object is hard to perform, but the first form of vibrations seems to look the same.

The deflections of the piezoelectric material on the circular membrane in the experiment and calculated on the basis of the analytical model prove to be very similar, which is an acknowledgement of the experiment results by the model data.

References

1. Dybała, J., Lubikowski, K., Rokicki, K., Szulim, P., Wikary, M.: Thermal analyses of exhaust system on combustion engine. *Journal of KONES* 19, 173–178 (2012)
2. Radkowski, S., Lubikowski, K., Pięta, A.: Vibration energy harvesting in the transportation system: a review. *Diagnostyka* nr 4(64), 39–44 (2012)

3. Chmielewski, A., Gumiński, R., Lubikowski, K., Radkowski, S., Szulim, P.: Thermodynamic analysis and experimental research on cogeneration system with Stirling engine. *Wulfenia Journal* 21(4), 107–118 (2014)
4. Chmielewski, A., Radkowski, S.: Modelowanie procesu ładowania akumulatora elektrochemicznego pracującego w układzie kogeneracyjnym. *Zeszyty Naukowe Instytutu Pojazdów* 2(98), 83–89 (2014)
5. Paradiso, J.A., Starner, T.: Energy scavenging for mobile and wireless electronics. *Pervasive Comput. IEEE* 4, 18–27 (2005)
6. Kornbluh, R.D.: Dielectric elastomers: Stretching the capabilities of energy harvesting. *MRS Bull* 37, 246–253 (2012)
7. Carroll, A., Heiser, G.: An analysis of power consumption in a smartphone. In: *Proc. 2010 USENIX Conf.* (2010)
8. Information materials company Polytec GmbH Measurement Solutions Made Possible by Laser Vibrometry (2012)
9. Kaliski, S.: *Drgania i fale*, PWN (1986)

Affordable 2D Laser Scanning Device for Accurate Acquisition of Environment Maps

Marek Wąsik

Institute of Control and Information Engineering, Poznan University of Technology,
ul. Piotrowo 3A, 60-965 Poznań, Poland
marek.s.wasik@doctorate.put.poznan.pl

Abstract. This paper presents a prototype of an accurate 2D laser scanner for environment map acquisition. The scanner is built using an off-the-shelf infrared laser distance sensor, which can rotate in a plane. It is driven by a small DC motor and its angular position is controlled by an encoder. The design of the scanner was aimed at obtaining high accuracy of geometric measurements, but the device has rather a low speed of scanning. The sensor was in-depth tested to determine its accuracy and application possibilities. Tests results are presented in this paper together with a comparison to selected commercial laser scanners.

Keywords: 2D laser scanning, laser distance sensor, distance measurements, map building.

1 Introduction

In mobile robotics, building the map is one of the main topics as same as localization and motion planning. The knowledge about the robot's environment is almost always necessary for proper operation of a robot. A detailed map is helpful in localization tasks and provides a lot of information about the robot's environment.

Building the map can be realized in many ways using many different sensors. One of the most popular sensors are the 2D laser scanners [1, 2]. They are well-known, easy to use, quite accurate and allow to easily build a 2D environment map [3]. Nevertheless, they are usually compact devices, and we do not have any possibility to modify their parameters, such as the angular resolution or field of view. The available laser scanners are also quite expensive.

Another much cheaper approach to map acquisition is a method based on an ultrasonic distance sensors (sonars) [4]. They have poor accuracy of distance measurements, and a wide beam that makes the angular resolution very low, but in some case the sonars is sufficient to build a rough map of an environment.

Quite often there are also used various methods based on some kind of image processing. It can be a typical vision system with an appropriate algorithms [5], or a system with added structured light, which illuminates the environment with a special pattern [6]. The recently popular Kinect sensor is often used for map building [7]. It is a sensor based on infrared structural light and an infrared camera to estimate the distance to object in its surroundings.

While the above-mentioned sensors provide a wide choice of mapping and localization, there is a lack of affordable and versatile sensors for the outdoor use, for large environments, and for the acquisition of very precise geometric maps of man-made scenes. Most of the available low-cost laser scanners, such like the Hokuyo products, trade the accuracy and angular resolution for the small size and low-power operation. Therefore they cannot be used to obtain precise maps of extensive environments that are required either in civil engineering, or in robotics as ground-truth for the mapping and self-localization systems based on less precise sensors. On the other hand, typical time-of-flight laser scanners, e.g, manufactured by SICK are quite expensive, while they still have limited angular resolution (up to 0.5°).

This paper presents a 2D laser scanner built using an off-the-shelf, laser distance measurement sensor and a custom design scanning mechanism that ensures precise and versatile environment scanning. This design results in a sensor that is affordable in terms of complexity and cost. It ensures good accuracy and allows to adjust the field of view and angular resolution according to the application.

2 Design of the Scanner

Our scanner was designed to scan an environment along a plane with high accuracy. The results of each scan is a set of points which creates an accurate 2D map.

The main body of the scanner is placed on a shaft and can rotate 360° around. Inside the main body there is placed a laser distance sensor: SICK DT50 [8]. It is a sensor which uses the time of flight method for measurements [9]. It has a range of up to 20 meters, the repeatability of 3 mm and a measurements output rate of 500 Hz.

The rotation of the main body is provided by a small geared DC motor. The motor is fixed to the main body of the scanner and drives the rotation of the scanner through an additional gear (Fig. 1). In this gear, one of the cogwheels is fixed directly to the motor shaft and the other cogwheel is fixed on the device's base exactly along an axis of the device rotation. It enables to mount an encoder directly on the rotation axis, to control the actual angular position of the scanner. A rotary incremental encoder with a resolution rate of 1000 pulses per revolution is used.

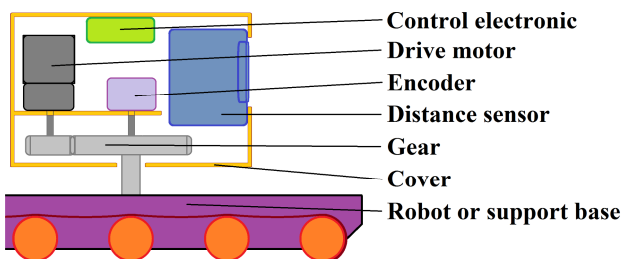


Fig. 1. Schematic of the laser scanner

There is also control electronic in the main body of the scanner. It is based on a Discovery STM32F4 development board. It controls all of the scanner components. Near the electronics there is space for a battery to power the device but it can also be powered from an external power source. The block diagram of the sensor's structure is shown in Fig. 2.

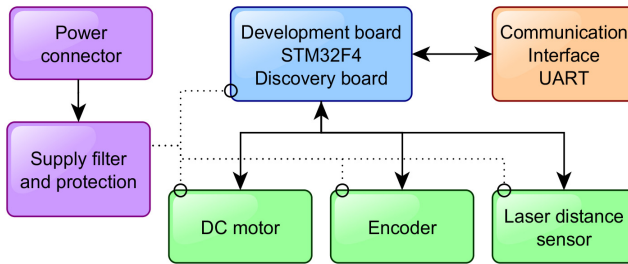


Fig. 2. Block diagram of the laser scanner

The main goal during the design of the scanner, was to achieve a very high accuracy of measurements. A high precision SICK distance sensor is used and low speed of scanner rotation is considered to ensure a high angular resolution of a measurements. A motor and a gear was selected to allow the scanner device to make a full 360 degrees turn in a time of about 10 seconds. The measurements are taken every 5 ms, therefore the full scan consists of about 2000 points. Additionally there is an assumption that the base of the scanner is not moving during the entire scan.

The above approach is much more accurate than of-the-shelf compact 2D laser scanners. This is because our device is not optimized for the speed of scanning. Thanks to that each scan consists of a much bigger number of points. Also in our device, the whole distance sensor is rotating instead of just a mirror which diffract the laser beam. It also increases the distance measurement accuracy.

The angular resolution of measurements are comparable with an angular resolution of the encoder. Nevertheless an angular velocity of a scanner device is approximately constant. Therefore, we are approximating an angular position of the scanner at the moment of the distance measurement using a linear regression from a history of the last 5 encoder measurements. It significantly increases the resolution of an angular position measurements.

The scanner returns data and communicates with other systems via the UART interface. It ensures various possibilities of connection. During the test, there was used a cable connection with a computer via an UART to USB converter. In a future there can be used an UART to Bluetooth converter module to ensure a wireless communication especially if many consecutive scans will be made. It ensures that cable will not be a problem during many rotations of the scanner in the same direction.

The scanning device can be used on a robotic platform for building a high accuracy map of an environment. It can also be used as an independent device which builds the map of an environment. Such a map can be especially useful to generate a very

accurate reference map of an environment, where are tested robots with less accurate systems. The scanning device is shown in Fig. 3.

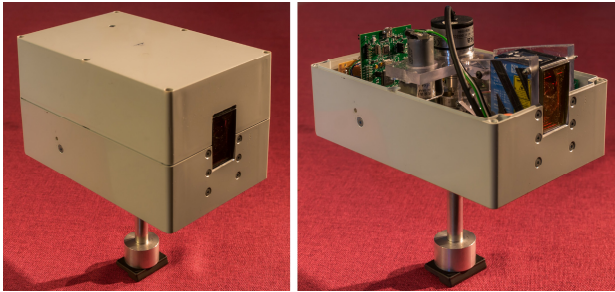


Fig. 3. Photography of the scanning device

Below we summarize the parameters of our scanning device:

- measuring range (from axis of rotation): 350–20 000 mm
- distance measurement resolution: 1 mm
- angle of rotation measurement resolution: 0.01°
- time of scanning (360°): 10 seconds
- number of range measurements in one scan: 2000

3 Accuracy Tests

3.1 Square Frame for Scanner Tests

To test the scanner device, we have built a square frame with dimensions of 1500 mm \times 1500 mm (Fig. 4). The frame is made from aluminum profiles, so it is insensitive to dampness (the wood beam could become twisting). Profiles are 80 mm high, what is enough to ensure, that the scanner will measure exactly the metal surface. Such a construction ensures the accuracy of the dimensions below 0.5 mm at any point, so it can be used as a reference shape for scanner testing. The internal side of the aluminum profile was covered with a paper tape to prevent potential light reflections [10].

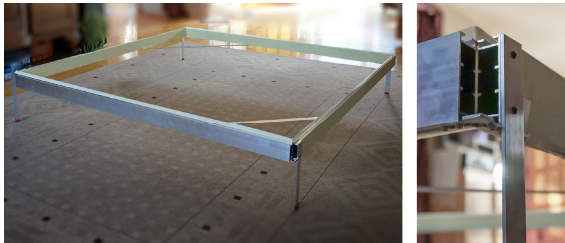


Fig. 4. Reference square 1500 mm \times 1500 mm for scanner device testing

3.2 The Scanner Test in Reference Environment

To test the scanner accuracy it was placed inside the reference frame near its center. Next, the scan was performed. Its results is shown on the left in the Fig. 5. The scanner was located at the point (0, 0) and the measurements were rotated to a right angle.

It is impossible to determine the position of the scanner inside the frame with an accuracy smaller than a few millimeters. Therefore to determine a real position of the scanner regard to the frame, there was used a genetic algorithm. The position in x and y direction (W_x, W_y) and rotation (α) of the frame regard to the scanner device was an unknown variables, which have to be search (genotype). We have to find a translation (W_x, W_y, α), which will transform our measurements points to a position of a square, with a center at point (0, 0) and with walls parallel to coordinate system.

For each phenotype, we have translated the measurements using a current parameters of W_x, W_y and α (1, 2). Next we have add up errors between the translated points and the nearest side of expected frame location (3). It was our fitness function which was minimized.

$$P'_{xi} = P_{xi} \cdot \cos \alpha + P_{yi} \cdot \sin \alpha + W_x \quad (1)$$

$$P'_{yi} = P_{xi} \cdot \sin \alpha - P_{yi} \cdot \cos \alpha + W_y \quad (2)$$

$$F_{fit} = \sum_{i=1}^N \min \left(\left| P'_{xi} - 750 \right|, \left| P'_{xi} + 750 \right|, \left| P'_{yi} - 750 \right|, \left| P'_{yi} + 750 \right| \right) \quad (3)$$

where:

P_{xi}, P_{yi} – x and y coordinates of the i-th measurement

P'_{xi}, P'_{yi} – x and y coordinates of the transformed i-th measurement

F_{fit} – fitness function of the genetic algorithm

As a result, the algorithm returns the most accurate position (W_x, W_y) and orientation of the square frame regard to the scanner, base on collected measurements. This result was shown on Fig. 5 with a thin continuous line. To realize the genetic algorithm, the simple macro script in Microsoft excel was used.

Using the above results, we have calculate an average standard deviation from all measurements. For each measurement we used an error between this point and the nearest side of the square frame (4).

$$\varepsilon_i = \min \left(\left| P_{xi} - W_{x1} \right|, \left| P_{xi} - W_{x2} \right|, \left| P_{yi} - W_{y1} \right|, \left| P_{yi} - W_{y2} \right| \right) \quad (4)$$

$$\sigma = \sqrt{\frac{\sum_{i=1}^N \varepsilon_i^2}{N}} \quad (5)$$

where:

ε_i – error of i -th measurement

P_{xi}, P_{yi} – x and y coordinates of the i -th measurement

W_{x1}, W_{x2} – x coordinate of a vertical sides of a square frame ($W_{x2} = W_{x1} + 1500$)

W_{y1}, W_{y2} – y coordinate of a horizontal sides from a frame ($W_{y2} = W_{y1} + 1500$)

N – number of measurements

σ – standard deviation of all measurements

In a result of equations (5), the average standard deviation of all measurements is 2.04 mm.

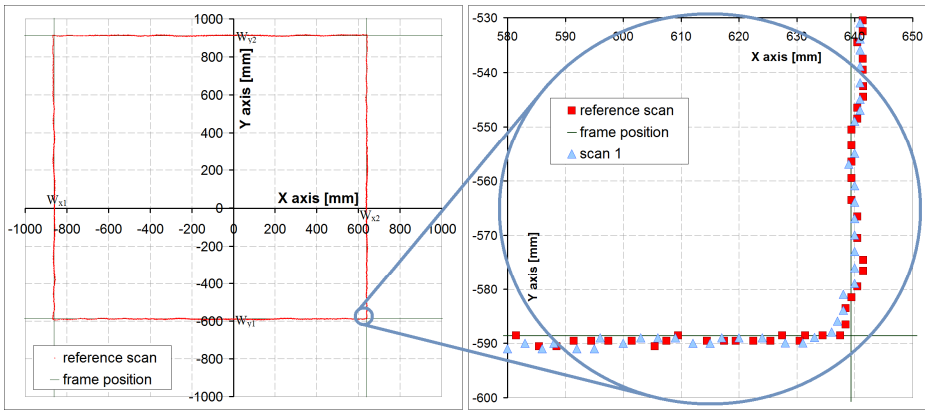


Fig. 5. Results of the measurements inside the test frame

The above calculated standard deviation can be a bit underrepresented, because earlier the position of a square frame was fit to the scanner measurements. Therefore we made another three scans without moving the scanner from its fixed location to verify the scanner accuracy. First of this additional scans is shown in the Fig. 5 on an enlarged fragment of the map. We calculate the standard deviation of this three new scans with an assumption, that the frame is still on the same place determined earlier. We have obtained for these scans the following standard deviations: 2.17, 2.09 and 2.21 mm. It gives an average standard deviation of 2.16 mm.

3.3 The Scanner Test in Hard Conditions of Low Laser Beam Incidence Angle

Further we have repeated tests with a square frame in a much less favorable case, while the scanner was situated close to the frame edge. In this situation, the angle of incidence of a laser beam is often very small, what causes an additional error in distance measurements. As previously, we made one reference scan to determine the location of the scanner with regard to the square frame. Next, we made three consecutive scans, without moving the scanner to calculate the measurement errors. It is shown in Fig. 6, while the scanner was situated in point (0, 0).

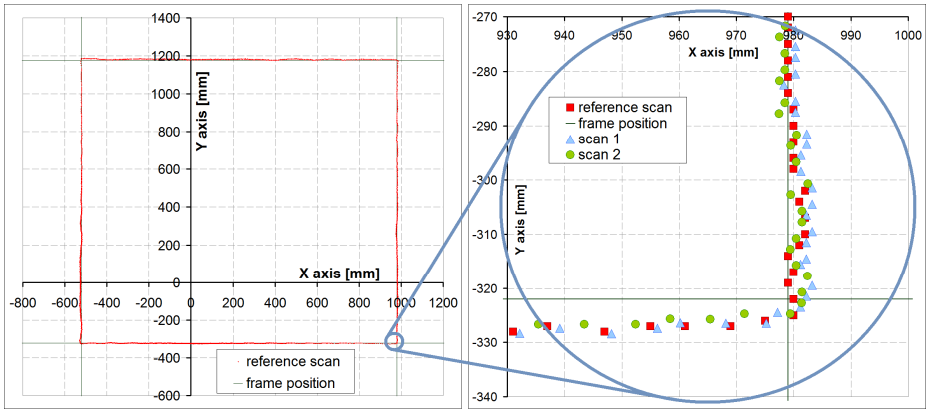


Fig. 6. Results of the measurements inside a tested frame with a scanner close to the frame edge

We can see that there are larger errors especially near the corner, where the laser beams have small angle of incidence. In this situation, the total standard deviation of each scan are 3.38, 2.46 and 3.01 mm. It gives an average standard deviation of 2.97 mm, what is a bit larger than in the first test. It shows that in order to ensure the highest scanning accuracy, the laser beam should have a large angle of incidence to the objects.

3.4 Comparison with Off-the-Shelf Compact 2D Laser Scanners

We have compared an accuracy of our laser scanner with other 2D scanners available off-the-shelf, such as Hokuyo URG-04LX [11] and Hokuyo UBG-04LX-F01 [12]. We have placed these sensors inside the square frame, exactly like our device in Fig. 5, in section 3.2. The enlarged fragment of the scans is shown in Fig. 7.

The calculated standard deviation of the measurements from URG-04LX is 4.72 mm and from UBG-04LX-F01 is 4.45 mm. It is worse than in our device (2.16 mm). Further the above scanners can operate only in angular range of 240°.

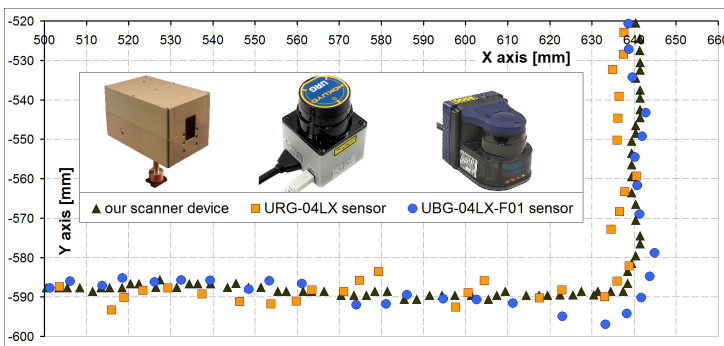


Fig. 7. Comparison of scans quality from a various sensors

4 Tests in a Real Environment

Measurements in a real environment do not allow to a quantitatively assess the scanning accuracy. This is due to the lack of a sufficiently accurate model of any real environment. Our scanner is based on a millimeter accuracy. In real buildings the walls are usually crooked more than few millimeters on their length.

We decided to verify the accuracy and repeatability of the scans by performing few scans and check the quality of their overlapping. We have perform a three scans in a simple room from a three different points, as shown in Fig. 8.

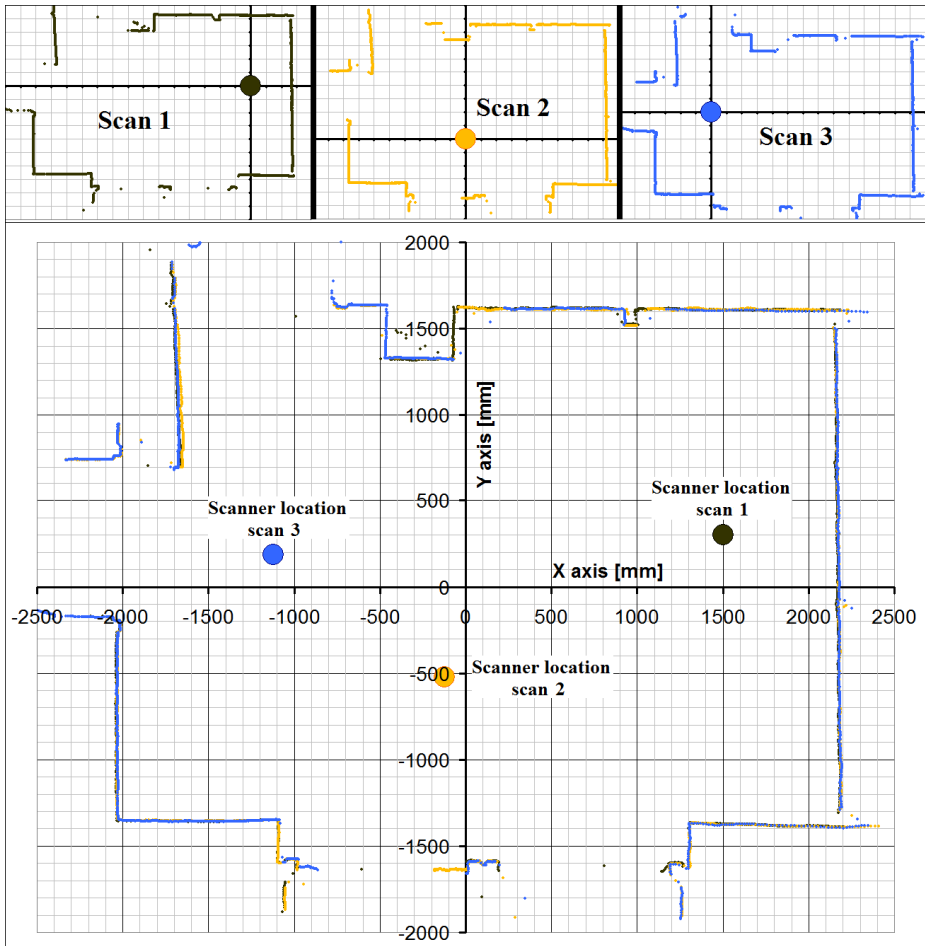


Fig. 8. Verification of scans overlapping, which was performed from a various location in a real environment

We can see that the scans fit together quite good. Especially in enlargement we had seen that the difference between the scans was not larger than those determined in section 3.

On the bottom of the map there was a window. We can see, that there is a small difference between the scans, especially for second scan. The glass window is transparent to the laser beam. However, for the beam incidence angles above 85° the laser light was diffused so much, that the glass was detected.

5 Conclusion

The presented laser scanning device allows to build a very accurate map of an environment. This is primarily achieved thanks to the dedicated, precise laser distance sensor. Also beneficial is the fact, that the entire sensor is rotating instead of just deviating the laser beam like in the popular, compact 2D laser scanners. Thanks to that, the laser distance sensor which is used can have big lens, what increases its sensitivity and precision of the measurements.

In our device, we control the rotation, what allows to adjust the rotation speed to the required angular resolution. It increases the accuracy of our scans, giving an appropriate number of points, with only the drawback of slow scanning.

During the tests we have validated that the device precisely scans the environment with a real object. The laser beam penetrates a glass surface, like a window and measures the distance to the next surface. The only exception is while the beam incident angle is very large (close to 90°). In this situation the laser beam often diffuses so much, that the glass surface is detected. Sometimes there was a problem with reflective surfaces, such as a polished wall of a tested frame, which reflects the beam and increases the distance measurement. Scanning of other surface which are normally existing in the office was not a problem.

Although the proposed sensor does not offer as compact design as the commercial products, and the speed of scanning is quite low, it enables to measure the 2D geometry (profile) of typical man-made environments with high precision, at least comparable to the time-of-flight 2D laser scanners that are characterized by an order of magnitude higher cost. These properties make our scanner suitable for the acquisition of geometric data in civil engineering and ground truth data in mobile robotics research.

References

1. Ye, C., Borenstein, J.: Characterization of a 2-D laser scanner for mobile robot obstacle negotiation. In: International Conference on Robotics and Automation (2002)
2. Kneip, L., Tache, F., Caprari, C., Siegwart, R.: Characterization of the compact Hokuyo URG-04LX 2D laser range scanner. ICRA09 (2009)
3. Gonzales, J., Ollero, A., Reina, A.: Map building for a mobile robot equipped with a 2D laser rangefinder. In: Proc. of the IEEE Int. Conf. on Robotics & Automation, ICRA (1994)

4. Elfes, A.: Sonar-Based Real World Mapping and Navigation. *IEEE J.Robotics and Automation* RA-3, 249 (1987)
5. Se, S., Lowe, D., Little, J.: Mobile Robot Localization and Mapping with Uncertainty using Scale-Invariant Visual Landmarks. *The International Journal of Robotics Research* 21(8), 735–758 (2002)
6. Jung, M., Myung, H., Hong, S., Park, D., Lee, H., Bang, S.: Structured Light 2D Range Finder for Simultaneous Localization and Map-building (SLAM) in Home Environments. In: *IEEE International Symposium on Micro-Nanomechanics and Human Science*, pp. 371–376 (2004)
7. Jung, H., Lyou, J.: 3D map building using the kinect mounted on a mobile robot. In: *IEEE International Conference on Industrial Technology, ICIT* (2014)
8. SICK AG Mid range distance sensors Dx50, DT50 Hi (11/19/2014 4:08:30 PM), <http://www.sick.com/group/>
9. Skrzypczynski, P.: Spatial Uncertainty Management for Simultaneous Localization and Mapping. In: *Proc. IEEE Int. Conf. on Robotics and Automation, Rome*, pp. 4050–4055 (2007)
10. Skrzypczynski, P.: On Qualitative Uncertainty in Range Measurements from 2D Laser Scanners. *Journal of Automation, Mobile Robotics and Intelligent Systems* 2(2), 35–42 (2008)
11. Hokuyo Automatic CO Scanning Laser Range Finder UBG-04LX-F01 (Rapid-URG) Specifications (11/19/2014), <http://www.hokuyo-aut.jp/>
12. Hokuyo Automatic CO Scanning Laser Range Finder URG-04LX-UG01 (Simple-URG) Specifications (11/19/2014), <http://www.hokuyo-aut.jp/>

Use of Automated Image Analysis in the Study of Mechanisms of the Formation of Nitrided Layers

Tomasz Wójcicki

Institute For Sustainable Technologies – National Institute, Radom, Poland
Tomasz.wojcicki@itee.radom.pl

Abstract. This paper presents a developed model solution designed to identify material properties, and characteristics of the manufacturing processes of surface layers, based on automatic image analysis of material microsections. The characteristics of the mechanisms of formation of nitrided layers, and those occurring during the process phenomena are discussed. The objectives of the use of the methods of digital image processing, and analysis, as well as specific sets of tasks are described. Among presented possibilities of the use of methods of digital image processing, and analysis, the following techniques are discussed: improving the quality of images, segmentation, morphological transformations, and pattern recognition. The presented model includes different stages of the analysis, such as: automatic selection of procedures involving the specified methods of image processing, and analysis, automatic identification of nitriding zones, and their characteristics, automatic identification of technology, and the characteristics of the gas nitriding process.

Keywords: image analysis, surface layer, gas nitriding, artificial intelligence.

1 Characteristics of Gas Nitriding Processes

Gas nitriding is a thermo-chemical treatment of iron alloys by nitrogen saturation of the metal surface by diffusion in order to improve their properties, such improvements including wear resistance, hardness, fatigue resistance, and corrosion resistance. In addition to gas nitriding, other types of nitriding methods are used, for example: ion nitriding, plasma nitriding, nitriding in fluidized beds, and nitriding in powders. Nitriding is the final operation in the technological process which can be combined with tempering or carburization. The nitriding process in terms of its duration can be: short term (when the duration does not exceed a few hours) which is typically used to improve corrosion resistance, or the long-term process (when the time is longer than a few hours) which normally is used for curing materials. During the process of gas nitriding, the nitrogen concentration in the surface layer changes. Nitrogen, which diffuses, forms a zone of chemical compounds consisting of pure nitrides, and the diffusion zone (internal nitriding), where the content of nitrides decreases until residual amounts remain in the material core.

The entire process can be controlled by creating, among other things, a nitriding atmosphere with a specific potential produced by different techniques, and by providing

the determined flow through the retort. In the case of bicomponent atmospheres, dilution ammonia (NH_3) by nitrogen (N_2) or dissociated ammonia ($\text{NH}_{3\text{diss}}$) decreases the supply of atomic nitrogen on the steel surface, which leads to the reduction of nitrogen concentration on the surface, and consequently reduces the growth of undesirable, porous, and brittle ϵ , $\epsilon+\gamma$ zones. The effect of the nitriding process is a surface layer, which has a structure, and phase composition depending on such parameters as temperature, duration of the process, the type of material from which an object is made, and the composition of the nitriding atmosphere. The materials subjected to nitriding contain nitride-forming elements Cr, V or Mo. During the nitriding process, phases appear such as ferrite, austenite, nitrides γ' (Fe_4N), and nitrides ϵ (Fe_2N). Thermo-chemical treatment in the form of gas nitriding is applied to many elements of engines and pumps used by the aviation industry, shipbuilding and the automobile industry, for example: connecting rods, cylinder liners, pistons, pins, and piston rings, gears, and shafts [1]. Nitriding is also commonly used to improve tools such as: forming tools, forging dies, injection molds, drawing dies, cutting tools made of high speed steel, drills, screw taps, milling cutters, etc. Gas nitriding processes are carried out in specially designed devices which, depending on the type of gas nitriding being conducted, may have different equipment. A typical setup used to conduct the gas nitriding process consists of: a retort with a system of heaters, dissociator, gas supply, and gas drainage systems, fans providing circulation of air, and a control system. In addition, the setup can be equipped with sensors to allow control of the parameters of the conducted processes, including the determination of the degree of dissociation of ammonia, and nitrogen potential, and sensors indicating the test results of the process (e.g., a magnetic sensor [2]).

2 Characteristics of Methods for Processing and Analysis of Digital Images

Technologies for automated processing, and analysis of digital images are widely used in many applications, both cognitive [3] as well as practical, and are used in different industries [4]. There are many methods of processing, and analysis of digital images, among which are basic task groups such as: image enhancement, segmentation, morphological transformations, and recognition. Image enhancement methods [5] are used to reduce the impact of distortions caused by nonlinear characteristics of optoelectronic sensor systems, or aberrations of lens systems used in vision systems. Image enhancement methods include point, and spatial operations. Point operations known as anamorphic are characterized by the fact that the result of the conversion of pixels depends only on the value of the analyzed pixels, without taking into account the relationship with other pixels. Spatial operations are characterized by the fact that the values of the analyzed pixels depend on the values of other pixels within a specific location or surroundings, dependent on the diameter of the so-called local operator. Methods for performing segmentation processes are another group of methods of processing, and image analysis. Image segmentation [6] that is also called labeling is an operation which separates the data being analyzed into images, in order to increase the efficiency of recognition processes, and interpretation of objects included therein

through their simplification. Segmentation methods include two basic groups – area, and contour. Area segmentation consists in dividing the image into homogeneous zones that meet the established criteria of homogeneity (e.g., intensity, color, texture). Areas identified correctly during the segmentation process should represent specific parts of reality. Contour segmentation is the detection of object contours that are shown in the analyzed image. Examples of methods of segmentation are: regions growth [7], watershed transformation [8], and thresholding [9].

Another group of methods of image processing, and analysis are morphological transformations that allow the processing of shapes of objects mapped in the analyzed image through the use of so-called structurizing elements [10], also known as structural elements, which are patterns of active centerpoints. Morphological transformations, in terms of the complexity of algorithms that create them, are divided into: simple transformations (basic), and complex transformations. Simple transformations are operations that cannot be replaced by other morphological transformations. Complex transformations are divided into first-order, and second, and higher orders. The first-order transformations are those whose actions are based on the submission of basic operations, where the number of occurrences of basic operations is limited to one. The second, and higher order transformations are those whose actions are based on a combination of basic operations, where the number of occurrences of basic operations for the second-order is two, and appropriately, for the higher orders, more than two. An important set of methods of image processing, and analysis is pattern recognition algorithms. Image recognition usually is composed of two steps. The first step is to measure the characteristics of detected objects, and the next step is to analyze the characteristics of the measured values for determining membership of an object in the previously defined classes of objects. Features which characterize the objects may change, and therefore it is not possible to unify them. The scope, and types of the methods of image processing, and analysis is very diversified, and depend on many factors, among which an important role is played by the type of the objects represented in the analyzed images, and the established time limits. The methods have specific advantages, and limitations that determine their practical applications. Selection of the appropriate methods for the solution of the given task significantly affects the obtained results.

3 Model of Analysis of Manufacturing Processes of Nitrided Layers Based on Automated Analysis of Digital Images

At present, there are computer programs to support the analysis of the structures of materials, but they do not allow inverse processes to be conducted, i.e., inferencing about the conditions in which the materials have been produced with a limited range of input data, in this case the image data. These types of processes are known in the field as reverse engineering, and are used, among other things, to gain information about methods used to manufacture specific products, which in relation to the practical aspects can be applied in the analysis of the causes of machinery damage or identification of technology used by the competition. It is assumed for purposes of this

model that the images of microsection materials are used for automated inferencing about values of the parameters characterizing the associated gas nitriding processes, and properties of the obtained layers. The structural model for analysis of mechanisms of preparation of nitrided layers based on automated analysis of digital images is shown in Fig. 1.

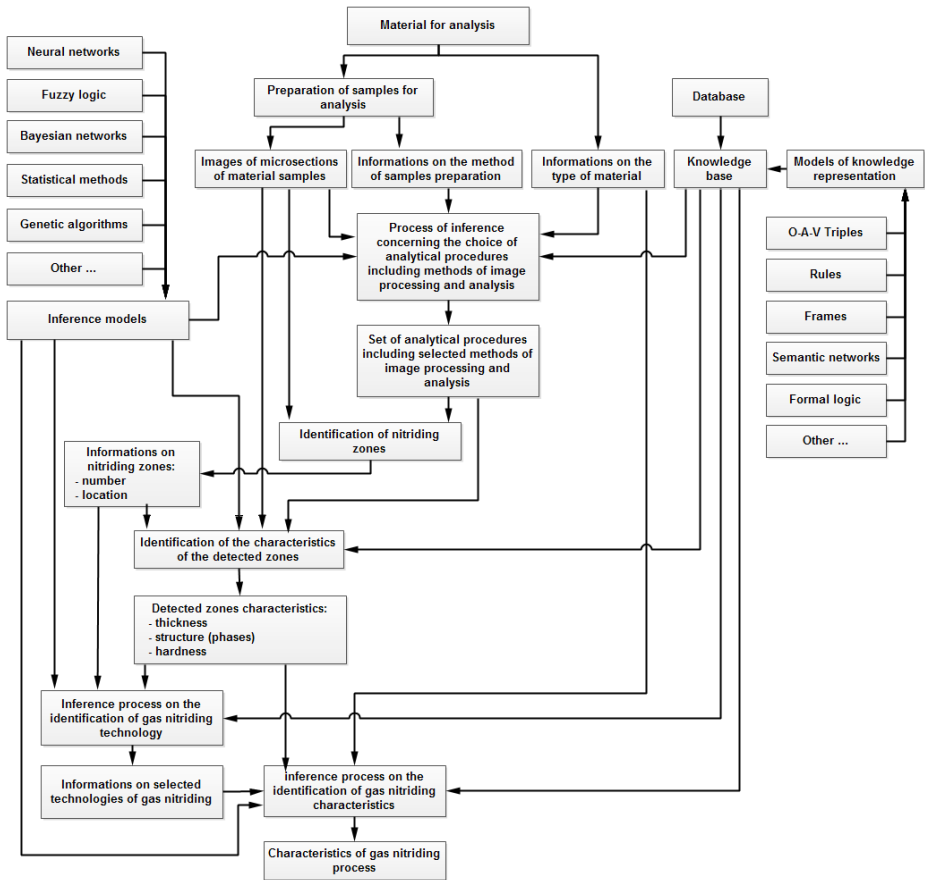


Fig. 1. The structural model for analysis of the mechanisms of preparation of nitrided layers based on automated analysis of digital images

The general formal model of the analysis process is as follows:

$$F_M : X_M \rightarrow Y_M \tag{1}$$

where: F_M – operator of the model, X_M – space of input values, Y_M – space of output values. The space of input values X_M is created by data covering: digital images of microsections of analyzed samples of material, information about the actual size of the mapped structures, information about the methods of preparation of microsections, and information about the types of material samples. The space of output values Y_M is

composed of: characteristics of the layers, information about the possible technologies used in gas nitriding, and characteristics of the processes by which it is possible to produce surface layers similar to those that are analyzed. Before performing the relevant processes of image analysis, and multi-step inference, it is necessary to prepare the input data in the form of digital images of material samples. The images should expose the characteristics of the material in the best possible way. There are many methods of preparing samples of materials in order to enhance the visibility of their structures, for example: etching, evaporating, and staining raid. Reagents for etching efficiently affect the grain boundaries, but, grains can also be more or less etched themselves. When the etched sample consists of several phases, then they are visible to different degrees, which permits the carrying out of their identification in the images. For this reason, it is important that the same structures that are subjected to analysis be prepared by identical methods.

The first stage in the main analysis is the inference about identification of procedures, which include methods of processing, and analysis of digital images for the identification of nitriding zones, and their characteristics. This stage is necessary due to differences in the representation of the nitriding zones, which depend, among other things, on the type of material, and the methods used to prepare samples of materials that may variously affect the obtained images. The inference process is implemented with the use of the deductive model [11] based on bivalent logic. In this solution, the knowledge about the known cases is represented in the form of logical rules consisting of premises, and conclusions. The advantage of this solution is that, if only certain specific rules will be used (which are confirmed in reality) the result will also be devoid of uncertainty. To write logical rules, the Horn clause format [12] has been used:

$$\mathfrak{R} : w_1 \wedge w_2 \wedge \dots \wedge w_n \rightarrow k \tag{1}$$

where: w_1, w_2, w_n – statements in the premise of the rule, k – conclusion of the rule. The result of the inference process is a set of methods of image processing, and analysis included in the analytical procedures, which permit the carrying out of further analytical processes, such as the identification of nitriding zones, and the characteristics of the detected zones. The second stage in the analysis is the identification of nitriding zones using the procedures identified in the inference stage. The analysis is preceded by the determination of the area of interest – ROI [13], which is a part of the image indicated for further processing (Fig. 2), and containing important information from the point of view of a task.

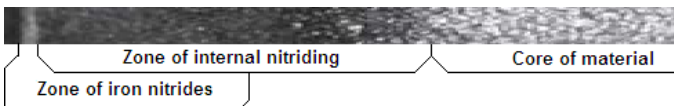


Fig. 2. ROI representing the part of the image of the sample of nitrided material in the form of AISI H13 tool steel

There is also important data on the physical size of the sample area mapped onto ROI. When the ROI is set, the processes related to image enhancement are then carried out, which include, depending on the method of sample material preparation, and material parameters, the following items:

- scaling in two-dimensional space,
- contrast enhancement using one of the functions of the type: $1 - e^{-C}$, $\ln(1+C)$, $\tanh(C)$, where: C – the previous value of contrast,
- filtration, compensation of the imperfections of the image acquisition process, and ineffective exposure of the object of analysis (filters: median [14], Gaussian [15]).

Procedures designed to identify nitriding zones are based on the analysis of the distribution of pixel brightness. In this case, the projection of the pixel brightness on the axis of the mapping of the distance from the sample surface to the core material is done by calculating the average values for each of the rows in the ROI starting from the fragments of the mapping of the material surface by the equation:

$$\bar{p}(y_j) = \frac{1}{r_x} \sum_{i=1}^{r_x} p(x_i) \quad (3)$$

where: x_i – pixel number in a single line of the ROI, y_j – pixel number in a single row of the ROI, r_x, r_y – number of pixels in columns, and rows constituting the rectangular ROI, $p(x_i)$ – brightness of the i -th pixel in the line of the ROI, $\bar{p}(y_j)$ – average brightness of pixels in the j -th row of the ROI. An example of the distribution of pixel brightness in the ROI of an image representing the metallographic microsection of a sample of nitrided material is shown in Fig. 3.

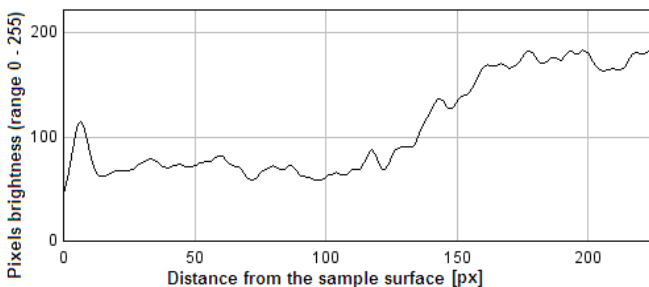


Fig. 3. Distribution of pixel brightness in an image representing part of the analyzed material (AISI H13 tool steel) from the surface to the core (distance: 220 pixels)

In the presented example, the nitride zone located on the surface of the sample is characterized by brighter pixels with respect to the surrounding regions (this area in a number of publications is also called a white zone [16]). In the graph showing the distribution of pixel brightness in the ROI, the zone is detected as a peak whose width

determines the thickness of the zone. After identifying the location of each zone, and its width in the pictures of material samples, the forecasting process of hardness distribution in the zone of internal nitriding (if this type of zone has been identified) is carried out. Detecting the hardness distribution in the zone of internal nitriding with the use of image analysis is based on a comparison of the pixel brightness distribution of the analyzed sample with pixel brightness distributions of samples made of the same material, prepared for testing by the same methods, using similar vision systems for which characteristics of the hardness distributions are known. It was assumed that the average pixel brightness values correspond to the known levels of hardness obtained in the analysis of the other material samples, regardless of the width of the zones (Fig. 4).

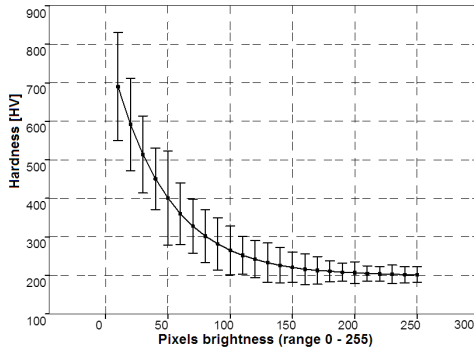


Fig. 4. Distribution of the pixels brightness mapping hardness of the zone of internal nitriding for images of material samples of AISI H13 tool steel

After determining the hardness distributions in the following nitriding zones, the next element of the analysis process is executed in the form of nitriding technology identification. After determining the hardness distributions in the following nitriding zones, the next element of the analysis process is executed in the form of nitriding technology identification. The inference is performed using a mechanism similar to the one used at the stage of the selection methods of image processing, and analysis, i.e., using a deductive model, and bivalent logic. The inference result is a set of potential gas nitriding technologies, which by their use make it possible to obtain surface layers characterized by similar properties of the sample analyzed. Premises, and conclusions of the rules which are used at this stage of the analysis include the facts that describe: nitriding zones (S), phases (F) contained in the gas nitriding technologies (G), where: $S \in \{S_a, S_w\}$, $F \in \{F_\epsilon, F_{\epsilon+\gamma}, F_\gamma, F_{\alpha+\gamma}, F_\alpha\}$, $G \in \{G_1, \dots, G_n\}$, $S_a \in P(\{F_\epsilon, F_{\epsilon+\gamma}, F_\gamma\})$, $S_w \in P(\{F_{\alpha+\gamma}, F_\alpha\})$, G_1, \dots, G_n – sets of features describing the gas nitriding technology, S_a – set of features describing the zone of iron nitrides, S_w – set of features describing the zone of internal nitriding, $F_\epsilon, F_{\epsilon+\gamma}, F_\gamma$ – sets of features describing the phases of the iron nitrides zone, $F_{\alpha+\gamma}, F_\alpha$ – sets of features describing the phases of the internal nitriding zone, P – power set. Below is an example of a rule for the deductive process of identifying nitriding technology:

$$\mathfrak{R} : \text{IF } S_a = \{F_{\varepsilon+\gamma'}, F_{\gamma'}\} \Rightarrow G = G_2 \quad (4)$$

The knowledge base can contain rules describing any technology of gas nitriding, including unregulated or regulated nitriding, with single or multicomponent atmospheres, e.g.: NH_3 , $NH_3 + N_2$, $NH_3 + NH_3diss$, $NH_3 + H_2$.

The last stage in the process of analysis is to identify the characteristics of the gas nitriding process. At this stage, the inference mechanism is based on fuzzy logic [17], and the Mamdani model [18] is used. Premises, and conclusions of fuzzy rules are composed of fuzzy sets mapping, parameters of nitriding processes, as well as the characteristics of the nitriding zones. Fuzzy sets M in the input or output space marked as S are characterized by the following features:

$$M = \{(s, \mu_M(s)), s \in S\}; \quad \mu_M : S \rightarrow [0,1] \quad (5)$$

A set of rules for analysis is selected from the entire collected knowledge base of rules by compliance with the type of sample material, and the compatibility of the type of technology selected in the previous stage. The structure of the rules for inference concerning the technology of unregulated nitriding, with a one component atmosphere, in the form of NH_3 is as follows:

$$\begin{aligned} \mathfrak{R}_j : \text{IF } (F_{\varepsilon}^0 \text{ is } M_j^{F_{\varepsilon}^0}) \text{ AND } (F_{\varepsilon+\gamma'}^0 \text{ is } M_j^{F_{\varepsilon+\gamma'}^0}) \text{ AND } (F_{\gamma'}^0 \text{ is } M_j^{F_{\gamma'}^0}) \\ \text{AND } (F_{\alpha+\gamma'}^0 \text{ is } M_j^{F_{\alpha+\gamma'}^0}) \text{ AND } (F_{\varepsilon}^N \text{ is } M_j^{F_{\varepsilon}^N}) \text{ AND } (F_{\varepsilon+\gamma'}^N \text{ is } M_j^{F_{\varepsilon+\gamma'}^N}) \\ \text{AND } (F_{\gamma'}^N \text{ is } M_j^{F_{\gamma'}^N}) \text{ AND } (F_{\alpha+\gamma'}^N \text{ is } M_j^{F_{\alpha+\gamma'}^N}) \\ \text{THEN } (Np_j \text{ is } M_j^{Np}) \text{ AND } (T_j \text{ is } M_j^T) \text{ AND } (t_j \text{ is } M_j^t) \end{aligned} \quad (6)$$

where: F_{ε}^0 , $F_{\varepsilon+\gamma'}^0$, $F_{\gamma'}^0$, $F_{\alpha+\gamma'}^0$ – initial thicknesses of the individual phases of the iron nitride zone, and the internal nitriding zone, $M_j^{F_{\varepsilon}^0}$, $M_j^{F_{\varepsilon+\gamma'}^0}$, $M_j^{F_{\gamma'}^0}$, $M_j^{F_{\alpha+\gamma'}^0}$ – fuzzy sets in the input space, representing the initial thicknesses of the individual phases of the iron nitrides, and internal nitriding zones, F_{ε}^N , $F_{\varepsilon+\gamma'}^N$, $F_{\gamma'}^N$, $F_{\alpha+\gamma'}^N$ – final thickness of the individual phases of the iron nitride, and internal nitriding zones, $M_j^{F_{\varepsilon}^N}$, $M_j^{F_{\varepsilon+\gamma'}^N}$, $M_j^{F_{\gamma'}^N}$, $M_j^{F_{\alpha+\gamma'}^N}$ – fuzzy sets in the output space, representing the initial thicknesses of the individual phases of the iron nitrides, and internal nitriding zones, Np_j – nitriding potential, T_j – process temperature, t_j – duration of the process, $j = (1..m)$ – rule number that describes dependencies for part of a nitriding process.

Inference at this stage is a process consisting of fuzzification (transforming sharp signals into fuzzy sets, using the specified membership functions, where it is assumed that they will form isosceles triangles having vertices corresponding to the sharp, and sides spanning the entire range of the corresponding domain) inference (creating

complex fuzzy sets in the output space for the nitriding potential, temperature, and time of the nitriding process), and defuzzification (calculating sharp values from complex fuzzy sets in the output space, using the center of gravity method [19]). In the case of regulated nitriding, where multicomponent atmospheres are used, the rules are much more complex because they also describe the proportions between the components of the atmosphere that may change during the process of nitriding. In such a case, a much more comprehensive knowledge base is also required consisting of rules which provide the possibility of obtaining sharp values for process parameters in the widest range of input data.

4 Summary

This article describes the methodology for the discovery of the properties of surface layers, and gas nitriding process parameters using those which have been manufactured, solely on the basis of automatic image analysis of material sample microsections. The developed method should be considered as a heuristic solution, due to the need to provide a priori knowledge which is used in the automatic inference processes which may not cover the required range of domain in each case analyzed. A limitation is also a reduction of input data (only digital images), which on the one hand is an advantage of this solution because it is not necessary to perform additional tests, but on the other hand this has a negative affect on the obtained results. The solution is an important step towards eliminating the human element in the process of research, and research automation. The use of this method in the real world can assist companies that operate in the area of production to improve the properties of materials by providing the tools to enable them to analyze products manufactured by the competition. It can also be used in the analysis of the causes of damage to equipment, and devices in field conditions without the need to use expensive laboratory equipment, and engage in long-term research. This method should be considered as a model in the development phase which is open-ended, which means that it can be modified in the future in order to increase its efficiency. One of the possibilities that could increase the efficiency of this solution is to build the knowledge base, which is used in several stages of the inference processes, as well as to provide possibilities of supporting the solution by analysis which do not include solely methods of image processing, and analysis, but also, for example: photoelectron spectroscopy [20] or other popular techniques.

References

1. Wach, P., Michalski, J., Tacikowski, J., Kowalski, S., Betiuk, M.: Gas nitriding and its variations in industrial applications. *Inżynieria Materiałowa* 29(6), 808–811 (2008)
2. Ratajski, J.: Monitoring the growth of the nitrated layer by the magnetic sensor – application examples. *Inżynieria Powierzchni* 1, 56–64 (2001)

3. Figiel, W., Kawalec-Latała, E.: Use of image processing and analysis to interpret sections of synthetic acoustic pseudoimpedance. *Gospodarka Surowcami Mineralnymi* 24(2/3), 371–385 (2008)
4. Stawowy, M.: Use of image analysis to solve transportation issues. *Prace Instytutu Podstaw Informatyki Polskiej Akademii Nauk* 862, 3–33 (1998)
5. Jinshan, T., Peli, E., Acton, S.: Image enhancement using a contrast measure in the compressed domain. *Signal Processing Letters IEEE* 10(10), 289–292 (2003)
6. Nieniewski, M.: Segmentation of digital images: watershed segmentation method. *Akademicka Oficyna Wydawnicza Exit. Warsaw* (2005) (in Polish)
7. Nagabhushana, S.: *Computer Vision and Image Processing*. New Age International Publishers, Delhi (2005)
8. Tanniru, P.: *Effects of Pre-processing and Postprocessing on the Watershed Transform*. San Jose State University (2007)
9. Bernsen, J.: Dynamic thresholding of gray-level images. In: *Proceedings of the Eighth International Conference on Pattern Recognition*, pp. 1251–1255. IEEE Computer Society Press, France (1986)
10. Tadeusiewicz, R., Korohoda, P.: *Computer analysis and image processing*. Wydawnictwo Fundacji Postępu Telekomunikacji, Cracow (1997) (in Polish)
11. Vijay, C., Hooker, J.: *Optimization methods for logical inference*. John Wiley & Sons, Canada (2011)
12. Padawitz, P.: *Computing in Horn clause theories*. Springer Publishing Company, USA (2012)
13. Moussa, H.: Efficient technique to detect the region of interests in mammogram images. *Journal of Computer Science* 8, 652–662 (2008)
14. Stoliński, S., Grabowski, S.: Experimental comparison of the median filters to remove impulse noise from color images. *Automatyka* 9 (2005) (in Polish)
15. Gotfryd, M.: Gaussian filter - properties, realisability, use. *Elektronika: konstrukcje, technologie, zastosowania* 51(4), 88–92 (2010)
16. Derewnicka, D.: Advanced testing method of nitrided layers after heat treatment. *Inżynieria Powierzchni* 2, 14–18 (2012)
17. Kosiński, W., Prokopowicz, P.: Algebra of fuzzy numbers - Applied Mathematics. *Matematyka dla Społeczeństwa* 46(5), 37–63 (2004)
18. Antonelli, M.: Learning concurrently partition granularities and rule bases of Mamdani fuzzy systems in a multi-objective evolutionary framework. *International Journal of Approximate Reasoning* 50(7), 1066–1080 (2009)
19. Van Broekhoven, E.: Bernard De Baets: Fast and accurate center of gravity defuzzification of fuzzy system outputs defined on trapezoidal fuzzy partitions. *Fuzzy Sets and Systems* 157, 904–918 (2006)
20. van der Heude, P.: *X-Ray Photoelectron Spectroscopy*. Wiley & Sons, Canada (2012)

Measurement of Selected Parameters Describing Biomechanical Phenomena Occurring in the Implant-Bone System

Marcin Zaczyk

Faculty of Mechatronics, Warsaw University of Technology
m.zaczyk@mchtr.pw.edu.pl

Abstract. The paper presents results of measurements of selected parameters describing phenomena that occur in implant-bone system in the case of a cement-less mounting of the mandrel within the closer shaft of a thigh bone. The main aim of the study was to observe phenomena, which take place in the implant-bone system and to determine values and character of displacements resulting from the applied load.

Keywords: implant-bone system, endoprosthesis of the hip joint, bone-implant mating.

1 Introduction

The paper describes a problem of mating of implant mandrel with the osseous tissue that surrounds it, as far as the mechanical load capacity of the implant-bone system is concerned. The paper focuses on measurement methods related to mechanical phenomena connected with mutual interactions between the implant and the bone. The realized measurements made it possible to describe in a more precise way the strength of the joint that undergoes a treatment consisting in application of an mandrel.

2 The Studied Object

The studied object was a cement-less mounting of an implant mandrel within an osseous tissue, for which a sample has been designed that made it possible to perform measurements of respective displacements under laboratory conditions. Physical samples were based on animal osseous preparations and a steel fragment of a mandrel of an implant-endoprosthesis. The closer shaft of the thigh bone was chosen as the fragment of the osseous preparation. It had a socket for the implant mandrel prepared inside (Fig. 1), in which a fragment of the mandrel with diameter of 17 mm and roughness $R_a = 0.32 \mu\text{m}$ was mounted. Within each osseous preparation an implant mandrel was mounted by pushing it into the osseous tissue over the same depth of 20 mm, keeping a keying fit (H7/p7 fit between the fragment of the mandrel and the bone socket was applied). Material properties of the osseous tissue were defined on

the basis of a determined real density of the osseous tissue, computed as a ratio of the volume of the osseous preparation to its mass; the fragment of implant mandrel was made of a high-grade implant steel (cobalt alloy) according to ISO standard 5832-12 [7–10].

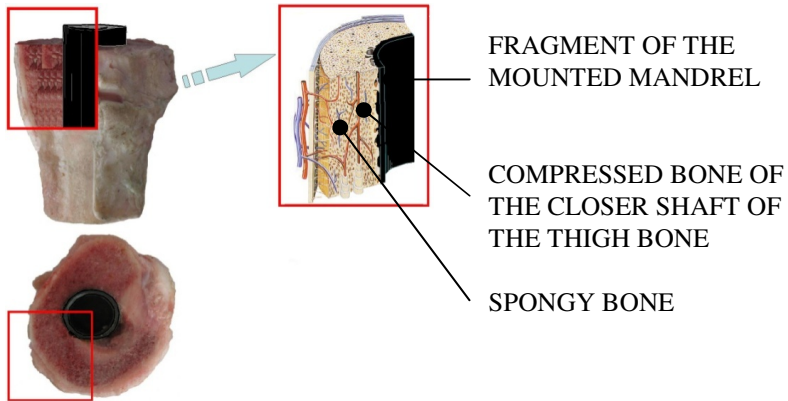


Fig. 1. Structure of the studied object used in the experimental part of the study

3 Method of the Study

The method of the study is based on experimental studies consisting in a compression test of samples that have been prepared beforehand, using osseous preparations and recording displacements within the samples. The main aim of the studies was to observe phenomena that take place within the implant-bone system and to determine value and character of the displacements, which take place within the osseous tissue and the mandrel of the implant as a result of the applied load.

The studies were realized in a compression cycle of the sample, determining influence of the applied load on displacement of a mandrel fragment with respect to the osseous preparation, in which the fragment has been mounted. The recording included measurements of displacements that occur between the osseous tissue and the mandrel mounted within it. Displacements in a direction perpendicular to loading was also recorded, in order to diagnose magnitude of elastic buckling of the sample in the compression test. The applied load was of a linear character with maximal value of 1200 N.

During the realized compression tests, the applied load made it possible to record behavior of the osseous tissue under a stress corresponding to its elastic strength, yet without an effect of destroying the tissue by the mandrel mounted within it by means of a compression process. Asymmetry of the geometry of the preparations of osseous samples made it necessary to apply ball-shaped spacers, which automatically eliminated the component forces, reducing them into a single force, whose direction was perpendicular to the occurring displacements. Such approach made it possible to eliminate numerous errors resulting from the asymmetry of the geometry of the osseous tissue used for creating the samples (Fig. 2).

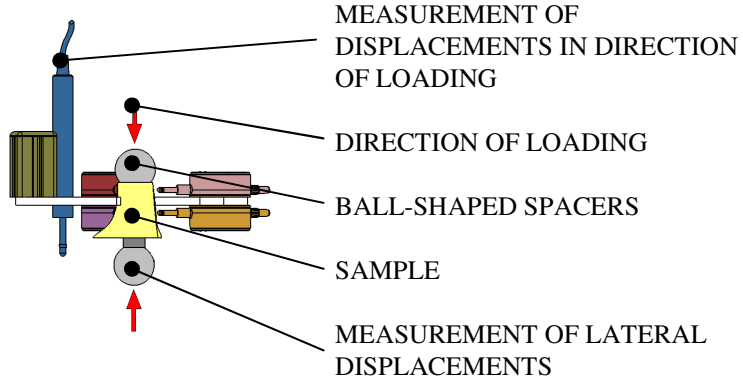


Fig. 2. Schematic of realization of the measurements for the applied load

4 Results of the Study

The compression tests of the samples performed at a laboratory provided data, which are listed in Tab. 1. The obtained results of the performed tests have revealed behavior of the implant-bone system at various densities of the osseous tissue. Moreover, measurements of the displacements have revealed what is their character as referred to the applied load as well as the density of the osseous tissue.

Table 1. Results of the recorded displacements for the cement-less mounting of the implant within the osseous tissue for the first studied object

Measurement step	Time of performing the test	Applied load	Displacement recorded in direction of loading		
			SAMPLE I with density of the osseous tissue of 1.3 g/cm^2	SAMPLE II with density of the osseous tissue of 1.6 g/cm^2	SAMPLE III with density of the osseous tissue of 1.8 g/cm^2
	[s]	[N]	[mm]		
1	0	0	0.000	0.039	0.018
2	5	50	0.000	0.039	0.018
3	10	100	0.000	0.039	0.018
4	20	150	0.000	0.063	0.028
5	25	200	0.075	0.097	0.039
6	30	250	0.125	0.130	0.075
7	35	300	0.237	0.160	0.111

Table 1. (continued)

8	40	350	0.271	0.190	0.181
9	45	400	0.30	0.220	0.251
10	50	450	0.349	0.250	0.369
11	55	500	0.393	0.280	0.487
12	60	550	0.594	0.305	0.551
13	65	600	0.796	0.325	0.615
14	70	650	0.794	0.355	0.613
15	75	700	0.793	0.425	0.613
16	80	750	0.788	0.485	0.614
17	85	800	0.783	0.501	0.617
18	90	850	0.785	0.515	0.618
19	95	900	0.7860	0.518	0.618
20	100	950	0.7860	0.529	0.618

5 Analysis of the Results

On the basis of the obtained results of the studies, it can be concluded that the implant-bone system at the initial phase of compression remains at an equilibrium, despite the fact that the load is being increased – no displacements have been recorded.

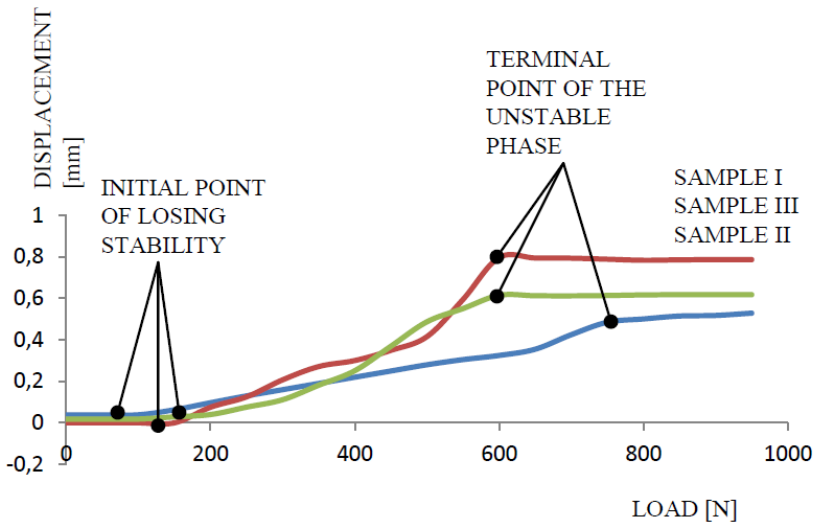


Fig. 3. Diagram illustrating dependency of the load in function of the displacement of the mandrel within the osseous preparation for the three investigated samples

In the case of each experiment performed, it was observed that the implant mandrel used to lose its grip to the bone while exceeding a pressure of a critical value, and once it reached a certain new value, the mandrel ceased to displace. It was accepted that this new value determines the terminal point of the unstable region. The observed state indicates that the pressure applied on the implant mandrel is small enough for the osseous tissue to resist the pressure, ensuring at the same time a stability of the implant-bone system. Exceeding this pressure results in deformation of the osseous tissue, and the implant mandrel starts to displace within the osseous preparation. The applied pressure in function of the displacement in direction of loading makes it possible to find the initial point of losing stability. A phase of the experiment, when in spite of increasing the load the displacement of the mandrel with respect to the bone does not change, can be accepted as the point of losing stability of the studied object.

The initial point of losing stability, observed in the case of each of the studied objects that have been tested, indicates that mating of the implant mandrel with the osseous tissue, in which it has been mounted, is of a peculiar character. Despite the fact that the used osseous tissues in each of the studied objects that have been tested had individual biomechanical features, such as e.g. density, the character of mating of the implant mandrel with the tissue remained the same.

6 Discussion

On the basis of the presented measurements related to the implant-bone system, it can be stated that the strength of the system is influenced by many biomechanical factors. The studies that have been realized made it possible to define the phenomena that take place in the implant-bone system during a standard operation, as far as mechanical aspect is concerned. The recorded displacements reveal phenomena of mutual interaction between the surface of the implant mandrel and the surrounding osseous tissue. Results of the studies proved that it is very hard to unequivocally define the phenomena, because a lot of them exist, and additionally they are correlated [1–3, 6]. At the boundary between the implant mandrel and the osseous tissue, there occur phenomena originating in material properties (mandrel being an isotropic material, and the osseous tissue being an orthotropic material) [1–3, 7]. During a compression process there occur frictional phenomena within the implant-bone system as well as phenomena of destroying the element that is weaker [3–5]. Beside these phenomena, there may take place a deformation of the body that is more compliant (the bone), resulting in a local break of the contact. As far as the current methods of experimental studies are concerned, it is hard to find an experimental approach to the phenomena of the contact between the implant and the bone and a presentation of mutual interaction between the bone and the implant. In the relevant publications, many measurement techniques can be found, which are aimed at determining strength of the implant or mechanical properties of the osseous tissues. However, these studies omit the implant-bone system, and are focused only on small fragments of the osseous tissues instead. The measurement technique presented in the paper focuses on the implant-bone system from a mechanical aspect on a macro-scale, and takes into consideration on that scale all the phenomena taking place on a micro-scale at the boundary of the implant mandrel.

References

1. Bergmann, G., Deuretzbacher, G., Heller, M., Graichen, F., Rohlmann, A., Strauss, J., Duda, G.N.: Hip contact forces and gait patterns from routine activities. *J. Biomech* 34(7), 859–871 (2001)
2. Berlemann, U., Crompton, P.A., Rincon, L.: Pullout strength of pedicle hooks with fixation screws: influence of screw length and angulation. *Eur. Spine J* 5(71-73) (1996)
3. Hollinger, J.O., Einhorn, T.A., Doll, B., Sfeir, C.: *Bone Tissue Engineering*. CRC Press, New York (2004)
4. Ogiso, M., Yamamura, M., Kuo, P.T.: Comparative pushout test of dense HA implants and HA-coated implants: findings in a canine study. *J. Biomed. Mater. Res* 39(3), 364–372 (1998)
5. Yuehwei, H., Draughn, A.: *Mechanical Testing of Bone and the Bone-Implant interface*. CRC Press, New York (2000)
6. Zaczyk, M., Jasińska-Choromańska, D.: Comparative Studies of Various Methods of Mounting the Implant Mandrel Within the Bone. *Journal of Automation, Mobile Robotics & Intelligent Systems* 6(3), 33–36 (2012)
7. Zaczyk, M., Choromańska, D.J.: Selected Mechanical Properties of the Implant-Bone Joint. In: Jabłoński, R., Březina, T. (eds.) *Mechatronics. AISC*, vol. 86, pp. 691–695. Springer, Heidelberg (2011)

Rotational Speed and Transducer Frequency as Factors Affecting Possibility to Detect Defects in Axisymmetric Elements with a Method of Eddy Currents

Andrzej Zbrowski and Wojciech Jóźwik

Institute for Sustainable Technologies – National Research Institute
Pułaskiego str. 6/10, Radom, Poland
{andrzej.zbrowski,wojciech.jozwik}@itee.radom.pl

Abstract. The article describes the influence of two factors on the possibility to detect material defects in an axisymmetric element with a method of eddy currents. The factors the authors focused their analysis on include a rotational speed of the element tested, a frequency of the transducer, additional a placement of the measuring head (either on an inner or an outer surface of the test object). The investigations were carried out for a rotational speed $n = 15; 30; 45; 60; 90; 120$ rpm, and a transducer frequency $f = 0.06; 0.1; 0.5; 1; 2$ kHz. An SSEC III PC defectoscope was used for the control. The tests were performed on two bearing rings of different type. In both cases, artificially made surface or subsurface defects, in form of 1 mm blind holes, were analyzed. The authors conducted 120 measurements of the size of inner and surface defects altogether, and then classified larger and smaller distortions of the initial signal values as surface and subsurface defects respectively.

Keywords: eddy current, defect detection, bearing ring.

1 Introduction

Production of bearing rings is a complex technological process composed of a number of additional mechanisms like forming, machining, hardening, or grinding. During each technological process, a ring may be damaged, which prevents safe utilization of a bearing. Statistical studies show that defects resulting from a day to day exploitation constitute only 25% of all defects of roller bearings [1], while the majority of their failures stem from defects caused at the time of production of rings.

In order to ensure that a “zero defect” requirement is met, it is necessary to closely analyze every ring that leaves the production line. This can be done, inter alia, using a method of eddy currents. The advantage of this method, compared to optical inspection methods, lies in its ability to detect subsurface material defects [2]. With reference to other methods enabling detection of subsurface defects (e.g. magnetic particle inspection, ultrasound tests, or X-rays), the eddy current method helps to reduce the costs in an on-line quality inspection in production. Moreover, utilization of this technique does not pollute the test object, a problem which is frequent in an ultrasound method due to the necessity to use a coupling agent, and a magnetic particle inspection in which a

ferromagnetic powder is applied. Compared to a method of X-radiation, the method of eddy currents is more advantageous due to the absence of ionizing radiation, whose presence calls for increased precautions [3]. Eddy current inspection does not allow visualization of the defect. Therefore, to determine its shape and placement in a bearing ring, it is necessary to use computed tomography imaging [4].

The main difficulty in automatic quality inspection of bearing rings lies in the necessity to conduct it in one production cycle of the manufacturing line [5], which limits the time of inspection to a few seconds only, or requires many testers to be mounted in a parallel manner.

The objective of the tests was to determine the influence rotational speed and transducer frequency have on the results of tests conducted using a method of eddy currents. The test results are the foundation for calibration of an industrial system for automatic control of roller bearing rings that was developed by the Institute for Sustainable Technologies – National Research Institute. Earlier investigations indicated that maintaining a gap between a measuring head and a test object makes the defect detection process more difficult due to sinusoidal disturbances caused by the run-out of a bearing ring [6]. The tests also showed that the measuring head should be in contact with the object tested.

In their investigations, the authors used two bearing rings (Figs. 1 and 2) with artificial test defects, that in both cases took the form of 1 mm blind holes located on or under the surface of the bearing ring. The defects made reflect real defects that can in fact appear during a technological process (e.g. blisters, cracks, or non-metallic inclusions).

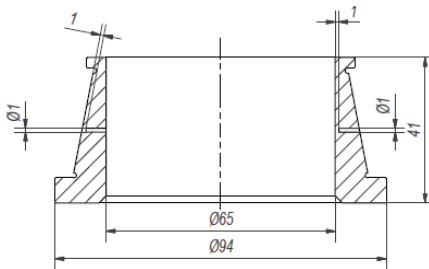


Fig. 1. Ring 1

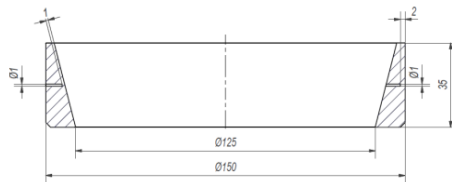


Fig. 2. Ring 2

For Fig.1 and Fig. 2 the dimensions are in mm.

2 State of the Art

The method of eddy currents is a non-destructive inspection method that uses electromagnetic induction to detect defects. Its greatest limitation is the fact that it can be used for conductive materials only.

The application of eddy current inspection to determine microstructure of metal elements is described in [7]. The authors used the method of eddy currents to characterize decarburizing depth. The tests were conducted using eddy currents with very low frequencies varying between 10 Hz and 100 Hz. The results of experiments conducted by the authors referred to were then compared to the results of destructive tests consisting in the measurement of a section's microhardness at 1 mm. These tests

can be performed in industrial applications concerning inspection of quality of hardened materials.

Eddy current testing enables noncontact measurement of vibrations of cutting tools [8]. A measuring probe is placed on a lathe cross slide, but a gap between the head of the probe and the tool handle is maintained. In the application in question, a high frequency of a transducer was used, which enabled the authors to measure the tool shift with an accuracy of $10\ \mu\text{m}$ in the 0–1 mm range.

There are devices employing more coils in a measuring head. In [9] the authors describe tests employing two measuring heads with 64 and 96 micro coils respectively, and indicate that utilization of novel measuring heads increases sensitivity of a test method.

3 Test Stand

The authors used an eddy current defectoscope SSEC II PC (Super Sensitive Eddy Current Instrument) with two analog and a digital signal as input signals. The analog signals correspond to real and imaginary parts of a signal, and they are used for communication between a defectoscope and a system for automatic inspection of a roller bearing, while the digital signal is used for communication between a computer and a defectoscope. The defectoscope's software enables the user to change work parameters like a frequency of a transducer or the amplification of a signal before and after demodulation (Fig. 3). Test results are saved as a text file, which enables easy analysis of a signal. Selected test results are presented in Fig. 4.

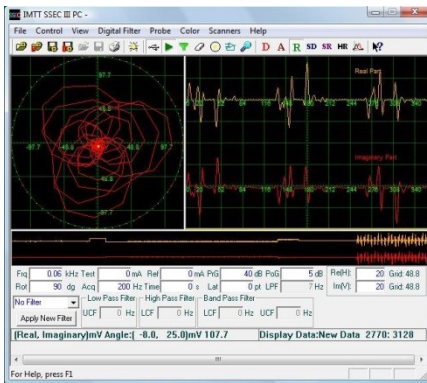


Fig. 3. Defectoscope software

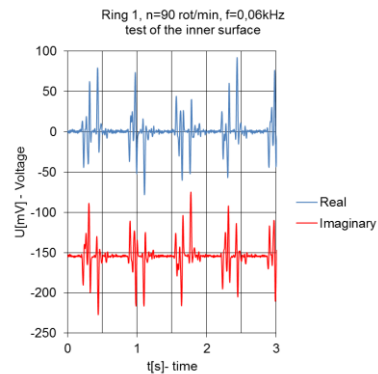


Fig. 4. Selected test results

Rings tested were placed in a three-jaw chuck driven by an actuator. To ensure contact between the test object and the measuring head, an adjustable grip was used. The stand is presented in Fig. 5.

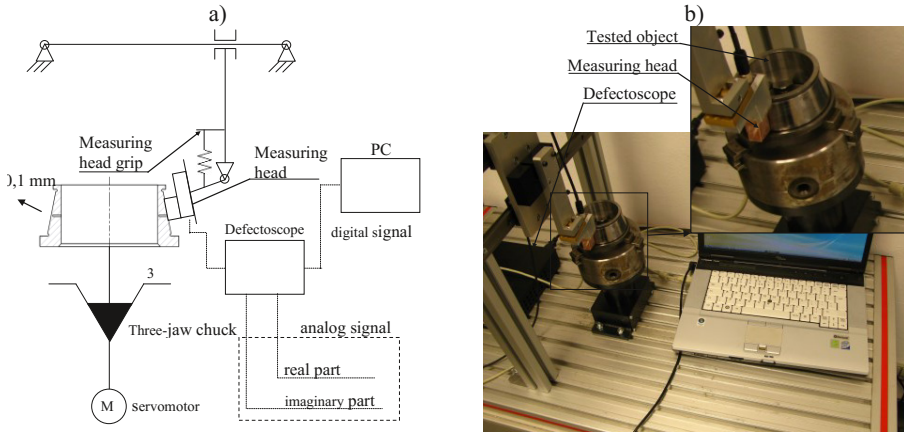


Fig. 5. Test stand: a – draft; b – view

4 Test Results

Test for Ring 1 and Ring 2 were conducted for the following parameters: rotational speed: $n = 15; 30; 45; 60; 90; 120$ rpm; transducer frequency: $f = 0.06; 0.1; 0.5; 1; 2$ kHz; internal and external placement of the measuring head (Fig. 6). The authors conducted 120 measurement altogether. The values they measured included subsurface and surface defects classified according to the intensity of input signal interferences (Fig. 7). Figs. 8 to 23 present collective test results. No subsurface defects were detected in Ring 2 at the time of inspection of its surface (Fig. 20, Fig. 22), in which case the defect signal value was “0”.

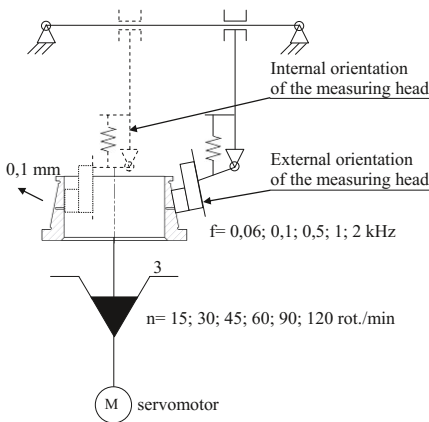


Fig. 6. Test parameters

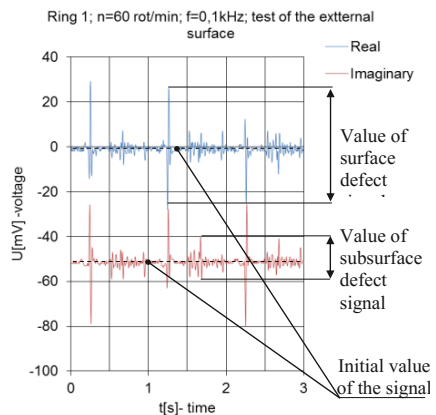


Fig. 7. Selected test results

Ring 1, test of inner surface, subsurface defect, real part of the signal

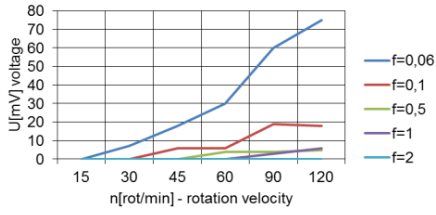


Fig. 8. Test results for Ring 1

Ring 1, test of inner surface, surface defect, real part of the signal

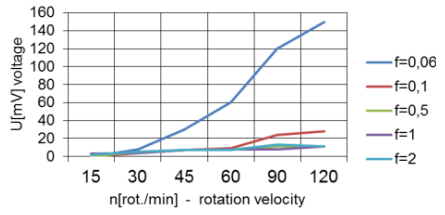


Fig. 9. Test results for Ring 1

Ring 1, test of inner surface, subsurface defect, imaginary part of the signal

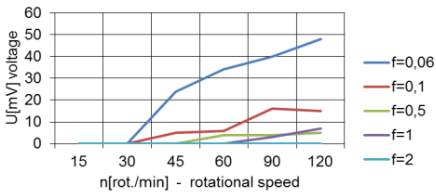


Fig. 10. Test results for Ring 1

Ring 1, test of inner surface, surface defect, imaginary part of the signal

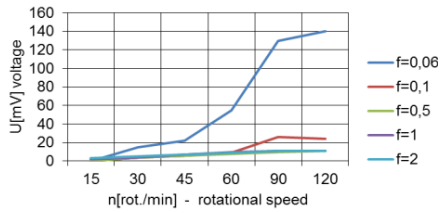


Fig. 11. Test results for Ring 1

Ring 1, test of external surface, subsurface defect, real part of the signal

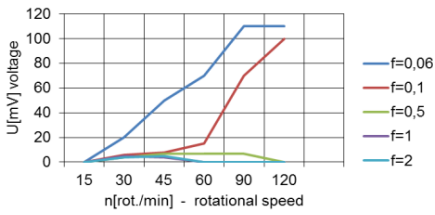


Fig. 12. Test results for Ring 1

Ring 1, test of external surface, surface defect, real part of the signal

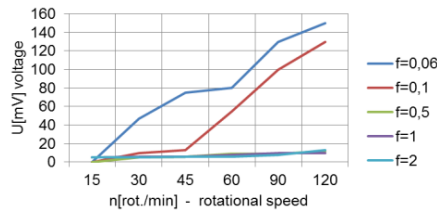


Fig. 13. Test results for Ring 1

Ring 1, test of external surface, subsurface defect, imaginary part of the signal

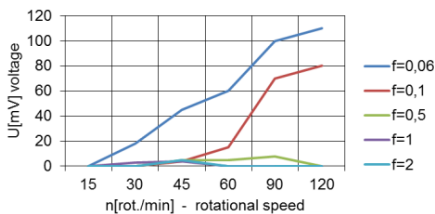


Fig. 14. Test results for Ring 1

Ring 1, test of external surface, surface defect, imaginary part of the signal

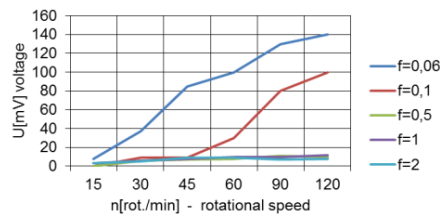


Fig. 15. Test results for Ring 1

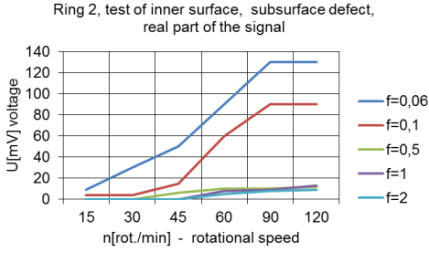


Fig. 16. Test results for Ring 2

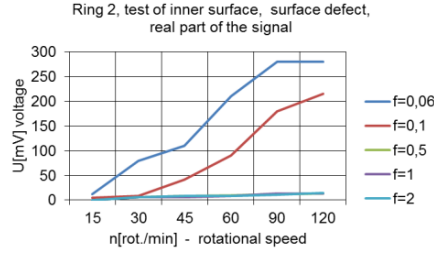


Fig. 17. Test results for Ring 2

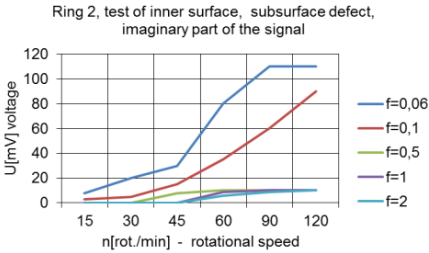


Fig. 18. Test results for Ring 2

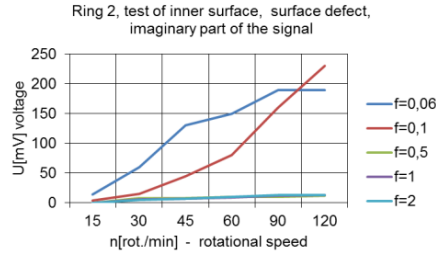


Fig. 19. Test results for Ring 2

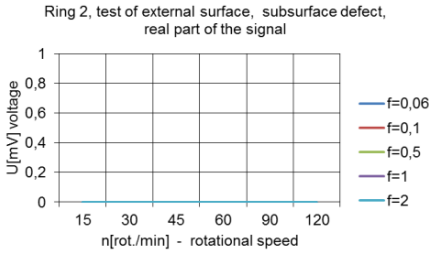


Fig. 20. Test results for Ring 2

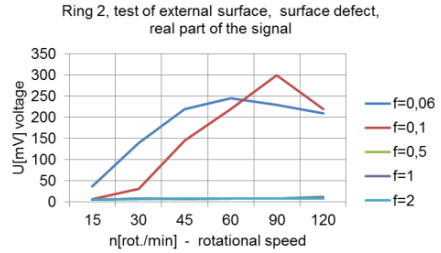


Fig. 21. Test results for Ring 2

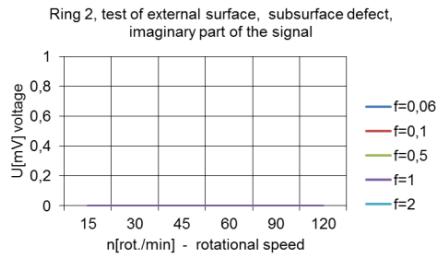


Fig. 22. Test results for Ring 2

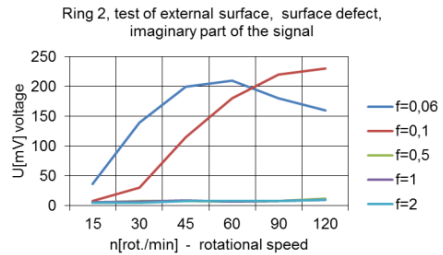


Fig. 23. Test results for Ring 2

5 Analysis of Results

The authors observed that transducer frequencies of 0.5, 1, and 2 kHz do not give satisfactory results. Therefore, in this section of the article results obtained for frequencies of 0.06 and 0.1 kHz are analysed.

Moreover, the authors noticed that the higher the rotational speed of the ring, the higher the signal of the defect (Figs. 24–27). However, for Ring 2 no increase in the value of the defect signal was observed at a rotational speed over 90 rpm (Fig. 26, Fig. 27).

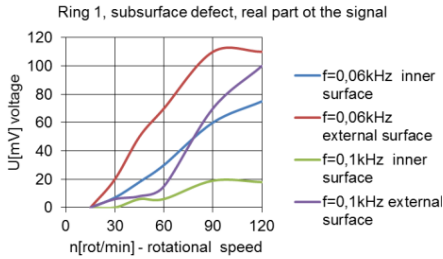


Fig. 24. Impact of rotational speed on the defect signal (Ring 1, subsurface defect)

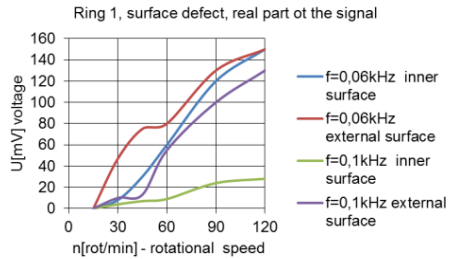


Fig. 25. Impact of rotational speed on the defect signal (Ring 1, surface defect)

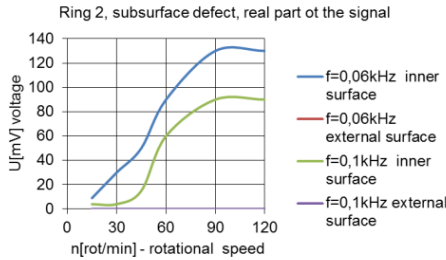


Fig. 26. Impact of rotational speed on the defect signal (Ring 2, subsurface defect)

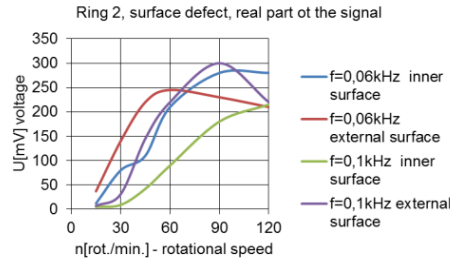


Fig. 27. Impact of rotational speed on the defect signal (Ring 2, surface defect)

The authors introduced a defect type coefficient “ K_{dt} ” that is a quotient of a subsurface defect signal value to a surface defect signal value. The coefficient is defined using the following equation (1):

$$K_{dt} = \frac{U_{sub.}}{U_{sur.}} \tag{1}$$

K_{dt} Defect type coefficient
 U_{sub} Subsurface defect signal value
 $U_{sur.}$ Surface defect signal value

The coefficient varies between 0.3 and 0.85 for Ring 1 (Fig. 28), and 0.4–0.8 for Ring 2, at a rotational speed of 30 rpm (Fig. 29). No subsurface defects were detected in Ring 2 at the time of analysis of its outer surface.

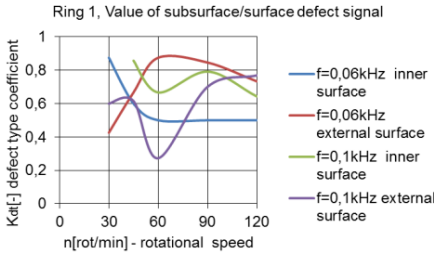


Fig. 28. Defect type coefficient for Ring 1

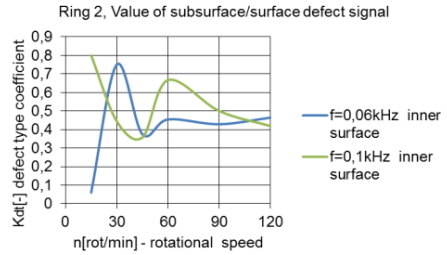


Fig. 29. Defect type coefficient for Ring 2

To verify what influence the placement of the measuring head has, the authors introduced a defect orientation coefficient “Kor” defined by equation 2.

$$K_{or} = \frac{U_{inn.}}{U_{ext.}} \tag{2}$$

- K Defect type coefficient
- $U_{inn.}$ Value of a defect signal measured on an inner surface
- $U_{ext.}$ Value of a defect signal measured on an external surface

In the case of Ring 1, at a transducer frequency of 0.06 kHz, higher rotational speed increased the value of the defect orientation coefficient from 0.2 to 1, for a surface defect, and from 0.35 to 0.7 for a subsurface defect. At a transducer frequency of 0.1 kHz, in both cases, the coefficient stabilized at the level of 0.2, at a rotational speed of 90 rpm (Fig. 30). Similar results were obtained for a surface defect in Ring 2, but at a frequency of 0.066 kHz (Fig. 31), while at a frequency of 0.1 kHz, and a concurrent increase in a rotational speed from 30 to 120 rpm, the defect orientation coefficient grew from 0.2 to 1.

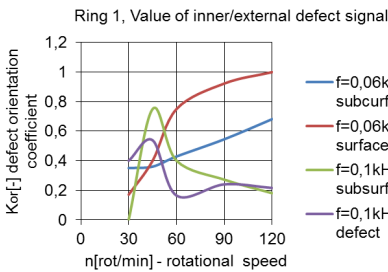


Fig. 30. Defect orientation coefficient for Ring 1

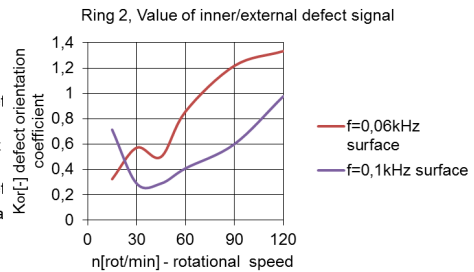


Fig. 31. Defect orientation coefficient for Ring 2

6 Conclusions

The tests showed that increasing rotational speed of studied objects facilitates detection of surface and subsurface defects. The value of the defect signal for Ring 2, compared to Ring 1, was twice as high, which resulted from greater linear speed of the surface tested.

The instrumentation the authors used in their tests enables detection of defects located at up to 1 mm under the surface of a test object. The value of the subsurface defect constitutes between 30 and 90% of the value of the surface defect, which is enough to consider the ring to be faulty.

The tests indicated that detection of defects in an inner surface, compared to defects located in an outer surface, is a far more complex process that is hampered by the deflation of the middle point of the measuring head from the tested surface by 0.6 mm (for Ring 1), and 0.3 (for Ring 2). To eliminate this problem, it is advisable to use a grip equipped with two measuring heads (one for each ring tested) in future investigations.

In special applications, the front of the measuring head needs to be properly formed to ensure full contact with the test object.

In the target system, quality inspection should be carried out at the transducer frequency of 0.06 kHz. Determining the appropriate rotational speed of a spindle driving the ring tested requires additional tests, as it is necessary to investigate how vibration of the measuring system affects test results.

Test results can be used in the design of device for automatic quality inspection of axisymmetric elements like pipes, shafts, or bushings.

Acknowledgements. Scientific work executed within the Strategic Programme “Innovative Systems of Technical Support for Sustainable Development of Economy” within Innovative Economy Operational Programme.

References

1. Matecki, K., Zbrowski, A., Matras, E.: Methods for detection of material defects in roller bearing rings employing eddy current inspection techniques. *Logistyka* 3, 4187–4197 (2014) (In Polish),
2. Zbrowski, A., Matecki, K.: Detection of sub-surface defects with the use of eddy current method. *Maintenance Problems* 1, 35–48 (2012) (in Polish)
3. Zbrowski, A., Matecki, K.: Identification of internal defects in roller bearing rings. *Maintenance Problems* 2, 229–243 (2012) (In Polish)
4. Zbrowski, A.: X-Ray Tomography in the Diagnostics of Roller Bearing Rings. *Solid State Phenomena* 223, 211–220 (2015)
5. Goch, G., Dijkman, M.: Holonic quality control strategy for the process chain of bearing rings. *CIRP Annals - Manufacturing Technology* 58, 433–436 (2009)
6. Zbrowski, A., Józwiak, W.: Influence of the gap between measuring head and tested object on the results of eddy current test method. *Solid State Phenomena* 223, 246–254 (2015)

7. Kahrobaee, S., Kashefi, M., Alam, A.S., Magnetic, N.D.T.: Technology for characterization of decarburizing depth. *Surface & Coatings Technology* 205, 4083–4088 (2011)
8. Devillez, A., Dudzinski, D.: Tool vibration detection with eddy current sensors in machining process and computation of stability lobes using fuzzy classifiers. *Mechanical Systems and Signal Processing* 21, 441–456 (2007)
9. Marchand, B., Decitre, J.M., Casula, O.: Innovative Flexible Eddy Current Probes for the Inspection of Complex Parts. In: 18th World Conference on Nondestructive Testing, Durban, South Africa, April 16-20 (2012)

Author Index

- Bazydło, Piotr 1, 11, 39, 49, 59
Bieńkowski, Adam 121
Bodnicki, Maciej 21
Borkowski, Zdzisław 171
- Charubin, Tomasz 255
Ciuk, Tymoteusz 101, 111
Czajka, Piotr 27
- Dąbrowski, Szymon 1, 39, 49, 59, 181
- Fotowicz, Paweł 67
- Gawlik, Grzegorz 75, 129
Gińko, Oskar 205
Grzybowski, Janusz 21
- Hamela, Marek 171, 181
- Idźkowski, Adam 83
- Jackiewicz, Dorota 197
Jakubowska, Małgorzata 181
Jóźwik, Wojciech 339
Juś, Andrzej 91, 189
- Kachniarz, Maciej 101, 111, 121, 129
Kaczmarek, Piotr 137
Kamiński, Marcin 171, 181, 237
Korczyński, Marian J. 293
Kozłowska, Anna 75, 129
- Łoboda, Waldemar 205
- Maciąg, Marek 205
Maciąg, Marek 255
Mankowski, Tomasz 137
- Mikhal, Aleksander A. 147, 157
Missala, Tadeusz 171, 181, 237
Mizak, Wojciech 27
- Nowak, Paweł 75, 91, 189
Nowicki, Michał 59, 197, 219, 237, 255, 265
- Oszwałdowski, Maciej 101, 111
- Pasternak, Iwona 171, 237
Petruk, Oleg 101, 111, 205
Pogorzelski, Dawid 181
- Råback, Peter 219
Radkowski, Stanisław 303
Ruokolainen, Juha 219
- Safinowski, Marcin 205
Salach, Jacek 101, 111, 121, 171, 219
Stefko, Kamil 219
Strupiński, Włodzimierz 101, 111, 171, 237
Švec Sr., Peter 197
Świętochowski, Paweł 83
Szałatkiewicz, Jakub 171
Szewczyk, Roman 1, 11, 39, 49, 59, 75, 91, 101, 111, 121, 129, 171, 181, 189, 197, 205, 219, 237, 245, 255, 265, 277
Szpakowska-Peas, Ewelina 225
- Tomasik, Jan 171, 181
Tomczynski, Jakub 137
Trzcinka, Krzysztof 101, 111, 205, 237, 245, 255

- Urbański, Michał 265, 277
- Volodarsky, Evengniy T. 285
- Walendziuk, Wojciech 83
- Warsza, Zygmunt L. 83, 147, 157, 285, 293
- Wąsik, Marek 313
- Waszczuk-Młyńska, Aleksandra 303
- Winiarski, Wojciech 101, 111, 171, 181,
205, 237, 255, 265
- Wójcicki, Tomasz 323
- Wojtasiak, Mateusz 75, 129
- Zaczyk, Marcin 333
- Zbrowski, Andrzej 339